Année 2016

UNIVERSITE DE CERGY PONTOISE

THESE

Présentée pour obtenir le grade de

DOCTEUR DE L'UNIVERSITE DE CERGY PONTOISE

Ecole doctorale: Sciences et Ingénierie
Specialité: Génie Electrique

Soutenance publique prévue le 12 Décembre 2016

Par

Maria EL ACHKAR

Contribution to the Sizing and Control of the Cascaded Doubly Fed Induction Generator

JURY

Rapporteurs	:	Prof. Farid Meibody-Tabar	Université de Lorraine, Nancy
		Prof. Gerard Champenois	Université de Poitiers
President	:	Prof. Brayima Dakyo	Université du Havre
Examinateur	:	Dr. Nicolas Patin	Université de Technologie de Compiègne
Directeur de thèse	:	Prof. Eric Monmasson	Université de Cergy Pontoise
Co-directeurs	:	Prof. Georges Salloum	Université Libanaise
		Dr. Sandrine Le Ballois	Université de Cergy Pontoise

Laboratoire SATIE-UCP/UMR 8029, 1 rue d'Eragny, 95031 Neuville sur Oise France

This work is dedicated to my parents and beloved one who believed in me, patiently encouraged me throughout the challenging years of research and helped me to achieve my goals.

Acknowledgment

The research outcomes presented throughout different chapters, has taken the SETE [1] team, SATIE [2] laboratory and CERGE [3] laboratory as a work platform, providing a significant assistance and consolidation in the compilation of this thesis. The work was carried out under the direct supervision of Prof. Eric Monmasson and Dr. Sandrine Le Ballois, both from SATIE, University of Cergy Pontoise, and Prof. Georges Salloum from CERGE at the Lebanese University.

Above all, i would like to express my gratefulness to my supervisor Prof. Eric Monmasson, head of SATIE pole, who kept his eye on my research scenes all over its lifespan, stretching my work horizon and creating constantly new prospects, being thereby a perfect role model for any Ph.D. student and so for me indeed.

Secondarily, my sincere gratitude goes to my co-supervisor Prof. Georges Salloum, head of CERGE research team, to whom I am indebted for his moral support, indispensable and significant help, steering this project to a prolific end result. The present thesis would not have been possible without his competent and timely contributions.

Many thanks to my second co-supervisor Dr. Sandrine Le Ballois, for her kindness in reviewing and progressively commenting my output, her remarks were very helpful in refining my reports.

I am also thankful to Dr. Nicolas Patin from LEC, University of Technology of Compiègne, for his helpful comments throughout the thesis stages.

My deep appreciation goes to Dr. Rita Mbayed, who harnessed her abilities and employed her experience, enlightening me to withstand and then get over my research obstacles.

1. Systèmes d'Energies pour les Transports et l'Environnement : Energy systems for transport and environment.
2. Systèmes et Applications des Technologies de l'Information et de l'Energie : Systems and Applications in Information and Energy Technologies
3. Commande Energies Renouvelables et Génies Electriques

I would like to thank the members of the assessment committee Prof. Brayima Dakyo, Prof. Gerard Champenois, Prof. Farid Meibody-Tabar, and Dr. Nicolas Patin for their interest in evaluating my work. The extensive time you sacrificed to review this thesis is much appreciated.

Regards and salutations to Don Abasse Boukari and all the personnel of SATIE laboratory for providing the best working conditions during my stays in France. I would also like to thank my colleagues in France and Lebanon who surrounded me with the healthiest familial and professional environment to successfully complete my research. Not missing engineer Elias Saleh for his important assistance in the experimental part, lending a big hand in the maintenance of the equipments when needed.

Special thanks go to my fellow Dr. Jawad Khoury with whom I stood in the middle of the storm and sailed to the safe harbor altogether, after 10 years of hard work and determination since our undergraduate studies.

At the end how can I finalize this acknowledgment without launching the biggest recognition to my father who is watching over me from where he rests, my mother, and my brother. Their endless support helped me getting through this tiring experience.

Finally big thanks to my fiancé for his continuous encouragement, strengthening and embracing me in the hardest times through my ups and downs. Together we stand stronger !

Abstract

This thesis is a contribution to the power sizing and the control of a Cascaded Doubly Fed Induction Generator (CDFIG). The machine model for simulation is based on a modular representation, derived from the Park model of two distinct Doubly Fed Induction Machines expressed in their own reference frames. The dynamic model of the cascaded machine is then extended to be described in a unified reference frame. This representation is convenient for the sizing of the machine and for the design of the controller. The steady state power operating margins of the cascaded machine are investigated. A generic analytic method is suggested to derive the active-reactive power domain. The limit curves are defined in terms of the rated quantities of the machine. The study takes into account the magnetic circuit saturation effect. It is proven that the power capability of the machine is determined by the stator current maximum values and is subject to several limitations. The analytical approach is tested and validated by experimental measurements. The CDFIG is controlled in grid-connected and standalone operation modes. In grid-connected application, the attention is paid to high power wind generation systems. A new maximum power tracking of a variable speed wind turbine is suggested. The generating plant is carried to provide a quasi-constant maximum power regardless wind fluctuations. In addition to active power optimization the power factor is adjusted according to the grid code requirements and the operating domain of the integrated unit. A virtual flux oriented vector control is applied for the decoupled regulation of active and reactive powers, leading to grid voltage sensorless operation. In standalone operating mode, the study treats in particular the embedded aircraft power system generation. Two distribution networks are considered: constant frequency AC network and DC network. In both cases, the control aims to maintain a constant output voltage. The operation of the CDFIG supplying unbalanced three-phase load is further explored. Control schemes to cope with unbalanced stator voltage conditions are developed. Two compensation methods are elaborated: the first dealing with dual rotating frames and the second is based on repetitive controller. Simulations with Matlab/Simulink software and experiments validate the control approaches.

keywords: Cascaded doubly fed induction machine, active-reactive power domain, maximum power point tracking, grid-connected wind turbine, standalone application, unbalanced load.

Résumé

Le travail présenté dans cette thèse est une contribution au dimensionnement et à la commande d'un générateur de type Cascade de Machines Asynchrones à Double Alimentation. Le modèle de la machine pour les simulations est basé sur une représentation modulaire qui découle du modèle de Park de deux machines asynchrones doublement alimentées distinctes, en respectant deux systèmes de référence. Le modèle dynamique est ensuite étendu pour décrire la machine dans un repère unifié. Cette représentation est cruciale pour le dimensionnement de la machine et la synthèse de la commande. Le domaine de fonctionnement de la cascade en régime permanent est exploré. Une méthode analytique générique est proposée pour établir les plages de puissances active-réactive. Les courbes limites sont définies par rapport aux grandeurs nominales de la machine. L'étude prend en compte l'effet de saturation du circuit magnétique. Il est prouvé que la capacité en puissance de la machine est déterminée par les valeurs maximales des courants statoriques et peut être soumise à plusieurs limitations. L'approche analytique est testée et validée par des mesures expérimentales. Deux cas sont considérés pour la commande de la cascade : un générateur raccordé au réseau et un générateur autonome. Pour la connexion au réseau l'application visée est les éoliennes de grande puissance. Une nouvelle méthode pour l'extraction de la puissance maximale d'une éolienne à vitesse variable est proposée. Le système est contrôlé dans le but de fournir une puissance maximale quasi-constante indépendamment des fluctuations du vent. En plus de l'optimisation de la puissance, le facteur de puissance est également ajusté selon les normes de raccordement standard imposées par les services système, et les limites de fonctionnement de l'unité intégrée. Une commande vectorielle sans capteur de tension, basée sur une orientation suivant un flux virtuel, est appliquée pour la régulation découplée des puissances active et réactive. Pour le fonctionnement en mode isolé, l'application visée est la génération électrique pour système avionique embarqué. Deux réseaux de distribution sont traités : réseau AC à fréquence fixe et réseau DC. Dans les deux cas, la commande est élaborée dans le but de maintenir une tension de sortie constante. Le fonctionnement de la cascade alimentant une charge triphasée déséquilibrée est également étudié. Des schémas de contrôle servant à la compensation du déséquilibre des tensions statoriques sont développés. Deux méthodes de compensation sont proposées : l'une basée sur le principe de deux repères tournants et l'autre sur un correcteur répétitif. Les approches présentées sont validées par simulation avec Matlab/Simulink et par expérimentation.

Mots-clés: Cascade de machines asynchrones doublement alimentées, domaine de puissances active-reactive, extraction maximale de puissance, éolienne connectée au réseau, application isolée, charge déséquilibrée.

Table of contents

Nomenclature

Acronyms

AC	Alternating Current
BDFIM	Brushless Doubly Fed Induction Machine
BDFRM	Brushless Doubly Fed Reluctance Machine
CDFIG	Cascaded Doubly Fed Induction Generator
CDFIM	Cascaded Doubly Fed Induction Machine
DC	Direct Current
DFIG	Doubly Fed Induction Generator
DFIM	Doubly Fed Induction Machine
EMF	ElectroMotive force
GSC	Grid Side Converter
IGBT	Insulated Gate Bipolar Transistors
MEA	More Electric Aircraft
MPPT	Maximum Power Point Tracking
MSC	Machine Side Converter
PCC	Point of Common Coupling
PF	Power Factor
PI	Proportional Integral
PMSG	Permanent Magnet Synchronous Generator
PMSM	Permanent Magnet Synchronous Machine
PWM	Pulse Width Modulation
RMS	Root Mean Square
SF-CDFIM	Single-Frame Cascaded Doubly Fed Induction Machine
TSO	Transmission System Operator
VF	Virtual Flux
VSCF	Variable Speed Constant Frequency
WECS	Wind Energy Conversion System
WT	Wind Turbine

Index and Exponents

$\underline{\hat{x}}$	Conjugate of phasor quantity
$\tilde{X}$	Estimated quantity
$\underline{x}^*$	Per unit form of phasor quantity
X^+/X^-	Positive/negative sequence component
X_n	Nominal quantity
X_s, X_r	Stator, rotor quantity
X_{dc}	Quantity related to the DC side of the converter
X_L	Quantity related to the load
X_{ref}	Refrence quantity

DFIM parameters

$\dot{\xi}_r$	Electrical speed of the (dq) frame with respect to rotor frame (rad/s)
$\dot{\xi}_s$	Electrical speed of the (dq) frame with respect to stator frame (rad/s)
ω_s/ω_r	Stator/rotor frequency (rad/s)
Φ_s/Φ_r	Stator/ rotor flux (Wb)
σ, σ_p	Coefficient of dispersion
ξ_r	Electrical Park frame angle for rotor quantities (rad)
ξ_s	Electrical Park frame angle for stator quantities (rad)
g	Slip ratio of the DFIM
g_c	Slip ratio of the CDFIM
L_r	Rotor cyclic inductance (H)
L_s	Stator cyclic inductance (H)
M_{sr}	Stator to Rotor mutual inductance (H)
p	Number of pole pairs
P_m	Mechanical power (W)
P_s/P_r	Stator/rotor active power (W)
Q_s/Q_r	Stator/rotor reactive power (var)
R_r	Rotor resistance (Ω)
R_s	Stator resistance (Ω)
T_{em}	Electromagnetic torque (Nm)

Physical quantities

Ω	Rotor mechanichal speed $\Omega = \dfrac{d}{dt}\theta_m$ (rad/s)
ω_g	Grid frequency (rad/s)
Φ	Virtual line flux (Wb)
θ_m	Rotor mechanichal angular position (rad)
C	DC-link capacitance (F)

e	EMF instantaneous value (V)
e_g	Grid voltage (V)
f	Frequency (Hz)
i	Current instantaneous value (A)
i_g	GSC input line current (A)
L_l, R_l	Inductance and resistance of supply side inductors (H, Ω)
P	Active power exchanged between the GSC and the grid (W)
Q	Reactive power exchanged between the GSC and the grid(var)
S	Apparent power (VA)
T	Torque (Nm)
u	Line-to-line voltage (V)
U_{dc}	DC bus voltage (V)
v	Voltage instantaneous value (V)
v_g	GSC input voltage (V)

Symbols

$\alpha\beta_r$	Rotor Clarke $\alpha\beta$ frame
$\alpha\beta_s$	Stator (stationary) Clarke $\alpha\beta$ frame
abc_r	Rotor abc frame
abc_s	Stator abc frame
dq	Park rotating frame
dq^+	Park frame rotating at $+\omega_s$
dq^-	Park frame rotating at $-\omega_s$
$(\underline{x})_{yz}$	Phasor quantity $\underline{x}$ expressed in the (yz) reference frame
$[x]_{3r}$	Vector expressed in the rotor three-phase (a, b, c) reference frame
$[x]_{3s}$	Vector expressed in the stator three-phase (a, b, c) reference frame
$[x]_{yz}$	Vector expressed in the (yz) reference frame
$\lvert F(j\omega)\rvert$	Norm of transfer function $F(s)$
$\lvert\underline{x}\rvert$	Magnitude of the alternating quantity x
$\underline{x}$	Phasor (complex) quantity $\underline{x} = X_d + jX_q$
$C(s)$	Controller transfer function
$F(s)$	Closed-loop transfer function
$G(s)$	Open-loop transfer function
s	Operator of Laplace
X	RMS value of quantity x
X_d, X_q	d-axis,q-axis components in Park reference frame
X_{d^+}, X_{q^+}	d-q components in dq^+ Park reference frame
$X^+_{d^+}, X^+_{q^+}$	Positive sequence d-q components in dq^+ Park reference frame

$X^-_{d^+}, X^-_{q^+}$	Negative sequence d-q components in dq^+ Park reference frame
X_{d^-}, X_{q^-}	d-q components in dq^- Park reference frame
$X^+_{d^-}, X^+_{q^-}$	Positive sequence d-q components in dq^- Park reference frame
$X^-_{d^-}, X^-_{q^-}$	Negative sequence d-q components in dq^- Park reference frame

Quantities related to the WT

β	Pitch angle (°)
λ	Tip speed ratio
C_p	Power coefficient
G	Gearbox ratio
R_p	Radius of turbine blade (m)
v_w	Instantaneous wind speed (m/s)
v_{mean}	Average of the wind speed (m/s)

Introduction

Due to the recent interest in renewable energy systems and embedded applications and the advance in power electronics, the development and control of Variable Speed Constant Frequency (VSCF) generators have become a very important research topic. Compared to constant speed electric systems, variable speed systems are more flexible, efficient and reliable. Among the possible types of VSCF generators is the Doubly Fed Induction Machine (DFIM). This generator is able to achieve independent control of active and reactive powers and supply constant frequency voltage at variable speed using partially rated converters [36]. The rating of the power converters used in the rotor circuit is determined by the range of the operating speed. The DFIG is widely used in many industrial grid-connected and standalone applications. Nevertheless, the main drawback of this classical structure is the presence of brushes and slip rings which increase significantly the maintenance cost, reduce the system reliability and make the machine unsuitable for embedded applications.

An alternative solution for conventional DFIM replacement is the Cascaded Doubly Fed Induction Machine (CDFIM) [44], [91]. This configuration retains the benefits of the single wound rotor induction machine in a brushless structure that provides robustness, reliability and low maintenance cost which are fundamental in the above-mentioned applications. Yet, the price to pay is a more complex structure that requires an efficient control design methodology.

This thesis is a contribution to the power sizing and the control of the CDFIM operating as a grid-connected and a standalone generator.

In grid-connected mode, the attention is paid to high power Wind Energy Conversion Systems (WECS). In standalone mode, the embedded electric aircraft generation system is considered. However the study remains valid to other industrial applications such as autonomous windmills and hydro-power systems.

Context outline

The wind energy technology is dynamically growing and experiencing a rapid development all over the world. This non-polluting and economically viable solution has become one of the most important and promising sources of renewable energy in

recent years. Nevertheless, the increasing penetration of large wind farms is disturbing the overall power system performance due to the uncontrollable generated power. Consequently, the connection and the dynamic behavior of Wind Turbines (WT) under different grid conditions are becoming an important concern, and new grid code requirements are introduced [37], [130], [132].

DFIG is the most used generator in high power WECS [80]. However, the presence of electric brushes involves permanent maintenance, hence lower reliability and extra cost [131]. Since wind energy applications are frequently located in remote places, a high level of reliability and long-term operation are required. Therefore, the CDFIG is a potential alternative solution to be used for windmill generation systems.

The WTs are commonly controlled using the well known Maximum Power Point Tracking (MPPT) method [29]. The turbine speed is adjusted to extract instantaneously the maximum available power for every wind velocity. This conventional technique, designated in this manuscript by "instantaneous MPPT", ensures maximum system efficiency and power optimization. However, fluctuating and uncontrollable active power is produced at the output of the generating unit due to the stochastic aspect of the wind. The power oscillations imply significant variations in electromagnetic torque which increase the stress on the generator and the grid side and disturb the network stability. In this regard, the increasing integration of wind plants into the grid requires new control methods to be implemented in order to sustain the power network stability. A new strategy for maximum power tracking, denoted "mean MPPT" for the rest of this thesis, is proposed. The system aims to provide a quasi-constant maximum power regardless wind fluctuations. The main motivation behind this method is to enhance the quality of the power feeding the grid for stability purposes, while maintaining high system efficiency.

The majority of research interests related to the CDFIG are concerned by the grid-connected wind energy systems [44], [55], [66], [109], [131]. Conversely, only few papers studied the CDFIG in standalone operation [87], [91], [141]. With its brushless structure, fractionally rated converters and constant frequency output voltage, the CDFIG is suitable for many industrial autonomous applications where VSCF operation is required such as wind energy, hydro-power and embedded systems. In this sense, in order to assess the full potential and capability of this generator, the standalone operation performance is worthy to be studied and new control strategies should be investigated.

The studies conducted in the literature on autonomous CDFIG have focused on normal and balanced grid conditions. Nevertheless, in practical use, unexpected conditions such as unbalanced loads exist and have a strong influence on the performance of the generator, the behavior of other connected loads and the standalone

configuration. For this reason appropriate algorithms are required to compensate the voltage unbalance and reject the impact of unbalanced load.

A standalone industrial application considered for simulation in this manuscript is an embedded aircraft power system generation. The recent aircraft industry tends toward the concept of a More Electric Aircraft (MEA). It involves the replacement of conventional equipments, based on mechanical, pneumatic and hydraulic, by electrical devices improving the performance, reliability and life cycle cost of the aircraft and reducing fuel consumption [95], [111]. To cope with the increasing demand of electrical power brought by the MEA, new architectures and voltage levels for the on-board electrical power distribution systems are applied [14], [35]. Three electrical networks are explored in aircraft systems: constant frequency AC network, variable frequency AC operation and/or DC distribution network.

Presently, aircraft embedded generators are based on a three-stage integrated synchronous machine [21], [113]. This structure is standalone, and avoids slip rings and brushes. However, the price to pay is its obvious complexity. In addition, constant frequency voltage at variable speed cannot be directly provided by synchronous generators. The CDFIM is presented as an alternative to substitute the three-stage synchronous machine presently in use in most of the aircraft power systems.

Regarding the CDFIM itself, the research effort has focused on the performance and the development of new control schemes under grid disturbances [44], [55], [66], and normal grid conditions [91], [108], [109]. Yet, the working range of the generator and its contribution to reactive power generation, as required by the corresponding grid codes and/or the load demands, were not treated in the literature. Although the power sizing of the generator is of great importance for practical applications. Indeed, it ensures the machine is being operated in a state within its ratings and allows to choose the appropriate machine that is best adapted for the desired application, according to its power capability. For this purpose, the power operating margin of the CDFIM is to be investigated.

Document organization

The remainder of the thesis is divided as follows:

The state of art includes an overview of brushless doubly fed induction machines in terms of performance and of brushless structure. A literature review is conducted on WECS presenting previous works on grid-connected generators and various control strategies of the integrated WTs. In embedded aircraft systems, the concept of MEA is considered. A state of art of voltage levels and architectures for the on-board

electrical power distribution systems as well as machine structures proposed for this application is presented.

Part I is dedicated to the modeling, analysis and power sizing of the CDFIM. The machine model is elaborated in Chapter 1. It is based on a modular representation of the system derived from the model of two wound rotor induction machines expressed in their own reference frames. The mathematical model of the CDFIM is then extended to describe the machine in a unified reference frame. This representation is more convenient for the power sizing and for the design of the machine controllers. Chapter 2 deals with the steady state power operating domain of the CDFIM. A generic analytic method is suggested to derive the active-reactive power margins. The limit curves are defined in terms of the rated quantities of the machine. The study includes the influence of the slip range and terminal voltage variation on the power limit curves. The effect of magnetic circuit saturation is further investigated. The analytical approach is tested and validated by experimental measurements.

Part II studies the CDFIM operating as a grid-connected generator in high power WECS. A new approach for maximum power tracking of a variable speed WT under normal grid conditions is presented. The generating unit intends to provide the maximum constant power associated to the average of the wind speed, predicted over a predefined interval. In addition to power optimization, the system is controlled to supply additional reactive current for Power Factor (PF) regulation, according to the grid code requirements and the operating domain of the integrated unit. On that basis, a decoupled vector control of active and reactive powers is established by means of a new voltage sensorless approach based on Virtual Flux (VF) orientation. The dynamic behavior and the overall description of the wind generation system based on the CDFIG are elaborated in Chapter 3. Chapter 4 is devoted to the VF oriented vector control of the global system. In Chapter 5, the new mean MPPT approach is exposed and compared to the conventional instantaneous MPPT algorithm.

Part III investigates the brushless CDFIM operating as a standalone generator. An application for embedded aircraft power system is considered. Two distribution networks are studied: constant frequency AC grid and DC grid. Chapter 6 and 7 deal with the constant frequency AC network. In the first place, normal grid conditions are considered. A classic vector control is elaborated in Chapter 6 to meet the output voltage requirements. The operation under unbalanced loads is then investigated. Advanced control schemes based on dual rotating frames and repetitive controllers are implemented in Chapter 7 to compensate the voltage imbalance and reject the unbalanced load impact on the generated stator voltages. Chapter 8 treats the DC network. The CDFIG is cascaded to a diode bridge rectifier. The controller aims to maintain a constant output DC voltage despite the load and speed variation.

State of Art

DFIGs are widely used in many industrial applications where VSCF electric power generation is required. They are exploited in grid-connected and standalone fields such as wind energy [99] [103], [128], hydro-power [114] and aircraft systems [62], [90]. In spite of variable speed prime movers, the DFIGs can be directly connected to a constant frequency grid thanks to the regulation of the rotor current. The frequency and amplitude of the rotor current are adapted to compensate any speed and/or load variation.

In grid-connected mode, the stator active and reactive powers are independently controlled. In standalone operation, the controller aims to achieve a constant output voltage despite the load and speed variations. When operated over a limited speed range, the power converters are sized for a fraction of the nominal power [36], [60].

Nevertheless, the limitation of the DFIG is its brushes and slip rings structure, which involves permanent maintenance and reduces the life time of the machine [118], [131]. Consequently, this classical structure is not completely adapted in applications where high level of reliability and long time maintenance periodicity are required.

An alternative to substitute the single wound rotor induction machine is the CDFIM [44], [91]. If the rotor windings of a given DFIM are supplied by another three-phase AC machine, a second DFIM is introduced leading to a complete brushless structure.

The converter ratings and behavior of the CDFIM is similar to the DFIM. Several previous works have investigated the operation of the CDFIM as a variable speed constant frequency generator in various applications including windmills [44], [109], small scale hydro-power systems [59], and embedded aircraft industry [86], [91].

Brushless doubly fed induction machines-State of art

Different structures of brushless doubly fed induction machines are reported in the literature. The main types are classified in the following.

The CDFIM

The CDFIM is the fundamental type of a brushless doubly fed induction machine [86]. The idea of this architecture goes back to more than a century ago [126]. The CDFIM is obtained by combining two individual wound rotor induction machines as shown in Figure 1. The rotors are mechanically and electrically coupled so that the brushes are no longer required for the direct connection of slip rings. Since the rotor voltages of both machines are equal, it is possible to control one induction machine with the stator of the other machine.

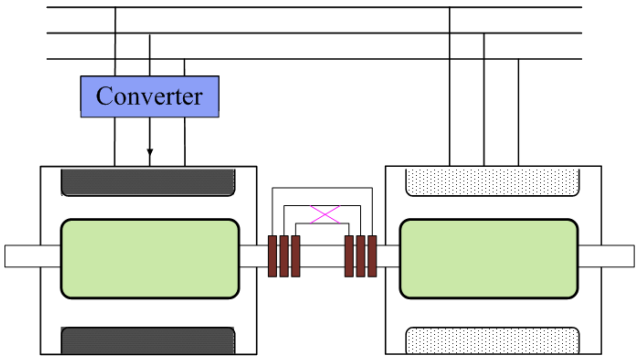

Figure 1: Principle of a CDFIM

The two machines can theoretically have any pole pairs combination with the rotors electrically connected in positive or in negative phase sequence. However, when it comes to machine efficiency and converter ratings, the most satisfying performances for generating systems are achieved by an inverse interconnection configuration [92]. It allows the torques to combine in the additive manner. The direct coupling sequence must be avoided.

The main difficulty when working with the CDFIM is its inherent complexity, and the existence of multiple reference frames. The major issue is to synthesize an efficient global control method for these two connected machines. A modeling methodology of the CDFIM based on dynamical equivalent circuits is suggested in [91]. It describes the machine not only for steady state operation but also in transient mode operations. This representation is used to design the machine controller based on the inversion principle of dynamical models. A space phasor model of the CDFIM in a common

arbitrary single reference frame is proposed and verified experimentally in [38], [107]. In this unified coordinate, the dynamic model of the CDFIM is independent of the rotor angle position and analogous to the standard induction machine, which allows to exploit similar control strategies [47], [109].

It shall be noted that although the CDFIM is the basic structure of a brushless doubly fed machine, such a machine connection is not practical for real industrial application. The weight and the size of the CDFIM are too important. A larger machine size is required to produce the same torque as a wound rotor induction machine [79]. Besides, due to the large amount of windings, the losses are higher than for a single DFIM of a comparable power rating [49]. To cope with these shortcomings and obtain more efficient and compact solution, the cascaded structure is improved and new topologies are studied. The most recognized structures are listed and described hereby.

The Single-Frame Cascaded Doubly Fed Induction Machine (SF-CDFIM)

The SF-CDFIM brings the idea of the CDFIM a step further by combining the two induction machines in one common frame as illustrated in Figure 2.

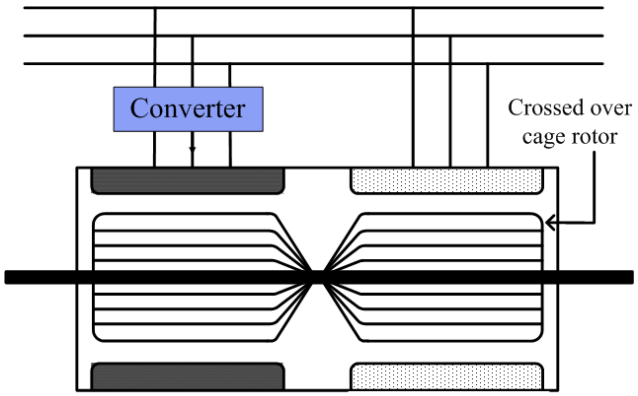

Figure 2: Principle of a SF-CDFIM

The SF-CDFM is mechanically more robust. The two stator windings are axially aligned. A cage rotor structure to replace the wound rotor is made out of rotor bars. The cage rotor is "crossed-over" between the two machine sections in order to produce an additive torque by the two individual machines. The power flow, frequency behavior, model and control strategies are the same as the CDFIM [49].

The Brushless Doubly Fed Induction Machine (BDFIM)

A second alternative for the CDFIM is the BDFIM. It is a compact machine solution. The principle of the proposed machine is presented in Figure 3. It merges

the two induction machines into one machine having two stator windings in the same slots.

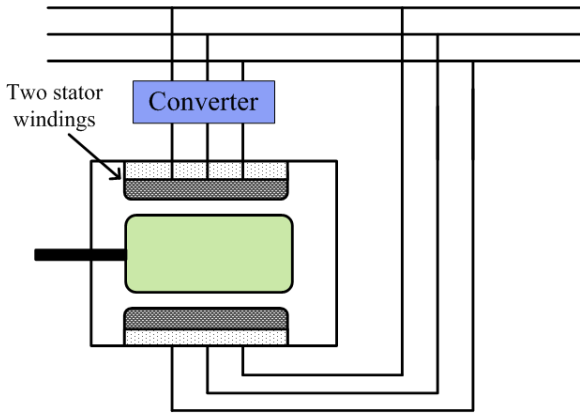

Figure 3: Principle of a BDFIM

It was proposed by Hunt in 1907 [51] with initially a special wound rotor. Then a particular cage rotor structure, which has much of the simplicity and robustness of a squirrel cage winding was developed by Broadway in 1970 to replace the wound rotor [25]. The stator windings of the BDFIM share a common magnetic circuit. Hence, to avoid direct transformer coupling between the two stator windings, additional constraints for the numbers of pole pairs are introduced. The two stators must have a different number of pole pairs. Besides, the numbers must differ by more than one to avoid unbalanced magnetic pull on the rotor [25]. The rotor is specially designed to induce a cross-coupling effect between the two stator windings through the rotor [107], [140], which is a prerequisite for torque to be produced from the machine. The machine performance and power density improve as this cross-coupling is improved.

The rotor is formed of a "multi-circuit single-layer bar winding" as shown in Figure 4 (known as the nested-loop), which is a particular cage structure. It consists of identical rotor poles (or nests of conductors). The number of rotor poles must equal the sum of the two stator winding pole pairs [25], [137].

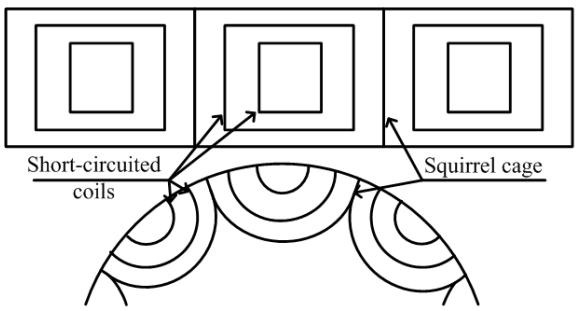

Figure 4: Multi-circuit single-layer bar winding [24]

The power and frequency relations of the CDFIM are applicable for the BDFIM.

Similar modeling approach and control strategies can be elaborated. However, the air-gap flux is very irregular because of rotor structure and the complicated combination of the stator and rotor poles [57].

Over the last years more researchers have studied this type of doubly fed brushless machine. Various models and control methods are investigated with attention being paid towards their application in wind power generation, although the benefits of the BDFIM for variable speed drives have also been demonstrated [20], [118].
A per phase equivalent circuit for the machine is suggested and experimentally validated in [116]. The equivalent circuit is used to estimate the parameters of the machine from experimental measurements. Based on this model, active and reactive power flow and performance analysis of the BDFIM is performed in [79]. A unified reference frame model of the CDFIM is proposed in [107]. Using this model, vector control schemes of the generator based on stator field orientation techniques are developed and experimentally tested in a number of works [108], [121]. The studies also included the operation of the generator during disturbances [131].

The Brushless Doubly Fed Reluctance Machine (BDFRM)

An alternative machine, the BDFRM is further introduced by Broadway [24] and later developed by Longya Xu [144], [145]. Theoretical analysis and different control strategies have been done by Betz and Jovanovic [18], [57], [58]. The stator of the BDFRM is identical to the BDFIM, but a reluctance type rotor is used instead of the cage rotor. The reluctance rotor structure can be classified into salient pole type, axially laminated type and radially laminated type. Different rotor structures are symbolized in Figure 5.

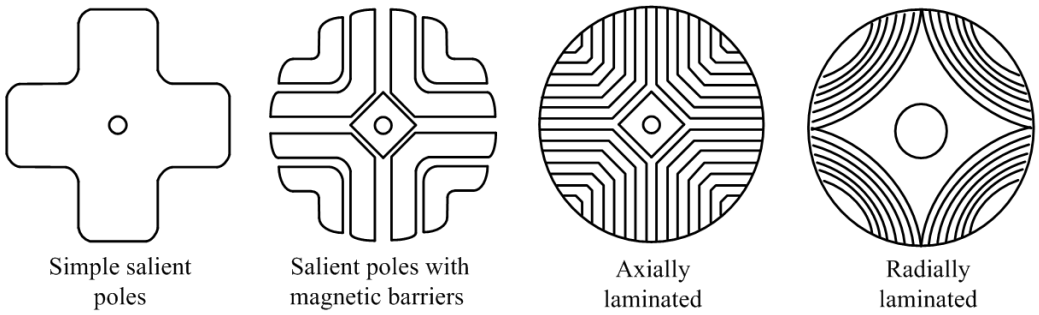

Figure 5: Rotor types of a BDFRM [63], [145], [146]

Based on finite element analysis, the various structures show different degrees of magnetic mutual coupling between the two stator windings, which in turn determine the machine power density and performance [145]. A good rotor design should have high saliency ratio and be manufacturable [63]. Among the possible rotor structures, a segmented rotor offers better coupling between stator windings than simple salient

pole rotor. The axially laminated rotor provides the highest mutual coupling and thus achieves a high torque capability but is subject to excessive eddy current losses [119], [145]. The salient pole rotor with magnetic barriers produces lower flux and mutual coupling but offers a very simple and rugged structure with lower iron losses [145]. The optimal reluctance rotor structure has not been established yet. However, recent developments have resulted in high saliency reluctance rotors based on a radially laminated structure which offers low iron losses, desirable performance with affordable manufacturing difficulty [63].

Compared to the BDFIM, the BDFRM is more efficient as there are no rotor currents present and hence no copper losses [57]. Besides, it is considerably easier to model and control since the BDFIM has an additional winding on the rotor. It is shown that the BDFRM *d-q* model and the equivalent circuit is similar to a DFIM [144]. However, the harmonic flux contents are higher and up to now only few experimental tests have been compiled.

Integrated high power WECS

Wind energy is receiving an increasing attention all over the world, as a non-polluting and economically viable solution. At the beginning of wind technology expansion, WTs were operating at constant speed by means of a stall control system. The generating unit is based on a multiple-stage gearbox and a squirrel cage induction generator [29]. The rotational speed is fixed at synchronous speed for all wind velocity so the generators can be directly connected to the utility power system. Subsequently, with the advent of power electronics and the elaboration of new control schemes in the field of electrical generators, variable speed WTs equipped with pitch angle control have become the dominating units for large wind farms. Variable speed operation reduces mechanical stress and acoustic noise, enables power production over a wide wind speed range and leads to a higher energy yield which increase significantly the WT efficiency [32], [84].

Variable speed WTs are controlled to optimize the performance of the wind energy generating unit. The turbine speed is adjusted as a function of the wind velocity in order to maximize the power captured from the wind. This operation is known as the maximum power point tracking algorithm. It can be realized over a wide wind speed and power ranges, depending on the WT characteristics. The typical power control regions of a WT are shown in Figure 6 [120]. At very low wind speeds, the WT is not active and cannot generate electric energy. There is insufficient power to spin the turbine. The WT starts operating when the wind velocity exceeds the cut-in wind

speed v_{min}. The MPPT algorithm is thus activated to ensure the optimization of the extracted power. The pitch angle is set to the optimal value. Above rated wind speed v_n the mechanical control (e.g. pitch angle control) is applied to limit the output power to its nominal value and/or keep the rotor speed within the desired range. Due to safety consideration, the turbine is shut down at speeds exceeding cut-out wind speed v_{max}.

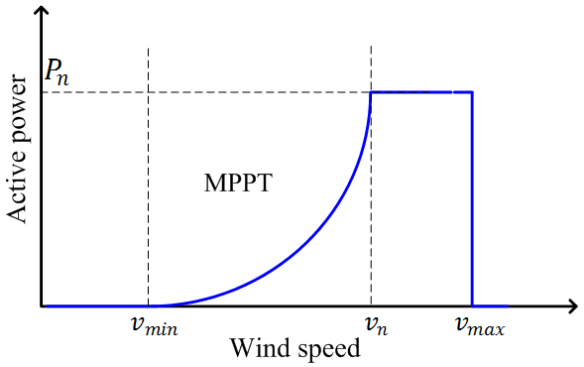

Figure 6: Power curve of a variable speed wind turbine

Studies in the literature investigating the control of a variable speed WECS are based on "instantaneous MPPT" algorithms. The system is carried to track instantaneously the optimal operating point of the WT and extract the maximum available power for every wind speed. This is achieved through the regulation of the WT rotational speed. Various techniques for instantaneous maximum power tracking have been widely discussed throughout the bibliography. One approach is to control the generator mechanical speed electrically using a direct closed control loop as in [12]. This method is easy to implement and provides fast tracking speed, but requires the measurement of both the instantaneous wind velocity and turbine rotational speed. The optimal mechanical speed set point is computed based on the WT characteristics and instantaneous wind speed measurements. However, the wind velocity is usually measured by an anemometer which increases the system cost and the accurate value is never obtained in practice [3]. Therefore, this MPPT method is rarely applied in the actual WECSs and alternative control models are developed [29].

Sensorless output maximization controls based on wind speed estimation have been reported by researchers. For instance, in [110] the wind velocity is estimated from the measured generator electrical power using a nonlinear input-output mapping based on a Gaussian radial basis function network. The estimated wind velocity is then used to determine the optimal mechanical speed command for maximum wind power extraction.

Alternatively, to track the optimal behavior of the WT, the mechanical speed can be indirectly controlled by regulating the generator electromechanical torque [26], [29],

[82]. This method is implemented based on the generator speed calculation and the torque estimation without the need of wind speed information. A similar approach is to control the generator output power instead of the torque, since it is related to the torque and speed of the generator system [29], [109], [128]. These two power feedback controls are in practical the most commonly used methods due to their simple implementation and good dynamic response. Advanced measures have been proposed for performance improvement. A sliding mode power control is suggested in [17], which ensures robustness to parametric uncertainties of the generator and the turbine as well as to electric grid disturbances. A mechanical speed-sensorless maximum power tracking with matrix converter is presented in [15]. The power reference value is derived without requiring a shaft speed sensor.

The instantaneous MPPT approach optimizes the power captured by the WT for every given wind velocity and ensures maximum efficiency of the wind generating unit. Nonetheless, the power generated by the WECS is fluctuating rapidly owing to the stochastic nature of wind speed. Several serious problems will be caused by the power fluctuations, such as the grid frequency fluctuation, the torque fluctuation and the voltage flicker at the buses of the power grid. This will affect the energy quality, increase the stress on the generator and the grid side and induce instability problems in power systems. Accordingly, new control strategies are to be explored in order to sustain the power system stability. Control methods to reduce the power fluctuation have been proposed in the literature [50]. Most are based on energy storage devices (ultra capacitor, battery, flywheel etc...). These methods are effective but involve high installation and maintenance cost. Different power smoothing methods without energy storage devices are recently introduced by controlling the inertia kinetic energy, the pitch angle and the DC-link voltage [50].

Due to the considerable progress of wind power generation systems, new grid codes are introduced for WT integration into the network. The new requirements, stated by Transmission System Operators (TSO), are becoming more restrictive and similar to conventional power plants [37], [130], [132]. Indeed, in addition to active power generation, extended reactive power supply is required under grid disturbances and normal grid conditions as well. Besides, when voltage dip occurs, wind farms must remain connected to the grid and then ride through the grid faults and contribute to voltage regulation and system stability after fault clearance.

DFIGs and Permanent Magnet Synchronous Generators (PMSGs) are the most popular adjustable speed generators for modern WECS. The PMSG is a robust brushless structure with a large capability of reactive power supply. The efficiency

and reliability of the generator are high owing to the high efficiency of permanent magnet materials and absence of brushes and slip rings. Moreover, PMSG based wind turbine can omit the gearbox, hence releasing the related maintenance difficulties and losses [29]. Nevertheless, the generator is connected to the grid through a full-scale power converter which increases significantly the system cost and reduces the system efficiency.

Presently, the predominant candidate for high power wind energy generating systems is the DFIG. The stator of the generator is directly connected to the grid, while the rotor is connected to the grid using fractionally rated converters. The reduced size converters offer an important benefit in cost and efficiency compared to the system with full-scale converters.

There are several literatures about modeling and control strategies of the grid-connected WECS based on DFIG. Numerous control schemes for independent regulation of active and reactive powers have been proposed [100], [127], [128]. Furthermore, the performance of the WT to grid disturbances have been extensively studied over the past years. A large number of research projects are carried out to improve the fault ride through capability and provide voltage support to the grid [60], [80], [112].

However, the disadvantage of the DFIG is its unavoidable use of brushes and slip rings, which reduce the system reliability. The CDFIG is an attractive brushless solution to replace the traditional DFIG in the WECS, especially in offshore places. It is driven by a low power converter and can be directly connected to the constant frequency power grid. The absence of brushes offers high reliability and low maintenance requirements. Moreover the increased number of pole pairs of the CDFIG results in decreasing the gear ratio, thus reducing the gearbox size.

Many strategies are developed for the independent active and reactive power control, and maximum power tracking of a WT based on the CDFIG. The most common approaches deal with stator flux orientation in the unified synchronous reference frame [47], [108], [109], [121]. Recently, the transient behavior of the grid-connected CDFIG is the main research topic. Ride-through capability and voltage regulation of the WT during grid faults [44], [67], [131], [132], and compensation of unbalanced network [28], [55], [123] are being investigated. Yet no consideration has been given to define the safe operating domain of the generator with regards to its ratings, and its contribution to reactive power generation required by grid codes.

Embedded aircraft application

In conventional aircraft architecture, most of the power converted by the engines is used as propulsive power. The remainder is converted into pneumatic, mechanical, hydraulic and electrical power to drive secondary aircraft subsystems (anti-icing system, engine-mounted accessories, utility and flight control actuation, lighting system etc...). This implies a complex power distribution system.

Advances in power electronics, electric drives and control devices have rekindled the concept of MEA in recent aircraft industry, for optimizing the performance and the life cycle cost of the aircraft and reducing fuel consumption [138]. Many non-propulsive functions that used to be operated by pneumatic, mechanical and hydraulic power in conventional aircraft, are being replaced by electric power. This concept offers significant benefits in reliability, increased efficiency on energy conversion, lower weight, less maintenance requirements and less fuel consumption [95], [111].

The concept of an electrically-based aircraft is not new. It has been considered by military aircraft designers since World War II, but a lack of electrical power generation capability and the volume of required power conditioning equipment rendered this approach unfeasible especially for commercial and civil transport applications [30].

Since the eighties, several projects have been developed to explore the MEA concept for military and civil applications. The National Aeronautics and Space Administration (NASA) has conducted a number of activities to foster the development of an All Electrical Aircraft [125]. The POA (Power Optimised Aircraft) project launched in 2002 was the first important integration initiative in Europe. The program aims to identify, optimize and validate innovative aircraft equipment which contributes to the reduction in consumption of non-propulsive power. It also studied the electrical loads management, which permits to introduce new technologies and architectures in on-board systems. In 2006, the MOET (More Open Electrical Technologies) project aims to establish the new industrial standard for commercial aircraft design and improve operational aircraft capacity. Today the MEA topics have a relevant role in the research projects managed by the CleanSky Joint Technology Initiative [21]. The main objective is to develop breakthrough technologies to improve the impact of air transport and reduce the environmental footprint of aviation (i.e. emissions and noise reduction but also green life cycle).

To cope with the increasing demand of electrical power brought by the MEA, new architectures and voltage levels for the on-board electrical power distribution systems are being applied [14], [35], [81]. The conventional aircraft generation considers AC electrical distribution power with a constant frequency supply (115 V AC–400 Hz).

An integrated drive generator converts the variable speed of the main engine into a constant speed to drive a constant frequency electric generator as on the Airbus A320, A330, and A340 [61]. Advancements in power electronics, control electronics, electric motor drives, and electric machines have removed the constant speed mechanical gearbox, introducing a new technology: the VSCF system [35]. The A380 is the first MEA generation to adopt variable frequency operation (360-720 Hz). On the next generation, the distribution voltage is doubled to 230 V AC (e.g. Boeing B787 and Airbus A350) giving the way to High Voltage Alternating Current (HVAC) distribution. The future generation of MEA aircrafts tend to use High Voltage Direct Current (HVDC) electric distribution system ± 270 V [53], [77], [117]. In military airplanes, the traditional voltage levels of 28 V DC and 115 V AC have evolved to 270 V DC in platforms like Boeing–Sikorsky project Comanche RAH-66 and Lockheed Martin F-22 and F-35. This standard reduces the conduction losses, wire sections and iron weight by decreasing the current level, and thus increases the system efficiency. Besides, only one rectifier per generator is needed. All the rectification blocks, integrated in most of the electric equipment, are eliminated. However, the interactions between the different components that compose the system may lead to performance degradation, even system instability [150].

Presently, the technology based on three-stage integrated synchronous machines is used for most of the aircraft power generation [21], [113]. This structure presents similar behavior as a classical wound excitation synchronous machine but excluding brushes and slip rings. It consists of three separated machines mounted on the same shaft. The first generator is a PMSM that supplies a rectifier/chopper set. Then the chopper is connected to a second synchronous machine with a stationary exciter and rotating three-phase windings. These windings are rectified with a rotating rectifier and applied to the rotor winding of the main generator [61]. This machine is safe and regulates the excitation of the main generator without brushes. However, the price to pay is its complexity, high price and maintenance difficulties.

In the literature other machine types are considered and analyzed for this application. Switched reluctance and brushless permanent magnet machines are candidates for future MEA generation systems [113]. Switched reluctance machines are characterized by an intrinsic high fault tolerance, temperature tolerance, robustness and construction simplicity. The main limitations are their lower power and torque density with respect to the PMSM, small air gap, high ventilation losses, and the need of a complicated power converter. PMSMs offer high efficiency, high torque, and high power density in addition to the greatest potential for sensorless control [14]. However, the main disadvantages are their unavoidable sensitivity to high temperatures, the lack of the field control and the impossibility to shut down their magnetic flux in case

of fault.

Another machine structure also proposed for aircraft power systems is the Hybrid Excitation Synchronous Machine (HESM). It is a compact brushless permanent magnet machine with flux control capability. The excitation flux is produced by two different sources: the permanent magnets and a DC field winding that is located on the stator frame to preserve a brushless structure. The latter source is used to control the flux in the air gap. The electrical excitation allows the regulation of the output voltage magnitude without the need of a controllable converter on the stator side. The modeling and the control of the HESM supplying an isolated load in embedded aircraft electrical power generation is treated in the literature. In [78] the HESM operates as a variable frequency generator. In [77], [94] the generator is used to supply a DC grid. Yet, experimental measurements reveal imperfections in the phase voltage waveform of the machine [76].

Nevertheless, constant frequency voltages cannot be directly provided by synchronous generators at variable speed. In such systems, the generator must be associated to a rectifier/inverter set inserted between the generator and the grid to achieve VSCF operation. This involves higher voltage distortion and full rated power converters that increase the system and maintenance cost. The only kind of electromechanical generators, operating at variable speed, which can be directly connected to a constant frequency grid are the doubly fed induction machines [89], [93]. Previous work proved that the CDFIM could be successfully used as VSCF generator in brushless electrical generation systems such as aircraft power supply [87], [91]. It can replace the three-stage synchronous machine presently in use in the aircraft industry.

The studies conducted in the literature on autonomous CDFIG are few and have focused only on symmetrical normal grid conditions. No research has investigated the unbalanced operation of the standalone generator due to connected unbalanced load.

On the other hand, the analysis and operation of a standalone single DFIG supplying unbalanced isolated load have been studied over the past years. Control schemes to cope with unbalanced stator voltage conditions are presented in several works based on repetitive control [54], dual rotating frames control [97], predictive rotor current controller [103], [104] and hybrid current controller [101].

Part I

Cascaded Doubly Fed Induction Machine Modeling and Analysis

Chapter 1

CDFIM Modeling

Introduction

The dynamic behavior of the CDFIM is derived from the model of two wound rotor induction machines combined electrically and mechanically through their rotors. The mathematical model of a DFIM is presented in a first place (section 1.1). The steady state performance of a CDFIM with respect to its main parameters is outlined in section 1.2. The most promising architecture configuration that has significant interest for generating systems is identified. In section 1.3 a CDFIG model for simulation is established using modular representation. It is based on the conventional Park model of two single DFIMs expressed in their own reference frames. Two configurations are elaborated: the grid-connected and the standalone. The model of the CDFIG is then extended in section 1.4 in order to describe the machine in a unified reference frame, which is more relevant for the development of an appropriate controller.

1.1 Modeling and analysis of the DFIM

1.1.1 Mathematical model

The dynamic behavior of a DFIM can be described using the theory of a rotating reference frame (dq). Under the hypothesis of linearity, symmetry and sinusoidal waveform, the machine voltage and flux equations in an arbitrary Park frame using complex (phasor) quantities are given by (1.1) to (1.4) [93], [127]. These expressions are derived by applying successively a Clarke transformation and a rotation of the coordinate system. The supersynchronous motor convention is adopted as shown in

Figure 1.1.

$$\underline{v}_s = R_s \underline{i}_s + \frac{d}{dt}\underline{\Phi}_s + j\dot{\xi}_s \underline{\Phi}_s \tag{1.1}$$

$$\underline{v}_r = R_r \underline{i}_r + \frac{d}{dt}\underline{\Phi}_r + j\dot{\xi}_r \underline{\Phi}_r \tag{1.2}$$

$$\underline{\Phi}_s = L_s \underline{i}_s + M_{sr} \underline{i}_r \tag{1.3}$$

$$\underline{\Phi}_r = L_r \underline{i}_r + M_{sr} \underline{i}_s \tag{1.4}$$

$\underline{x} = X_d + jX_q$ denotes the space phasor form of the actual quantity x.

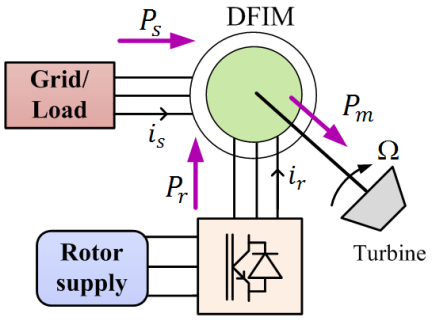

Figure 1.1: DFIM in supersynchronous motor convention

ξ_s and ξ_r are the electrical Park frame angles with respect to the stator and rotor coordinates respectively. They are related to the mechanical angular position of the rotor θ_m by the following relation:

$$\xi_s = \xi_r + p\theta_m \tag{1.5}$$

The reference frames are illustrated in Figure 1.2. $(\alpha\beta_s)$ is the stationary bi-phase reference frame, $(\alpha\beta_r)$ the rotor bi-phase frame and (dq) the rotating Park frame.

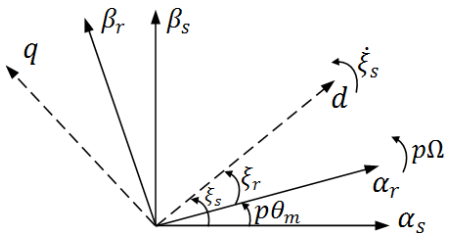

Figure 1.2: Reference frame representation of a DFIM

Moreover the active and reactive powers are expressed as follows, $\hat{\underline{x}}$ being the conjugate

of the phasor quantity.

$$P_s = \frac{3}{2}\Re\left\{\underline{v}_s\hat{\underline{i}}_s\right\} = \frac{3}{2}\left(V_{sd}I_{sd} + V_{sq}I_{sq}\right) \tag{1.6}$$

$$Q_s = \frac{3}{2}\Im\left\{\underline{v}_s\hat{\underline{i}}_s\right\} = \frac{3}{2}\left(V_{sq}I_{sd} - V_{sd}I_{sq}\right) \tag{1.7}$$

$$P_r = \frac{3}{2}\Re\left\{\underline{v}_r\hat{\underline{i}}_r\right\} = \frac{3}{2}\left(V_{rd}I_{rd} + V_{rq}I_{rq}\right) \tag{1.8}$$

$$Q_r = \frac{3}{2}\Im\left\{\underline{v}_r\hat{\underline{i}}_r\right\} = \frac{3}{2}\left(V_{rq}I_{rd} - V_{rd}I_{rq}\right) \tag{1.9}$$

The electromagnetic torque is given by:

$$T_{em} = \frac{3}{2}pM_{sr}\Im\left\{\underline{i}_s\hat{\underline{i}}_r\right\} \tag{1.10}$$

Other equivalent expressions of the torque can be also derived:

$$T_{em} = \frac{3}{2}p\Im\left\{\underline{i}_s\hat{\underline{\Phi}}_s\right\} \tag{1.11}$$

$$= \frac{3}{2}p\Im\left\{\underline{\Phi}_r\hat{\underline{i}}_r\right\} \tag{1.12}$$

The Park (dq) frame can be chosen arbitrary. Three remarkable cases are distinguished:

- Stator reference frame: $\xi_s = 0$, $\xi_r = -p\theta_m$. Thus $\dot{\xi}_s = 0$ and $\dot{\xi}_r = -p\Omega$. In this frame all the machine quantities evolve at ω_s at steady state. It will be adopted for the modeling of the generator.
- Rotor reference frame: $\xi_r = 0$, $\xi_s = p\theta_m$. Thus $\dot{\xi}_r = 0$ and $\dot{\xi}_s = p\Omega$. Here, the quantities evolve at ω_r.
- Synchronous reference frame: $\dot{\xi}_s = \omega_s$ and $\dot{\xi}_r = \omega_s - p\Omega$. All the quantities are constant at steady state. This type of coordinate is convenient for the implementation of control algorithms.

Considering the fixed stator reference frame, relations (1.1) to (1.4) become

$$\underline{v}_s = R_s\underline{i}_s + L_s\frac{d}{dt}\underline{i}_s + M_{sr}\frac{d}{dt}\underline{i}_r \tag{1.13}$$

$$\underline{v}_r = R_r\underline{i}_r + L_r\frac{d}{dt}\underline{i}_r - jp\Omega L_r\underline{i}_r + M_{sr}\frac{d}{dt}\underline{i}_s - jp\Omega M_{sr}\underline{i}_s \tag{1.14}$$

A dynamical equivalent circuit of the DFIM can be derived from the above equations as illustrated in Figure 1.3. It describes the machine in steady state and dynamic mode operations [93]. $\underline{i}\mu$ is the stator magnetizing current, m is the transformer (stator to rotor) turns ratio and σL_r is the leakage inductance located at the rotor

side. They are given by:

$$\underline{i}\mu = \underline{i}_s + m\underline{i}_r \tag{1.15}$$

$$m = \frac{M_{sr}}{L_s} \tag{1.16}$$

$$\sigma = 1 - \frac{M_{sr}^2}{L_s L_r} \tag{1.17}$$

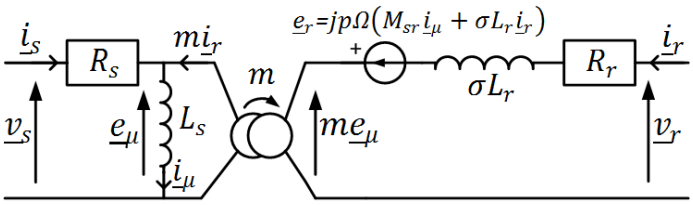

Figure 1.3: Dynamical equivalent circuit of DFIG

The electromechanical conversion is localized in the back EMF e_r, more precisely in the term $jp\Omega M_{sr}\underline{i}_\mu$. The dynamical equivalent circuit can be translated into a block diagram established in the stationary stator frame as shown in Figure 1.4.

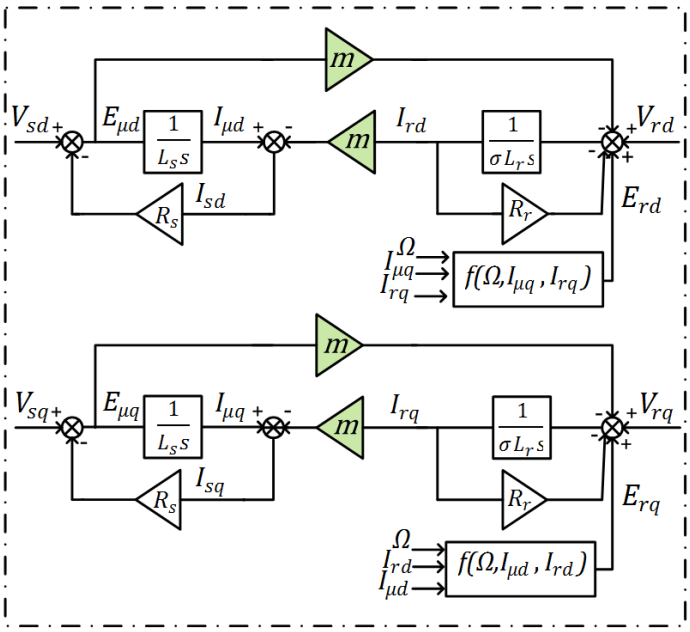

Figure 1.4: Block diagram of DFIG in the fixed stator frame

The stator and rotor quantities are transformed from their three-phase reference frame into the defined (dq) coordinate and vice versa (Figure 1.5) using Clarke and Park transformations established in Appendix A. It is noted that this block diagram is implemented on Matlab/Simulink for the modeling of the DFIM.

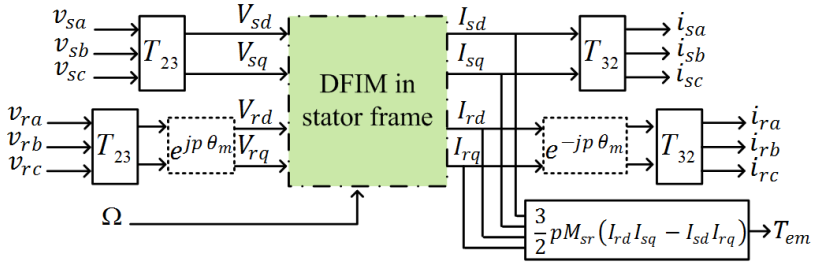

Figure 1.5: Block diagram of the DFIG

As can be noticed from Figure 1.4, the machine is equivalent to a three-phase current source having the following input and output vectors:

$$u = [\underline{v}_s, \underline{v}_r]^t \tag{1.18}$$

$$y = [\underline{i}_s, \underline{i}_r]^t \tag{1.19}$$

In generator mode, the mechanical speed Ω is seen as an input parameter.

1.1.2 Steady state operation

Based on a simplified model of the machine, where copper and iron losses and magnetic leakages are neglected, the DFIM is characterized by the following:

$$P_r = -gP_s \tag{1.20}$$

$$P_m = P_r + P_s = (1-g)P_s \tag{1.21}$$

$$\omega_s = \omega_r + p\Omega \tag{1.22}$$

The expressions describe the steady-state operation with sinusoidal quantities. They correspond to supersynchronous motor convention where P_s is the entering stator power, P_r is the entering rotor power and P_m the outgoing mechanical power. g is the slip ratio defined as follows:

$$g = \frac{\omega_s - p\Omega}{\omega_s} = \frac{\omega_r}{\omega_s} \tag{1.23}$$

1.2 Analysis of the CDFIM

The CDFIM is composed of two wound rotor induction machines connected in cascade (Figure 1.6). The stator of the Power machine (DFIM2) is directly connected to the grid, whereas the stator windings of the Control machine (DFIM1) are supplied from a power frequency converter. The two rotors are mechanically and electrically

coupled eliminating the need of brushes [48], [86]. In what follows, 1 and 2 subscripts will be employed to refer to DFIM1 and DFIM2 quantities respectively.

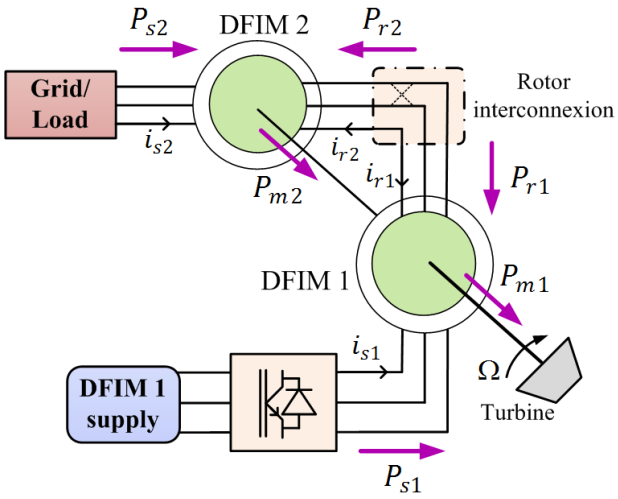

Figure 1.6: CDFIM in supersynchronous motor convention

The major interest of a CDFIM is the operation in synchronous mode [11], [16]. The machine is able to operate stably as a brushless variable speed generator over a wide speed range with controllable dynamic response [31]. The synchronous operation occurs when the rotor currents induced by both Power and Control machines evolve with the same frequency [79]. This way, the Power machine windings can be controlled through the rotors from the Control machine stator in a brushless manner. Therefore, according to the mechanical speed variation, the Control machine stator frequency is adjusted in order to maintain the synchronous mode and achieve constant output frequency. Besides, by controlling the voltage phase and magnitude, the output voltage magnitude and the amount of active and reactive powers provided by the generator can be dynamically controlled in a similar way to a single DFIG [47], [92].

The structure of the CDFIM depends on the following main parameters:

- the numbers of pole pairs p_1 and p_2 of both DFIMs.
- the interconnection type between the rotors windings of the two DFIMs characterized by using the coefficient λ_c

$$\lambda_c = \begin{cases} 1 & \text{for a direct coupling sequence} \\ -1 & \text{for an inverse coupling sequence} \end{cases} \tag{1.24}$$

These parameters have a significant impact on the behavior of the CDFIM in terms of power flow, converters sizing and system efficiency. Theoretically, the two wound rotor induction machines can have any pole pair combination with rotors connected in inverse or direct coupling sequence. Nevertheless a detailed analysis of all the possible CDFIM architecture configurations has been established in [91], [92] in order

to identify the most promising ones. Applying the same supersynchronous motor convention for both machines as shown in Figure 1.6, (1.20) to (1.23) are rewritten as:

$$P_{r1} = -g_1 P_{s1} \quad (1.25) \qquad P_{r2} = -g_2 P_{s2} \quad (1.29)$$

$$P_{m1} = P_{r1} + P_{s1} = (1-g_1)P_{s1} \quad (1.26) \qquad P_{m2} = P_{r2} + P_{s2} = (1-g_2)P_{s2} \quad (1.30)$$

$$\omega_{s1} = \omega_{r1} + p_1\Omega \quad (1.27) \qquad \omega_{s2} = \omega_{r2} + p_2\Omega \quad (1.31)$$

$$g_1 = \frac{\omega_{s1} - p_1\Omega}{\omega_{s1}} = \frac{\omega_{r1}}{\omega_{s1}} \quad (1.28) \qquad g_2 = \frac{\omega_{s2} - p_2\Omega}{\omega_{s2}} = \frac{\omega_{r2}}{\omega_{s2}} \quad (1.32)$$

Considering ideal rotor interconnection, the instantaneous power is conserved. Thus the rotor interconnection is described as follows [91]:

$$P_{r1} = -P_{r2} \quad (1.33)$$

$$\omega_{r1} = \lambda_c \omega_{r2} \quad (1.34)$$

The above equations are used to derive the power and frequency behavior of the CDFIM at steady state. From (1.27), (1.31) and (1.34) the two stator frequencies are related by (1.35)

$$\omega_{s1} = \lambda_c \omega_{s2} + (p_1 - \lambda_c p_2)\,\Omega \quad (1.35)$$

The CDFIM slip ratio is defined as

$$g_c = \frac{g_2}{g_1} \quad (1.36)$$

$$= \lambda_c \frac{\lambda_c \omega_{s2} + (p_1 - \lambda_c p_2)\,\Omega}{\omega_{s2}} \quad (1.37)$$

The synchronous speed Ω_s of the CDFIM is defined to be the mechanical speed that cancels g_c.
Referring to (1.25), (1.29) and (1.33) the power flow in the CDFIM is characterized by the following relations:

$$P_{s1} = -g_c P_{s2} \quad (1.38)$$

$$P_{m1} = -(1-g_1) g_c P_{s2} \quad (1.39)$$

$$P_{m2} = (1-g_2) P_{s2} \quad (1.40)$$

$$P_m = P_{m1} + P_{m2} = (1-g_c) P_{s2} \quad (1.41)$$

The global behavior of the cascade considering all configurations is synthesized in Table 1.1 where $\Delta p = p_1 - p_2$ and $\Sigma p = p_1 + p_2$.

λ_c	Pole pairs conf.	g_c	synchr. speed	$\frac{P_{s1}}{P_{s2}}$	$\frac{P_{m1}}{P_{s2}}$	$\frac{P_{m2}}{P_{s2}}$	$\frac{P_{m1}+P_{m2}}{P_{s2}}$
1	$p_1 = p_2 = p$	1	does not exist	-1	$-\frac{p\Omega}{\omega_{s2}}$	$\frac{p\Omega}{\omega_{s2}}$	0
	$p_1 \neq p_2$	$\frac{\omega_{s2}+\Delta p\Omega}{\omega_{s2}}$	$-\frac{\omega_{s2}}{\Delta p}$	$-g_c$	$-\frac{p_1\Omega}{\omega_{s2}}$	$\frac{p_2\Omega}{\omega_{s2}}$	$-\frac{\Delta p\Omega}{\omega_{s2}}$
-1	$p_1 = p_2 = p$	$\frac{\omega_{s2}-2p\Omega}{\omega_{s2}}$	$\frac{\omega_{s2}}{2p}$	$-g_c$	$\frac{p\Omega}{\omega_{s2}}$	$\frac{p\Omega}{\omega_{s2}}$	$\frac{2p\Omega}{\omega_{s2}}$
	$p_1 \neq p_2$	$\frac{\omega_{s2}-\Sigma p\Omega}{\omega_{s2}}$	$\frac{\omega_{s2}}{\Sigma p}$	$-g_c$	$\frac{p_1\Omega}{\omega_{s2}}$	$\frac{p_2\Omega}{\omega_{s2}}$	$\frac{\Sigma p\Omega}{\omega_{s2}}$

Table 1.1: Configurations and power flow

According to the power flow performance, it can be deduced that the direct interconnection configuration must be avoided. In fact for $p_1 = p_2$ there is no global electromechanical conversion thus the CDFIM performs as a static transformer, and for $p_1 \neq p_2$ the signs of the two mechanical powers are different thus the two DFIMs operate in a combined motor/generator mode. The only satisfying performances are achieved by an inverse coupling sequence since the total mechanical power is provided by both DFIMs, proportionally to their respective number of pole pairs. In order to obtain a good efficiency, the mechanical power P_{m2} must be maximized, whereas P_{m1} must be minimized. A configuration with $p_2 \geq p_1$ is the most interesting solution that provides a high system efficiency with the lowest per unit losses [64]. The inverse coupling sequence results in the following frequency and speed relations [47], [118]:

$$g_c = \frac{\omega_{s2} - \Sigma p\Omega}{\omega_{s2}} \tag{1.42}$$

$$\omega_{s1} = \Sigma p\Omega - \omega_{s2} = -g_c\omega_{s2} \tag{1.43}$$

$$\Omega_s = \frac{\omega_{s2}}{\Sigma p\Omega} \tag{1.44}$$

It is noted from (1.38) that the power transmitted to DFIM1 stator i.e. to the converters is proportional to the slip ratio of the CDFIM (similar to the DFIM). Thus, for a limited speed range (centered around the synchronous speed), the converters are sized for a fraction of the CDFIM nominal power. The advantage of the CDFIM resides not only in the brushless structure but also in the ability to minimize the power delivered to/by the converters.

The CDFIM operates in both subsynchronous ($\Omega < \Omega_s$) and supersynchronous ($\Omega > \Omega_s$) speed ranges. The behavior of the machine depending on the operational speed is presented in Table 1.2. The results correspond to supersynchronous motor

convention.

	Generator mode		Motor mode	
	subsynchronous	supersynchronous	subsynchronous	supersynchronous
g_c	>0	<0	>0	<0
P_m	<0	<0	>0	>0
P_{s2}	<0	<0	>0	>0
P_{s1}	>0	<0	<0	>0

Table 1.2: Operation mode of the CDFIM

It is noted that the stator-1 power P_{s1} can flow in both directions. In generator mode, the power is entering in the stator-1 windings during subsynchronous operation, while in supersynchronous operation P_{s1} is fetched from the stator to the converter. At synchronous speed ($g_c = 0$), the stator-1 frequency is equal to zero in order to maintain a constant output frequency and P_{s1} is theoretically null (if losses are neglected).

1.3 Modeling of the CDFIG

A modular representation of the CDFIG (decoupled state space model) is elaborated. It is based on the conventional model of two distinct wound rotor induction machines expressed in their own three-phase reference frames and combined in inverse rotor interconnection. Two cases are considered: grid-connected CDFIG and standalone CDFIG.

1.3.1 Rotor interconnection model

As mentioned in the previous section, only inverse coupling configuration has a significant interest for generation system applications. Thus a rotor interconnection model is derived based on the relations between the three-phase rotor-1 and rotor-2 voltages and currents [93].

$$[v_{r2}]_{3r2} = C\,[v_{r1}]_{3r1} \tag{1.45}$$

$$[i_{r2}]_{3r2} = D\,[i_{r1}]_{3r1} \tag{1.46}$$

C and D being the interconnection matrices given by:

$$C = \begin{bmatrix} 1 & 0 & 0 \\ 0 & 0 & 1 \\ 0 & 1 & 0 \end{bmatrix}; \qquad D = \begin{bmatrix} -1 & 0 & 0 \\ 0 & 0 & -1 \\ 0 & -1 & 0 \end{bmatrix} \tag{1.47}$$

Relations (1.45) and (1.46) describe an inverse coupling sequence between the two rotor windings with a supersynchronous motor convention employed for both machines. The system representing the rotor interconnection has two input quantities ($[v_{r1}]_{3r1}$, $[i_{r2}]_{3r2}$) and two output quantities ($[v_{r2}]_{3r2}$, $[i_{r1}]_{3r1}$).

1.3.2 Grid-connected generator model

In a grid-connected CDFIG configuration, the output stator-2 voltage is imposed by the utility grid, and the stator-1 is fed by a voltage source power converter. Thus, the system has as main inputs the stator voltages ($[v_{s1}]_{3s1}$, $[v_{s2}]_{3s2}$), and as outputs the stator currents ($[i_{s1}]_{3s1}$, $[i_{s2}]_{3s2}$). A modular representation of the generator can be adopted based on two distinct machines as illustrated in Figure 1.7.

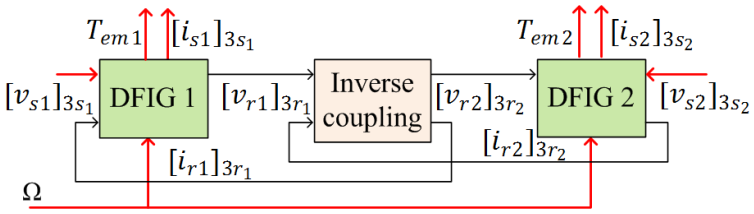

Figure 1.7: Model of a grid-connected CDFIG

DFIG1 operates as a voltage source supplied by its stator side whereas DFIG2 operates as a current source. The two machines are connected through inverse coupling sequence described by (1.45), (1.46). A simple interconnection of all the building blocks forms the global model of the CDFIG. Based on the representation of the DFIM established in section 1.1.1, the machine is equivalent to a three-phase current source. The input and output quantities are respectively ($[v_s]_{3s}$, $[v_r]_{3r}$) and ($[i_s]_{3s}$, $[i_r]_{3r}$). This representation is coherent for the modeling of DFIG2. However, in order to transform the equivalent model of DFIG1 into a three-phase voltage source as described in Figure 1.7, a proper Point of Regulation (PR) is defined by adding fictitious capacitors and resistors to the rotor windings of the DFIM1 as shown in Figure 1.8 [78].

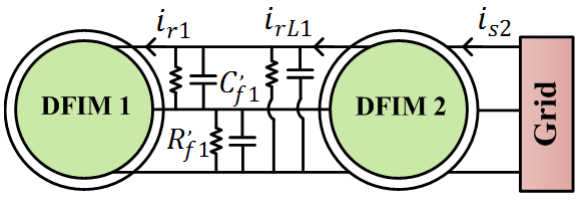

Figure 1.8: Point of Regulation equivalent circuit of the grid-connected CDFIG

The rotor voltage can now be expressed in terms of the machine currents using a first order transfer function. Therefrom, a new voltage equation that includes the rotor

voltage among the output variables is introduced. The equivalent circuit of a rotor phase is represented in Figure 1.9 with $C_{f1} = 3C'_{f1}$ and $R_{f1} = R'_{f1}/3$. l_{r1} being the rotor self inductance.

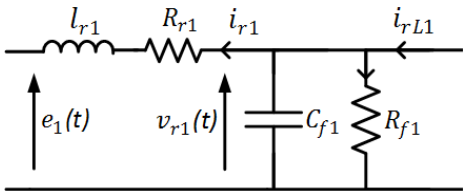

Figure 1.9: Equivalent RLC circuit at a rotor phase

The Kirchhoff law yields to (1.48). i_{rL1} is the load current.

$$\frac{d}{dt}v_{r1} = \frac{1}{C_{f1}}\left(i_{rL1} - i_{r1} - \frac{v_{r1}}{R_{f1}}\right) \tag{1.48}$$

The Park transformation applied to the three-phase quantities results in (1.49) in the stator (dq_1) frame.

$$\frac{d}{dt}\underline{v}_{r1} = \frac{1}{C_{f1}}\left(\underline{i}_{rL1} - \underline{i}_{r1} - \frac{\underline{v}_{r1}}{R_{f1}} + jp\Omega C_{f1}\underline{v}_{r1}\right) \tag{1.49}$$

The introduction of this voltage equation into the block diagram of Figure 1.4, forms the following new input output vectors that are in accordance with Figure 1.7, given that $\underline{i}_{rL1}$ must be virtually equal to $\underline{i}_{r1}$.

$$u' = [\underline{v}_{s1}, \underline{i}_{rL1}]^t \tag{1.50}$$

$$y' = [\underline{v}_{r1}, \underline{i}_{s1}]^t \tag{1.51}$$

Since the introduction of the fictitious capacitances and resistances should not perturb the operating point of the machine, the R-C elements must be selected carefully. At no load, the RLC circuit in Figure 1.9 is equivalent to a second order system expressed as:

$$\frac{v_{r1}(s)}{e_1(s)} = \frac{1}{1 + \frac{R_{r1}}{R_{f1}} + s(R_{r1}C_{f1} + \frac{l_{r1}}{R_{f1}}) + l_{r1}C_{f1}s^2} \tag{1.52}$$

The damping ratio of the system is $\zeta = \dfrac{R_{r1}C_{f1} + l_{r1}/R_{f1}}{2\sqrt{l_{r1}C_{f1}(1 + R_{r1}/R_{f1})}}$. The natural frequency is $\omega_0 = \sqrt{\dfrac{R_{f1} + R_{r1}}{l_{r1}R_{f1}C_{f1}}}$.

R_{f1} and C_{f1} are chosen properly to fulfill the following criteria:

- The damped resonance frequency $\omega_{dr} = \omega_0\sqrt{1-\zeta^2}$ should be at least 10 times greater than the maximum operating frequency $\omega_{r1,max}$;
- The peak resonance $20\log\dfrac{1}{2\zeta\sqrt{1-\zeta^2}}$ has to be less than $30db$;
- The voltage gain at $\omega_{r1,max}$ less than $0.1db$;
- The power dissipated in the damped resistance R_{f1} should not exceed 1% of the machine nominal power.

A solution for C_{f1} and R_{f1} that verifies the aforementioned conditions is given in appendix B.

It has to be noted that the addition of capacitors only, creates a PR but induces high peak resonance which might yield to numerical instability problems. For this reason a damping resistor is connected in parallel.

1.3.3 Stand alone generator model

In standalone operation, the generator supplies an isolated load. The main inputs of the CDFIG are the load current and stator-1 voltage ($[v_{s1}]_{3s1}$, $[i_{sL2}]_{3s2}$). The outputs are the terminal voltage and stator-1 current ($[v_{s2}]_{3s2}$, $[i_{s1}]_{3s1}$). A modular representation of the system is presented in Figure 1.10.

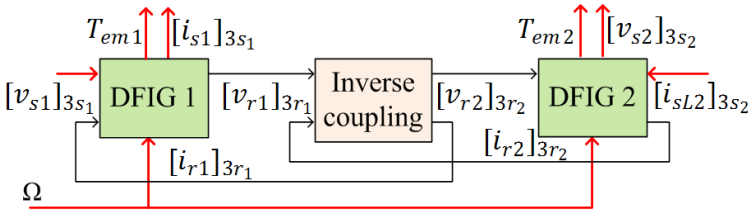

Figure 1.10: Model of a standalone CDFIG

The DFIMs M1 and M2 both operate as an autonomous voltage source having as output variables the rotor voltage and the stator voltage respectively. In order to transform the equivalent model of each DFIG into a three-phase voltage source with its corresponding input-output vectors as described in Figure 1.10, two PR are defined at the rotor side of DFIM1 and at the stator side of DFIM2 as depicted in Figure 1.11.

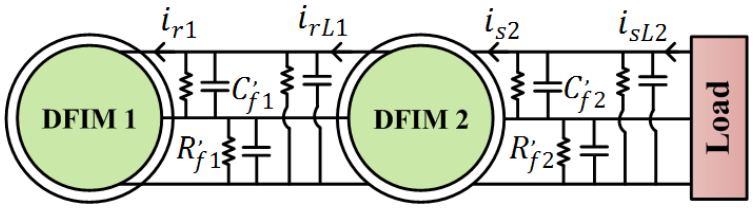

Figure 1.11: Point of Regulation equivalent circuit of the standalone CDFIG

The same procedure is followed for DFIM2. A new voltage equation that includes the stator voltage among the output variables is introduced. The Kirchhoff law in the (dq_2) stationary reference frame induces:

$$\frac{d}{dt}\underline{v}_{s2} = \frac{1}{C_{f2}}\left(\underline{i}_{sL2} - \underline{i}_{s2} - \frac{\underline{v}_{s2}}{R_{f2}}\right) \tag{1.53}$$

with $C_{f2} = 3C'_{f2}$; $R_{f2} = R'_{f2}/3$ and $\underline{i}_{sL2}$ the load current. The introduction of this equation in the block diagram of Figure 1.4 transforms the machine model into a voltage source with the following new input output vectors where $\underline{i}_{sL2} \simeq \underline{i}_{s2}$:

$$u' = [\underline{v}_{r2}, \underline{i}_{sL2}]^t \tag{1.54}$$

$$y' = [\underline{v}_{s2}, \underline{i}_{r2}]^t \tag{1.55}$$

At no load each stator phase is equivalent to an RLC circuit that corresponds to a second order system. Here likewise the fictitious capacitances and resistances are chosen carefully to satisfy the conditions defined above.

The two representations of the CDFIG, developed in this section, are implemented on Matlab/Simulink for simulations in order to validate new control strategies for a grid-connected and a standalone application. It shall be noted that the presence of the fictitious R-C elements in each of the two DFIMs is crucial for the modeling part of the CDFIG, in order to preserve a modular representation of the system. Yet they will be discarded during the control implementation since the cutoff frequency of the RLC circuits is much greater than the closed-loop system bandwidth.

1.4 Unified reference frame vector representation

The idea of the CDFIM was introduced more than a century ago [126]. However, despite its advantages this generator was not widely used, mainly due to the inherent complexity of its structure and the difficulty of controlling and working with such a system. The complexity arises from the existence of two wound rotor induction machines with different pole pair distributions, interconnected through inverse rotor coupling sequence. This complex architecture increases the order of the system together with the number of degrees of freedom and dynamical state variables; it also generates a multiple reference frames system.
In fact the set of equations (1.1)-(1.10) describe the behavior of each DFIM in its proper (dq) reference frame related to a certain pole pair distribution. Therefore the CDFIM can be described using two different reference frames (dq_1) and (dq_2) related

to DFIM1 and DFIM2 respectively.

– The Control machine M1 is represented in its corresponding reference frame (dq_1) by the following expressions:

$$\underline{v}_{s1} = R_{s1}\underline{i}_{s1} + \frac{d}{dt}\underline{\Phi}_{s1} + j\dot{\xi}_{s1}\underline{\Phi}_{s1} \tag{1.56}$$

$$\underline{v}_{r1} = R_{r1}\underline{i}_{r1} + \frac{d}{dt}\underline{\Phi}_{r1} + j\dot{\xi}_{r1}\underline{\Phi}_{r1} \tag{1.57}$$

$$\underline{\Phi}_{s1} = L_{s1}\underline{i}_{s1} + M_{sr1}\underline{i}_{r1} \tag{1.58}$$

$$\underline{\Phi}_{r1} = L_{r1}\underline{i}_{r1} + M_{sr1}\underline{i}_{s1} \tag{1.59}$$

$$T_{em1} = \frac{3}{2}p_1 M_{sr1}\Im\left\{\underline{i}_{s1}\hat{\underline{i}}_{r1}\right\} \tag{1.60}$$

$$P_{s1} = \frac{3}{2}\Re\left\{\underline{v}_{s1}\hat{\underline{i}}_{s1}\right\} \tag{1.61}$$

$$Q_{s1} = \frac{3}{2}\Im\left\{\underline{v}_{s1}\hat{\underline{i}}_{s1}\right\} \tag{1.62}$$

where:

$$\xi_{s1} = \xi_{r1} + p_1\theta_{m1} \tag{1.63}$$

– The same equations are used to describe the Power machine M2 in its reference frame (dq_2).

Consequently at steady state, the Control machine and the Power machine *d-q* quantities operate at different frequencies that are linked by the rotor interconnection model.

The inverse coupling configuration given by (1.45) and (1.46) can be expressed in rotating (dq) reference frames. A Park transformation is applied to the rotor quantities of DFIM1 and DFIM2 respectively using successively a Clarke transformation (1.64), (1.65) and a rotation of the coordinate system (1.66), (1.67).

$$T_{32}\left[v_{r2}\right]_{\alpha\beta_{r2}} = CT_{32}\left[v_{r1}\right]_{\alpha\beta_{r1}} \tag{1.64}$$

$$T_{32}\left[i_{r2}\right]_{\alpha\beta_{r2}} = DT_{32}\left[i_{r1}\right]_{\alpha\beta_{r1}} \tag{1.65}$$

$$P^{-1}(\xi_{r2})\left[v_{r2}\right]_{dq_2} = T_{23}CT_{32}P^{-1}(\xi_{r1})\left[v_{r1}\right]_{dq_1} \tag{1.66}$$

$$P^{-1}(\xi_{r2})\left[i_{r2}\right]_{dq_2} = T_{23}DT_{32}P^{-1}(\xi_{r1})\left[i_{r1}\right]_{dq_1} \tag{1.67}$$

Rearranging (1.66), (1.67) leads to the following rotor interconnection relation in complex form. The conjugate operation arises from inverse coupling.

$$(\underline{v}_{r2})_{dq2} = e^{-j(\xi_{r1}+\xi_{r2})}(\hat{\underline{v}}_{r1})_{dq1} \tag{1.68}$$

$$(\underline{i}_{r2})_{dq2} = -e^{-j(\xi_{r1}+\xi_{r2})}(\hat{\underline{i}}_{r1})_{dq1} \tag{1.69}$$

It is noted that ξ_{r1} and ξ_{r2} are the rotor frame angles of each machine with respect to its arbitrary (dq) frame. The complex quantities $\underline{x}_{r1}$ and $\underline{x}_{r2}$ are expressed in two distinct frames (dq_1) and (dq_2) that are related to two different machines DFIM1 and DFIM2 respectively, which are connected in inverse coupling sequences and presenting different pole pair distribution. Then the rotor interconnection rotating term is set up to link the two frames.

Since the elaboration of a control scheme based on multiple reference frames is complex, it is convenient to describe the CDFIM in a unified dq reference frame with a given pole-pair distribution, related to one of the two DFIMs [38], [107]. This way, all quantities are induced at the same frequency which could be more relevant for vector control synthesis and the development of an efficient controller despite the complexity of the system [106]. Hereinafter, the common reference frame related to the Power machine is adopted for the vector representation of the CDFIM. The different reference frames related to each induction machine are illustrated in Figure 1.12. Four fundamental frames can be distinguished:

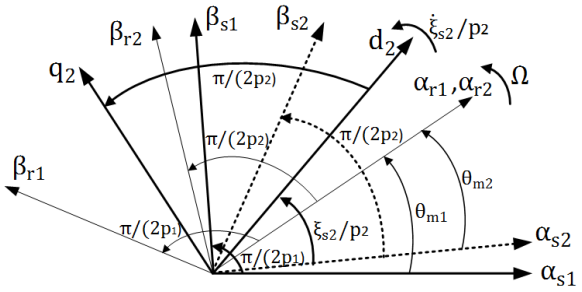

Figure 1.12: Multiple reference frames (mechanical angles)

- the stationary reference $(\alpha\beta_{s2})$ related to the Power machine with p_2 pole pair distribution;
- the static $(\alpha\beta_{s1})$ frame related to the Control machine with p_1 pole pair distribution;
- the rotor reference frames $(\alpha\beta_{r1})$ and $(\alpha\beta_{r2})$ associated to M1 and M2 respectively. They are located respectively at a mechanical angular position $(\theta_{m1}, \theta_{m2})$ from $(\alpha\beta_{s1}, \alpha\beta_{s2})$;
- the unified Power machine reference frame (dq_2) with p_2 pole pair distribution situated at the mechanical angle $\dfrac{\xi_{s2}}{p_2}$ from $(\alpha\beta_{s2})$.

The transformation into a common reference frame should take into consideration the different pole pair distributions, the angle between the two rotating frames and the inverse coupling sequence. Based on the rotor interconnection model, the vector transformation of a quantity $\underline{x}$ from the Control machine (dq_1) reference frame to the

Power machine (dq_2) reference frame, or vice versa, is performed by:

$$(\underline{x})_{dq_2}=e^{-j(\xi_{r1}+\xi_{r2})}(\underline{\hat{x}})_{dq_1} \tag{1.70}$$

$$(\underline{x})_{dq_1}=e^{-j(\xi_{r1}+\xi_{r2})}(\underline{\hat{x}})_{dq_2} \tag{1.71}$$

Applying the vector transformation (1.71) to the DFIM1 quantities in (1.56) to (1.62) and (1.68), (1.69), the vector model of the CDFIM in the common Power machine synchronous reference frame ($\dot{\xi_{s2}} = \omega_{s2}$) is expressed as follows:

$$\underline{v}_{s2} = R_{s2}\underline{i}_{s2} + \frac{d}{dt}\underline{\Phi}_{s2} + j\omega_{s2}\underline{\Phi}_{s2} \tag{1.72}$$

$$\underline{v}_{s1} = R_{s1}\underline{i}_{s1} + \frac{d}{dt}\underline{\Phi}_{s1} + j\left(\omega_{s2} - \Sigma p\Omega\right)\underline{\Phi}_{s1} \tag{1.73}$$

$$\underline{v}_{r2} = R_{r2}\underline{i}_{r2} + \frac{d}{dt}\underline{\Phi}_{r2} + j\left(\omega_{s2} - p_2\Omega\right)\underline{\Phi}_{r2} \tag{1.74}$$

$$\underline{v}_{r1} = R_{r1}\underline{i}_{r1} + \frac{d}{dt}\underline{\Phi}_{r1} + j\left(\omega_{s2} - p_2\Omega\right)\underline{\Phi}_{r1} \tag{1.75}$$

$$\underline{\Phi}_{s2} = L_{s2}\underline{i}_{s2} + M_{sr2}\underline{i}_{r2} \tag{1.76}$$

$$\underline{\Phi}_{s1} = L_{s1}\underline{i}_{s1} + M_{sr1}\underline{i}_{r1} \tag{1.77}$$

$$\underline{\Phi}_{r2} = L_{r2}\underline{i}_{r2} + M_{sr2}\underline{i}_{s2} \tag{1.78}$$

$$\underline{\Phi}_{r1} = L_{r1}\underline{i}_{r1} + M_{sr1}\underline{i}_{s1} \tag{1.79}$$

The rotor quantities are related by:

$$\underline{v}_{r2} = \underline{v}_{r1} \tag{1.80}$$

$$\underline{i}_{r2} = -\underline{i}_{r1} \tag{1.81}$$

Let $\underline{v}_r = \underline{v}_{r2} = \underline{v}_{r1}$ and $\underline{i}_r = \underline{i}_{r2} = -\underline{i}_{r1}$, expressions (1.74),(1.75) and (1.78),(1.79) result in:

$$\underline{\Phi}_r = \underline{\Phi}_{r2} - \underline{\Phi}_{r1} = L_r\underline{i}_r + M_{sr2}\underline{i}_{s2} - M_{sr1}\underline{i}_{s1} \tag{1.82}$$

$$\underline{v}_{r2} - \underline{v}_{r1} = R_r\underline{i}_r + \frac{d}{dt}\underline{\Phi}_r + j\left(\omega_{s2} - p_2\Omega\right)\underline{\Phi}_r = 0 \tag{1.83}$$

where $\underline{\Phi}_r$ is a fictitious quantity representing the rotor circuit loop flux linkage, and:

$$L_r = L_{r1} + L_{r2}; \quad R_r = R_{r1} + R_{r2} \tag{1.84}$$

Moreover, stator active and reactive powers in this common synchronous reference frame are resumed as:

$$P_{s1} = \frac{3}{2}\Re\left\{\hat{\underline{v}}_{s1}\underline{i}_{s1}\right\} \tag{1.85}$$

$$Q_{s1} = \frac{3}{2}\Im\left\{\hat{\underline{v}}_{s1}\underline{i}_{s1}\right\} \tag{1.86}$$

$$P_{s2} = \frac{3}{2}\Re\left\{\underline{v}_{s2}\hat{\underline{i}}_{s2}\right\} \tag{1.87}$$

$$Q_{s2} = \frac{3}{2}\Im\left\{\underline{v}_{s2}\hat{\underline{i}}_{s2}\right\} \tag{1.88}$$

Finally the electromagnetic torque of the CDFIM is expressed as:

$$T_{em} = T_{em1} + T_{em2} \tag{1.89}$$

$$= -\frac{3}{2}p_1 M_{sr1}\Im\left\{\hat{\underline{i}}_{s1}\underline{i}_r\right\} + \frac{3}{2}p_2 M_{sr2}\Im\left\{\underline{i}_{s2}\hat{\underline{i}}_r\right\} \tag{1.90}$$

In another form

$$T_{em} = \frac{3}{2}p_1\Im\left\{\hat{\underline{i}}_{s1}\underline{\Phi}_{s1}\right\} + \frac{3}{2}p_2\Im\left\{\underline{i}_{s2}\hat{\underline{\Phi}}_{s2}\right\} \tag{1.91}$$

Thanks to the unified frame vector model, the complex generator has a similar structure as a single DFIM. This allows the development of control strategies and analysis tools analog to the classical wound rotor induction machine.

Conclusion

The mathematical model and steady state behavior of a CDFIM are developed in this chapter. The inverse rotor coupling configuration is the most promising architecture for generating systems. It achieves satisfying performances in terms of power flow, converter sizes and system efficiency. A modular representation of the generator is elaborated based on the model of two distinct wound rotor induction machines expressed in their own reference frames. Both grid-connected and standalone configurations are implemented. The model is then extended to describe the machine in a unified reference frame. This representation is more appropriated for the power sizing of the machine and the elaboration of control strategies.

Chapter 2

Power Operating Domain of the CDFIM

Introduction

The chapter deals with the steady state power operating domain of a CDFIM with regards to its rated parameters. The power sizing of the generator is of great importance for practical applications. It ensures the machine is being operated inside its safe working range. Besides, it allows to choose the machine that is best adapted for the intended application, according to its power capability limits.
Based on the vector model of the machine in the unified synchronous rotating frame, a rigorous analytic method is elaborated in section 2.1 to derive the active and reactive power margins of the cascade. Generic power limit curve expressions are then established in section 2.2 based on a per unit representation of the machines. Therefore, the problem formulation can be adapted to any power range of machines and the obtained conclusions remain true. The active versus reactive power diagram of the CDFIM is built in section 2.3 followed by multiple simulation results revealing the influence of the slip range and terminal voltage variation on the reactive power capability of the machine (sections 2.4 and 2.5). A particular attention is paid to medium and high power scale machines in section 2.6, leading to simplified limit curve equations. It is noted that these ranges are target in most industrial applications. The impact of magnetic circuit saturation on the power generation domain is included in section 2.7. The study reveals a more restrictive domain due to the saturation phenomenon in the machine. Finally the operating domain is tested experimentally in section 2.8 using a laboratory scale machine. The experimental results validate the analytical limits.

2.1 Power limitation curves

To ensure that the electrical machine operates within its safe limits, the steady state operating domain of the CDFIM in terms of active and reactive powers is investigated regarding the rated quantities of the machine i.e. $|\underline{i}_{s2n}|$, $|\underline{v}_{s2n}|$, $|\underline{i}_{rn}|$, $|\underline{v}_{rn}|$, $|\underline{i}_{s1n}|$, $|\underline{v}_{s1n}|$, and P_{s2n}. $|\underline{x}| = \sqrt{X_d^2 + X_q^2}$ refers to the amplitude (the maximum value) of the alternating quantity. The complex structure of the cascade results in increasing the number of parameters that define its limit margins. The nominal quantities $|\underline{i}_{s2n}|$ and P_{s2n} are imposed by the characteristics of DFIM2, $|\underline{i}_{rn}|$ and $|\underline{v}_{rn}|$ given by (2.1), (2.2) depend on the design of both DFIM1 and DFIM2 whereas $|\underline{i}_{s1n}|$ and $|\underline{v}_{s1n}|$ are determined by the DFIM1 rating. The terminal voltage $|\underline{v}_{s2}|$ is defined by the grid. It is considered to be constant, equal to its nominal value during normal operation.

$$|\underline{i}_{rn}| = \min\left\{|\underline{i}_{r1n}|, |\underline{i}_{r2n}|\right\} \tag{2.1}$$

$$|\underline{v}_{rn}| = \min\left\{|\underline{v}_{r1n}|, |\underline{v}_{r2n}|\right\} \tag{2.2}$$

In order to derive the operating power diagram of the CDFIM, the output active and reactive powers (P_{s2}, Q_{s2}) are expressed as a function of each rated quantity distinctly at steady state. Then the corresponding limit curves are depicted in an active versus reactive power chart, and the resultant power domain of the cascade will be bounded by the most restraining limit curves [10], [33].
Considering the Power machine synchronously rotating frame with the q-axis aligned along the stator voltage phasor $\underline{v}_{s2}$, and neglecting the voltage drop across the stator resistance R_{s2} which is an acceptable assumption for high power machines, the following equations are deduced at steady state:

$$V_{s2d} = 0, \quad V_{s2q} = |\underline{v}_{s2}| \tag{2.3}$$

$$\Phi_{s2q} \simeq 0, \quad \Phi_{s2d} \simeq V_{s2q}/\omega_{s2} \tag{2.4}$$

$$P_{s2} = \frac{3}{2} V_{s2q} I_{s2q} \tag{2.5}$$

$$Q_{s2} = \frac{3}{2} V_{s2q} I_{s2d} \tag{2.6}$$

2.1.1 Power machine stator current limitation

Referring to (2.5) and (2.6), a relation between the Power machine stator current amplitude and the output powers can be easily established as:

$$P_{s2}^2 + Q_{s2}^2 = \left(\frac{3}{2} |\underline{v}_{s2}| \, |\underline{i}_{s2}|\right)^2 \tag{2.7}$$

2.1.2 Rotor current limitation

In the defined voltage oriented frame, the stator and rotor current *d-q* components are related by (2.8), (2.9) using equations (1.76) and (2.4).

$$I_{s2d} = \frac{\Phi_{s2d}}{L_{s2}} - \frac{M_{sr2}}{L_{s2}} I_{rd} \tag{2.8}$$

$$I_{s2q} = -\frac{M_{sr2}}{L_{s2}} I_{rq} \tag{2.9}$$

Introducing the value of I_{s2d}, I_{s2q} in (2.5)-(2.6) yields to

$$P_{s2} = -\frac{3M_{sr2}}{2L_{s2}} V_{s2q} I_{rq} \tag{2.10}$$

$$Q_{s2} = \frac{3}{2L_{s2}\omega_{s2}} V_{s2q}^2 - \frac{3M_{sr2}}{2L_{s2}} V_{s2q} I_{rd} \tag{2.11}$$

Hence, the active and reactive powers are expressed in terms of the rotor current amplitude as follows:

$$P_{s2}^2 + \left(Q_{s2} - \frac{3\left|\underline{v}_{s2}\right|^2}{2L_{s2}\omega_{s2}} \right)^2 = \left(\frac{3M_{sr2}\left|\underline{v}_{s2}\right|\left|\underline{i}_r\right|}{2L_{s2}} \right)^2 \tag{2.12}$$

2.1.3 Rotor voltage limitation

At steady state, the rotor current and voltage are related by the following expressions in the mentioned synchronous frame using (1.74), (1.78), (2.8) and (2.9).

$$V_{rd} = R_{r2} I_{rd} - g_2 \omega_{s2} \sigma_2 L_{r2} I_{rq} \tag{2.13}$$

$$V_{rq} = R_{r2} I_{rq} + g_2 \omega_{s2} \sigma_2 L_{r2} I_{rd} + g_2 \frac{M_{sr2}}{L_{s2}} V_{s2q} \tag{2.14}$$

With $g_2\omega_{s2} = \omega_{s2} - p_2\Omega$.
Therefore, the quantities I_{rd}, I_{rq} can be expressed in terms of V_{rd}, V_{rq} by (2.15) and (2.16).

$$I_{rd} = \frac{1}{C_2}\left(R_{r2} V_{rd} + g_2 \omega_{s2} \sigma_2 L_{r2} V_{rq} - g_2^2 \omega_{s2} \sigma_2 \frac{L_{r2} M_{sr2}}{L_{s2}} V_{s2q} \right) \tag{2.15}$$

$$I_{rq} = \frac{1}{C_2}\left(-g_2 \omega_{s2} \sigma_2 L_{r2} V_{rd} + R_{r2} V_{rq} - g_2 R_{r2} \frac{M_{sr2}}{L_s 2} V_{s2q} \right) \tag{2.16}$$

Including the above relations in (2.10) and (2.11) yields to:

$$P_{s2} - A_2 V_{s2q}^2 = -\frac{3}{2}\frac{M_{sr2}}{L_{s2}C_2} V_{s2q} \left(-g_2\omega_{s2}\sigma_2 L_{r2} V_{rd} + R_{r2} V_{rq}\right) \tag{2.17}$$

$$Q_{s2} - B_2 V_{s2q}^2 = -\frac{3}{2}\frac{M_{sr2}}{L_{s2}C_2} V_{s2q} \left(R_{r2} V_{rd} + g_2\omega_{s2}\sigma_2 L_{r2} V_{rq}\right) \tag{2.18}$$

where:

$$A_2 = \frac{3 g_2 R_{r2} M_{sr2}^2}{2 L_{s2}^2 C_2} \tag{2.19}$$

$$B_2 = \frac{3}{2 L_{s2}\omega_{s2}} \left(1 + \frac{g_2^2 \omega_{s2}^2 L_{r2}^2 \sigma_2 (1-\sigma_2)}{C_2}\right) \tag{2.20}$$

$$C_2 = R_{r2}^2 + \left(g_2\omega_{s2}\sigma_2 L_{r2}\right)^2 \tag{2.21}$$

(2.17) and (2.18) result in the following power relation.

$$\left(P_{s2} - A_2 \left|\underline{v}_{s2}\right|^2\right)^2 + \left(Q_{s2} - B_2 \left|\underline{v}_{s2}\right|^2\right)^2 = \frac{1}{C_2}\left(\frac{3 M_{sr2} \left|\underline{v}_{s2}\right| \left|\underline{v}_r\right|}{2 L_{s2}}\right)^2 \tag{2.22}$$

2.1.4 Control machine stator current limitation

The active and reactive powers can be expressed in terms of M1 stator current, since the Power machine and the Control machine currents are related. Indeed, a relation between the two stator currents can be established at steady state using (1.76), (1.82) and (1.83).

$$\frac{R_r \underline{\Phi}_{s2}}{M_{sr2}} - \frac{R_r L_{s2}}{M_{sr2}}\underline{i}_{s2} + j g_2\omega_{s2}\left(\frac{L_r \underline{\Phi}_{s2}}{M_{sr2}} - M_{sr1}\underline{i}_{s1} - \frac{L_{s2}L_r\sigma_p}{M_{sr2}}\underline{i}_{s2}\right) = 0 \tag{2.23}$$

Where $\sigma_p = 1 - \dfrac{M_{sr2}^2}{L_{s2}L_r}$.
Decomposing into *d-q* components, (2.23) becomes as follows in the synchronous stator voltage oriented coordinate.

$$\frac{L_{s2}R_r}{M_{sr2}} I_{s2d} = \frac{R_r}{M_{sr2}}\Phi_{s2d} - g_2\omega_{s2}\frac{L_r}{M_{sr2}}\Phi_{s2q} + g_2\omega_{s2} M_{sr1} I_{s1q} + g_2\omega_{s2}\frac{L_{s2}L_r\sigma_p}{M_{sr2}} I_{s2q} \tag{2.24}$$

$$\frac{L_{s2}R_r}{M_{sr2}} I_{s2q} = \frac{R_r}{M_{sr2}}\Phi_{s2q} + g_2\omega_{s2}\frac{L_r}{M_{sr2}}\Phi_{s2d} - g_2\omega_{s2} M_{sr1} I_{s1d} - g_2\omega_{s2}\frac{L_{s2}L_r\sigma_p}{M_{sr2}} I_{s2d} \tag{2.25}$$

Rearranging (2.24) and (2.25), I_{s2d}, I_{s2q} are expressed as a function of I_{s1d}, I_{s1q}:

$$I_{s2d} = \frac{M_{sr2}}{L_{s2}C_1}\left[-g_2^2\omega_{s2}^2 L_r\sigma_p M_{sr1}I_{s1d} + g_2\omega_{s2}R_r M_{sr1}I_{s1q} + \frac{g_2^2\omega_{s2}^2L_r^2\sigma_p + R_r^2}{M_{sr2}\omega_{s2}}V_{s2q}\right] \tag{2.26}$$

$$I_{s2q} = \frac{M_{sr2}}{L_{s2}C_1}\left[-g_2\omega_{s2}R_r M_{sr1}I_{s1d} - g_2^2\omega_{s2}^2 L_r\sigma_p M_{sr1}I_{s1q} + g_2\frac{R_r M_{sr2}}{L_{s2}}V_{s2q}\right] \tag{2.27}$$

Substituting (2.26), (2.27) in (2.5) and (2.6) leads to

$$P_{s2} - A_1V_{s2q}^2 = \frac{3M_{sr2}}{2L_{s2}C_1}V_{s2q}\left[-g_2\omega_{s2}R_r M_{sr1}I_{s1d} - g_2^2\omega_{s2}^2 L_r\sigma_p M_{sr1}I_{s1q}\right] \tag{2.28}$$

$$Q_{s2} - B_1V_{s2q}^2 = \frac{3M_{sr2}}{2L_{s2}C_1}V_{s2q}\left[-g_2^2\omega_{s2}^2 L_r\sigma_p M_{sr1}I_{s1d} + g_2\omega_{s2}R_r M_{sr1}I_{s1q}\right] \tag{2.29}$$

where:

$$A_1 = \frac{3g_2R_rM_{sr2}^2}{2L_{s2}^2C_1} \tag{2.30}$$

$$B_1 = \frac{3\left[R_r^2 + \sigma_p\left(g_2\omega_{s2}L_r\right)^2\right]}{2\omega_{s2}L_{s2}C_1} \tag{2.31}$$

$$C_1 = R_r^2 + \left(g_2\omega_{s2}L_r\sigma_p\right)^2 \tag{2.32}$$

Therefrom, the output powers are expressed as a function of the Control machine stator current as follows.

$$\left(P_{s2} - A_1\left|\underline{v}_{s2}\right|^2\right)^2 + \left(Q_{s2} - B_1\left|\underline{v}_{s2}\right|^2\right)^2 = \frac{1}{C_1}\left(\frac{3g_2\omega_{s2}M_{sr1}M_{sr2}\left|\underline{v}_{s2}\right|\left|\underline{i}_{s1}\right|}{2L_{s2}}\right)^2 \tag{2.33}$$

2.1.5 Control machine stator voltage limitation

In order to derive the limit expression defined by the Control machine stator voltage, a relation between P_{s2}, Q_{s2} and $|\underline{v}_{s1}|$ should be elaborated.
At steady state operation, (1.73), (1.76) and (1.77) become:

$$\underline{v}_{s1} = R_{s1}\underline{i}_{s1} + jg_c\omega_{s2}\left(L_{s1}\underline{i}_{s1} + L_{s2}\frac{M_{sr1}}{M_{sr2}}\underline{i}_{s2}\right) - jg_c\omega_{s2}\frac{M_{sr1}}{M_{sr2}}\underline{\Phi}_{s2} \tag{2.34}$$

With $g_c\omega_{s2} = \omega_{s2} - \Sigma p\Omega$.
Relation (2.34) is described in terms of *d-q* components as follows in the mentioned

oriented frame:

$$V_{s1d} = R_{s1}I_{s1d} - g_c\omega_{s2}L_{s1}I_{s1q} - g_c\omega_{s2}L_{s2}\frac{M_{sr1}}{M_{sr2}}I_{s2q} \tag{2.35}$$

$$V_{s1q} = R_{s1}I_{s1q} + g_c\omega_{s2}L_{s1}I_{s1d} + g_c\omega_{s2}L_{s2}\frac{M_{sr1}}{M_{sr2}}I_{s2d} - g_c\omega_{s2}\frac{M_{sr1}}{M_{sr2}}\Phi_{s2d} \tag{2.36}$$

Consequently, the expressions of I_{s1d}, I_{s1q} are deduced in (2.37) and (2.38).

$$I_{s1d} = \frac{1}{D_0}\Big[R_{s1}V_{s1d} + g_c\omega_{s2}L_{s1}V_{s1q} - g_c^2\omega_{s2}^2L_{s1}L_{s2}\frac{M_{sr1}}{M_{sr2}}I_{s2d} + g_c\omega_{s2}R_{s1}L_{s2}\frac{M_{sr1}}{M_{sr2}}I_{s2q} + g_c^2\omega_{s2}L_{s1}\frac{M_{sr1}}{M_{sr2}}V_{s2q}\Big] \tag{2.37}$$

$$I_{s1q} = \frac{1}{D_0}\Big[R_{s1}V_{s1q} - g_c\omega_{s2}L_{s1}V_{s1d} - g_c^2\omega_{s2}^2L_{s1}L_{s2}\frac{M_{sr1}}{M_{sr2}}I_{s2q} - g_c\omega_{s2}R_{s1}L_{s2}\frac{M_{sr1}}{M_{sr2}}I_{s2d} + g_cR_{s1}\frac{M_{sr1}}{M_{sr2}}V_{s2q}\Big] \tag{2.38}$$

where:

$$D_0 = R_{s1}^2 + \left(g_c\omega_{s2}L_{s1}\right)^2 \tag{2.39}$$

Introducing the relations of I_{s1d}, I_{s1q} in (2.28) and (2.29), the power expressions are put in the following form:

$$P_{s2} = \frac{3M_{sr2}}{2L_{s2}C_1}V_{s2q}\left(K_1V_{s1d} + K_2V_{s1q} + K_3I_{s2d} + K_4I_{s2q} + K_5V_{s2q}\right) \tag{2.40}$$

$$Q_{s2} = \frac{3M_{sr2}}{2L_{s2}C_1}V_{s2q}\left(K_2V_{s1d} - K_1V_{s1q} + K_4I_{s2d} - K_3I_{s2q} + K_6V_{s2q}\right) \tag{2.41}$$

Then, replacing I_{s2d}, I_{s2q} with their corresponding expressions using (2.5) and (2.6) leads to the following relations between the output powers and M1 stator voltage.

$$\frac{2}{3}P_{s2}\left(\frac{L_{s2}C_1}{M_{sr2}} - K_4\right) - \frac{2}{3}K_3Q_{s2} - K_5V_{s2q}^2 = V_{s2q}\left(K_1V_{s1d} + K_2V_{s1q}\right) \tag{2.42}$$

$$\frac{2}{3}Q_{s2}\left(\frac{L_{s2}C_1}{M_{sr2}} - K_4\right) + \frac{2}{3}K_3P_{s2} - K_6V_{s2q}^2 = V_{s2q}\left(K_2V_{s1d} - K_1V_{s1q}\right) \tag{2.43}$$

The above equations are squared and rearranged leading to the following form:

$$A_0\left(P_{s2}^2 + Q_{s2}^2\right) - B_0\left|v_{s2}\right|^2P_{s2} - C_0\left|v_{s2}\right|^2Q_{s2} = \left(K_1^2 + K_2^2\right)\left|\underline{v}_{s1}\right|^2\left|v_{s2}\right|^2 - \left(K_5^2 + K_6^2\right)\left|v_{s2}\right|^4 \tag{2.44}$$

(2.44) can be also written as (2.45):

$$\left(P_{s2}-\frac{B_0}{2A_0}\left|\underline{v}_{s2}\right|^2\right)^2+\left(Q_{s2}-\frac{C_0}{2A_0}\left|\underline{v}_{s2}\right|^2\right)^2=\left(\frac{C_0^2+B_0^2}{4A_0^2}-\frac{K_5^2+K_6^2}{A_0}\right)\left|v_{s2}\right|^4 + \frac{(K_1^2+K_2^2)}{A_0}\left(\left|\underline{v}_{s1}\right|\left|v_{s2}\right|\right)^2 \quad (2.45)$$

where

$$A_0=\frac{4}{9}\left[\left(\frac{L_{s2}^2C_1}{M_{sr2}^2}-K_4\right)^2+K_3^2\right] \quad (2.46)$$

$$B_0=\frac{4}{3}\left[K_5\left(\frac{L_{s2}^2K_1}{M_{sr2}^2}-K_4\right)+K_3K_6\right] \quad (2.47)$$

$$C_0=\frac{4}{3}\left[K_6\left(\frac{L_{s2}^2C_1}{M_{sr2}^2}-K_4\right)-K_3K_5\right] \quad (2.48)$$

K_1, K_2, K_3, K_4, K_5 and K_6 expressions are given by:

$$K_1=\frac{g_2\omega_{s2}L_{s2}M_{sr1}}{M_{sr2}D_0}\left(-R_rR_{s1}+g_cg_2\omega_{s2}^2L_{s1}L_r\sigma_p\right) \quad (2.49)$$

$$K_2=\frac{g_2\omega_{s2}^2L_{s2}M_{sr1}}{M_{sr2}D_0}\left(-g_cL_{s1}R_r-g_2R_{s1}L_r\sigma_p\right) \quad (2.50)$$

$$K_3=-\frac{g_c\omega_{s2}L_{s2}M_{sr1}}{M_{sr2}}K_2 \quad (2.51)$$

$$K_4=\frac{g_c\omega_{s2}L_{s2}M_{sr1}}{M_{sr2}}K_1 \quad (2.52)$$

$$K_5=g_2R_r+\frac{g_cM_{sr1}}{M_{sr2}}K_2 \quad (2.53)$$

$$K_6=\frac{L_{s2}}{M_{sr2}^2}\left(g_2^2\omega_{s2}L_r^2\sigma_p+\frac{R_r^2}{\omega_{s2}}\right)-\frac{g_cM_{sr1}}{M_{sr2}}K_1 \quad (2.54)$$

On the basis of (2.7), (2.12), (2.22), (2.33), and (2.45), the power limitation curves are described by various circles. The limit is defined by setting the machine quantities to their nominal values: $|\underline{i}_{s2n}|$, $|\underline{v}_{s2n}|$, $|\underline{i}_{rn}|$, $|\underline{v}_{rn}|$, $|\underline{i}_{s1n}|$ and $|\underline{v}_{s1n}|$.

2.2 Generic operating domain

A more generic study is presented in this section. The analysis is based on per unit representation of the machine in order to formulate generalized conclusions to any power range of machines. The main innovation is that it achieves a power operating domain of the CDFIM regardless the power scale of the considered system [7].

2.2.1 Per unit system

Base values of the per unit system, for each induction machine, are defined in Table 2.1. The nominal amplitude of the alternating quantity is used as reference. X_n denotes the RMS rated value of quantity x and m the transformer (stator to rotor) turns ratio given by: $m = \dfrac{M_{sr}}{L_s} \simeq \dfrac{V_{rn}}{V_{sn}}$.

Quantity	Base value
Stator voltage base V_{sb}	$\sqrt{2}V_{sn}$
Stator current base I_{sb}	$\sqrt{2}I_{sn}$
Stator impedance base Z_{sb}	V_{sb}/I_{sb}
Rotor voltage base V_{rb}	$mV_{sb} \simeq \sqrt{2}V_{rn}$
Rotor current base I_{rb}	$I_{sb}/m \simeq \sqrt{2}I_{rn}$
Rotor impedance base Z_{rb}	$V_{rb}/I_{rb} = m^2 Z_{sb}$
Base power S_b	$\frac{3}{2}V_{sb}I_{sb} = S_n$
Base angular frequency ω_b	$2\pi f_n$

Table 2.1: Per unit system applied to each DFIM

Therefore the DFIM electrical parameters, referred to the stator side, can be expressed in per unit form as follows:

$$r_{si} = \frac{R_{si}}{Z_{sbi}}; \quad x_{si} = \frac{L_{si}\omega_{bi}}{Z_{sbi}}; \quad x_{hi} = \frac{M_{sri}\omega_{bi}}{m_i Z_{sbi}} \tag{2.55}$$

$$r_{ri} = \frac{R_{ri}}{m_i^2 Z_{sbi}}; \quad x_{ri} = \frac{L_{ri}\omega_{bi}}{m_i^2 Z_{sbi}} \quad i = \{1, 2\} \tag{2.56}$$

Notice that the above notation results in $x_{hi} = x_{si}$.
For each DFIM, the per unit expressions of stator and rotor quantities are derived using the corresponding machine base as:

$$\underline{i}_{si}^* = \frac{\underline{i}_{si}}{I_{sbi}}; \quad \underline{v}_{si}^* = \frac{\underline{v}_{si}}{V_{sbi}}; \quad \underline{\Phi}_{si}^* = \frac{\underline{\Phi}_{si}\omega_{bi}}{V_{sbi}}; \quad p_{si} = \frac{P_{si}}{S_{bi}}; \quad \omega_{si}^* = \frac{\omega_{si}}{\omega_{bi}} \tag{2.57}$$

$$\underline{i}_{ri}^* = \frac{\underline{i}_{ri}}{I_{rbi}}; \quad \underline{v}_{ri}^* = \frac{\underline{v}_{ri}}{V_{rbi}}; \quad \underline{\Phi}_{ri}^* = \frac{\underline{\Phi}_{ri}\omega_{bi}}{V_{rbi}}; \quad q_{si} = \frac{Q_{si}}{S_{bi}}; \quad i = \{1, 2\} \tag{2.58}$$

The power ratio between the machines is given by:

$$\tau = \frac{S_{b1}}{S_{b2}} \tag{2.59}$$

and since

$$V_{sbi} I_{sbi} = V_{rbi} I_{rbi} \tag{2.60}$$

thus, the following relation can be established:

$$V_{rb1}I_{rb1} = \tau V_{rb2}I_{rb2} \tag{2.61}$$

Two new parameters ρ_I and γ are further introduced, describing the rotor current relation and the rotor impedance base ratio respectively.

$$I_{rb1} = \rho_I I_{rb2} \tag{2.62}$$

$$\gamma = \frac{\rho_I^2}{\tau} \tag{2.63}$$

2.2.2 CDFIM vector model in per unit

Based on the above mentioned per unit system, the CDFIM vector model in the unified Power machine synchronous frame is expressed as follows.

$$\underline{v}_{s2}^* = r_{s2}\underline{i}_{s2}^* + \frac{1}{\omega_b}\frac{d}{dt}\underline{\Phi}_{s2}^* + j\omega_{s2}^*\underline{\Phi}_{s2}^* \tag{2.64}$$

$$\underline{v}_{s1}^* = r_{s1}\underline{i}_{s1}^* + \frac{1}{\omega_b}\frac{d}{dt}\underline{\Phi}_{s1}^* + jg_c\omega_{s2}^*\underline{\Phi}_{s1}^* \tag{2.65}$$

$$\underline{v}_{r2}^* = r_{r2}\underline{i}_{r2}^* + \frac{1}{\omega_b}\frac{d}{dt}\underline{\Phi}_{r2}^* + jg_2\omega_{s2}^*\underline{\Phi}_{r2}^* \tag{2.66}$$

$$\underline{v}_{r1}^* = r_{r1}\underline{i}_{r1}^* + \frac{1}{\omega_b}\frac{d}{dt}\underline{\Phi}_{r1}^* + jg_2\omega_{s2}^*\underline{\Phi}_{r1}^* \tag{2.67}$$

$$\underline{\Phi}_{s2}^* = x_{s2}\underline{i}_{s2}^* + x_{h2}\underline{i}_{r2}^* \tag{2.68}$$

$$\underline{\Phi}_{s1}^* = x_{s1}\underline{i}_{s1}^* + x_{h1}\underline{i}_{r1}^* \tag{2.69}$$

$$\underline{\Phi}_{r2}^* = x_{r2}\underline{i}_{r2}^* + x_{h2}\underline{i}_{s2}^* \tag{2.70}$$

$$\underline{\Phi}_{r1}^* = x_{r1}\underline{i}_{r1}^* + x_{h1}\underline{i}_{s1}^* \tag{2.71}$$

The output powers are given by (2.72), (2.73).

$$p_{s2} = \Re\left\{(\underline{v}_{s2}^*\hat{\underline{i}}_{s2}^*)\right\} \tag{2.72}$$

$$q_{s2} = \Im\left\{(\underline{v}_{s2}^*\hat{\underline{i}}_{s2}^*)\right\} \tag{2.73}$$

The rotor quantities are related as follows, corresponding to a supersynchronous motor convention:

$$\underline{i}_r^* = \underline{i}_{r2}^* = -\rho_I\underline{i}_{r1}^* \tag{2.74}$$

$$\underline{v}_r^* = \underline{v}_{r2}^* = \frac{\tau}{\rho_I}\underline{v}_{r1}^* \tag{2.75}$$

It is noted that the angular frequency bases ω_{b1} and ω_{b2} are considered to be equal to a reference frequency ω_b (e.g. the grid frequency).
The steady state equivalent circuit of the CDFIM is deduced in Figure 2.1.
$x_{si\sigma} = x_{si} - x_{hi}$ and $x_{ri\sigma} = x_{ri} - x_{hi}$ are respectively the stator and rotor leakage reactance.

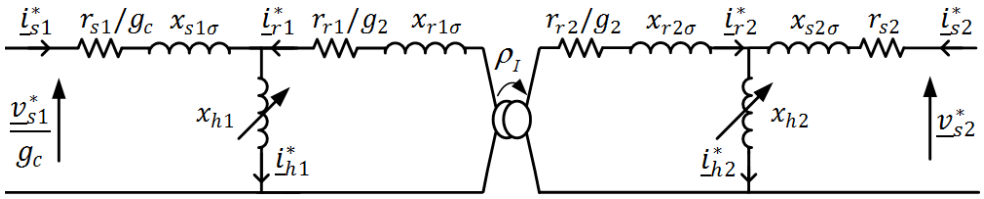

Figure 2.1: Steady state equivalent circuit of the CDFIM in the Power machine synchronous frame

2.2.3 General power curve limits

The generic limit curve expressions are derived from section 2.1 by applying the per unit transformation to the CDFIM parameters. The equations are summarized as follows.

$$p_{s2}^2 + q_{s2}^2 = \left(|\underline{v}^*_{s2n}|\,|\underline{i}^*_{s2n}|\right)^2 \tag{2.76}$$

$$p_{s2}^2 + \left(q_{s2} - \frac{|\underline{v}^*_{s2n}|^2}{x_{s2}\omega^*_{s2}}\right)^2 = \left(|\underline{v}^*_{s2n}|\,|\underline{i}^*_{rn}|\right)^2 \tag{2.77}$$

$$\left(p_{s2} - a_2\,|\underline{v}^*_{s2n}|^2\right)^2 + \left(q_{s2} - b_2\,|\underline{v}^*_{s2n}|^2\right)^2 = \frac{1}{c_2}\left(|\underline{v}^*_{s2n}|\,|\underline{v}^*_{rn}|\right)^2 \tag{2.78}$$

$$\left(p_{s2} - a_1\,|\underline{v}^*_{s2n}|^2\right)^2 + \left(q_{s2} - b_1\,|\underline{v}^*_{s2n}|^2\right)^2 = \frac{1}{c_1}\left(\rho_I g_2 \omega^*_{s2} x_{h1}\,|\underline{v}^*_{s2n}|\,|\underline{i}^*_{s1n}|\right)^2 \tag{2.79}$$

$$\left(p_{s2} - a_0\,|v^*_{s2n}|^2\right)^2 + \left(q_{s2} - b_0\,|v^*_{s2n}|^2\right)^2 = c_0\,|\underline{v}^*_{s2n}|^4 + c_{01}\left(|\underline{v}^*_{s2n}|\,|\underline{v}^*_{s1n}|\right)^2 \tag{2.80}$$

where:

$$a_2 = \frac{g_2 r_{r2}}{c_2} \tag{2.81}$$

$$b_2 = \frac{1}{x_{s2}\omega^*_{s2}}\left(1 + \frac{g_2^2 \omega^{*2}_{s2} x_{r2}^2 \sigma_2 (1-\sigma_2)}{c_2}\right) \tag{2.82}$$

$$c_2 = r_{r2}^2 + \left(g_2 \omega^*_{s2} \sigma_2 x_{r2}\right)^2 \tag{2.83}$$

$$\sigma_2 = 1 - \frac{x_{h2}^2}{x_{s2} x_{r2}} = 1 - \frac{x_{h2}}{x_{r2}} \tag{2.84}$$

and

$$a_1 = \frac{g_2\gamma\left(r_{r1}+\gamma r_{r2}\right)}{c_1} \tag{2.85}$$

$$b_1 = \frac{\left(r_{r1}+\gamma r_{r2}\right)^2 + g_2^2\omega_{s2}^{*2}\left(x_{r1}+\gamma x_{r2}\right)\left(x_{r1}+\gamma\sigma_2 x_{r2}\right)}{\omega_{s2}^{*}x_{s2}c_1} \tag{2.86}$$

$$c_1 = \left(r_{r1}+\gamma r_{r2}\right)^2 + g_2^2\omega_{s2}^{*2}\left(x_{r1}+\gamma\sigma_2 x_{r2}\right)^2 \tag{2.87}$$

and

$$a_0 = \frac{\left(c_1k_5 - k_4k_5 + k_3k_6\right)}{k_0} \tag{2.88}$$

$$b_0 = \frac{\left(c_1k_6 - k_4k_6 - k_3k_5\right)}{k_0} \tag{2.89}$$

$$c_0 = \frac{1}{k_0}\left[\left(c_1k_6 - k_4k_6 - k_3k_5\right)^2 - k_5^2 - k_6^2 + \left(c_1k_5 - k_4k_5 + k_3k_6\right)^2\right] \tag{2.90}$$

$$c_{01} = \frac{1}{k_0}\rho_I.\tau\left(k_1^2 + k_2^2\right) \tag{2.91}$$

$$d_0 = r_{s1}^2 + \left(g_c\omega_{s2}^{*}x_{s1}\right)^2 \tag{2.92}$$

$$k_0 = \left(c_1 - k_4\right)^2 + k_3^2 \tag{2.93}$$

k_1, k_2, k_3, k_4, k_5, and k_6 expressions are given by:

$$k_1 = \frac{g_2\omega_{s2}^{*}x_{h1}}{d_0}\left[g_cg_2\omega_{s2}^{*2}x_{s1}\left(x_{r1}+\gamma\sigma_2x_{r2}\right) - r_{s1}\left(r_{r1}+\gamma r_{r2}\right)\right] \tag{2.94}$$

$$k_2 = \frac{g_2\omega_{s2}^{*2}x_{h1}}{d_0}\left[-g_cx_{s1}\left(r_{r1}+\gamma r_{r2}\right) - g_2r_{s1}\left(x_{r1}+\gamma\sigma_2x_{r2}\right)\right] \tag{2.95}$$

$$k_3 = -g_c\omega_{s2}^{*}x_{h1}k_2 \tag{2.96}$$

$$k_4 = g_c\omega_{s2}^{*}x_{h1}k_1 \tag{2.97}$$

$$k_5 = g_2\left(r_{r1}+\gamma r_{r2}\right) + \frac{g_cx_{h1}}{\gamma x_{h2}}k_2 \tag{2.98}$$

$$k_6 = \frac{1}{\gamma x_{h2}}\left[g_2^2\omega_{s2}^{*}\left(x_{r1}+\gamma x_{r2}\right)\left(x_{r1}+\gamma\sigma_2x_{r2}\right) + \frac{\left(r_{r1}+\gamma r_{r2}\right)^2}{\omega_{s2}^{*}}\right] - \frac{g_cx_{h1}}{\gamma x_{h2}}k_1 \tag{2.99}$$

The nominal quantities in the per unit system are expressed as:

$$|\underline{i}_{s1n}^{*}| = 1\text{p.u.}; \quad |\underline{i}_{rn}^{*}| = \frac{\min\left\{|\underline{i}_{r1n}|, |\underline{i}_{r2n}|\right\}}{I_{r2b}} \leq 1 \tag{2.100}$$

$$|\underline{v}_{s1n}^{*}| = 1\text{p.u.}; \quad |\underline{v}_{rn}^{*}| = \frac{\min\left\{|\underline{v}_{r1n}|, |\underline{v}_{r2n}|\right\}}{V_{r2b}} \leq 1 \tag{2.101}$$

$$|\underline{i}_{s2n}^{*}| = 1\text{p.u.}; \quad |\underline{v}_{s2n}^{*}| = 1\text{p.u.}; \qquad \omega_{s2}^{*} = 1\text{p.u.} \tag{2.102}$$

As can be expected, the limit curve expressions depend on the electrical parameters

and the ratings of both induction machines i.e. $|\underline{i}^*_{rn}|$, $|\underline{v}^*_{rn}|$, ρ_I, and τ. Therefore, for a given range of machines, the power operating boundaries of the CDFIM and its ability to supply reactive power would be affected by the choice of the Control and the Power machines. Consequently, a proper combination should be adopted in order to achieve the optimal performance of the cascade. Moreover, it shall be noted that the power capability of the CDFIM is affected by the slip range and the terminal voltage. The impact of the latter parameters on the power domain, is discussed in the following sections.

2.3 Power operating margins

The above mentioned limit boundaries are all depicted in a single power chart, that illustrates the reactive and active powers in its x and y-axes respectively. The resultant steady state operating domain of the CDFIM is determined by the most restrictive limit curves. The power capability traces of a laboratory scale CDFIM are depicted in Figure 2.2. The parameters of the machine are shown in Appendix B, Section B.1. The results correspond to normal grid conditions with a given slip ratio $g_c = -0.1$. With respect to supersynchronous motor conventions, generated active and reactive powers are considered to be negative.

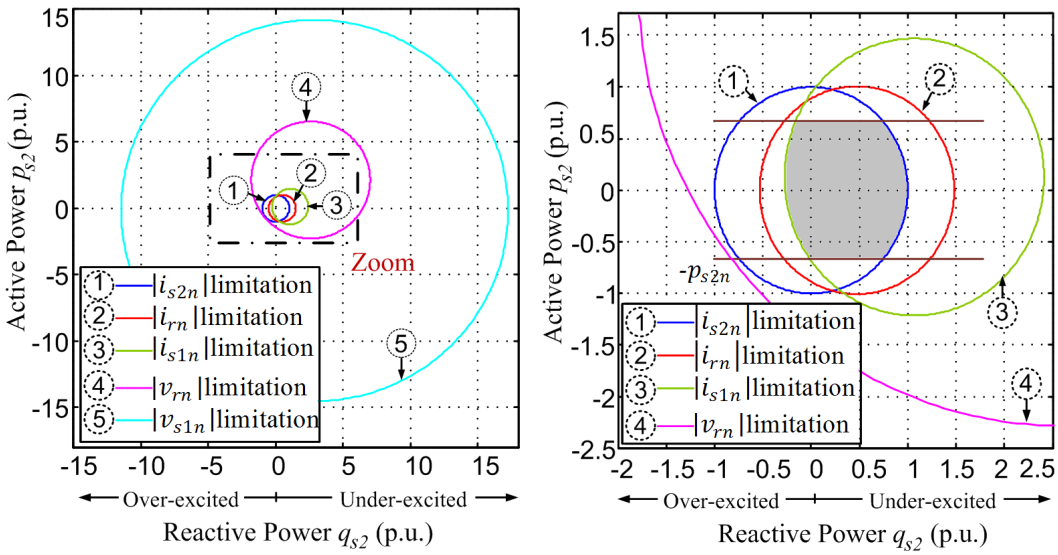

Figure 2.2: Power operating domain of the laboratory scale CDFIM

As can be observed in Figure 2.2, the power margins of the CDFIM are determined by the stator currents. The capacitive reactive power production (over-excited mode) is limited by the Control machine stator current $|\underline{i}^*_{s1n}|$ and the inductive reactive power consumption (under-excited mode) is limited by the Power machine stator

current $|\underline{i}^*_{s2n}|$. Furthermore, for a limited slip range, the voltage limitation curves $|v^*_{s1n}|$ and $|v^*_{rn}|$ do not intervene in the determination of the resultant power operating limits. However for high slip values, they can affect and reduce the power production domain as it will be shown in Section 2.4.

Remarks

1. Equations (2.7), (2.12), (2.22), (2.33), and (2.45) are useful to directly derive the voltages and currents in all the machine windings for a given operating point i.e. P_{s2} and Q_{s2}. Knowing these quantities will help to determine the copper losses i.e. the heating in the machine as well as its magnetic state. This has a direct impact on the design of the machine in terms of copper winding section and iron sizing.
2. The steady state operating domain of a single DFIM is investigated in [36], [60], [129]. The power boundaries are defined by the limit curves (2.76) to (2.78). It is shown that the power capability of the machine is limited by the stator current $|\underline{i}^*_{sn}|$ in under-excited mode and the rotor current $|\underline{i}^*_{rn}|$ in over-excited mode. Consequently, it can be deduced that the power operating margins of the CDFIM and its capability to generate reactive power are reduced compared to the DFIM2 set alone.
3. As mentioned previously, the operating domain of the CDFIM is determined by the parameters and characteristics of both DFIMs. Thus is it convenient to highlight the importance of adopting an adequate combination of the Power and Control machines that ensures optimal behavior of the cascaded machine. Considering the laboratory scale DFIMs given in Appendix B, two combinations can be adopted: configuration A defines M2 as the Power machine and M1 as the Control machine (as adopted in the remaining of this manuscript), then configuration B substitutes the position of the two DFIMs. The resultant operating limits using (2.76) to (2.80) for both configurations are shown in Figures 2.3a and 2.3b.

   As can be deduced, only configuration A can have significant interest for generating systems. In fact, the CDFIM can operate at the entire active power region and is able to generate reactive power over a wide active power range. Whereas in configuration B the power operating domain is extremely reduced. The CDFIM cannot operate at nominal active power and can barely generate reactive power for a very limited range. The operation of the CDFIM requires reactive power consumption instead. Although both machines have the same power rating, the difference resides in the rotor current ratio (i.e. ρ_I) and the p.u. electrical parameters of each DFIM.

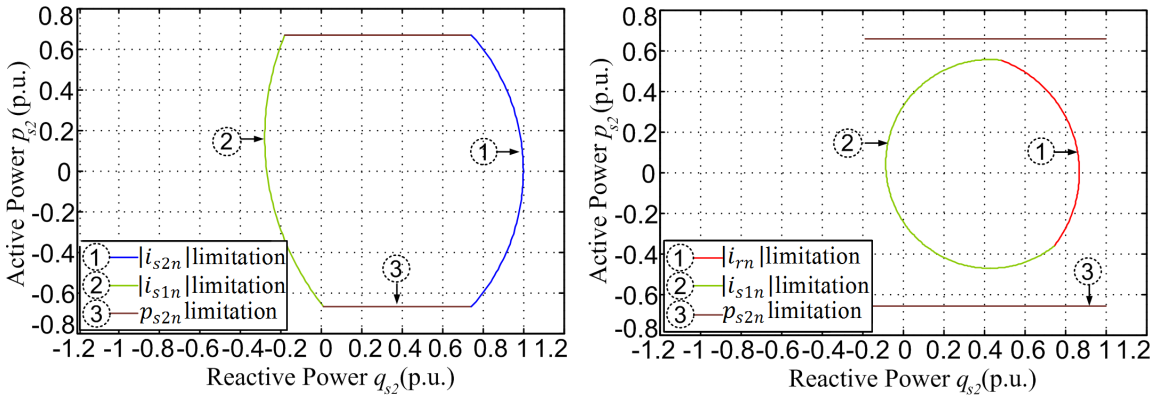

(a) Configuration A (b) Configuration B

Figure 2.3: Power operating domain of a CDFIM

4. Up to this point the stator resistance R_{s2} was neglected. A more accurate power domain is obtained by including the voltage drop across the resistance. In the mentioned stator voltage orientated reference frame, the flux expression (2.4) becomes:

$$\Phi_{s2q} = \frac{R_{s2} I_{s2d}}{\omega_{s2}}, \quad \Phi_{s2d} = \frac{|\underline{v}_{s2}|}{\omega_{s2}} - \frac{R_{s2} I_{s2q}}{\omega_{s2}} \tag{2.103}$$

Applying the modification to (2.24) and (2.25), the expression of $|\underline{i}^*_{s1n}|$ limit curve becomes:

$$\left(p_{s2} - a_{11} \left|\underline{v}^*_{s2}\right|^2\right)^2 + \left(q_{s2} - b_{11} \left|\underline{v}^*_{s2}\right|^2\right)^2 = \frac{1}{c_{11}} \left(\rho_I g_2 \omega^*_{s2} x_{h1} x_{h2} \left|\underline{v}^*_{s2n}\right| \left|\underline{i}^*_{s1n}\right|\right)^2 \tag{2.104}$$

where:

$$a_{11} = \frac{g_2 x_{h2}^2 \gamma \left(r_{r1} + \gamma r_{r2}\right) + g_2^2 r_{s2} \left(x_{r1} + \gamma x_{r2}\right)^2 + \dfrac{r_{s2}}{\omega^{*2}_{s2}} \left(r_{r1} + \gamma r_{r2}\right)^2}{c_{11}} \tag{2.105}$$

$$b_{11} = \frac{x_{s2} \left(r_{r1} + \gamma r_{r2}\right)^2 + g_2^2 \omega^{*2}_{s2} \left(x_{r1} + \gamma x_{r2}\right) \left(x_{r1} + \gamma \sigma_2 x_{r2}\right)}{\omega^*_{s2} c_{11}} \tag{2.106}$$

$$\begin{aligned} c_{11} = {} & \left[x_{s2} \left(r_{r1} + \gamma r_{r2}\right) + g_2 r_{s2} \left(x_{r1} + \gamma x_{r2}\right)\right]^2 \\ & + \left[\frac{r_{s2}}{\omega^*_{s2}} \left(r_{r1} + \gamma r_{r2}\right) - g_2 x_{s2} \omega^*_{s2} \left(x_{r1} + \gamma \sigma_2 x_{r2}\right)\right]^2 \end{aligned} \tag{2.107}$$

It yields to the power diagram illustrated in figure 2.4. As can be noticed, the influence of the resistance is negligible.

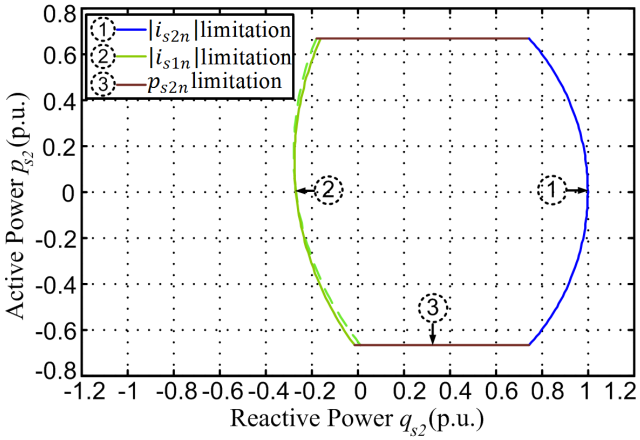

Figure 2.4: Power operating limits. Solid: r_{s2} is neglected; dashed: r_{s2} is considered

2.4 Influence of slip range variation

The analytic expressions established above show that $|\underline{i}^*_{s1n}|$ and $|\underline{v}^*_{rn}|$ limit curves depend on the slip ratio g_2 and $|\underline{v}^*_{s1n}|$ limit expression is a function of g_2 and g_c which, in turn are related as:

$$g_2 = 1 - \frac{p_2}{\Sigma p}\,(1 - g_c) \tag{2.108}$$

Since the converter processes only the slip power, g_c is usually limited e.g. to ± 0.3 in order to reduce the power converter size. Thereafter the variation range of g_2 depends on the configuration retained for p_1 and p_2.

Based on (2.78), (2.79) and (2.80), the influence of a slip variation on each of the aforementioned limitation traces is emphasized in the following. Simulation results are collected in Figures 2.5 and 2.6 for the laboratory scale machine.

1. $|\underline{v}^*_{rn}|$ **limit curve** By increasing g_2, the radius decreases and curve (4) moves to the right and up as one can clearly see in Figure 2.5, which may reduce the CDFIG capability to provide active and reactive powers for high values of g_2 as depicted in Figure 2.5d.

2. $|\underline{v}^*_{s1n}|$ **limit curve** It can be noticed that the limit curve is mostly involved by g_c. An increase in $|g_c|$ reduces the limit trace defined by $|\underline{v}^*_{s1n}|$, but does not affect the actual limits of the operating domain.

3. $|\underline{i}^*_{s1}|$ **limit curve** On the basis of equations (2.79) and (2.85) to (2.87), one can prove that by increasing g_2, the radius and the value of b_1 increase. Besides a_1 increases for small values of g_2 but then begins to decrease when g_2 exceeds a particular value. Thus, when g_2, increases the limit curve (3) expands and moves to the right and down. Knowing that the variation in the radius is more substantial than the shifting value, an increase in g_2 would enlarge the power production margin of the CDFIG as highlighted in Figure 2.6.

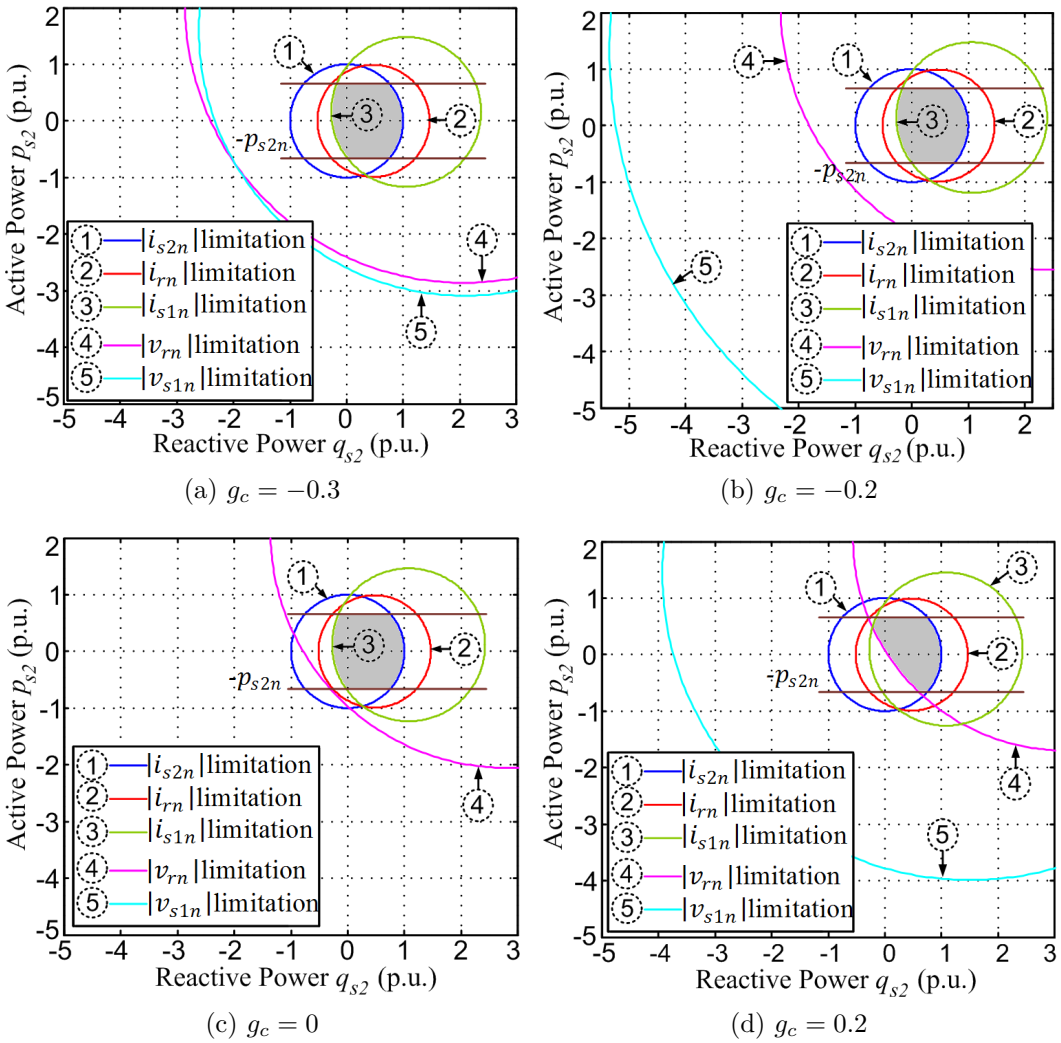

(a) $g_c = -0.3$ (b) $g_c = -0.2$

(c) $g_c = 0$ (d) $g_c = 0.2$

Figure 2.5: Influence of slip variation on the power operating range of a CDFIM

Conversely, for small values of g_2 the limit curve is extremely reduced as the radius is proportional to the slip value. Indeed for $g_2 < 0.1$ the cascade is not able to operate at nominal active power anymore. Since the ability to provide active and reactive power is usually limited by the $|\underline{i}^*_{s1n}|$ limitation curve, it is important to retain a high value of g_2 at every operating speed, in order to optimize the power generation domain of the system as shown in Figure 2.6. A null value of the slip ratio is prohibited and a change of the sign is to be avoided. At this point, it is convenient to highlight the effect of the number of pole pairs on the power operating range. Referring to (2.108), one can easily deduce that for the limited slip range $g_c \in [-0.3; 0.3]$, a CDFIM with equal number of pole pairs results in better performances and optimizes g_2 for the entire speed operating region.

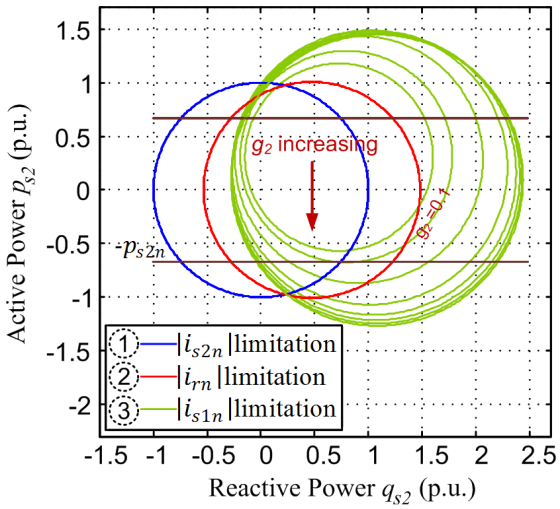

Figure 2.6: Variation of the currents limitation curve with respect to the slip ratio g_2

Under realistic operating conditions and optimal induction machine combinations, the simulation of various power machine scales over a wide speed range shows that the $|\underline{v}^*_{s1n}|$ limitation curve has no influence on the resultant power domain as the corresponding radius is much greater than the radius of the current curves. Thus its expression can be excluded from the determination of the power operating region of the CDFIM. Whereas the rotor voltage limit curve $|\underline{v}^*_{rn}|$ may, in some configurations, affect and reduce the power production margins for high slip values.

The previous tests were also performed on a 300 kW machine and they have led to the same conclusions. It seems justified then to conclude, that the reactive power production (over-excited mode) of a CDFIM is determined by the stator current limit $|\underline{i}^*_{s1n}|$ for a limited speed range, and by rotor voltage limit $|\underline{v}^*_{rn}|$ for large slips; whereas the reactive power consumption (under-excited mode) is limited by the stator current limit $|\underline{i}^*_{s2n}|$ for the entire operating region.

2.5 Influence of a terminal voltage variation

Previous results considered a constant voltage supply at nominal conditions. The impact of a voltage variation on the operating region of the CDFIM is explored hereinafter. Simulation results are presented in Figure 2.7 for different terminal voltages. As can be noticed, subsequent to a voltage drop, the limit area shrinks but the eccentricity moves to the left and down. This can be deduced from equations (2.76) and (2.79). The radius of the limit curves are reduced and curve (3) is shifted. As a result, the power operating region of the CDFIM is reduced over a wide power range. Nevertheless, the machine will be able to generate more reactive power at low active power operation which is interesting in the case of grid voltage sag.

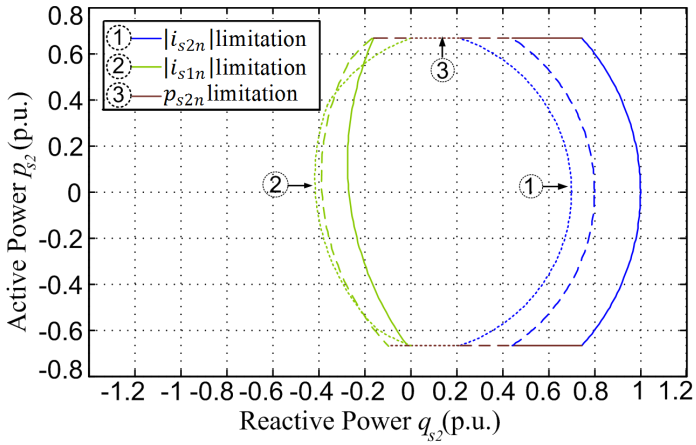

Figure 2.7: Power operating range of CDFIM at different terminal voltages. Solid:$|\underline{v}^*_{s2}| = |\underline{v}^*_{s2n}|$; dashed:$|\underline{v}^*_{s2}| = 0.8\,|\underline{v}^*_{s2n}|$, dotted:$|\underline{v}^*_{s2}| = 0.7\,|\underline{v}^*_{s2n}|$

2.6 Power limit curves for industrial application scale machines

In medium and high power scale machines, that are the most used in industrial applications, the following condition is widely verified

$$r_{ri} <<< x_{ri} \tag{2.109}$$

Therefore the above limit curve expressions can be further reduced leading to the following simplified relations:

$$p_{s2}^2 + q_{s2}^2 = \left(|\underline{v}^*_{s2n}|\,|\underline{i}^*_{s2n}|\right)^2 \tag{2.110}$$

$$p_{s2}^2 + \left(q_{s2} - \frac{|\underline{v}^*_{s2n}|^2}{x_{s2}\omega^*_{s2}}\right)^2 = \left(|\underline{v}^*_{s2n}|\,|\underline{i}^*_{rn}|\right)^2 \tag{2.111}$$

$$\left(p_{s2} - a\,|\underline{v}^*_{s2n}|^2\right)^2 + \left(q_{s2} - b\,|\underline{v}^*_{s2n}|^2\right)^2 = c\left(|\underline{v}^*_{s2n}|\,|\underline{i}^*_{s1n}|\right)^2 \tag{2.112}$$

$$\left(p_{s2} - \alpha\,|\underline{v}^*_{s2n}|^2\right)^2 + \left(q_{s2} - \beta\,|\underline{v}^*_{s2n}|^2\right)^2 = \left(\frac{|\underline{v}^*_{s2n}|\,|\underline{v}^*_{rn}|}{g_2\omega^*_{s2}\sigma_2 x_{r2}}\right)^2 \tag{2.113}$$

where

$$a = \frac{\gamma\left(r_{r1} + \gamma r_{r2}\right)}{g_2\omega^{*2}_{s2}\left(x_{r1} + \gamma\sigma_2 x_{r2}\right)^2}; \qquad \alpha = \frac{g_2 r_{r2}}{\left(g_2\omega^*_{s2}\sigma_2 x_{r2}\right)^2} \tag{2.114}$$

$$b = \frac{x_{r1} + \gamma x_{r2}}{\omega_{s2*} x_{s2}\left(x_{r1} + \gamma\sigma_2 x_{r2}\right)}; \qquad \beta = \frac{1}{x_{s2}\omega^*_{s2}\sigma_2} \tag{2.115}$$

$$c = \frac{\tau\gamma x_{h1}^2}{\left(x_{r1} + \gamma\sigma_2 x_{r2}\right)^2} \tag{2.116}$$

The power limit traces of a high power CDFIM based on two identical 300 kW induction machines are depicted in Figure 2.8 for a slip ratio $g_c = 0.3$ The parameters of the machine are given in Appendix B Section B.2. The minor difference between the initial and the simplified limit curves prove the coherence of the new limit expressions.

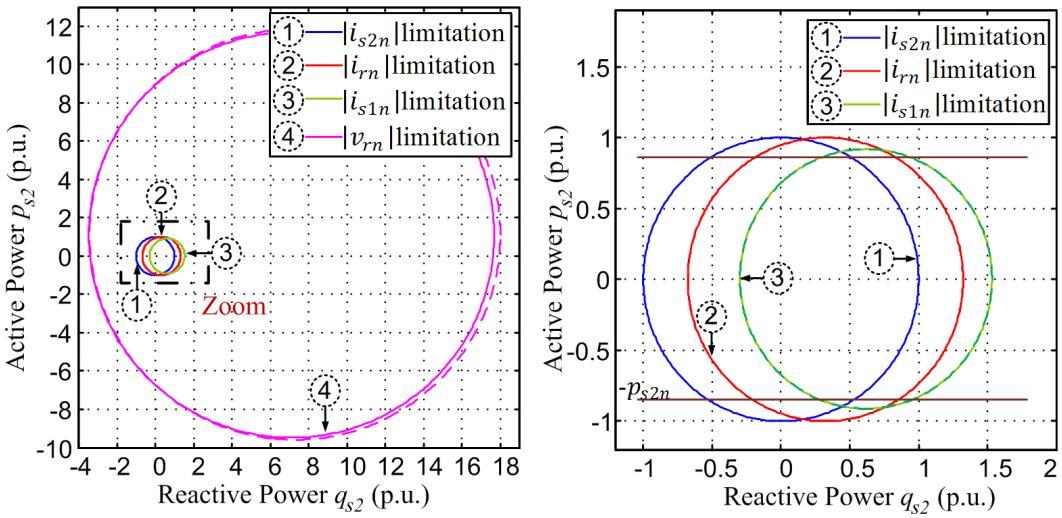

Figure 2.8: Power operating limits of a 300 kW CDFIM . Solid: initial limit expressions; dashed: simplified expressions

As highlighted previously, the ability of the CDFIG to generate reactive power is limited. Its limit depends on the electrical parameters and ratings of both induction machines. The simplified limit curve expressions can be used to revise the design of the machine in order to achieve better performances in terms of power capability.
In order to increase the reactive power production margins of the generator, the radius of curve (3) must be increased and/or the center must be shifted left and down. This is translated by an increase in the value of 'c' and a decrease in the values of 'a' and 'b'. Reference to (2.114) to (2.116) the following conclusions can be deduced:

- An increase in the power ratio τ enlarges the power operating domain. However this value is practically limited ($\tau \leq 1$) and cannot be significantly increased.
- The reactive power capability can be expanded by increasing x_{h1} (i.e x_{s1}). This also reduces the magnetizing current of the machine.
- Increasing x_{h2} (i.e x_{s2}) and/or decreasing x_{r1} and x_{r2} amplifies 'a', 'b' and 'c'. Since the variation in the radius is more substantial than the shifting value, this will result in increasing the reactive power limit of the CDFIM. The variation rate is limited by the condition on $\sigma_2 > 0$.

Accordingly, a modification up to 3% in the p.u. electrical parameters of the 300 kW CDFIM is illustrated in Figure 2.9 in dashed line. The reactive power margin is indeed increased by 8%.

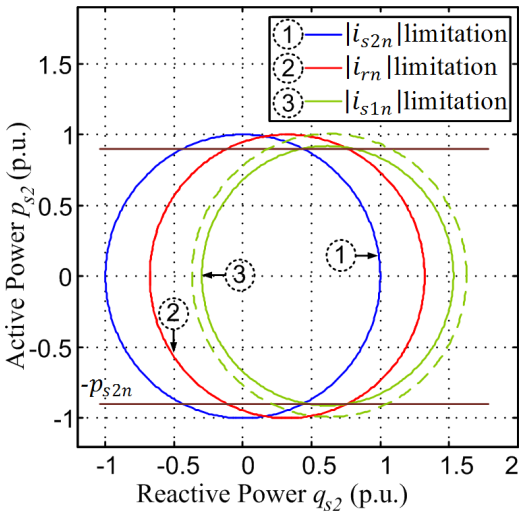

Figure 2.9: Reactive power capability of the CDFIG

2.7 Magnetic core saturation

The above results and conclusions are valid under the assumption of no magnetic core saturation. The proposed analytic study considers linear magnetic conditions with constant inductances that do not vary with the currents. However, since the Control machine operates at variable flux levels, it would be interesting to emphasize the impact of the magnetic circuit saturation on the power operating margins of the CDFIG (refer to Figure 2.1). The saturation phenomenon of induction machine is treated in the literature [16]. A magnetizing curve can be determined based on experimental measurements. The steady state equivalent circuit of a DFIM is illustrated in Figure 2.10.

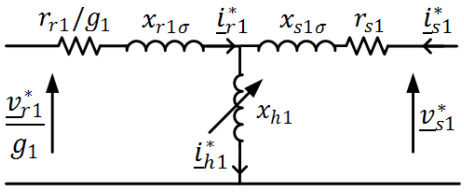

Figure 2.10: Steady state equivalent circuit of the DFIM

No-load tests are performed on the Control machine. The machine is supplied at variable voltage from rotor side and the stator voltage and rotor current are measured. The saturation curve of the laboratory scale machine is depicted in Figure 2.11.

During capacitive reactive power generation (over-excited mode), the control flux is increased. Consequently the iron core is magnetically saturated especially when the Control machine is heavily excited. This is reflected by a decrease in the magnetizing reactance x_{h1} and a significant increase in the Control machine stator current (in comparison with the case where magnetic saturation is neglected).

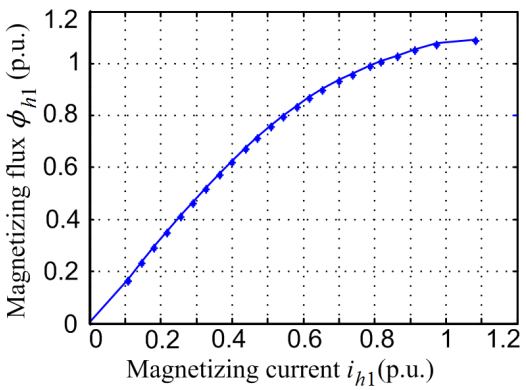

(a) $\phi_{h1} = f(i_{h1})$

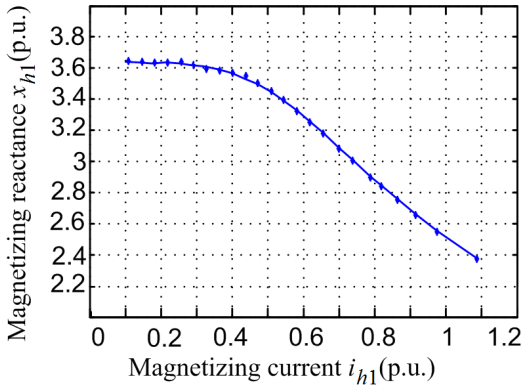

(b) $x_{h1} = f(i_{h1})$

Figure 2.11: Saturation curves

Since the control current is the limiting variable in this mode of operation and x_{h1} is directly related to the radius of the limit curve (refer to (2.79)), it can be deduced that the magnetic saturation significantly limits the capability of the generator to supply capacitive reactive power. In under-excited (inductive) mode, the limiting variable is the Power machine stator current. Thus the reactive power capability is not influenced by the magnetic saturation since the power machine flux is stable at constant output voltage.

Taking into consideration the magnetizing curve and the variation of x_{h1} for every operating point, a new limit bound for the laboratory scale machine is derived by interpolation. For a given active-reactive power operating point (p_{s2}, q_{s2}) from the theoretical non saturated limit curve, the magnetizing current i_{h1} is determined based on the steady state equivalent circuit of the CDFIM (refer to Figure 2.1). Then, reference to the saturation curve in Figure 2.11b, the real magnetizing reactance x_{h1} is deduced. In that case, the new reactive power that can be supplied by the machine under this active power operation and taken into consideration saturation, will be moved to q'_{s2} that is on the new curve. Its value is computed using (2.79). This procedure can be generalized and the new limit bound is plotted in Figure 2.12. As can be noted, the limit curve in presence of saturation is more restricted as it is shown in dashed line. Thus, the reactive power capability of the generator (over-excited domain) is reduced.

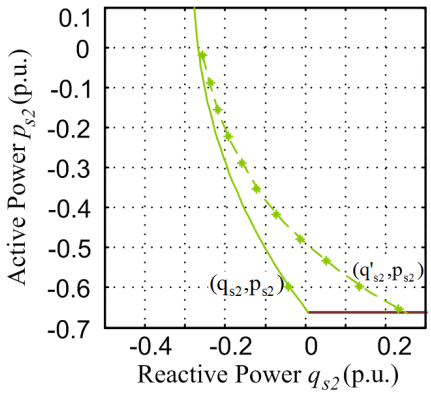

Figure 2.12: Effect of magnetic core saturation on reactive power generation. Solid: without saturation, dashed: with saturation.

2.8 Experimental validation

2.8.1 Experimental bench

The purpose of this section is to validate experimentally the presented analytical approach and verify the steady state power operating limits of the CDFIG. The laboratory scale bench is illustrated in Figure 2.13. The CDFIM is driven by a

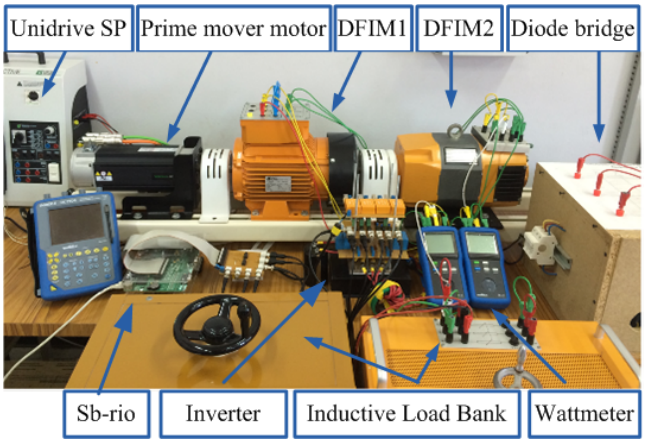

Figure 2.13: CDFIM: experimental test bench

servo-controlled synchronous motor of 2 kW. The mechanical speed of the prime mover is adjusted by a universal drive UNIDRIVE SP control unit. Notice that the DFIMs are magnetically independent. Their shafts are directly coupled and the rotor windings are interconnected through inverse sequence. Similar to the simulation, the test is undertaken for $g_c = -0.1$. In this case the Control machine just consumes active power (due to the losses in the machine), thus the machine is supplied through a diode bridge rectifier cascaded to a Pulse Width Modulation (PWM) inverter (FUJI 7MBP50RA120 module) based on Insulated Gate Bipolar Transistors (IGBT). The IGBT inverter operates at 5 kHz, its control signals are generated by a Xilinx

Spartan-3 FPGA integrated on a single board rio (Sb-rio). The FPGA is programmed from a block diagram representation in Labview interface.

For the experimental validation, the machine is operating in generator mode. The CDFIG is driven at constant speed ($\Omega = \frac{55\pi}{2}$rad/s). A variable inductive load is connected to the CDFIG in order to describe the peripheral limit curve of the theoretical operating domain. The machine is controlled to retain at steady state the nominal output voltage $|\underline{v}_{s2n}|$ regardless of the load variation. This is achieved through the regulation of the Control machine voltage $\underline{v}_{s1}$ in open loop operation. Subsequently, for each operating point, the current and voltage measurements at steady state are collected and compared to the nominal parameters of the CDFIG.

2.8.2 Experiments

In order to emphasize the impact of magnetic circuit saturation on the power operating margins of the CDFIG, two experimental tests are conducted. The first test is performed at reduced output voltage to prevent saturation phenomenon. The second test is conducted at a higher voltage that induces magnetic circuit saturation. The results are presented in per unit form with respect to the reduced power and voltage bases.

Experiments Avoiding Magnetic Circuit Saturation

While avoiding the magnetic saturation, several operating points from the peripheral limit curve of the theoretical non saturated domain were reached by varying the inductive and resistive loads as depicted in Figure 2.14a. The corresponding $|\underline{i}^*_{s1}|$ measurements are collected in Figure 2.14b. As foreseen, the nominal current is induced in the stator of the Control machine M1, with a relative error of 5-7%. This confirms that the reactive power capabilities of the CDFIG are limited by the Control machine stator current ratings. Whereas the remaining current and voltage quantities persist under their rated value pursuant to (2.7), (2.12), (2.22), (2.33), and (2.45); which proves the validity of the analytic method elaborated in this manuscript. The experimental measurements at steady state, for the particular point A (refer to Figure 2.14a) are shown in Figure 2.15. The minor differences between the expected values and those obtained experimentally arise from iron losses in the machine that were neglected in the computation of the power curve expressions in addition to inevitable measurement errors. It is noted that the Power machine is operating at a stator frequency $\omega_{s2} = 100\pi$ rad/s. It induces a rotor frequency $\omega_{r2} = -\omega_{r1} = 45\pi$ rad/s and a Control machine stator frequency $\omega_{s1} = 10\pi$ rad/s. These values satisfy the frequency relations (1.27, 1.31, 1.34 and 1.43) established in Chapter 1 for the inverse

coupling interconnection.

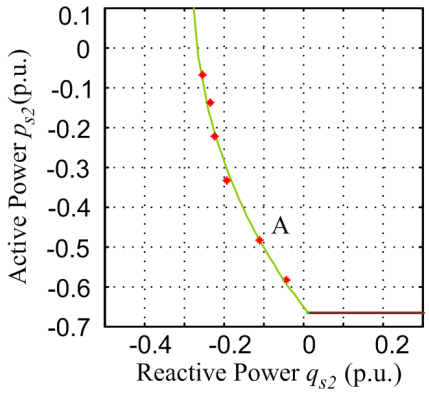

(a) Operating points from the theoretical non saturated peripheral limit curve

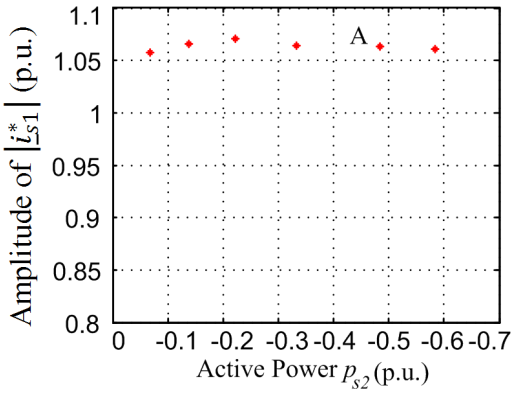

(b) Variation of M1 stator current when describing the power limit curve

Figure 2.14: Experimental test 1 (avoiding saturation)

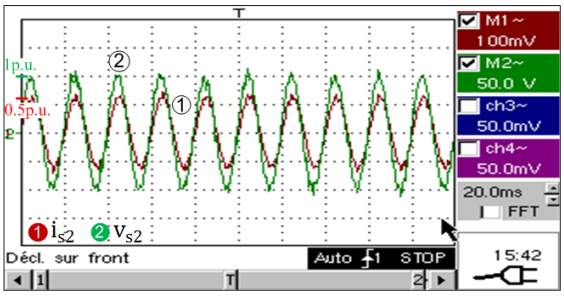

(a) Load current and voltage $-i_{s2}$,v_{s2}

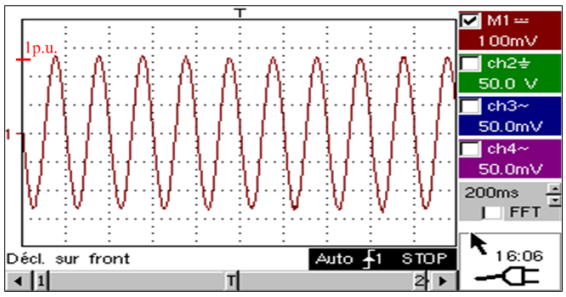

(b) M1 current i_{s1}

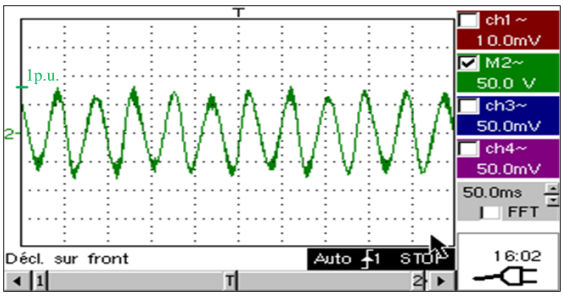

(c) Rotor line-to-line voltage u_r

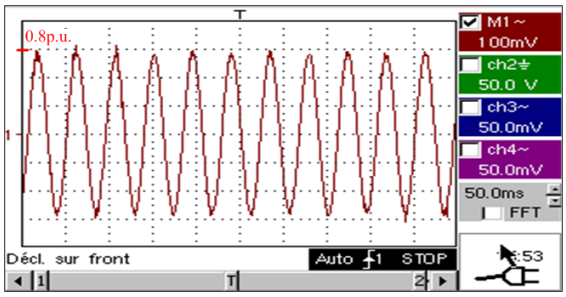

(d) Rotor current i_r

Figure 2.15: Experimental results avoiding saturation (point A)

Experiments Considering Magnetic Circuit Saturation

While testing at higher voltage, the saturation occurs. The response of the CDFIG at steady state is analyzed under different loads lying within the theoretical non saturated operating limits (solid line) as presented in Figure 2.16a. In this case, the

nominal control current is theoretically expected. However, it can be noted in Figure 2.16b that due to saturation phenomenon, a greater current is required to compensate the output voltage magnitude.

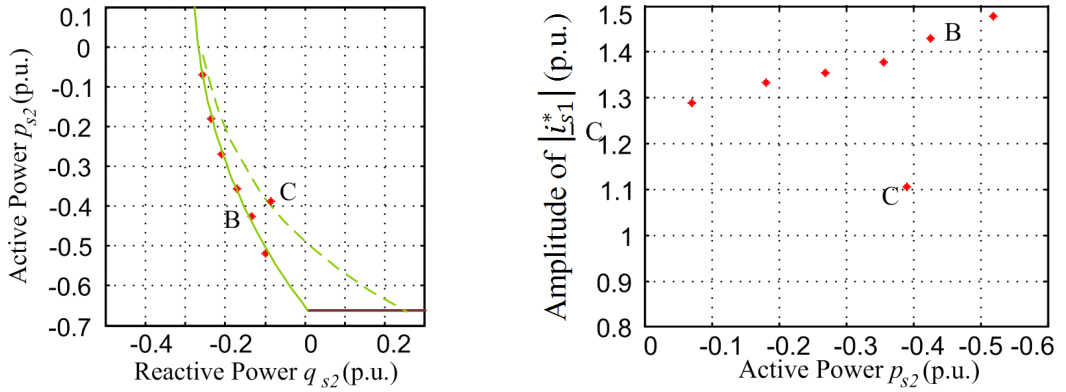

(a) Operating points from the theoretical non saturated and the saturated peripheral limit curves

(b) Variation of M1 stator current when describing the power limit curves

Figure 2.16: Experimental test 2 (considering saturation)

As a result, the capability of the CDFIG to supply capacitive reactive power is reduced when core saturation is considered because of significant effect on the control current. The experimental results at steady state, for the particular point B (refer to Figure 2.16a) are shown in Figure 2.17.

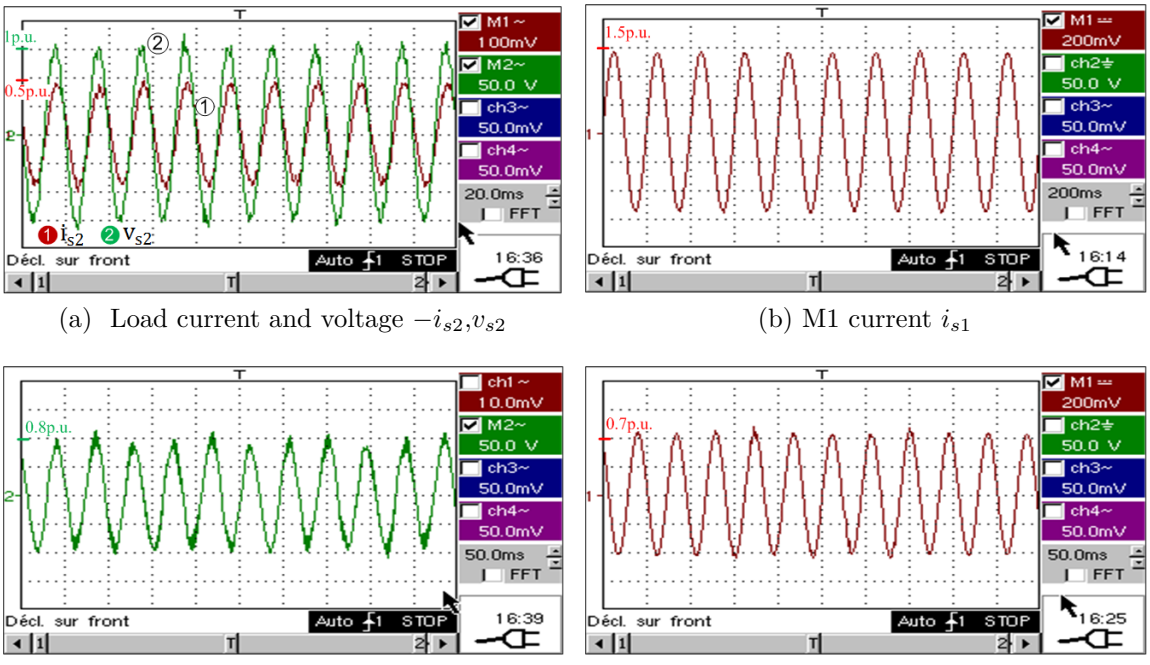

(a) Load current and voltage $-i_{s2}$,v_{s2}

(b) M1 current i_{s1}

(c) Rotor line-to-line voltage u_r

(d) Rotor current i_r

Figure 2.17: Experimental results considering saturation (point B)

As can be seen, the control current exceeds significantly its nominal value, whilst the remaining quantities are kept below their ratings. In order to study the impact of the saturation, an additional test is performed at a point C that corresponds to the theoretical saturated limit curve (dashed line in Figure 2.16a). The steady state variation of the control current is shown in Figure 2.18. The current induced in the Control machine stator windings is equal to 1.1 p.u. This value is close to the nominal current, which proves that indeed the point C defines a new limit bound.

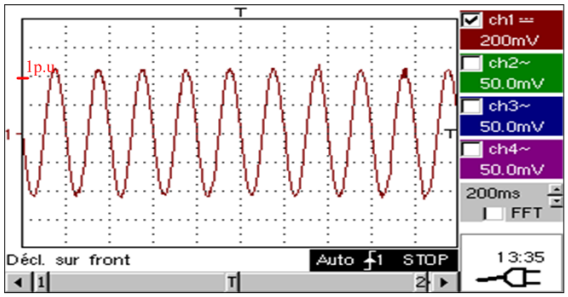

Figure 2.18: Experimental measurement of i_{s1} at point C

Conclusion

The chapter investigates the steady state power operating domain of a CDFIM that is of great interest when it comes to sizing a machine in a practical application. A rigorous generic analytic method is proposed to derive the limit area in which the machine can operate safely without exceeding its rated quantities. It is shown that the power boundaries depend on the combination and design of both induction machines. An important result of this study is that the inductive reactive power consumption limit is determined by the Power machine stator current $|\underline{i}_{s2n}|$, whereas the capacitive reactive power production is limited by the Control machine stator current $|\underline{i}_{s1n}|$ and is reduced compared to the DFIM set alone. The power operating margin is subject to further limitations resulting from terminal voltage drops and speed variations. The effect of magnetic circuit saturation is further discussed. The reactive power generation domain is reduced due to the saturation phenomenon. Experiments performed on a laboratory scale CDFIG validate the presented approach with and without saturation.

The results presented in this work give way to a new prospect. The simplified limit curve expressions suggest that a possible revision of the design of the machine might yield to better performances in terms of power capability.

The power limit range of the CDFIM should be taken into consideration in the next chapters, in order to ensure the machine being operated within its ratings.

Part II

Grid Connected Cascaded Doubly Fed Induction Generator in High Power Wind Energy Conversion Systems

Chapter 3

WECS Modeling

Introduction

The growth of the wind energy sector is significant in view of increasing pollution and lack of fossil fuels. In the early development of the wind technology, the majority of the WTs have been operated at constant speed. With recent advances in power electronics and electrical generators control, variable speed WTs equipped with pitch angle control have become the dominating unit. The variable speed operation improves the efficiency and the reliability of the system by increasing the output power production and reducing the mechanical stresses, the acoustic noise and the torque pulsations [32] [84].

The DFIGs are among the predominant units for high power WECS, since they are able to supply constant frequency electric power at variable speed operation. Independent regulation of active and reactive powers is accomplished by means of converters sized for a fraction of the nominal power (30-35%) depending on the slip (operating speed) range and the reactive power requirements [36], [60], [148]. Nevertheless, the main drawback of this classical structure is the presence of brushes and slip rings which increase significantly the maintenance cost and reduce the life time of the machine [122], [131]. The CDFIG arises as an alternative solution to the DFIG by virtue of its similar behavior, and brushless structure.

This chapter is devoted to the modeling of a grid-connected WECS based on a CDFIG. It offers an overall description of the system. The mechanical part is modeled in a first place (section 3.2). It includes the model of the wind turbine, the gearbox and the generator shaft. The model of a non stationary wind speed based on spectral analysis follows in section 3.3. Concerning the electrical part, the model of the grid-connected CDFIG designed in Chapter 1 is retained. The mathematical model of the power frequency converter is elaborated in section 3.4.

3.1 Configuration of a WECS based on a CDFIG

The configuration of a WECS based on a CDFIG is illustrated in Figure 3.1. The generator is driven by a variable speed wind turbine. The stator of the Power machine (M2) is directly connected to the main supply, whereas the stator windings of the Control machine (M1) are supplied at variable frequency via a reduced size power converter. In order to operate at variable speed in both subsynchronous and supersynchrounous mode, a bidirectional power converter is required to allow the slip power transfer P_{s1} in both directions. This is achieved using a back-to-back converter based on IGBT transistors with PWM control [27], [100]. During supersynchronous generator mode, the slip power is supplied to the grid. The Machine Side Converter (MSC) is operating as a rectifier and the Grid Side Converter (GSC) as an inverter. In subsynchronous generator mode the slip power is fetched from the network to the Control machine. In this case the GSC operates as a rectifier and the MSC as an inverter.

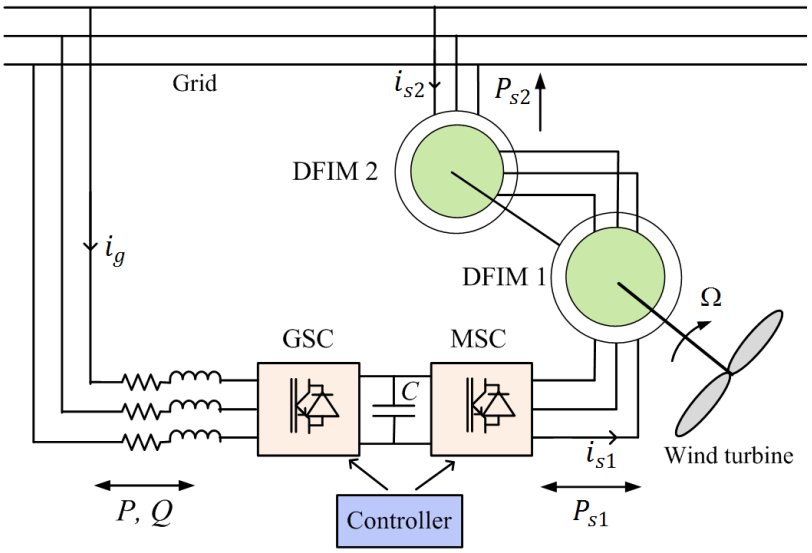

Figure 3.1: Configuration of a WECS based on a CDFIG

A modular representation of the grid-connected wind generating system is investigated. Normal grid conditions are considered. Figure 3.2 represents the different components of the WECS. Each unit is modeled as an object and connected to the others by means of input signals and output variables as shown in the figure. The model and block diagram of the current source grid-connected CDFIG is elaborated in section 1.3.2. It is based on the mathematical model of two single DFIMs connected in inverse rotor coupling sequence. The remaining components are detailed hereinafter. The system model is implemented on Matlab/Simulink software to test and validate new control schemes. The parameters of a 300 kW WECS are given in Appendix B.

The CDFIG is based on two identical 300 kW DFIMs.

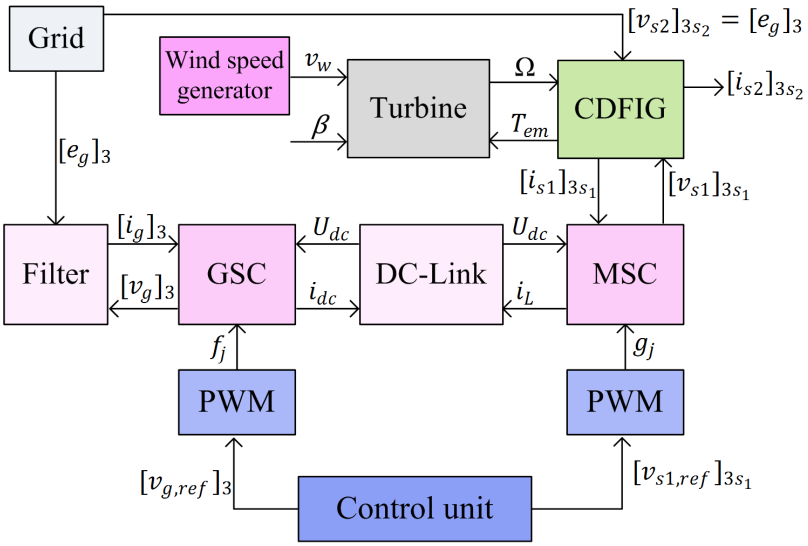

Figure 3.2: Global diagram of the WECS PWM control

3.2 WT model

The wind turbine generating system represented in Figure 3.3 consists of a horizontal axis wind turbine with three blades, coupled to the generator through a gearbox. The latter converts low speeds of the turbine to the higher speeds of the generator.

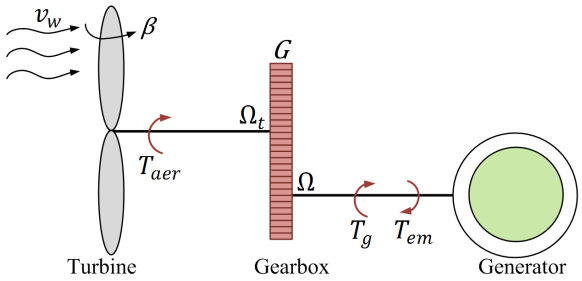

Figure 3.3: Representation of a WECS

According to Betz' law, WTs can extract only a fraction of the power from the wind which is limited by the power coefficient of the turbine C_p. Therefore the aerodynamic power captured by a WT can be expressed as follows [124], [134]:

$$P_{aer} = \frac{1}{2} C_p \rho \pi R_p^2 v_w^3 \tag{3.1}$$

ρ being the air density, R_p the radius of the turbine blade and v_w the wind velocity. Hence an aerodynamic torque described by (3.2) is generated at the wind turbine

shaft to drive the CDFIG; where Ω_t is the mechanical speed of the wind turbine.

$$T_{aer} = \frac{P_{aer}}{\Omega_t} = \frac{1}{2} C_p \rho \pi R_p^2 v_w^3 \frac{1}{\Omega_t} \tag{3.2}$$

The power coefficient $C_p(\lambda, \beta)$ characterizes each wind turbine [2]. It is defined as a function of the pitch angle β and the tip speed ratio λ which, in turn, is given by:

$$\lambda = \frac{R_p \Omega_t}{v_w} \tag{3.3}$$

The parameters of a 300 kW wind generating system are presented in Appendix B, Section B.2. The power coefficient expression is given by (3.4) [4].

$$C_p(\lambda, \beta) = 0.5109 \left(\frac{116}{\lambda_i} - 0.4\beta - 5 \right) e^{\frac{-21}{\lambda_i}} + 0.0068\lambda \tag{3.4}$$

$$\frac{1}{\lambda_i} = \frac{1}{\lambda + 0.08\beta} - \frac{0.035}{\beta^3 + 1} \tag{3.5}$$

The variation of the power coefficient as a function of tip speed ratio is illustrated in figure 3.4 for different values of the pitch angle.

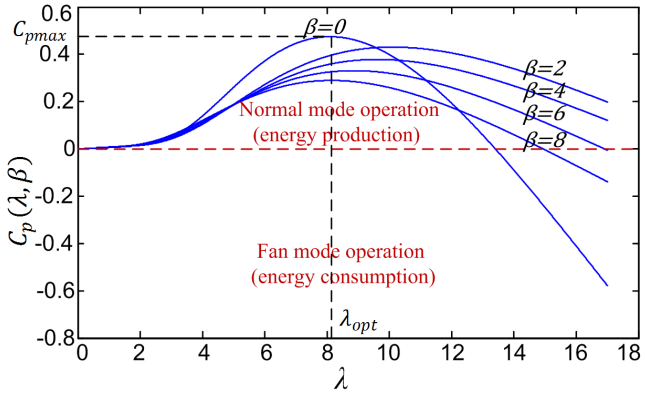

Figure 3.4: Power coefficient versus tip speed ratio characteristics for different values of β

It can be noticed that for each value of β, there is a value of λ for which the power coefficient is maximum. The optimal operating point, for the particular WT used in this study, occurs when $\beta = \beta_{opt} = 0°$ and $\lambda = \lambda_{opt} = 8.1$. It induces the absolute maximum power coefficient $C_{pmax} = 0.475$ that allows the maximization of the power captured by the WT. Consequently, according to (3.3), there is a particular mechanical speed to be followed for a specified wind velocity in order to achieve this optimal behavior. This operation is known as the Maximum Power Point Tracking (MPPT) and will be investigated in Chapter 5. Two methods will be presented for tracking the optimal operation of a wind turbine based on a CDFIG and maximizing the

generated power: the conventional "instantaneous MPPT" algorithm and a novel "mean MPPT strategy". In the first classical approach, the system is carried to extract instantaneously the maximum available power for every wind speed. Whereas the mean MPPT strategy intends to generate the maximum constant power related to the average of the wind speed.

The gearbox is mathematically model by (3.6) and (3.7), G being the gearbox ratio and T_g the aerodynamic couple referred to the generator side.

$$\Omega_t = \frac{\Omega}{G} \tag{3.6}$$

$$T_g = \frac{T_{aer}}{G} \tag{3.7}$$

A simplified representation of the generating unit is to consider the system as a model with two lumped masses: the WT and the generator, having respectively the moment of inertia J_t and J_g [134]. Accordingly, the dynamic equation at the generator shaft is modeled by [1]:

$$J\frac{d\Omega}{dt} = T_g + T_{em} - f_v\Omega \tag{3.8}$$

Here J is the combined moment of inertia of the turbine and the generator, f_v is the viscous friction coefficient and T_{em} and Ω represent the electromechanical torque and the rotational speed of the generator, respectively.

$$J = \frac{J_t}{G^2} + J_g \tag{3.9}$$

Reference to the above equations, the block diagram of the mechanical part is built in Figure 3.5.

3.3 Wind speed model

An accurate representative wind speed model is fundamental for the elaboration of new control methods and the assessment of the overall system behavior. Since WTs are maintained normal to wind direction for maximum power extraction, an horizontal wind speed model is adequate and can be established based on Van der Hoven and Von Karman power spectrum.

1. With respect to the supersynchronous motor convention adopted to the CDFIM model, $T_{em} < 0$ in generator operating mode.

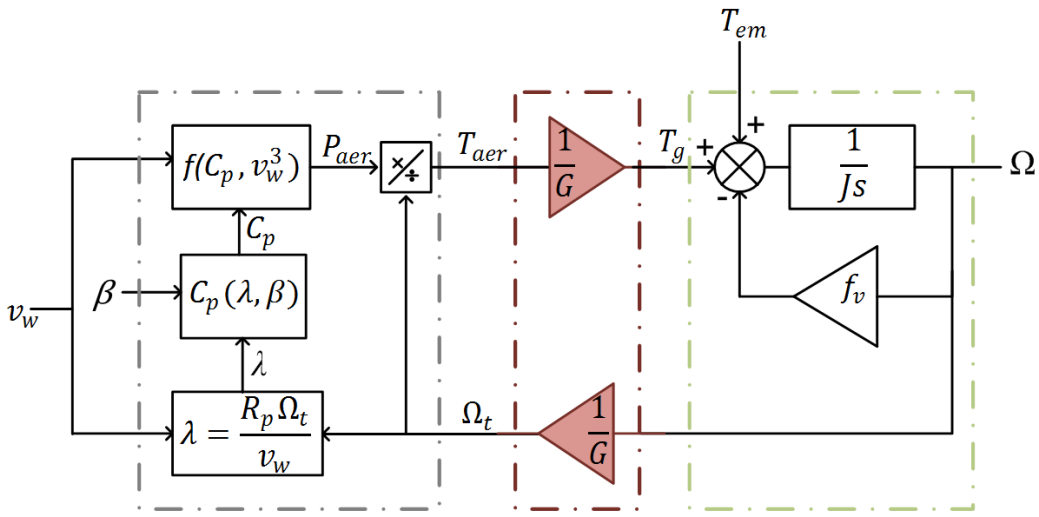

Figure 3.5: Bloc diagram of the WT

The wind speed $v_w(t)$ is analytically expressed by the superposition of two components, a slow varying component $v_m(t)$ and a turbulence component $v_t(t)$:

$$v_w(t) = v_m(t) + v_t(t) \tag{3.10}$$

The low frequencies component $v_m(t)$, for medium and long term variations is most commonly described by the Weibull distribution having the following probability density function (*pdf*) [56]:

$$f(v_m) = \frac{k}{c}\left(\frac{v_m}{c}\right)^{k-1} \mathrm{e}^{-\left(\frac{v_m}{c}\right)^k} \tag{3.11}$$

where k is a shape parameter and c is a scale parameter. The *pdf* is essential to determine the expected generated power and the economic viability of the project. The high frequencies component $v_t(t)$, for short term variations can be described by a normal distribution with zero mean value and a standard deviation related to the slow component variation.

These two components can be clearly identified in Van der Hoven's power spectrum depicted in Figure 3.6 [135]. It represents a large frequency band power spectral analysis of horizontal wind speed made over more than six decades, calculated in the range 0.00047 to 900 cycles/h. The power spectrum shows two eddy energy peaks that occur respectively at a low and a high frequency which are separated by an energy gap. Regardless some differences in details, the spectrum retains the same pattern under varying sites and synoptic conditions [135]. It is noted that the partition of the wind speed into two different components (equation (3.10)) is valid due to the presence of the spectral gap between both the short term and the medium and long

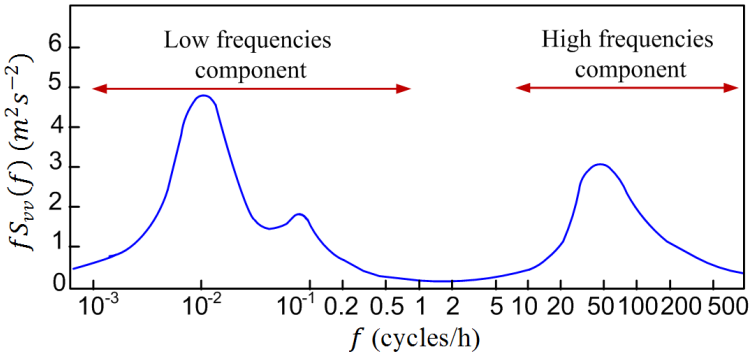

Figure 3.6: Van der Hoven's spectrum for horizontal wind speed

term components. The turbulence component contains the frequencies above the spectral gap with a time range of seconds to minutes and the slow varying component includes all frequencies below the spectral gap with a time scale of hours, days, etc. Accordingly, it can be stated that the average of the instantaneous wind speed over a period T_a lying within the spectral gap (10 to 20 min) is virtually equal to the medium and long term component [19]:

$$v_{mean} = \frac{1}{T_a} \int_{to-\frac{T_a}{2}}^{to+\frac{T_a}{2}} v_w(t)\mathrm{d}t \simeq v_m(to) \tag{3.12}$$

Therefore, it can be deduced that the high frequencies wind speed fluctuations induced by the turbulence term do not intervene in the average produced energy, which is determined by only the medium and long term variation. However, it has a major impact on the power quality generated by the wind turbine which may disturb the network stability. On that basis, the generation of a constant output power, irrespective of wind speed fluctuations, would sustain the power system stability.

A wind speed generator is implemented in this work using Van der Hoven and Von Karman power spectrum [19], [85] where the low frequencies component is treated as a stationary process and the turbulence component as a non stationary process. The slow varying component is modelled according to Van der Hoven's power spectrum associated to a specific site. A mathematical representation described by (3.13), (3.14) is generated by sampling the low frequency domain of the spectrum.

$$v_m(t) = \sum_{i=0}^{N} A_i \cos\left(w_i t + \phi_i\right) \tag{3.13}$$

where w_i, $i \in \{1, .., N\}$, is the discrete angular frequency, $S_{vv}(w_i)$ is the corresponding power spectral density, ϕ_i is a random value in the range $[-\pi, \pi]$ generated with a uniform distribution, and A_i the amplitude of the harmonic at frequency w_i computed

as in (3.14)

$$A_i = \frac{2}{\pi}\sqrt{\frac{1}{2}\left[S_{vv}(w_i) + S_{vv}(w_{i+1})\right]\left[w_{i+1} - w_i\right]} \tag{3.14}$$

The initial value A_0 represents the long time scale wind speed average $\bar{v}_w$ calculated at a period greater than the largest period in the Van der Hoven's model.

The Van der Hoven's spectrum cannot be employed for the implementation of the turbulence component, which is regarded as a non stationary process. Its characteristics should depend on the medium and long term wind speed variations. Accordingly, a non stationary turbulence model can be stochastically described based on Von Karman power spectrum with adjustable parameters:

$$S_{vv}(w) = \frac{0.475\sigma^2 \dfrac{L}{v_m}}{\left(1 + (w\dfrac{L}{v_m})^2\right)^{\frac{5}{6}}} \tag{3.15}$$

where σ is the turbulence intensity and L the turbulence length. As it can be noticed, the model depends on the terrain properties and on the low frequencies wind speed evolution. The short term component is simulated using a shaping filter (3.16) with adjustable parameters and a white noise input [85].

$$H_v(s) = \frac{K_v}{(1 + T_v s)^{\frac{5}{6}}} \tag{3.16}$$

The static gain K_v is calculated in a way to have a normalized standard deviation of the colored noise $n_c(t)$, at the output of the filter. The turbulence expression is thus obtained by multiplying the colored noise $n_c(t)$ by the expected standard deviation $\hat{\sigma_v}$ of the wind speed:

$$v_t(t) = \hat{\sigma_v} n_c(t) \tag{3.17}$$

In order to reduce the computing time, the 5/6 order filter is approximated by a rational filter. One solution is to adopt the following transfer function [85]:

$$\hat{H}_v(s) = K_v \frac{(1 + m_a T_v s)}{(1 + T_v s)\,(1 + m_b T_v s)} \tag{3.18}$$

with $m_a = 0.4$ and $m_b = 0.25$. The parameters K_v and T_v of the filter are generated and adjusted periodically according to the low frequency speed variation. The simulation of the short term component is obtained based on the following procedure. Two sampling periods are adopted: T_{p1}, in minutes ranges to sample the slow varying component $v_m(t)$ and T_p, in seconds ranges to sample the turbulence component (white noise).

1. Generate the discrete value $v_{m,i}$ using the sampling period T_{p1}.
2. For each step i of this procedure, update the parameters of the rational filter according to the following expressions:

$$T_v^i = \frac{L}{v_{m,i}} \tag{3.19}$$

$$\hat{\sigma}_v^i = k_{\sigma,v} v_{m,i} \tag{3.20}$$

$$K_v^i = \sqrt{\frac{\pi}{T_p S^i \delta w}} \tag{3.21}$$

K_v^i is determined through the condition of a normalized standard deviation as mentioned above with:

$$S^i = \sum_{j=0}^{J} \frac{1 + (m_a T_v^i j \delta w)^2}{\left[1 + (T_v^i j \delta w)^2\right]\left[1 + (m_b T_v^i j \delta w)^2\right]} \tag{3.22}$$

$$J = \frac{\pi}{T_p \delta w} \tag{3.23}$$

δw is the sampling step of the angular frequency and $k_{\sigma,v}$ the slope of the regression curve.

3. Generate the colored noise $n_c^i(t)$ using the discrete form of the filter $\hat{H}(z)$ with the sampling period T_p
4. Calculate the wind speed as follows:

$$v_w(t) = v_{m,i}(t) + \hat{\sigma}_v^i n_c^i(t) \tag{3.24}$$

Figure 3.7 illustrates a non stationary wind speed profile simulated over a time duration of 45 min with $L = 180$ m, $k_{\sigma,v} = 0.16, T_p = 1$ s, $T_{p1} = 60$ s and $\delta w = 0.002$ rad/s.

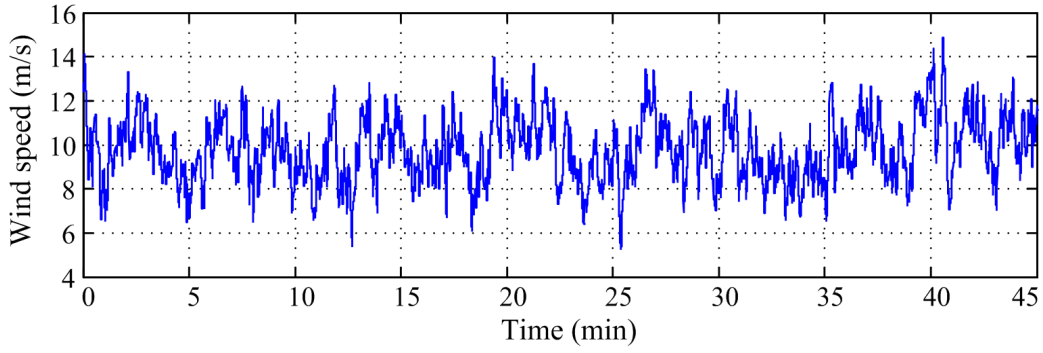

Figure 3.7: A non stationary wind speed profile

3.4 Back-to-back converter model

The back-to-back converter comprises two voltage source PWM converters connected in cascade through a DC bus as represented in Figure 3.8. Each converter includes three legs consisting of six IGBTs and six anti-parallel diodes. The DC capacitor linking the MSC and the GSC stabilizes the DC-link voltage. In order to achieve full control of the grid current, the DC-link voltage is boosted to a level higher than the amplitude grid line-to-line voltage [12]. A grid filter is placed between the GSC and the grid. The inductor transforms the input circuit into a current source, reduces high frequency components of line current and provides boost feature to the GSC [69].

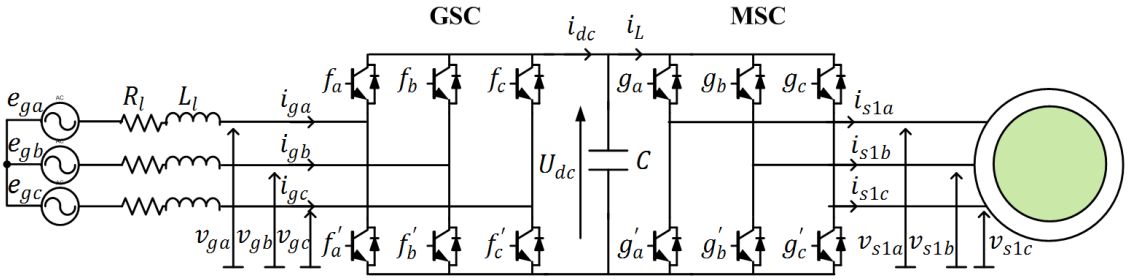

Figure 3.8: Structure of a back-to-back converter

Among the main advantages of the back-to-back PWM converter are [70], [100], [136]:

- Low harmonic distortion of the line current.
- Bidirectional power flow, thus operation of the CDFIG in subsynchronous and supersynchronous modes.
- Quasi sinusoidal input current.
- Adjustment and stabilization of the DC bus voltage.
- Regulation of the reactive power flow and the input power factor.

3.4.1 Converter model

As illustrated in Figure 3.2, the converter model receives as inputs the DC voltage, along with the three-phase line currents. It calculates the DC current and the three-phase modulated voltages (the converter terminal voltages) given the three-phase reference voltages generated by the control unit.

The converter modeling is elaborated under the assumptions of ideal switching, continuous conduction mode and no losses. A generic model of a two level static converter is represented in Figure 3.9. where:

- U_{dc} is the constant DC bus voltage.
- i_t is the modulated DC current.

– i_{1a}, i_{1b}, i_{1c} are the three-phase line currents.
– v_{1a}, v_{1b}, v_{1c} are the modulated three-phase voltages .
– S_i, S_i' are the bidirectional ideal switches.

It is noted that the convention of an inverter are considered in the figure, then the model will be adapted to the GSC and MSC pursuant to the notation in Figure 3.8.

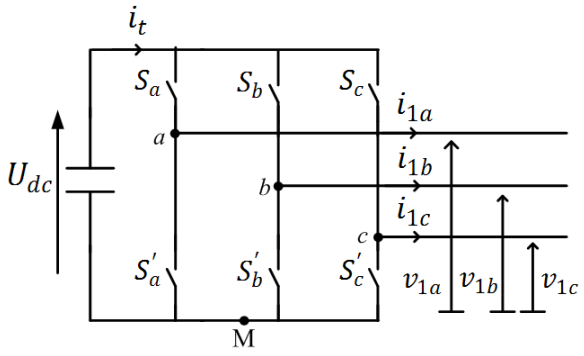

Figure 3.9: Generic model of a static converter

In order to describe the full operation of the PWM converter, two relationships shall be established: the first one gives the three-phase voltages in terms of the DC voltage; the second one computes the DC current given the three-phase currents. Switching functions associated with the converter legs are introduced to describe the converter switching states. k_j is the switching function associated with the leg j ($j = a, b, c$). These functions are generated by comparing the reference voltage from the output of the controller to the sawtooth carrier.

$$k_j = \begin{cases} 1 & \text{if } v_{1j,ref}(t) > v_{carrier}(t), \\ & \text{thus } S_j \text{ is ON and } S_j' \text{ is OFF.} \\ 0 & \text{if } v_{1j,ref}(t) < v_{carrier}(t), \\ & \text{thus } S_j \text{ is OFF and } S_j' \text{ is ON.} \end{cases} \tag{3.25}$$

Accordingly, the following voltage expression is computed.

$$v_{jM} = k_j U_{dc} \tag{3.26}$$

On the other side, relation (3.27) is always verified.

$$\begin{bmatrix} v_{aM} - v_{bM} \\ v_{bM} - v_{cM} \\ v_{cM} - v_{aM} \end{bmatrix} = \begin{bmatrix} v_{1a} - v_{1b} \\ v_{1b} - v_{1c} \\ v_{1c} - v_{1a} \end{bmatrix} \tag{3.27}$$

The unity of the solution is obtained by considering the zero-sequence component of

the three-phase voltages nil, leading to:

$$\begin{bmatrix} v_{1a} \\ v_{1b} \\ v_{1c} \end{bmatrix} = \frac{U_{dc}}{3} \begin{bmatrix} 2 & -1 & -1 \\ -1 & 2 & -1 \\ -1 & -1 & 2 \end{bmatrix} \begin{bmatrix} k_a \\ k_b \\ k_c \end{bmatrix} \tag{3.28}$$

The current in each converter leg is computed by (3.29). Then Kirchhoff law yields to (3.30).

$$i_{S_j}(t) = k_j i_{1j}(t) \tag{3.29}$$

$$i_t = k_a i_{1a} + k_b i_{1b} + k_c i_{1c} \tag{3.30}$$

The voltage source PWM converter is modeled by (3.28), (3.30) in the three-phase coordinate.

3.4.2 DC-link model

The DC bus model receives as inputs the DC currents of the MSC and the GSC and calculates the DC voltage as follows. The Kirchhoff current law yields to (3.31).

$$C\frac{d}{dt}U_{dc} = i_{dc} - i_L \tag{3.31}$$

3.4.3 Filter model

Applying the mesh analysis (Figure 3.8), the three-phase voltage balance across the inductors is:

$$\begin{bmatrix} e_{ga} \\ e_{gb} \\ e_{gc} \end{bmatrix} = \begin{bmatrix} v_{ga} \\ v_{gb} \\ v_{gc} \end{bmatrix} + R_l \begin{bmatrix} i_{ga} \\ i_{gb} \\ i_{gc} \end{bmatrix} + L_l \frac{d}{dt} \begin{bmatrix} i_{ga} \\ i_{gb} \\ i_{gc} \end{bmatrix} \tag{3.32}$$

In a Park coordinate rotating at the grid frequency ω_g, (3.32) becomes:

$$E_{gd} = V_{gd} + R_l I_{gd} + L_l \frac{d}{dt} I_{gd} - L_l \omega_g I_{gq} \tag{3.33}$$

$$E_{gq} = V_{gq} + R_l I_{gq} + L_l \frac{d}{dt} I_{gq} + L_l \omega_g I_{gd} \tag{3.34}$$

Besides, the instantaneous input active and reactive powers are given by (3.35), (3.36).

$$P = \frac{3}{2}(E_{gd} I_{gd} + E_{gq} I_{gq}) \tag{3.35}$$

$$Q = \frac{3}{2}(E_{gq} I_{gd} - E_{gd} I_{gq}) \tag{3.36}$$

Conclusion

In this chapter, the mathematical model of a grid-connected wind energy generating system based on a CDFIG is presented. A simplified model of the wind turbine based on two lumped masses is implemented. The power frequency converter feeding the generator is based on a back-to-back PWM converter. It allows bidirectional power flow between the generator and the grid. The evolution of a horizontal wind speed is synthesized taking into consideration two components. The slow varying component is computed based on Van der Hoven power spectrum associated to a specific site. The turbulence component is considered as a non stationary process. It is implemented using Von Karman model and assumed to be dependent on the medium and long term wind speed evolution.

The control scheme of an integrated wind power plant will be investigated in the next chapters. It requires the regulation of the MSC together with the GSC.

Chapter 4

Vector Control of the WECS

Introduction

This chapter deals with the vector control of a grid-connected WECS based on a CDFIG. The integration of new generating plants into the network requires the regulation of the two back-to-back converters: the MSC and the GSC. A voltage sensorless approach based on virtual flux orientations is elaborated for the independent control of the active and reactive power flow. The GSC is manipulated in order to keep a constant DC-link voltage level and adjust the amount of reactive power exchanged with the grid. The MSC is controlled to achieve decoupled regulation of the machine output stator active and reactive powers.

In grid-connected operation, the system intends to extract the maximum power and achieve optimal behavior of the wind turbine. However, due to the considerable progress of wind power generation systems, new grid code requisites are introduced. In addition to power optimization, the system must provide additional reactive current to support network stability through voltage regulation. On that basis, the reactive power capability of the integrated unit and the contribution of the GSC to reactive power production are to be investigated.

The chapter is organized as follows. The control strategy of the global system is addressed in section 4.1. The virtual flux orientation approach is introduced in section 4.2. The vector control of the GSC is investigated in section 4.3. Section 4.4 is devoted to the control of the MSC. Despite the complexity of the CDFIG representation, an efficient controller is implemented based on the vector model of the generator in a unified rotating frame. The steady state power operating margin of the generating plant and its contribution to reactive power supply during grid faults and normal conditions is detailed in section 4.5.

4.1 Control strategy of the back-to-back converter

The integration of wind energy conversion plants into the grid involves the control of both the MSC and the GSC. The objective of the CDFIG controller is to achieve maximum power extraction of the wind turbine. A decoupled vector control of the MSC enables independent regulation of the CDFIG output active and reactive powers. The active power is adjusted in order to track the optimal operating point of the WT and maximize the power generated by the integrated unit. The reactive power is controlled to support the network stability through power factor regulation. As for the GSC the main function is to retain a constant DC-link voltage level regardless of the direction of power flow between the Control machine and the grid. It can also contribute to the reactive power supply.

Hereinafter, a decoupled vector control strategy, based on virtual flux orientation is proposed for the regulation of both converters. The grid voltage sensors are replaced by a VF estimator, so the orientation frame angles are no longer computed from grid voltage measurement. Among the main advantages of the VF orientation are: lower harmonic distortion, sinusoidal current even under unbalanced and distorted grid conditions, more stable orientation devoid of measurement noise, voltage sensorless operation that improves reliability and reduces installation cost [70], [71]. The overall control structure of the generating system is described in Figure 4.1 and will be detailed in the following sections.

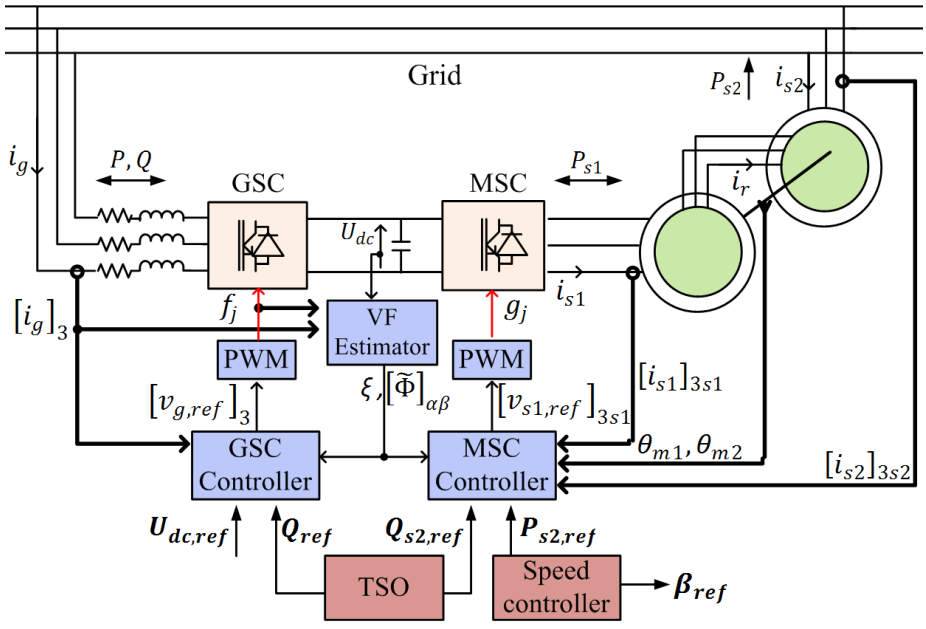

Figure 4.1: Voltage sensorless control of WECS based on CDFIG

The output active power set point ($P_{s2,ref}$) is derived by the WT speed controller in order to achieve optimal operation of the WT according to the adopted MPPT

method. The reactive power set points ($Q_{s2,ref}, Q_{ref}$) are provided by the Transmission System Operators (TSO) according to the grid code requirements and the power capabilities of the generating plant i.e the CDFIG and the GSC (as will be investigated in section 4.5).

4.2 Virtual Flux estimator

The virtual-flux-based approach was introduced by [72] for the control of a three-phase PWM boost rectifier. It assumes that the grid line voltages, in combination with the AC side inductors are quantities related to a virtual AC motor as shown in Figure 4.2; where R_l and L_l represent respectively the stator resistance and leakage inductance of the virtual motor.

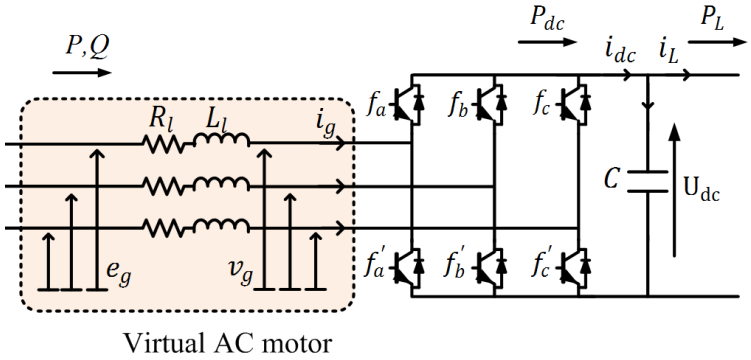

Figure 4.2: GSC circuit diagram with AC side presented as virtual motor

Accordingly, it can be stated that the grid voltage $\underline{e}_g$ would be induced by a virtual air gap line flux $\underline{\Phi}$ which are related by (4.1) using phasor vectors:

$$\underline{\Phi} = \int \underline{e}_g dt \tag{4.1}$$

On the other side, a virtual flux expression can be derived based on the converter input voltage $\underline{v}_g$ and the line current $\underline{i}_g$ as follows:

$$\underline{\Phi} = \underline{\Phi}_m + \underline{\Phi}_L \tag{4.2}$$

$$= \int (\underline{v}_g + L\frac{d}{dt}\underline{i}_g)dt \tag{4.3}$$

$\underline{\Phi}_m$ being the converter virtual flux vector and $\underline{\Phi}_L$ the inductor virtual flux vector. Given the measured DC-link voltage U_{dc} and the converter switching states f_j, the

converter input voltages are estimated as follows using (3.28).

$$\begin{bmatrix} \tilde{v}_{ga} \\ \tilde{v}_{gb} \\ \tilde{v}_{gc} \end{bmatrix} = \frac{U_{dc}}{3} \begin{bmatrix} 2 & -1 & -1 \\ -1 & 2 & -1 \\ -1 & -1 & 2 \end{bmatrix} \begin{bmatrix} f_a \\ f_b \\ f_c \end{bmatrix} \tag{4.4}$$

In the stationary ($\alpha\beta$) coordinate, relation (4.4) becomes:

$$\tilde{V}_{g\alpha} = \frac{2}{3} U_{dc} \left(f_a - \frac{f_b}{2} - \frac{f_c}{2} \right) \tag{4.5}$$

$$\tilde{V}_{g\beta} = \frac{U_{dc}}{\sqrt{3}} \left(f_b - f_c \right) \tag{4.6}$$

Therefore, neglecting the line resistance R_l and referring to (4.3), (4.5) and (4.6) the virtual flux components in ($\alpha\beta$) reference frame are estimated as:

$$\tilde{\Phi}_\alpha = \int \frac{2}{3} U_{dc} \left(f_{12} - \frac{f_{22}}{2} - \frac{f_{32}}{2} \right) dt + L_l I_{g\alpha} \tag{4.7}$$

$$\tilde{\Phi}_\beta = \int \frac{U_{dc}}{\sqrt{3}} \left(f_{22} - f_{23} \right) dt + L_l I_{g\beta} \tag{4.8}$$

Under sinusoidal and balanced grid condition, the line voltages are approximated by:

$$\underline{e_g} = \frac{d}{dt} (|\underline{\Phi}|\, e^{j\omega_g t}) = j\omega_g \underline{\Phi} \tag{4.9}$$

Resulting in the following estimated line voltages in stationary frame. ω_g being the grid frequency.

$$\tilde{E}_{g\alpha} = -\omega_g \tilde{\Phi}_\beta \tag{4.10}$$

$$\tilde{E}_{g\beta} = \omega_g \tilde{\Phi}_\alpha \tag{4.11}$$

It should be noted that the low pass filter behavior of the integrator in (4.7) and (4.8) reduces the noise of the estimated quantities.

4.3 GSC control

The objective of the GSC controller is to keep the DC-link voltage constant regardless of the magnitude and direction of the Control machine power P_{s1}. It can also adjust the amount of reactive power exchanged with the grid. Various control strategies for the GSC have been proposed in the literature [73], [100], [127], [136]. A decoupled vector approach using VF orientation is briefly discussed in the following.

It enables independent control of the active and reactive powers flowing between the supply and the converter. The DC voltage and the reactive power are adjusted through the regulation of the line current d-q components.

Considering the VF oriented reference frame, which is a rotating coordinate system aligned to the virtual flux $\underline{\Phi}$, the dynamic behavior of the GSC can be described as follows:

$$E_{gd} = V_{gd} + RI_{gd} + L\frac{d}{dt}I_{gd} - L\omega_g I_{gq} = 0 \tag{4.12}$$

$$E_{gq} = V_{gq} + RI_{gq} + L\frac{d}{dt}I_{gq} + L\omega_g I_{gd} = \left|\underline{e}_g\right| = \omega_g \left|\underline{\Phi}\right| \tag{4.13}$$

$$P = \frac{3}{2}E_{gq}I_{gq} \tag{4.14}$$

$$Q = \frac{3}{2}E_{gq}I_{gd} \tag{4.15}$$

Neglecting the filter and converter losses, the power flow between AC and DC sides is approximated by:

$$U_{dc}i_{dc} \approx P \tag{4.16}$$

Applying the GSC average model, the DC link voltage expression is derived by (4.17):

$$\frac{d}{dt}U_{dc} = \frac{1}{C}\left(i_{dc} - i_L\right) \tag{4.17}$$

Based on the above relations, the open loop block diagram of the GSC in the VF oriented frame is built in Figure 4.3.

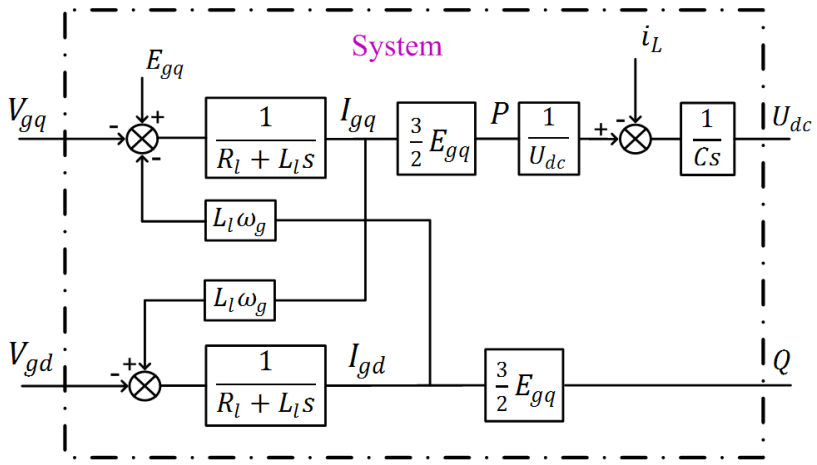

Figure 4.3: Open loop block diagram of the GSC in the VF oriented frame

As noted in the figure, a decoupled vector control can be applied to the converter with two parallel cascaded loops. The reactive power Q is regulated by action on the line current d-component; and the active power P i.e. the DC link voltage U_{dc}

is controlled by adjusting the current q-component. The current set points $I_{gd,ref}$ and $I_{gq,ref}$ are provided respectively by the reactive power and the DC link voltage controllers. The inner loop regulates the line currents. Feed forward terms are added to compensate the cross coupling perturbations associated with line inductance and the grid voltage. The vector control scheme of the GSC using hierarchical loops and Proportional Integral (PI) controllers is illustrated in Figure 4.4.

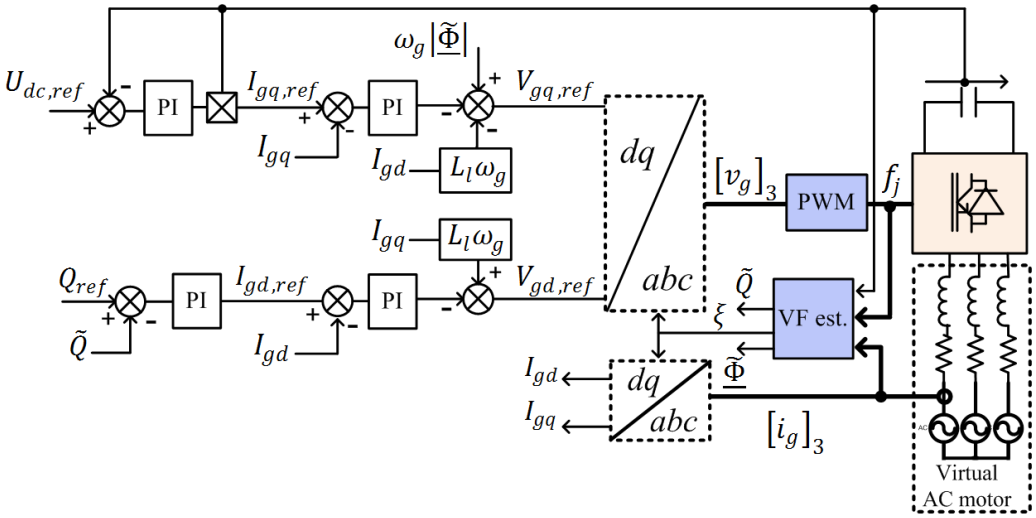

Figure 4.4: VF oriented Vector control scheme of GSC

The Park transformation angle to the VF (dq) frame is defined based on the estimated virtual flux components as:

$$\xi = \arctan\left(\frac{\tilde{\Phi}_\beta}{\tilde{\Phi}_\alpha}\right) \tag{4.18}$$

Furthermore, the instantaneous active an reactive powers are computed using the measured line current and the estimated virtual flux as follows:

$$\tilde{P} = \frac{3}{2}\left(E_{g\alpha}I_{g\alpha} + E_{g\beta}I_{g\beta}\right) = \frac{3}{2}\omega_g\left(\tilde{\Phi}_\alpha I_{g\beta} - \tilde{\Phi}_\beta I_{g\alpha}\right) \tag{4.19}$$

$$\tilde{Q} = \frac{3}{2}\left(E_{g\beta}I_{g\alpha} - E_{g\alpha}I_{g\beta}\right) = \frac{3}{2}\omega_g\left(\tilde{\Phi}_\alpha I_{g\alpha} + \tilde{\Phi}_\beta I_{g\beta}\right) \tag{4.20}$$

The output of the line current controller forms the the AC side voltage references $V_{gd,ref}, V_{gq,ref}$ expressed in the VF reference frame. The three-phase references $[v_{g,rerf}]_3$ for the PWM control are generated by an inverse Park transformation from (dq) to (abc) coordinate.

4.4 MSC control

In the targeted integrated wind turbine application, the controller must provide independent regulation of the output active and reactive powers of the generator. Thanks to the unified frame vector model of the CDFIG, a decoupled vector control can be implemented, equivalent to the well known stator field oriented control of a single grid-connected DFIG [105], [128]. The approach is based on cascaded loops with two regulation paths, devoted to adjust the stator current direct and quadrature axis components distinctly.

Equations (4.21) to (4.28) summarize the dynamic behavior of the CDFIG in the common Power machine synchronous reference frame.

$$\underline{v}_{s2} = R_{s2}\underline{i}_{s2} + \frac{d}{dt}\underline{\Phi}_{s2} + j\omega_{s2}\underline{\Phi}_{s2} = \underline{e}_g \tag{4.21}$$

$$\underline{v}_{s1} = R_{s1}\underline{i}_{s1} + \frac{d}{dt}\underline{\Phi}_{s1} + j\left(\omega_{s2} - \Sigma p\Omega\right)\underline{\Phi}_{s1} \tag{4.22}$$

$$0 = R_r\underline{i}_r + \frac{d}{dt}\underline{\Phi}_r + j\left(\omega_{s2} - p_2\Omega\right)\underline{\Phi}_r \tag{4.23}$$

$$\underline{\Phi}_{s2} = L_{s2}\underline{i}_{s2} + M_{sr2}\underline{i}_r \tag{4.24}$$

$$\underline{\Phi}_{s1} = L_{s1}\underline{i}_{s1} - M_{sr1}\underline{i}_r \tag{4.25}$$

$$\underline{\Phi}_r = L_r\underline{i}_r + M_{sr2}\underline{i}_{s2} - M_{sr1}\underline{i}_{s1} \tag{4.26}$$

$$P_{s2} = \frac{3}{2}\Re\left\{\left(\underline{v}_{s2}\underline{i}^{\star}_{s2}\right)\right\} \tag{4.27}$$

$$Q_{s2} = \frac{3}{2}\Im\left\{\left(\underline{v}_{s2}\underline{i}^{\star}_{s2}\right)\right\} \tag{4.28}$$

The orientation of the d-axis along the M2 stator flux vector $\underline{\Phi}_{s2}$ ensures a complete decoupled regulation between the output active and reactive powers. Neglecting the voltage drop across the stator resistance R_{s2}, the stator flux $\underline{\Phi}_{s2}$ and the grid voltage virtual flux $\underline{\Phi}$ are approximately equal. This way, grid voltage sensorless operation is achieved through VF orientation technique using the transformation frame angle $\xi_{s2} = \xi$.

In utility grid case, the stator flux is imposed by the grid and is considered to be constant under normal conditions. Thus, in the above mentioned coordinate system, where the d axis is aligned to the rotating virtual flux phasor $\underline{\Phi}$, the following relations are established:

$$\Phi_{s2q} \simeq 0, \quad \Phi_{s2d} \simeq \left|\underline{\Phi}_{s2}\right| = \left|\underline{\Phi}\right|, \quad \frac{d}{dt}\Phi_{s2d} = 0 \tag{4.29}$$

$$V_{s2d} = 0, \quad V_{s2q} = \left|\underline{v}_{s2}\right| = \omega_g\left|\underline{\Phi}\right| \tag{4.30}$$

$$P_{s2} = \frac{3}{2}\left(V_{s2q}I_{s2q}\right) \tag{4.31}$$

$$Q_{s2} = \frac{3}{2}\left(V_{s2q}I_{s2d}\right) \tag{4.32}$$

Referring to (4.23), (4.24) and (4.26), the Power machine and the Control machine stator currents are related by (4.33), where $\omega_{r2} = \omega_{s2} - p_2\Omega$ and $\sigma_p = 1 - \dfrac{M_{sr2}^2}{L_{s2}L_r}$.

$$\begin{aligned}&\frac{R_r}{M_{sr2}}\underline{\Phi}_{s2} + \frac{L_r}{M_{sr2}}\frac{d}{dt}\underline{\Phi}_{s2} - \frac{R_r L_{s2}}{M_{sr2}}\underline{i}_{s2} - \frac{L_{s2}L_r\sigma_p}{M_{sr2}}\frac{d}{dt}\underline{i}_{s2} - M_{sr1}\frac{d}{dt}\underline{i}_{s1}\\ &+ j\omega_{r2}\left(\frac{L_r}{M_{sr2}}\underline{\Phi}_{s2} - M_{sr1}\underline{i}_{s1} - \frac{L_{s2}L_r\sigma_p}{M_{sr2}}\underline{i}_{s2}\right) = 0\end{aligned} \tag{4.33}$$

Moreover a relation can be established between the Control machine stator current and voltage $\underline{i}_{s1}$ and $\underline{v}_{s1}$ respectively and the Power machine stator current $\underline{i}_{s2}$. Rearranging (4.22), (4.24) and (4.25) leads to:

$$\begin{aligned}\underline{v}_{s1} = {} & R_{s1}\underline{i}_{s1} + L_{s1}\frac{d}{dt}\underline{i}_{s1} - \frac{M_{sr1}}{M_{sr2}}\frac{d}{dt}\underline{\Phi}_{s2} + \frac{L_{s2}M_{sr1}}{M_{sr2}}\frac{d}{dt}\underline{i}_{s2}\\ &+ jg_c\omega_{s2}\left(L_{s1}\underline{i}_{s1} - \frac{M_{sr1}}{M_{sr2}}\underline{\Phi}_{s2} + \frac{L_{s2}M_{sr1}}{M_{sr2}}\underline{i}_{s2}\right)\end{aligned} \tag{4.34}$$

Introducing the expression of $\dfrac{d}{dt}\underline{i}_{s1}$ from (4.33) in (4.34), results in the following relation:

$$\begin{aligned}\underline{v}_{s1} = {} & -\frac{R_r L_{s1}L_{s2}}{M_{sr1}M_{sr2}}\underline{i}_{s2} - \frac{L_{s2}}{M_{sr2}}\left(\frac{\sigma_p L_r L_{s1}}{M_{sr1}} - M_{sr1}\right)\frac{d}{dt}\underline{i}_{s2} + R_{s1}\underline{i}_{s1} + \frac{L_{s1}R_r}{M_{sr1}M_{sr2}}\underline{\Phi}_{s2}\\ &+ \left(\frac{L_r L_{s1}}{M_{sr1}M_{sr2}} - \frac{M_{sr1}}{M_{sr2}}\right)\frac{d}{dt}\underline{\Phi}_{s2} + j\left(g_c\omega_{s2}\frac{M_{sr1}L_{s2}}{M_{sr2}} - \omega_{r2}\frac{\sigma_p L_r L_{s1}L_{s2}}{M_{sr1}M_{sr2}}\right)\underline{i}_{s2}\\ &+ j\left(g_c\omega_{s2} - \omega_{r2}\right)L_{s1}\underline{i}_{s1} + j\left(\omega_{r2}\frac{L_r L_{s1}}{M_{sr1}M_{sr2}} - g_c\omega_{s2}\frac{M_{sr1}}{M_{sr2}}\right)\underline{\Phi}_{s2}\end{aligned} \tag{4.35}$$

Decomposing into *d-q* components, expression (4.35) becomes as follows in the VF reference frame:

$$\frac{R_r L_{s1}L_{s2}}{M_{sr1}M_{sr2}}I_{s2d} + \frac{L_{s2}}{M_{sr2}}\left(\frac{\sigma_p L_r L_{s1}}{M_{sr1}} - M_{sr1}\right)\frac{d}{dt}I_{s2d} = -V_{s1d} + a_d = U_{s1d} \tag{4.36}$$

$$\frac{R_r L_{s1}L_{s2}}{M_{sr1}M_{sr2}}I_{s2q} + \frac{L_{s2}}{M_{sr2}}\left(\frac{\sigma_p L_r L_{s1}}{M_{sr1}} - M_{sr1}\right)\frac{d}{dt}I_{s2q} = -V_{s1q} + a_q = U_{s1q} \tag{4.37}$$

As observed, $\underline{v}_{s1}$ and $\underline{i}_{s2}$ *d-q* components are linked by a first order linear transfer function:

$$I_{s2d,q}(s) = \frac{K_p}{1+\tau_p s}U_{s1d,q}(s) \tag{4.38}$$

$$K_p = \frac{M_{sr1}M_{sr2}}{R_r L_{s1}L_{s2}}; \qquad \tau_p = \left(\frac{\sigma_p L_r}{R_r} - \frac{M_{sr1}^2}{L_{s1}R_r}\right) = \frac{\sigma_1 L_{r1} + \sigma_2 L_{r2}}{R_r} > 0 \tag{4.39}$$

The terms a_d and a_q, defined in the following, refer to the d-q coupling disturbances

composed of a cross perturbation and a back EMF related to $\underline{\Phi}_{s2}$.

$$a_d = R_{s1} I_{s1d} + \frac{L_{s1} R_r}{M_{sr1} M_{sr2}} \Phi_{s2d} - \left(g_c \omega_{s2} \frac{M_{sr1} L_{s2}}{M_{sr2}} - \omega_{r2} \frac{\sigma_p L_r L_{s1} L_{s2}}{M_{sr1} M_{sr2}} \right) I_{s2q} - \left(g_c \omega_{s2} - \omega_{r2} \right) L_{s1} I_{s1q} \tag{4.40}$$

$$a_q = R_{s1} I_{s1q} + \left(g_c \omega_{s2} \frac{M_{sr1} L_{s2}}{M_{sr2}} - \omega_{r2} \frac{\sigma_p L_r L_{s1} L_{s2}}{M_{sr1} M_{sr2}} \right) I_{s2d} + \left(g_c \omega_{s2} - \omega_{r2} \right) L_{s1} I_{s1d} + \left(\omega_{r2} \frac{L_r L_{s1}}{M_{sr1} M_{sr2}} - g_c \omega_{s2} \frac{M_{sr1}}{M_{sr2}} \right) \Phi_{s2d} \tag{4.41}$$

Referring to (4.31), (4.32), (4.36) and (4.37), the open loop transfer function of the grid-connected CDFIG, defined in the VF (dq_2) reference frame is presented in Figure 4.5.

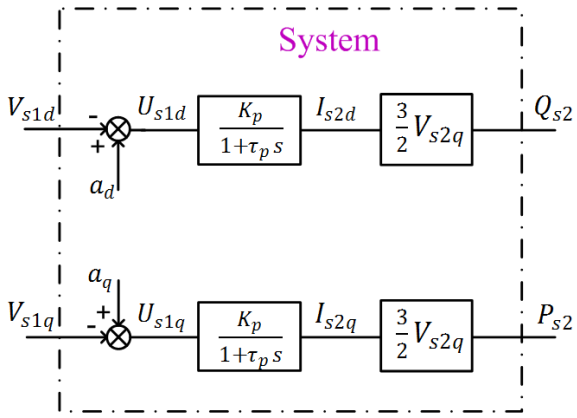

Figure 4.5: Open loop transfer function of a grid-connected CDFIG in VF frame

As can be deduced, a decoupled sensorless vector control of the CDFIG is achieved with the VF orientation. The output active and reactive powers can be independently adjusted through hierarchical loops. P_{s2} and Q_{s2} are controlled through the action on the Power machine stator current I_{s2q} and I_{s2d} respectively. The latter are driven by the Control machine stator voltage V_{s1q} and V_{s1d}.

Accordingly, a vector control consisting of two nested loops is implemented on each axis using PI controllers. Due to the symmetry of the machine model in the defined oriented frame, identical controllers are implemented on each axis. The outer loop controls the active and reactive powers. The output of the power controller generates the stator current set points $I_{s2d,ref}, I_{s2q,ref}$. The inner loop regulates the Power machine stator current and provides the voltage demands $V_{s1d,ref}, V_{s1q,ref}$. Compensation terms $\tilde{a}_d, \tilde{a}_q$, based on (4.40) and (4.41), are added to the output of the controller by feed forward action to overcome the effect of the coupling disturbances. It provides linear transfer functions in order to simplify the controller design and ensure good dynamic response and tracking of the reference values. The terms are computed based on the virtual flux estimation and the stator current measurements

in the (dq_2) frame.

4.4.1 Stator current control loop

The study is carried out on a 300 kW CDFIG. The parameters of the machine are given in Appendix B. The current control loop is depicted in Figure 4.6.

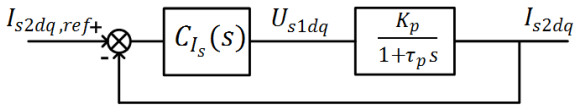

Figure 4.6: Stator current loop block diagram

The plant to be controlled is a first order transfer function $G_{I_s}(s)$ (4.42). Numerically, the cutoff frequency is $\omega_{I_s} = 33$ rad/s.

$$G_{I_s}(s) = \frac{I_{s2d,q}}{U_{s1d,q}} = \frac{K_p}{1+\tau_p s} = \frac{79.86}{1+0.0303s} \tag{4.42}$$

A PI current controller $C_{I_s}(s)$ is designed in order to satisfy the following specifications:

- Zero steady state error
- The settling time of the closed-loop is three times smaller than the open-loop settling time.

The first order inner closed-loop dynamic is represented by (4.43).

$$F_{I_s}(s) = \frac{I_{s2d,q}}{I_{s2dq,ref}} = \frac{1}{1+0.01s} \tag{4.43}$$

4.4.2 Power control loop

The power outer loop is illustrated by the block diagram in Figure 4.7. The stator current dynamic is taken into consideration. The open-loop transfer function is given by (4.44). The settling time is equal to the inner closed-loop settling time.

$$G_P(s) = \frac{Q_{s2}}{I_{s2d,ref}} = \frac{P_{s2}}{I_{s2q,ref}} = F_{I_s}(s)\frac{3}{2}V_{s2q} \tag{4.44}$$

The PI controller $C_P(s)$ is synthesized to meet the following specifications:

- Zero steady state error
- Settling time eight times greater than the currents settling time.

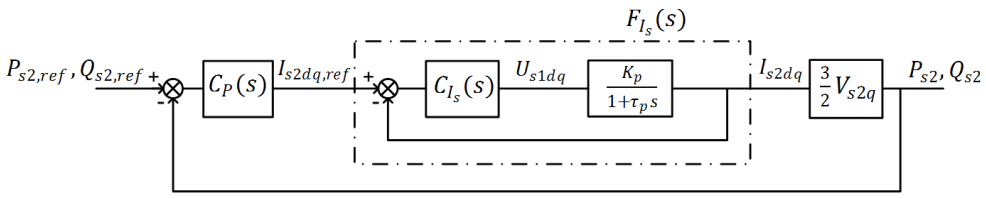

Figure 4.7: Outer power loop block diagram

4.4.3 Control scheme

Based on the stator current measurements ($\underline{i}_{s1}, \underline{i}_{s2}$) and the derived value of the virtual line flux $\underline{\tilde{\Phi}}$, the MSC control scheme using voltage sensorless approach is described in Figure 4.8.

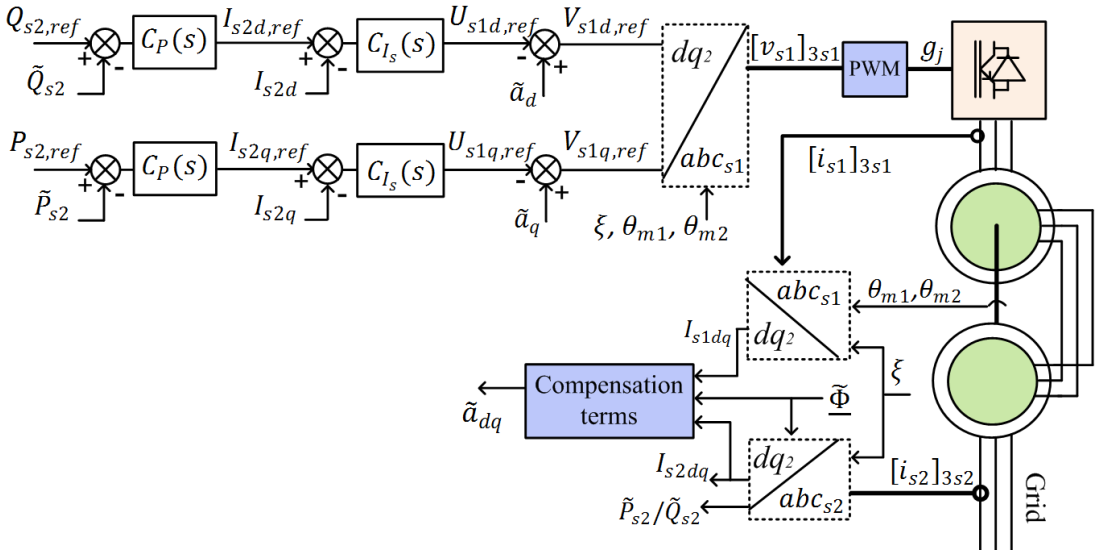

Figure 4.8: VF oriented Vector control scheme of MSC

The Power machine stator current is transformed from the original (abc_{s2}) coordinate to the VF oriented frame (dq_2) by performing a Clarke transformation to ($\alpha\beta_{s2}$) followed by a Park transformation (4.45) using the frame angle ξ_{s2}.

$$(\underline{x})_{dq_2} = e^{-j\xi_{s2}}(\underline{x})_{\alpha\beta_{s2}} \tag{4.45}$$

The Control machine stator currents are first transformed from (abc_{s1}) to ($\alpha\beta_{s1}$) by means of the Clarke transformation. Then, the vector transformation from ($\alpha\beta_{s1}$) reference to (dq_2) frame is performed by (4.46) which is based on the relation defined in (1.70).

$$(\underline{x})_{dq_2} = e^{-j(\xi_{s2}-p_1\theta_{m1}-p_2\theta_{m2})}(\underline{\hat{x}})_{\alpha\beta_{s1}} \tag{4.46}$$

Here likewise, the instantaneous output active and reactive powers are estimated as

follows:

$$\tilde{P}_{s2} = \frac{3}{2}\omega_g \left(\tilde{\Phi}_\alpha I_{s2\beta} - \tilde{\Phi}_\beta I_{s2\alpha}\right) \tag{4.47}$$

$$\tilde{Q}_{s2} = \frac{3}{2}\omega_g \left(\tilde{\Phi}_\alpha I_{s2\alpha} + \tilde{\Phi}_\beta I_{s2\beta}\right) \tag{4.48}$$

The voltage references $V_{s1d,ref}, V_{s1q,ref}$ at the output of the controller are established in the VF rotating reference frame (dq_2). The signals must be transformed into the M1 three-phase stator frame (abc_{s1}) in order to form the sinusoidal reference values for the PWM modulation. This is achieved through a vector transformation (by rotation) using relation (4.49) followed by an inverse Clarke transformation. It induces the DFIM2 stator quantities to operate at ω_g for any rotational speed.

$$(\underline{x})_{\alpha\beta_{s1}} = e^{-j(\xi_{s2} - p_1\theta_{m1} - p_2\theta_{m2})}(\underline{\hat{x}})_{dq_2} \tag{4.49}$$

4.5 Power operating domain of the generating unit

The increasing penetration of wind turbine is challenging the network stability, due to the uncontrollable generated power that arises from wind fluctuations. For this reason, the grid codes are adapted for wind power integration into the grid. The requirements defined by the TSO for large wind farms are becoming more restrictive and similar to conventional power plants in order to preserve the network stability and contribute to voltage regulation [1], [37], [43], [130]. In fact, in addition to active power production, extended reactive power supply is required not only under grid disturbances but also in steady state operation. Indeed, following network faults, the unit plant should withstand voltage sags and remain connected to the grid and must provide reactive power for voltage regulation purposes. Besides, during normal tolerated steady state operation, the integrated unit should operate at different power factors (leading or lagging) depending on the voltage level at the Point of Common Coupling (PCC). On that basis, the system must be able to produce or consume reactive power in order to compensate voltage variations and retain the terminal voltage within the tolerate range. Figure 4.9 illustrates the power factor range for two different TSOs under normal operating conditions [1],[139].

As shown, this diagram may vary slightly from one TSO to the other because of the differences in the grid structures. The aforementioned requisites are to be satisfied at the PCC. Thus, the required reactive current can be provided using the CDFIG itself, the GSC, FACTS, transformers equipped with on-load tap changers, shunt reactors and capacitors, cables or other reactive power sources [13], [139].

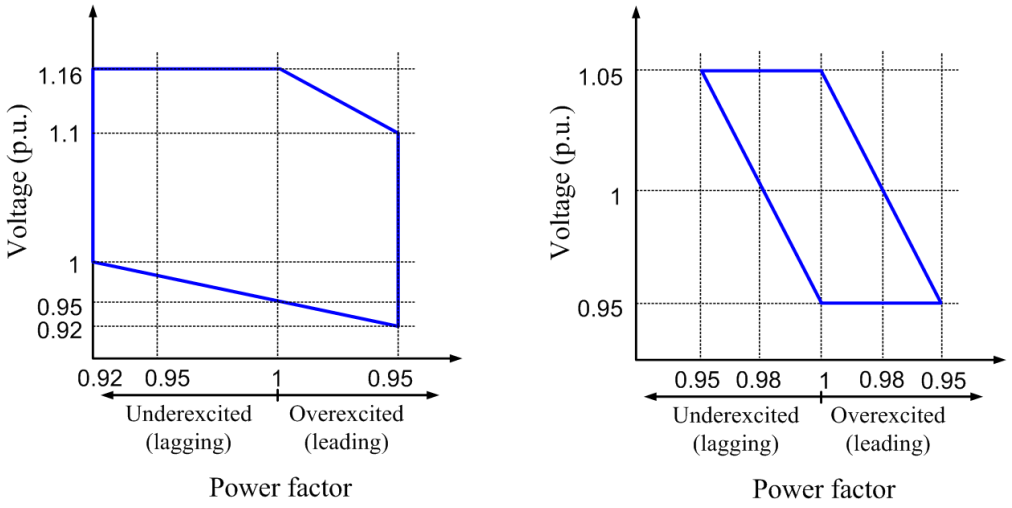

(a) German grid code (b) Spanish grid code

Figure 4.9: Power factor requirements given by two TSOs for steady state operation

In order to meet network requirements without exceeding the ratings of the system, it is imperative to define the working range of the generating unit in terms of active and reactive powers, and its ability to provide reactive power for voltage regulation under different terminal voltage levels. The steady state operating limits of the CDFIG with respect to its rated parameters is elaborated in Chapter 2. The analysis has shown that reactive power consumption is limited by DFIM2 stator current nominal value $|\underline{i}_{s2n}|$, while the reactive power production is delimited by DFIM1 stator current maximal value $|\underline{i}_{s1max}|$. The latter being determined by DFIM1 and MSC ratings. Therefore, to benefit from maximum reactive power capability, the MSC should be able to carry the stator current nominal value $|\underline{i}_{s1n}|$ and a portion of the nominal voltage $|\underline{v}_{s1n}|$. The power limit curves of the CDFIG are recalled hereinafter:

$$P_{s2}^2 + Q_{s2}^2 = \left(\frac{3}{2}\,|\underline{v}_{s2}|\,|\underline{i}_{s2n}|\right)^2 \tag{4.50}$$

$$\left(P_{s2} - A_1\,|\underline{v}_{s2}|^2\right)^2 + \left(Q_{s2} - B_1\,|\underline{v}_{s2}|^2\right)^2 = \left(\frac{3g_2\omega_{s2}M_{sr1}M_{sr2}\,|\underline{v}_{s2}|\,|\underline{i}_{s1max}|}{2L_{s2}C_1^2}\right)^2 \tag{4.51}$$

The analysis can be further extended to include the contribution of the GSC in reactive power production. The main task of the controllers is to maintain constant the voltage of the DC bus. However, it can supply reactive current and increase therefore the power operating domain of the global generating system. The capability of the converter depends on its rated line current $\left|\underline{i}_{gn}\right|$ and the DC link capacitance. Referring to (4.14) and (4.15), the power exchanged between the network and the

GSC can be expressed as a function of the line current amplitude as:

$$P^2 + Q^2 = (\frac{3}{2} \left|\underline{e_g}\right| \left|\underline{i_g}\right|)^2 \tag{4.52}$$

Since the objective of the GSC is to ensure M1 active power transfer for DC voltage regulation, the priority is always given to active power. Consequently, neglecting converters losses, the additional reactive power that can be provided by the GSC is expressed as:

$$Q = \sqrt{(\frac{3}{2} \left|\underline{e_g}\right| \left|\underline{i}_{gn}\right|)^2 - P_{s1}^2} \tag{4.53}$$

Notice that the active power P_{s1} transmitted to the Control machine depends on the output power P_{s2} and the rotational speed Ω. Taking into account the losses in the machine, the power transmitted to the rotor of a DFIM is expressed as follows

$$-g\,(P_s - P_{js})\, = P_r - P_{jr} \tag{4.54}$$

Applying (4.54) for both machines and considering supersynchronous motor convention, the power transmitted to the converter becomes

$$P_{s1} = -g_c P_{s2} + g_c P_{js2} + \frac{1}{g_1} P_{jr2} + \frac{1}{g_1} P_{jr1} + P_{js1} \tag{4.55}$$

P_{js} and P_{jr} denote the copper losses in stator and rotor resistance respectively and are given by:

$$P_{js} = \frac{3}{2} R_s \left|\underline{i}_s\right|^2 \tag{4.56}$$

$$P_{jr} = \frac{3}{2} R_r \left|\underline{i}_r\right|^2 \tag{4.57}$$

Furthermore, assuming optimal operation of the wind turbine, the mechanical speed is derived as follows with reference to (3.1) and (3.3).

$$\Omega = \sqrt[3]{\frac{2 P_{s2} \lambda_{opt}^3 G^3}{\rho \pi R_p^5 C_{pmax}}} \tag{4.58}$$

Combining (4.50),(4.51) and (4.53), the total power capability of the 300 kW generating unit is illustrated in Figure 4.10 comprising a 150 kVA converter. It is worth pointing out that the power limit chart should be implemented in the controller to ensure the system being operated within its ratings. Then, the distribution of the reactive power set points between the available VAR sources is subject to an optimization problem. Referring to Figure 4.10, it can be deduced that following voltage

drops, the operating area of the generating unit is significantly reduced. Thus, it is convenient to mention that under normal grid conditions, the priority is accorded to active power generation for maximal power tracking of the WT, yet it can be switched to reactive power priority during voltage sag to participate to voltage regulation. Indeed, it would be interesting to decrease voluntarily the active power generation so as to provide the required reactive power stated by the grid codes.

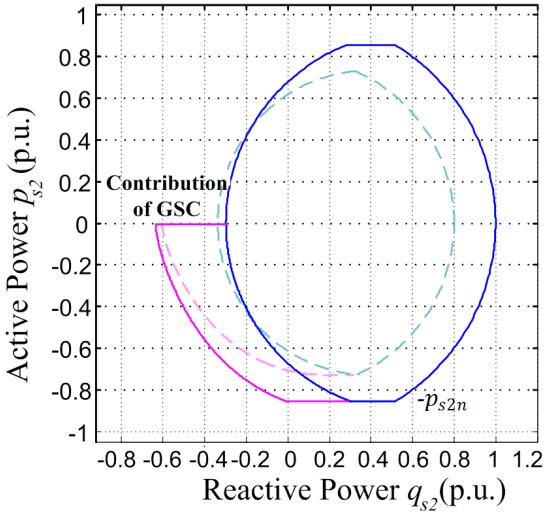

Figure 4.10: Power operating domain of a 300 kW WT at different terminal voltages. Solid:$\left|\underline{e}_g\right| = \left|\underline{e}_{gn}\right|$; dashed:$\left|\underline{e}_g\right| = 0.8\left|\underline{e}_{gn}\right|$

Conclusion

The control scheme of a grid-connected WECS based on a CDFIG is presented in this chapter. A virtual flux oriented vector control is applied for the decoupled regulation of active and reactive powers, leading to grid voltage sensorless operation. The controller is based on two cascaded loops implemented on each converter. The main function of the GSC controller is to maintain a constant DC-link voltage. The MSC is optimizing the power generated by the WT through independent regulation of the CDFIG output active and reactive powers. Despite the complex mathematical model of the generator, an efficient controller is implemented thanks to the unified frame vector representation. Moreover, the generating unit is dynamically controlled to provide additional reactive power according to the new grid code requirements. Accordingly, the steady state power operating domain of the integrated unit is established to ensure the system being operated within its ratings. It is shown that reactive power capability of the CDFIG can be enlarged by including the contribution of the GSC.

Chapter 5

Maximum Power Point Tracking strategies for Wind Generation Systems under normal grid conditions

Introduction

Variable speed WECS are controlled to maximize the power generated by the WT by tracking its optimal behavior. This operation is known as the MPPT algorithm.

Instantaneous MPPT algorithms are elaborated in the literature to track instantaneously the optimal operating point of the WT and extract the maximum available power for every wind speed. However, due to the stochastic aspect of the wind speed and its turbulence high frequencies component, fluctuating and uncontrollable power is generated by the WT which affects the injected energy quality and results in network disturbances. In order to retain the power system stability, a novel method for tracking the optimal operation, while providing enhanced energy quality is elaborated in this chapter. The proposed method, denoted "mean MPPT", intends to generate the maximum constant power related to the average of the wind speed.

After a brief description of the instantaneous MPPT algorithm in section 5.1, the proposed new mean MPPT strategy is analyzed in section 5.2. For the purpose of comparison, the two methods are implemented on the elaborated model of WT based on the CDFIG. The generating unit is regulated based on the virtual flux oriented vector control established in Chapter 4. Simulation tests are performed on Matlab/Simulink environment using the non stationary wind speed model. The results validate the new control approach and emphasize the characteristics of each

method regarding the system efficiency and the quality of the produced energy.

5.1 Instantaneous MPPT approach

Various techniques for instantaneous maximum power tracking of WECS have been widely discussed throughout the bibliography. The generating unit is seeking to extract the maximum available power for every wind velocity and track instantaneously the optimal operating point. This can be achieved through a direct regulation of the generator mechanical speed. Alternatively the turbine speed can be indirectly adjusted at its optimal value by controlling the torque or the active power of the generator [29].

This section offers a brief description of the conventional well known instantaneous MPPT algorithm. It reveals the dynamic response of the wind energy plant in order to highlight the WT performance and establish a comparative study with the new mean MPPT approach. The method followed hereinafter to achieve the optimal behavior consists in controlling the stator output active power P_{s2} of the CDFIG, which is made equal to the maximum available aerodynamic power. Based on the generator rotational speed, the active power set point is computed through the speed power characteristic curve of the WT. Referring to (3.1) and (3.3) the optimal active power to be generated is derived by (5.1) and the blade pitch angle is set to its optimal value $\beta = 0°$.

$$P_{s2,ref} = -\frac{1}{2} C_{pmax} \rho \pi R_p^5 \left(\frac{\Omega}{G \lambda_{opt}} \right)^3 \tag{5.1}$$

Notice that the reference value depends on the mechanical speed which is determined by wind changes. Thus the output power will be affected by wind speed high frequencies oscillations.

The instantaneous MPPT control scheme is implemented on the 300 kW power plant model based on the CDFIG using Matlab/Simulink environment. The system is regulated by means of the virtual flux oriented vector control. The test is conducted under normal grid conditions using the wind profile established in Figure 3.7. Simulation results are collected in Figure 5.1. The active power per unit values are with respect to the nominal active power base P_{s2n}. As it can be observed, the tip speed ratio and the power coefficient are varying in the immediate vicinity of their optimal value λ_{opt} and C_{pmax} respectively. Consequently, the wind power generating system is keeping good track of the optimal behavior, with the objective to maximize the power captured by the wind turbine for every wind speed. It is worth pointing out that prominent deviations in the power coefficient Cp arise from sudden variations in the wind speed caused by wind gust.

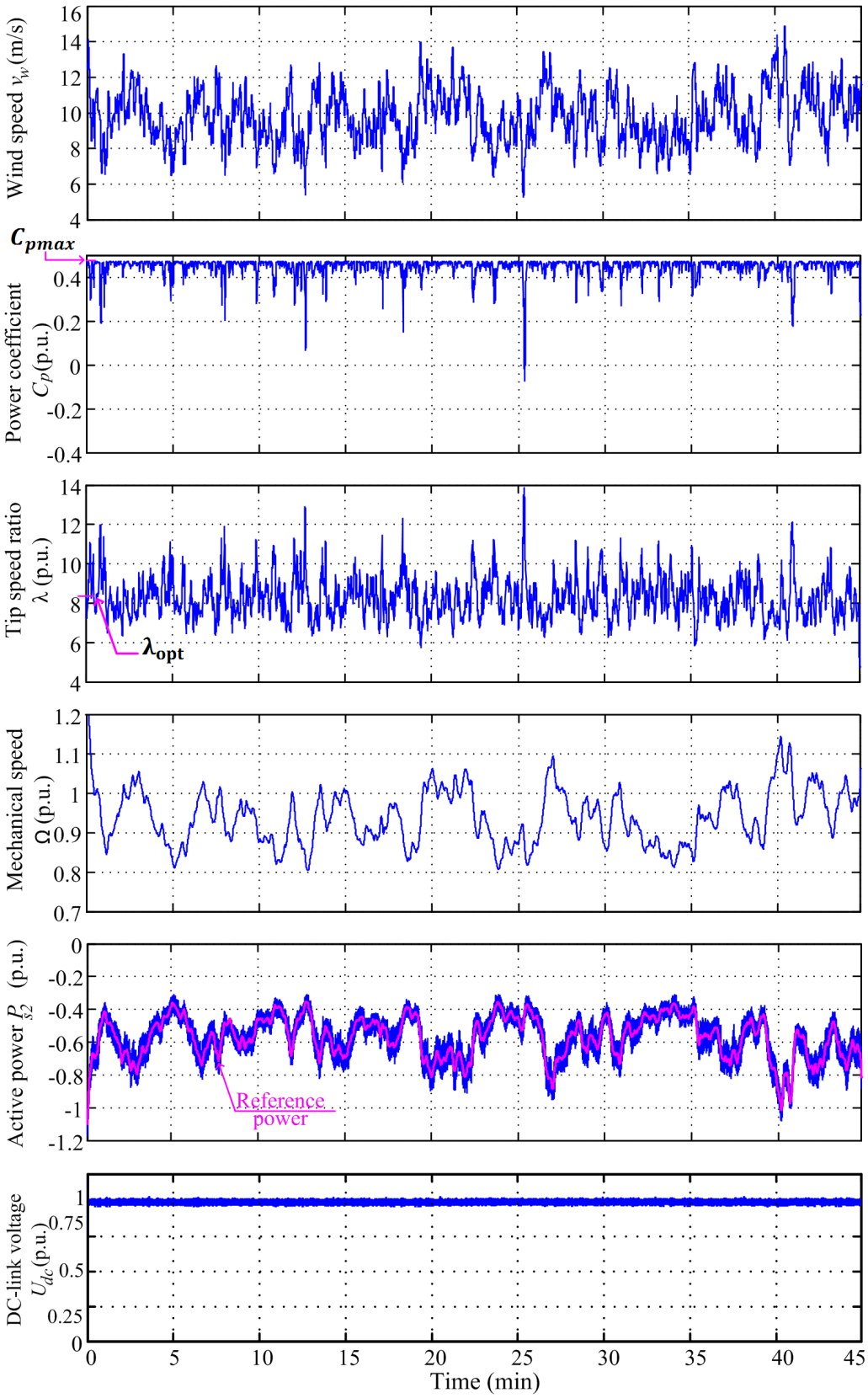

Figure 5.1: Wind turbine behavior in response to the instantaneous MPPT algorithm

The variation of the generator mechanical speed indicates that the controlled system is able to operate in both subsynchrounous and supersynchronous mode. As a result the power transmitted to the converters is either fetched from or feeding the utility grid. The DC-bus is properly controlled in order to maintain a constant voltage level.

The instantaneous MPPT strategy ensures maximum system efficiency. However, this power optimization is at the expense of the power quality and the network stability. As foreseen, uncontrollable fluctuating power is generated by the WT due to the wind speed high frequencies component. The oscillations in stator output power can be clearly observed in Figure 5.1. These fluctuations affect the quality of the energy injected into the network, and induce as well high variations in the generator electromechanical torque that increase the stress on the grid side.

5.2 Mean MPPT strategy

Simulation results in previous section has shown that, despite the high system efficiency and power optimization, the instantaneous MPPT method generates oscillations in the output power that induce network disturbances. The aim of the new mean MPPT strategy is to enhance the energy quality feeding the grid by providing quasi-constant output power regardless the wind speed variations, in order to sustain the power system stability. In addition, the controlled unit must ensure high efficiency and benefit from the maximum available wind power so as to achieve the optimal operation. Accordingly, the principle of the proposed method is to produce the maximum constant power that refers to the average of the wind speed v_{mean}, predicted over a predefined period T_a [8], [9]. This can be accomplished through the regulation of the CDFIG stator active power using the sensorless decoupled vector scheme with virtual flux orientation. The suggested method involves at each step the prediction of the mean wind speed v_{mean} over the upcoming interval, then the optimal power set point to be provided by the speed controller is derived as:

$$P_{s2,ref} = -\frac{1}{2} C_{pmax} \rho \pi R_p^2 v_{mean}^3 \tag{5.2}$$

The main issues regarding the presented approach are the prediction of the mean wind velocity and the choice of the interval length T_a. Referring to (3.12), if the time scale T_a is chosen within the spectrum gap, the average of the instantaneous wind speed is virtually equal to the medium and long term component. Consequently, the turbulence component associated to high frequencies oscillation is removed, and the mean value is defined by only the slow varying component of the wind speed. There from, the generating plant is carried to reach the optimal operation and ensure high

efficiency through the optimization of the power related to the slow varying term of the wind speed. Moreover, since the low frequencies component $v_m(t)$ is slow varying on a time duration T_a, it can be stated that the average v_{mean}, which is approximated to $v_m(t)$, will slightly differ between two consecutive intervals. Accordingly, a linear prediction technique is adopted hereinafter that predicts directly the average of the wind speed at a time step ahead given a finite number n of observations over the passed intervals.

The linear prediction method is a time series analysis concerned with system modeling in a time varying environment [68], [115]. Since wind speed signal is a time varying process, the development of a parametric model using a limited number of observations can be useful for prediction or forecasting. The linear prediction model assumes that the output signal of a system is a linear combination of its past samples and present and past inputs. The objective is to find the model that fits best the signal waveform, which is the mean wind speed in our case. Since the input is unknown, the future mean value is predicted based on the present and past observations, using the following linear transformation (5.3). This model is known as auto-regressive (AR) or all-pole model.

$$y_p(i+1) = a_1 y(i) + a_2 y(i-1) + ... + a_m y(i-m+1) \tag{5.3}$$

where y is the output observation, a_k, $k = 1, ..., m$ are the model coefficients and m is the model order. The model order must be selected carefully, and the model coefficient are computed periodically at every step based on a modeling window. The latter contains a finite number n of the latest mean wind speed observations (present and past samples) and is used to find the best model of the signal, then this model can be used to predict the mean wind speed for a time step ahead. Notice that the model is adjusted periodically with every new observation.

The model parameters are estimated using the least squares error method. Indeed, since the linear prediction model cannot fit perfectly the signal waveform, a model error is generated. The prediction error $e(i)$, also known as residual, is the difference between the real value y and the predicted value y_p at the same instant. It is expressed as:

$$e(i) = y(i) - y_p(i) \tag{5.4}$$

Including the modeling error, equation (5.3) is reprinted as:

$$y(i) = a_1 y(i-1) + a_2 y(i-2) + ... + a_m y(i-m) + e(i) \tag{5.5}$$

Applying the above relation on the n samples, a set of equations can be written and rearranged as follows:

$$Y = XA + E \tag{5.6}$$

where:

$$Y = \begin{bmatrix} y(i)\ y(i-1)\ ...\ y(i-j) \end{bmatrix}^T \tag{5.7}$$

$$A = \begin{bmatrix} a_1\ a_2\ ...\ a_m \end{bmatrix}^T \tag{5.8}$$

$$E = \begin{bmatrix} e(i)\ e(i-1)\ ...\ e(i-j) \end{bmatrix}^T \tag{5.9}$$

$$X = \begin{bmatrix} y(i-1) & y(i-2) & ... & y(i-m) \\ y(i-2) & y(i-3) & ... & y(i-(m+1)) \\ . & . & & . \\ . & . & & . \\ . & . & & . \\ y(i-(j+1)) & & ... & y(i-(m+j)) \end{bmatrix} \tag{5.10}$$

$$j = n - (m+1) \tag{5.11}$$

The total squared error given by (5.12), describes the energy in the error signal

$$D = E^T E = \sum_{l=i-j}^{i} e^2(l) \tag{5.12}$$

In least squares method the model parameters a_k are derived through the minimization of the total squared error D with respect to each of the parameters. As a result, the elements in matrix A can be found as:

$$A = (X^T X)^{-1} X^T Y \tag{5.13}$$

Consequently, according to (5.13) the model coefficients are calculated at every step using the corresponding model window. Then the predicted mean value of the upcoming interval is computed using (5.3).

In brief, the mean MPPT procedure is resumed as follows:

1. Predict at time t_0 the mean wind speed associated to the interval $t_0 + T_a$. This is achieved through linear prediction method with a limited number of observations using relations (5.13) then (5.3).
2. The predicted mean value is retained as a set point for the computation of the constant power reference value $P_{s2,ref}$ using equation (5.2).

3. The previous steps are repeated periodically at time $t_0 + iT_a$.

The mean MPPT approach is validated on Matlab/Simulink under the same conditions of section 5.1. The simulation tests are carried out using the wind profile implemented in Figure 3.7. The model order and the number of observations for the linear prediction are chosen according to the minimum squared error based on several wind profiles. Numerically, $m = 3$ and $n = 10$. Moreover, a leading capacitive power factor $\cos\phi_{ref} = 0.98$ is imposed at the PCC. Hereinafter the reactive current demand is supplied by the CDFIG, providing it complies with the limit operating domain of the machine. Accordingly the reactive power reference values are computed as:

$$Q_{s2,ref} = (P + P_{s2}) \tan\phi_{ref} \tag{5.14}$$

$$Q_{ref} = 0 \tag{5.15}$$

Simulation results are reported in Figure 5.2 over a span of 45 min and an average period T_a= 10min. As can be noticed, the generating unit is providing constant power over the defined interval T_a irrespective of wind fluctuations, which improves the energy quality feeding the network and decreases the stress on the generator and the grid side by damping electrical torque oscillations. At this point, it is convenient to highlight that the wind energy contributes to the production of electric energy as well as rotational mechanical power. Subsequently, a lack or excess in the wind turbine input power will give rise respectively to a deceleration or acceleration in the mechanical rotational speed in order to provide the required output power demand. Then the pitch angle control can be activated in order not to exceed the rated power and desired speed range (yet the mechanical control is discarded in this study). Indeed, according to the shaft dynamic model (3.8), the power relation (5.16) is verified.

$$P_{aer} + P_m = P_f + P_{mec} \tag{5.16}$$

The power flow at the turbine shaft is illustrated in Figure 5.3. P_f is the frictional losses and P_{mec} the mechanical power stored in the shaft inertia. Notice that with respect to supersynchronous motor convention, the CDFIG mechanical power P_m is negative in generator mode operation.

Here likewise, the generator is operating in both subsynchronous and supersynchronous modes as shown in Figure 5.2. The generator speed corresponding to the average wind velocity (at optimal operation) can be set at any point by the choice of the gearbox ratio. Of course, to stay within the desired limited slip range, this point should be around the synchronous speed.

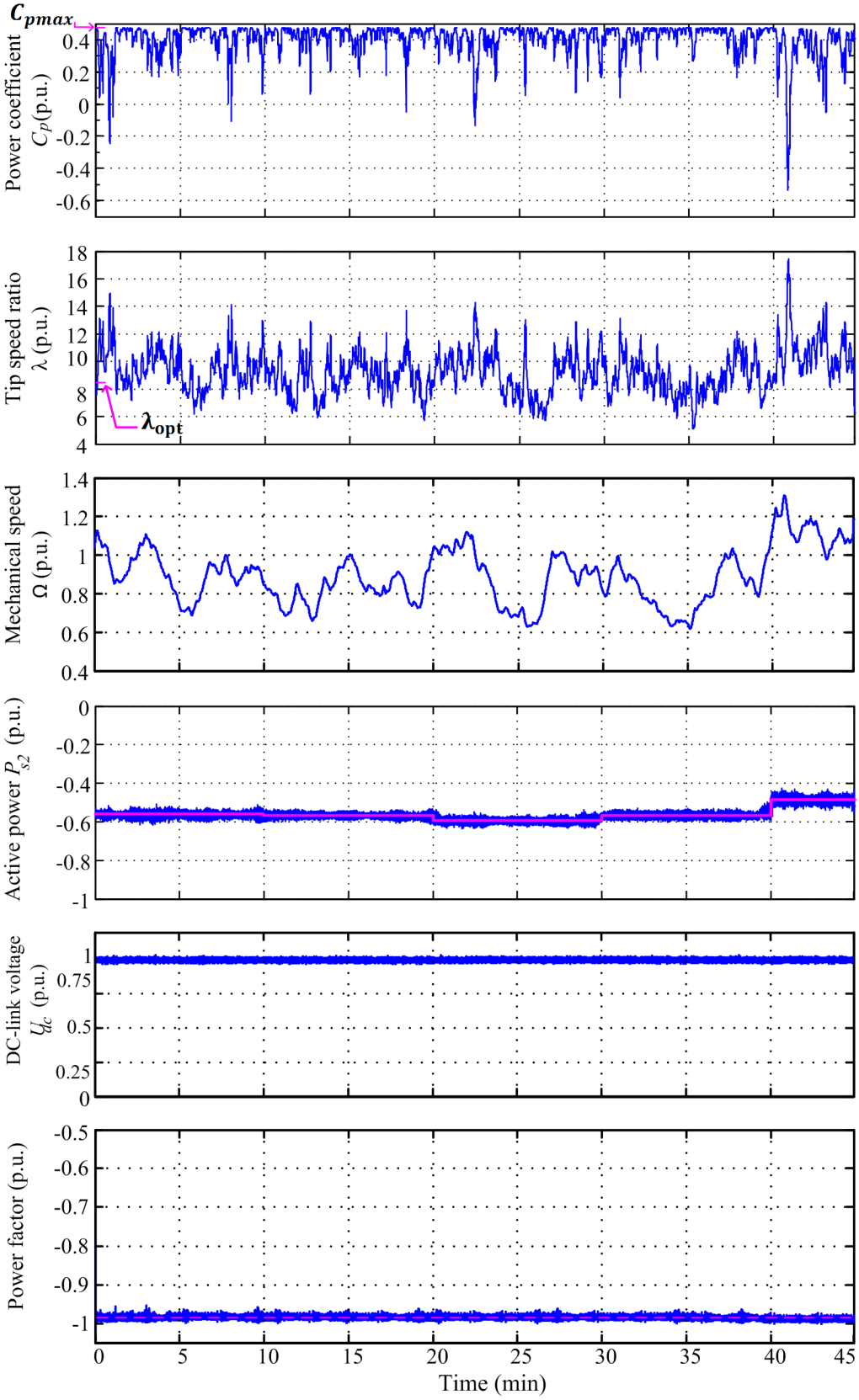

Figure 5.2: Wind turbine behavior in response to the mean MPPT algorithm

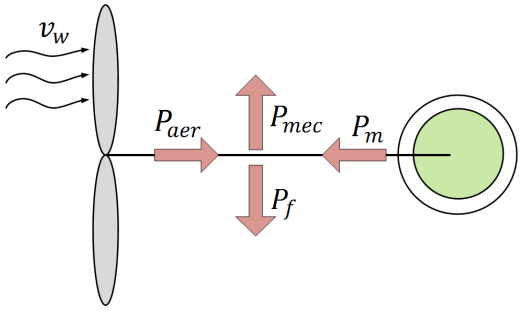

Figure 5.3: Wind turbine power flow

In addition to power quality improvement, the controlled unit manages to ensure the power factor requirements by providing the appropriate amount of reactive power. It also sustains a constant DC voltage regardless of load variations with a relative error less than 2%, as it can be observed in Figure 5.2.

Furthermore, it shall be noted that the mean MPPT algorithm may reduce the CDFIG ratings for a given wind profile. In fact, the characteristics are determined by the average of the wind speed, whereas for the instantaneous MPPT strategy the machine characteristics are defined by the maximum wind speed value.

Nevertheless, the implementation of this new MPPT method reduces somewhat the efficiency of the system compared to the classical MPPT strategy. Indeed the average produced active power, for the given simulation time duration, is decreased by roughly 5%. Simulation results validate that the system is tracking the optimal behavior of the wind turbine. However, the deviations of C_p and λ with respect to their optimal value is more substantial, for the reason that the controlled system is optimizing the power related to the average of the wind speed rather than the instantaneous value.

Conclusion

This chapter presents maximum power tracking techniques of a variable speed WECS based on a CDFIG. The conventional instantaneous MPPT algorithm is first presented. Then, a novel mean MPPT approach is elaborated for tracking the optimal operation of the WT. The controlled unit is carried to produce the maximum constant power associated to the average value of the wind speed, predicted over a predefined interval. In comparison with the instantaneous MPPT method, the proposed new strategy improves the quality of the generated power by feeding constant power irrespective of wind oscillations. This tracking method decreases the stress on the generator and the grid side and supports the network stability. However, the system

efficiency is reduced since the controlled unit optimizes the power that refers to the slow varying component of the wind speed instead of the instantaneous value.

The MPPT approaches are validated by simulation using Matlab/Simulink environment. The generating system is regulated based on the decoupled VF oriented vector control investigated in Chapter 4. The dynamic reactive power control of the integrated unit enables power factor regulation at the PCC according to grid code requisites.

Part III

Standalone Cascaded Doubly Fed Induction Generator

Chapter 6

CDFIG Supplying Isolated Constant Frequency AC Loads

Introduction

The CDFIG is a good candidate for VSCF systems, specially in applications where high level of reliability and long time maintenance periodicity are required. This brushless structure can be directly connected to a constant frequency grid, despite speed variations. The generator is driven by low power converter, fixed by the range of the operating speed. This chapter establishes the control of a standalone CDFIG supplying an isolated load, and operating as a variable speed constant frequency generator. Despite the complexity of the generator modeling an efficient controller can be elaborated based on the theory of a unified reference frame vector representation. In standalone operation, the controller aims to adjust the amplitude and frequency of the output voltage irrespective of load and speed variations. Here, the generating system considered for simulation is designed for supplying an isolated three-phase load dedicated to embedded aircraft applications but can be adapted to other industrial applications such as autonomous wind energy and hydro-power systems.

In section 6.1, the model of the standalone generator in embedded aircraft electric power generation systems is presented. The control of the generator is detailed in section 6.2. The terminal voltage is adjusted through a decoupled vector control with two nested loops. In section 6.3, the control approach is validated by simulation using Matlab/Simulink environment with both load and rotational speed variations. An experimental validation of the proposed control strategy follows in section 6.4. The performance of the controlled system is further tested under unbalanced load in section 6.5.

6.1 Model of the standalone CDFIG

The configuration of a standalone CDFIG in embedded aircraft industry is presented in Figure 6.1. The global structure is similar to a single DFIG [62], [88]:

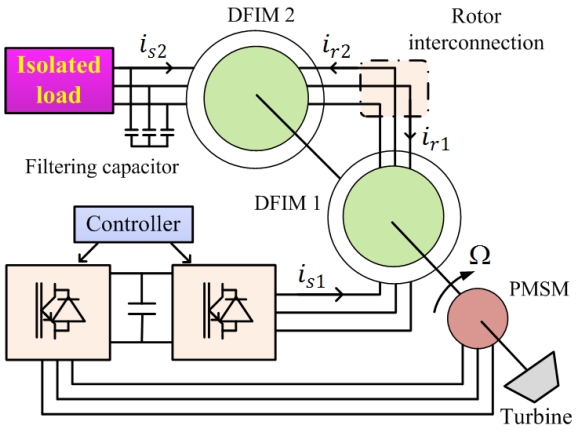

Figure 6.1: Configuration of an autonomous system based on a CDFIG

the stator of DFIM2 is directly connected to the grid, whereas the stator of DFIM1 is fed by a power frequency converter. The windings are connected to a voltage source inverter supplied by a rectifier which in turn is connected to a PMSG, allowing initial excitation of the CDFIG and full autonomous capabilities to the system. For a limited speed range, the converters are sized for a fraction of the nominal power. When a bidirectional back-to-back power converter is used, the machine can operate in both subsynchronous and supersynchronous modes. In this case a proper control of the PMSG is required to keep the DC-link voltage constant regardless of the direction of the power flow [62]. However the study presented in the following is focused on the control of the CDFIG (i.e. the MSC).

A modular representation of the system is elaborated based on the conventional model of two distinct DFIGs combined in inverse coupling sequence as shown in Figure 6.2. The model and block diagram of the standalone voltage source CDFIG are detailed in section 1.3.3. As well the inverter model is presented in section 3.4.1.

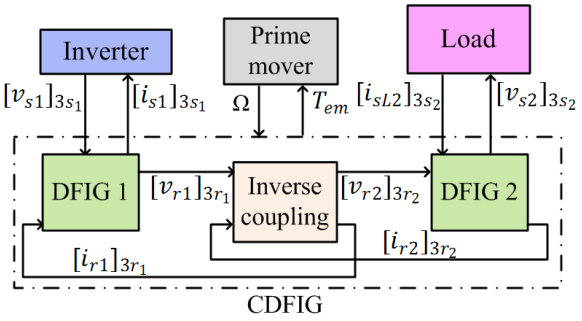

Figure 6.2: Global model of a standalone CDFIG

The loads can be modeled using an equivalent current source. Regarding the mechanical part in aircraft application, the electromagnetic torque of the CDFIG can be neglected with regard to the turbine torque [91]. Thus, the mechanical speed is considered to be a varying parameter imposed by external source, independently of the load variation. The global model of the system is established by a simple interconnection of the different components. This modular representation is implemented on Matlab/Simulink for simulations in order to validate new control techniques and evaluate the behavior and response of the generator regarding speed and load variations.

6.2 Control strategy

In the targeted application, the CDFIG is driven at a variable speed and supplies an isolated three-phase load. The controller must provide constant frequency and amplitude for the terminal voltage in spite of load and/or speed variations. Thanks to the unified frame vector model, the complex CDFIG generator has similar structure as a single DFIG. This allows the development of control strategies and analysis tools analogous to the ones used for a classical wound rotor induction machine [34], [99], [102]. An indirect stator field oriented decoupled vector control is adopted to adjust the output voltage $\underline{v}_{s2}$ of the CDFIG. The approach is based on cascaded loops with two regulation paths, devoted to adjust the rotor current d-axis and q-axis components distinctly. The voltage magnitude is controlled through the regulation of the Power machine stator flux $\underline{\Phi}_{s2}$. Unlike the utility grid case, in standalone applications the stator flux is no longer imposed by the grid and can be adjusted by action on one of the rotor current components. The other component is used to force the reference frame orientation [6].

The equations of the CDFIG in the common Power machine synchronous reference frame using phasor quantities and supersynchronous motor conventions are recalled hereafter:

$$\underline{v}_{s2} = R_{s2}\underline{i}_{s2} + \frac{d}{dt}\underline{\Phi}_{s2} + j\omega_{s2}\underline{\Phi}_{s2} \tag{6.1}$$

$$\underline{v}_{s1} = R_{s1}\underline{i}_{s1} + \frac{d}{dt}\underline{\Phi}_{s1} + j\left(\omega_{s2} - \Sigma p\Omega\right)\underline{\Phi}_{s1} \tag{6.2}$$

$$0 = R_r\underline{i}_r + \frac{d}{dt}\underline{\Phi}_r + j\left(\omega_{s2} - p_2\Omega\right)\underline{\Phi}_r \tag{6.3}$$

$$\underline{\Phi}_{s2} = L_{s2}\underline{i}_{s2} + M_{sr2}\underline{i}_r = L_{s2}\underline{i}_{\mu 2} \tag{6.4}$$

$$\underline{\Phi}_{s1} = L_{s1}\underline{i}_{s1} - M_{sr1}\underline{i}_r \tag{6.5}$$

$$\underline{\Phi}_r = L_r\underline{i}_r + M_{sr2}\underline{i}_{s2} - M_{sr1}\underline{i}_{s1} \tag{6.6}$$

$\underline{i}_{\mu 2} = \underline{i}_{s2} + m_2\underline{i}_r$ being the stator magnetizing current. If stator field orientation is considered with the d-axis aligned along the stator flux vector $\underline{\Phi}_{s2}$, the following relations are deduced:

$$\Phi_{s2q} = I_{\mu 2q} = 0; \quad \Phi_{s2d} = |\underline{\Phi}_{s2}| = L_{s2}I_{\mu 2d} \tag{6.7}$$

Introducing (6.7) in (6.4) and decomposing into *d-q* components yields to:

$$I_{s2q} = -\frac{M_{sr2}}{L_{s2}}I_{rq} \tag{6.8}$$

$$I_{s2d} = I_{\mu 2d} - \frac{M_{sr2}}{L_{s2}}I_{rd} \tag{6.9}$$

Referring to (6.1), (6.7), (6.8) and (6.9) the dynamic behavior of the magnetizing current (i.e. stator flux) is expressed as:

$$\frac{L_{s2}}{M_{sr2}}I_{\mu 2d} + \frac{L_{s2}^2}{R_{s2}M_{sr2}}\frac{d}{dt}I_{\mu 2d} = \frac{L_{s2}}{R_{s2}M_{sr2}}V_{s2d} + I_{rd} \tag{6.10}$$

$$V_{s2q} = R_{s2}I_{s2q} + \omega_{s2}L_{s2}I_{\mu 2d} \tag{6.11}$$

At steady state, the grid voltage magnitude should be maintained constant. Neglecting the resistive voltage drop with regard to the back EMF $\omega_{s2}L_{s2}I_{\mu 2d}$, the following relations are obtained:

$$V_{s2d} \simeq 0 \tag{6.12}$$

$$V_{s2q} \simeq \omega_{s2}L_{s2}I_{\mu 2d} \simeq |\underline{v}_{s2}| \tag{6.13}$$

It can be noticed from (6.10) that $I_{\mu 2d}$ and I_{rd} are linked by a first order transfer function. The voltage d-axis component V_{s2d} is considered as a disturbance.

$$I_{\mu 2d}(s) = \frac{K_\mu}{1+\tau_\mu s}I_{rd}(s); \qquad K_\mu = \frac{M_{sr2}}{L_{s2}}; \qquad \tau_\mu = \frac{L_{s2}}{R_{s2}} \tag{6.14}$$

Since the influence of V_{s2d} is negligible, the magnetizing current, i.e. the stator flux, can be directly controlled by adjusting the rotor current d-component. The magnetizing current demand $I_{\mu 2d,ref}$ is determined by the output stator voltage reference value.

According to (6.13), the current set point is computed as:

$$I_{\mu 2d,ref} = \frac{|\underline{v}_{s2}|_{ref}}{L_{s2}\omega_{s2,ref}} \tag{6.15}$$

In this context, the rotor current q-component forms a degree of freedom, it is thus manipulated to force the vector orientation of (dq_2) along the stator flux. The required I_{rq} set point is derived from the condition of $\Phi_{s2q} = 0$ as:

$$I_{rq,ref} = -\frac{L_{s2}}{M_{sr2}} I_{s2q} \tag{6.16}$$

Notice that I_{rq} must track its reference under the action of a fast control loop (compared to the flux control loop) to reach an effective reference orientation. This approach may be denoted: "indirect stator flux orientation vector control". The orientation condition means that the stator flux orientation frame angle (the Park angle) ξ_{s2} can be derived from a simple integral of the output frequency demand $\omega_{s2,ref}$ as shown in (6.17). It does not have to be computed from stator voltage measurement, since the orientation is forced by the condition (6.16).

$$\xi_{s2} = \int \omega_{s2,ref} dt \tag{6.17}$$

Consequently the orientation is more stable and devoid of measurement noise and stator voltage harmonic distortion. These harmonics would be intensified if the orientation angle was calculated from voltage measurement.

Referring to (6.3) and (6.6), a relation can be established between the machine currents as:

$$(R_r + j\omega_{r2}L_r)\,\underline{i}_r + L_r\frac{d}{dt}\underline{i}_r + j\omega_{r2}M_{sr2}\underline{i}_{s2} + M_{sr2}\frac{d}{dt}\underline{i}_{s2} - j\omega_{r2}M_{sr1}\underline{i}_{s1} - M_{sr1}\frac{d}{dt}\underline{i}_{s1} = 0 \tag{6.18}$$

where $\omega_{r2} = (\omega_{s2} - p_2\Omega)$. Substituting the quantity of $\frac{d}{dt}\underline{i}_{s2}$ using (6.4) gives:

$$(R_r + j\omega_{r2}L_r)\,\underline{i}_r + \sigma_p L_r\frac{d}{dt}\underline{i}_r + j\omega_{r2}M_{sr2}\underline{i}_{s2} + M_{sr2}\frac{d}{dt}\underline{i}_{\mu} - j\omega_{r2}M_{sr1}\underline{i}_{s1} = M_{sr1}\frac{d}{dt}\underline{i}_{s1} \tag{6.19}$$

On the other side, the Control machine stator current and voltage $\underline{i}_{s1}$ and $\underline{v}_{s1}$ respectively and the rotor current $\underline{i}_r$ are related as (6.20) with $g_c\omega_{s2} = \omega_{s2} - \Sigma p\Omega$

$$\underline{v}_{s1} = R_{s1}\underline{i}_{s1} + L_{s1}\frac{d}{dt}\underline{i}_{s1} - M_{sr1}\frac{d}{dt}\underline{i}_r + jg_c\omega_{s2}L_{s1}\underline{i}_{s1} - jg_c\omega_{s2}M_{sr1}\underline{i}_r \tag{6.20}$$

Introducing the expression of $\frac{d}{dt}\underline{i}_{s1}$ from (6.19) into (6.20) yields to:

$$\underline{v}_{s1} = \frac{L_{s1}R_r}{M_{sr1}}\underline{i}_r + \left(\frac{\sigma_p L_r L_{s1}}{M_{sr1}} - M_{sr1}\right)\frac{d}{dt}\underline{i}_r + R_{s1}\underline{i}_{s1} + \frac{L_{s1}M_{sr2}}{M_{sr1}}\frac{d}{dt}\underline{i}_\mu - jp_1\Omega L_{s1}\underline{i}_{s1} + j\left(\omega_{r2}\frac{L_r L_{s1}}{M_{sr1}} - g_c\omega_{s2}M_{sr1}\right)\underline{i}_r + j\omega_{r2}\frac{L_{s1}M_{sr2}}{M_{sr1}}\underline{i}_{s2} \quad (6.21)$$

Then decomposing into *d-q* components, the following expressions are obtained:

$$\frac{L_{s1}R_r}{M_{sr1}}I_{rd} + \left(\frac{\sigma_p L_r L_{s1}}{M_{sr1}} - M_{sr1}\right)\frac{d}{dt}I_{rd} = V_{s1d} - a_d = U_{s1d} \quad (6.22)$$

$$\frac{L_{s1}R_r}{M_{sr1}}I_{rq} + \left(\frac{\sigma_p L_r L_{s1}}{M_{sr1}} - M_{sr1}\right)\frac{d}{dt}I_{rq} = V_{s1q} - a_q = U_{s1q} \quad (6.23)$$

As it can be noticed $\underline{v}_{s1}$ and $\underline{i}_r$ *d-q* components are linked by a first order linear transfer function:

$$I_{rd,q}(s) = \frac{K_r}{1+\tau_r s}U_{s1d,q}(s); \qquad K_r = \frac{M_{sr1}}{L_{s1}R_r}; \qquad \tau_r = \left(\frac{\sigma_p L_r}{R_r} - \frac{M_{sr1}^2}{L_{s1}R_r}\right) > 0 \quad (6.24)$$

The factors a_d and a_q, given by the following relations, define the *d-q* disturbances composed of a cross coupling perturbation and back EMF related to DFIM2 stator flux.

$$a_d = R_{s1}I_{s1d} + \frac{L_{s1}M_{sr2}}{M_{sr1}}\frac{d}{dt}I_{\mu 2d} + p_1\Omega L_{s1}I_{s1q} - \left(\omega_{r2}\frac{L_r L_{s1}}{M_{sr1}} - g_c\omega_{s2}M_{sr1}\right)I_{rq} - \omega_{r2}\frac{L_{s1}M_{sr2}}{M_{sr1}}I_{s2q} \quad (6.25)$$

$$a_q = R_{s1}I_{s1q} - p_1\Omega L_{s1}I_{s1d} + \left(\omega_{r2}\frac{L_r L_{s1}}{M_{sr1}} - g_c\omega_{s2}M_{sr1}\right)I_{rd} + \omega_{r2}\frac{L_{s1}M_{sr2}}{M_{sr1}}I_{s2d} \quad (6.26)$$

Consequently the rotor current components I_{rd} and I_{rq} can be adjusted by action on the Control machine stator voltage V_{s1d} and V_{s1q} respectively. On the basis of previous relations, the open loop transfer function of the standalone CDFIG in the predefined field oriented synchronous frame is deduced. The transfer function to be regulated is thus illustrated in Figure 6.3.

As can be observed, a decoupled vector control of the CDFIG can be achieved with the stator flux orientation. An indirect regulation of the output voltage magnitude can be performed through hierarchical loops using PI controllers (refer to Figure 6.6). An outer loop to adjust DFIM2 stator flux and an inner faster loop to control the rotor current and force the indirect field orientation. The output of $I_{\mu 2d}$ loop forms the rotor current command $I_{rd,ref}$. The disturbance generated by V_{s2d} is negligible. The voltage references $V_{s1d,ref}, V_{s1q,ref}$ are provided by the rotor current controllers.

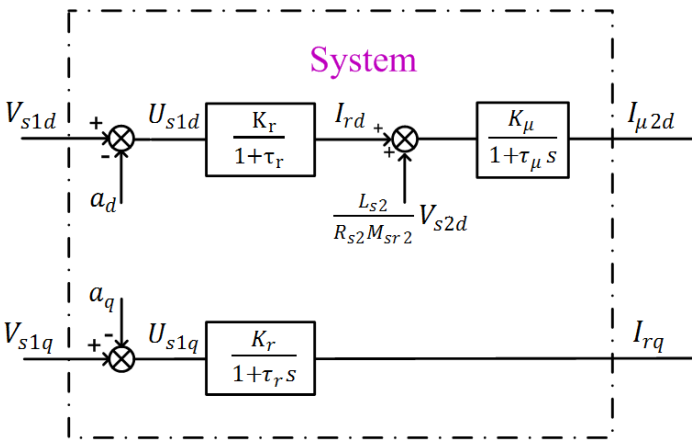

Figure 6.3: Open loop transfer function of the standalone generator

Due to the symmetry in the machine model, identical controllers are implemented on each axis. Compensation terms $\tilde{a}_d$, $\tilde{a}_q$, based on (6.25) and (6.26), may be added by a feed-forward action to the output of the PI controllers to provide linear transfer function and overcome the coupling perturbations. The stator flux derivative terms are not included in the compensation terms since they are nil at steady state.

6.2.1 Rotor current control loop

For this standalone application, the study is detailed for a laboratory scale CDFIG. The parameters are given in Appendix B. However simulation tests are also carried out on the high power scale 300 kW machine. The results are given in Appendix C.

The plant to be regulated is a first order transfer function $G_{I_r}(s)$ given by (6.27). The cutoff frequency is $\omega_{I_r} = 164$ rad/s. The rotor current control loop is illustrated by the block diagram in Figure 6.4.

$$G_{I_r}(s) = \frac{I_{rd,q}}{U_{s1d,q}} = \frac{K_r}{1+\tau_r s} \tag{6.27}$$

A PI controller $C_{I_r}(s)$ is synthesized in order to achieve the following requirements:

- Zero steady state error
- The settling time of the closed-loop is equal to the open-loop settling time.

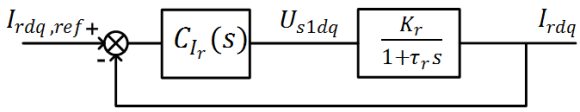

Figure 6.4: Block diagram of rotor current loop

6.2.2 Flux control loop

The outer loop is illustrated in Figure 6.5, where $F_{I_r}(s)$ represents the inner loop dynamic. The open-loop dynamic of the magnetizing current $I_{\mu 2d}$ is characterized by (6.28).

$$\frac{I_{\mu 2d}}{I_{rd,ref}} = F_{I_r}(s)\frac{K_\mu}{1+\tau_\mu s} \tag{6.28}$$

Numerically, the open-loop cutoff frequency is $\omega_{I_\mu} = 4.9$ rad/s. The settling time is much greater than the internal closed-loop settling time.

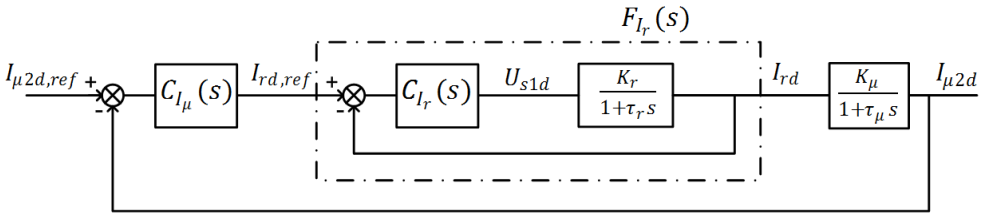

Figure 6.5: Block diagram of outer loop

Therefore, it is possible to discard the rotor current closed-loop dynamic $F_{I_r}(s)$ for the design of the outer loop PI controller. Thus, the transfer function to be regulated is:

$$G_{I_\mu}(s) = \frac{I_{\mu 2d}}{I_{rd}} = \frac{K_\mu}{1+\tau_\mu s} \tag{6.29}$$

The PI is designed to meet the following specifications:

- Zero steady state error
- The settling time of the closed-loop is five times smaller than the open-loop settling time.

6.2.3 Currents estimator

As shown in previous paragraph, the rotor current and the stator flux should be regulated. Yet these quantities are not accessible and an estimator should be implemented. A simple open loop current estimator is proposed hereinafter [91]:

$$\underline{\tilde{\Phi}}_{s2} = L_{s2}\underline{\tilde{i}}_{\mu 2} = \int (\underline{v}_{s2} - R_{s2}\underline{i}_{s2})\, dt \tag{6.30}$$

$$\underline{\tilde{i}}_r = \frac{1}{M_{sr2}}\left(\underline{\tilde{\Phi}}_{s2} - L_{s2}\underline{i}_{s2}\right) \tag{6.31}$$

6.2.4 Control Scheme

Using the measured stator voltage and currents $(\underline{v}_{s2}, \underline{i}_{s2}, \underline{i}_{s1})$, and the derivative values of the rotor and magnetizing currents $\left(\underline{\tilde{i}}_r, \underline{\tilde{i}}_\mu\right)$, the control scheme of the

standalone CDFIG is implemented in Figure 6.6.

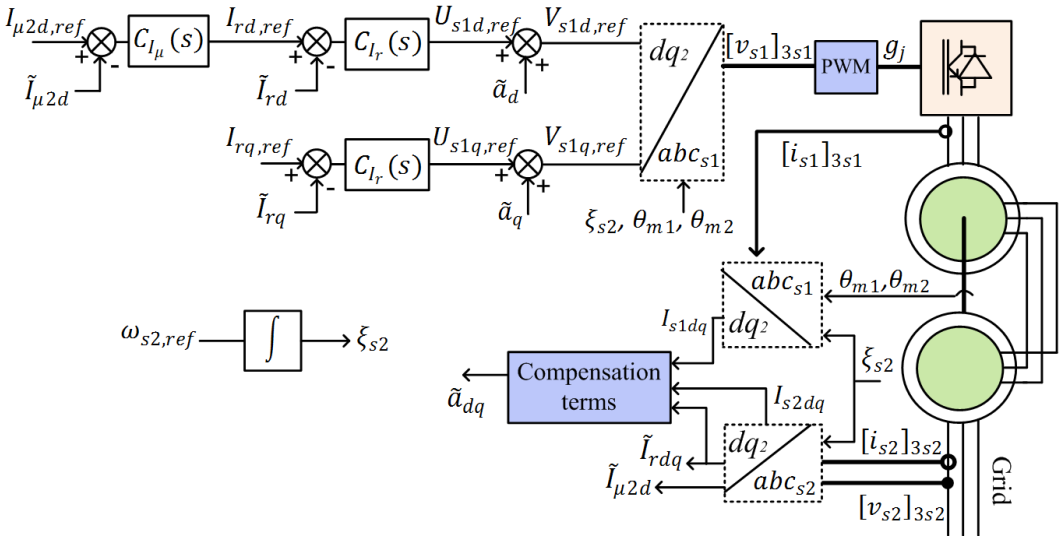

Figure 6.6: Control scheme of standalone CDFIG

The Power machine stator quantities are transformed from the original (abc_{s2}) to the predefined rotating (dq_2) frame by performing a Clarke transformation to ($\alpha\beta_{s2}$) followed by a Park transformation (6.32) with the frame angle ξ_{s2}.

$$(\underline{x})_{dq_2} = e^{-j\xi_{s2}}(\underline{x})_{\alpha\beta_{s2}} \tag{6.32}$$

As for the Control machine, the stator currents are transformed from (abc_{s1}) to ($\alpha\beta_{s1}$) by means of the Clarke transformation. Then, the vector transformation from the ($\alpha\beta_{s1}$) reference to DFIM2 (dq_2) synchronous frame is performed by (6.33):

$$(\underline{x})_{dq_2} = e^{-j(\xi_{s2}-p_1\theta_{m1}-p_2\theta_{m2})}(\underline{\hat{x}})_{\alpha\beta_{s1}} \tag{6.33}$$

$$(\underline{x})_{\alpha\beta_{s1}} = e^{-j(\xi_{s2}-p_1\theta_{m1}-p_2\theta_{m2})}(\underline{\hat{x}})_{dq_2} \tag{6.34}$$

At the output of the controller, the voltage references $V_{s1d,ref}, V_{s1q,ref}$ are established in DFIM2 synchronous frame (dq_2). Therefore a transformation (by rotation) back to the DFIM1 three-phase stator frame (abc_{s1}) is required to engender the sinusoidal reference values for the inverter. It is attained based on relation (6.34), which induces the DFIM2 stator quantities to operate at the demand frequency $\omega_{s2,ref}$ for any shaft speed, during steady state and transient conditions. Notice that it is possible to directly control the voltage magnitude $|\underline{v}_{s2}| = \sqrt{V_{s2d}^2 + V_{s2q}^2}$ since it is proportional to the magnetizing current $I_{\mu 2d}$ as per (6.13). However, regulation of the stator flux instead of the line voltage reduces the noise and harmonic distortion due to the low pass filter behavior of the integrator.

6.3 Simulation results

Simulations are carried out to test and validate the performance of the proposed control strategy. Two tests are conducted. The first is done at constant speed and variable load, the second is performed at variable speed. The results are evaluated with respect to the BS EN 2282 [1] requirements. The transient envelopes of the output Root Mean Square (RMS) voltage as specified by this standard are given in Figure 6.7.

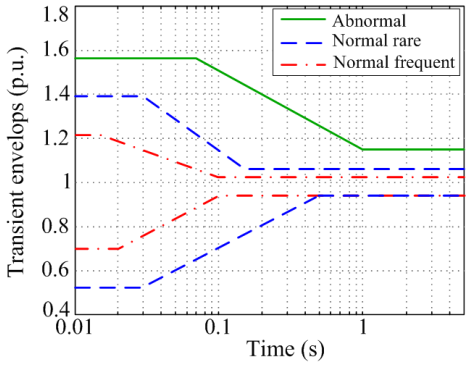

Figure 6.7: Transient envelopes of the RMS voltage specified by BS EN 2282

6.3.1 Simulation with load variation

The generator is driven at constant speed ($\Omega = 1.1$p.u.) feeding an inductive load with a lagging Power Factor PF=0.9. Under these conditions, and based on the power operating domain of the CDFIG, the corresponding machine cannot operate at rated active power load. In order to clarify this point, the power generation capability of the CDFIM at ($\Omega = 1.1$p.u.) is depicted in Figure 6.8.

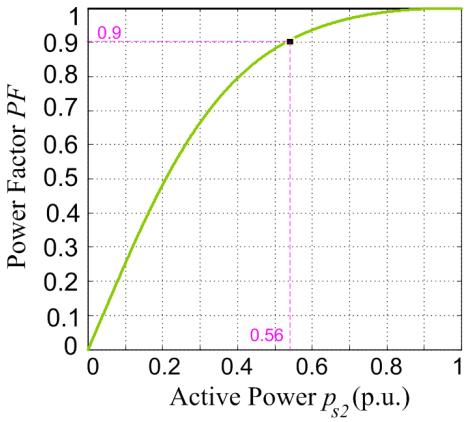

Figure 6.8: Power factor capability of the CDFIG

1. BS EN 2282: Characteristics of aircraft electrical supplies

Here, the domain is computed in terms of the active power and the power factor based on the following relation:

$$PF = \frac{P_{s2}}{\sqrt{P_{s2}^2 + Q_{s2}^2}} \tag{6.35}$$

As can be seen, the maximum load P_{max} presenting a lagging PF of 0.9 that is included in the operating domain is 56% of the full active load. Accordingly, step changes in the load from 25% up to 100% of the maximum active power P_{max} are performed on the generator. Results are collected in Figure 6.9.

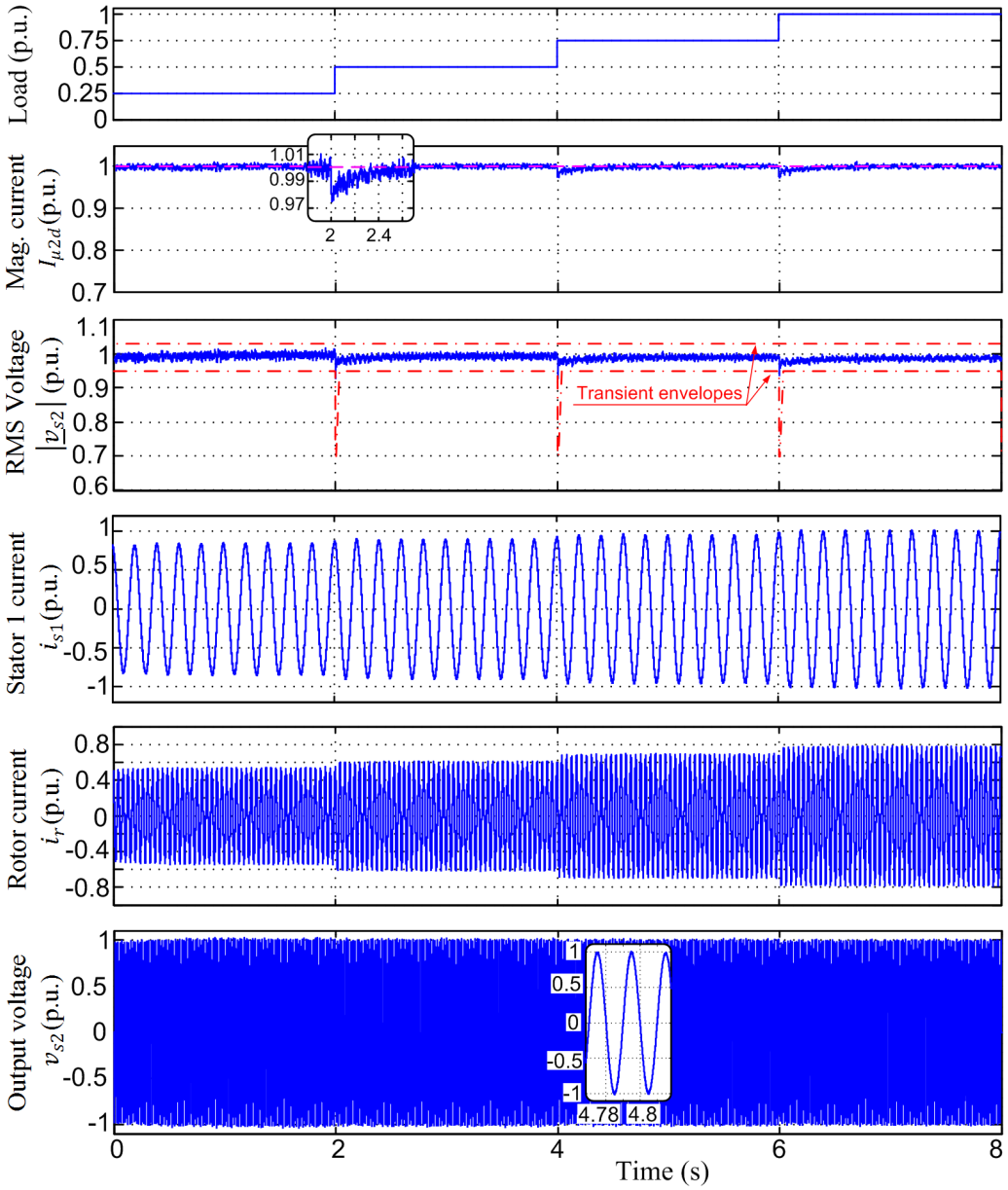

Figure 6.9: Response of the CDFIG under load variation

As observed, the magnetizing current is keeping good track of its reference value

despite load variations. Small disturbances occur after step changes in the load due to a temporary loss of orientation that is immediately compensated. The output voltage is properly controlled at constant frequency and magnitude pursuant to the grid code imposed by BS EN 2282, with a relative steady state error $< 3\%$. This small deviation in the magnitude derives from the neglect of R_{s2} in expression (6.15). The evolution of the Control machine stator current and the rotor current regarding the load variation is further illustrated. As the connected load increases, a greater current is required to maintain a constant output voltage. The control of the CDFIG is also tested under more severe load variations. The results are shown in Figure 6.10. They are satisfactory and comply with the requirements.

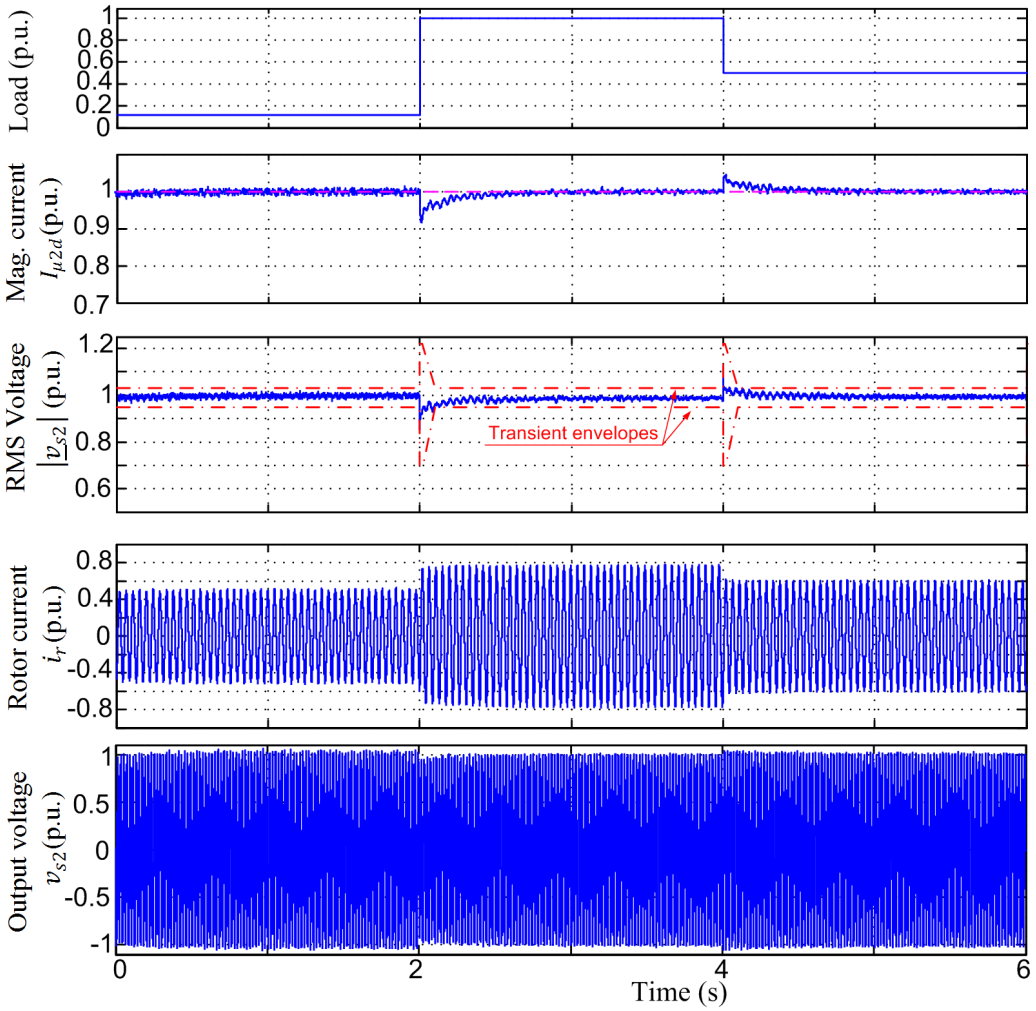

Figure 6.10: Response of the CDFIG under severe load variation

6.3.2 Simulation with speed variation

The simulation is performed at 90% of P_{max} with speed varying between -30% and $+30\%$ of the synchronous speed ($\Omega_s = 1$p.u.). The response of the CDFIG to

speed variations is illustrated in Figure 6.11.

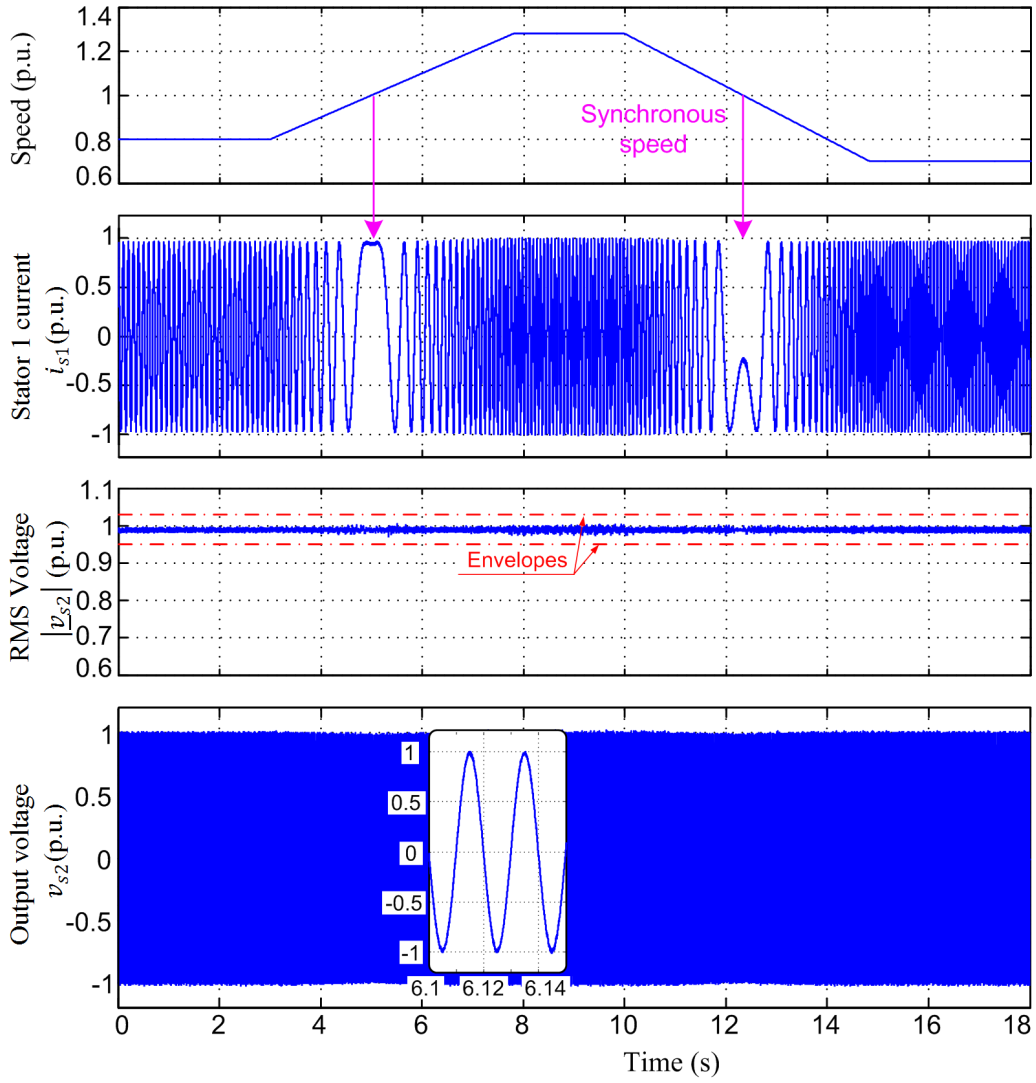

Figure 6.11: Response of the CDFIG under speed variation

It can be deduced that a variable speed constant frequency operation is achieved since the grid frequency is maintained constant (equal to 1p.u.) regardless of speed variations. Furthermore the speed disturbance is properly rejected by the controller so the voltage amplitude is kept within steady state limits imposed by BS EN 2282. The machine operates in both subsynchronous and supersynchronous modes and stator-1 frequency ω_{s1} is adapted to compensate any speed variation.

6.4 Experiments

Experiments are performed on the laboratory scale machine to validate the performance of the proposed control strategy. Two tests are conducted: control with load variation and with speed variation. In order to simplify the implementation

of the control algorithm and reduce the execution time, the compensation terms are discarded. The PI controllers are able to suppress the d-q perturbation effects.
An incremental encoder of 4096 pulses per revolution (ppr) is mounted on the shaft to detect the rotor position. It should be noted that the absolute rotor positions are required for the transformation of the machine variables to the (dq_2) reference frame. The initial rotor position of each DFIM is thus needed to obtain correct alignment.

6.4.1 Experiments under load variation

The first test is done at constant speed ($\Omega = 1.1$p.u.) with a resistive load varying from 25% up to 100% of the nominal stator current. The experimental results are collected in Figure 6.12.

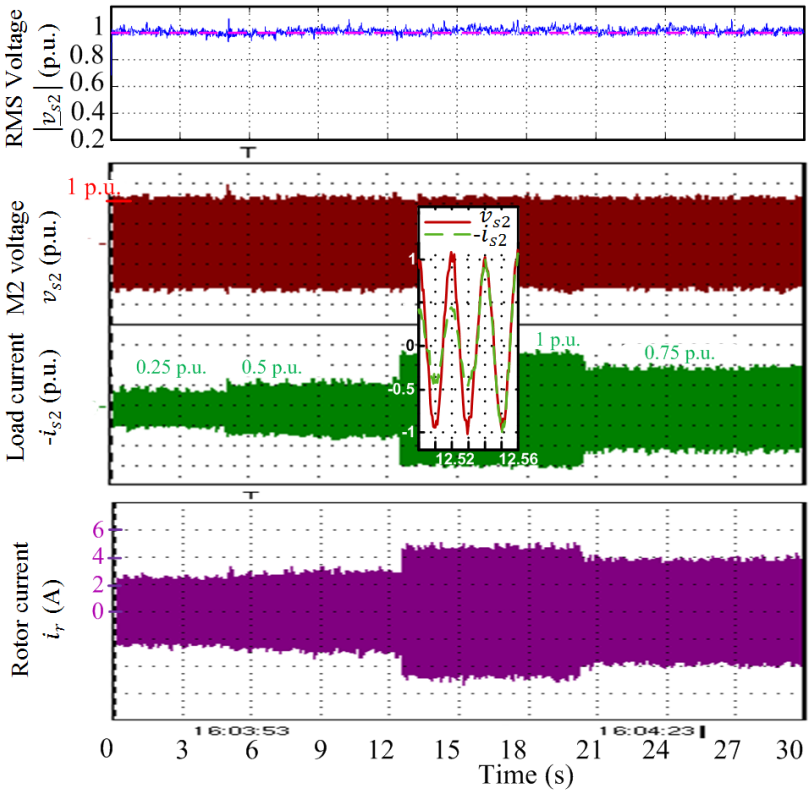

Figure 6.12: Experimental results under load variation

The output voltage is properly controlled at constant frequency and magnitude. The voltage amplitude remains equal to its reference despite the load variation. The rotor current responds correctly to the load change. As expected, the rotor current increases when the load increases.

6.4.2 Experiments under speed variation

The test is done at 50% of nominal stator current. The machine is tested in both subsynchronous and supersynchronous modes. The speed goes from $1.1\Omega_s$ down to $0.8\Omega_s$ and then increases to $1.2\Omega_s$. The experimental measurements are given in Figure 6.13.

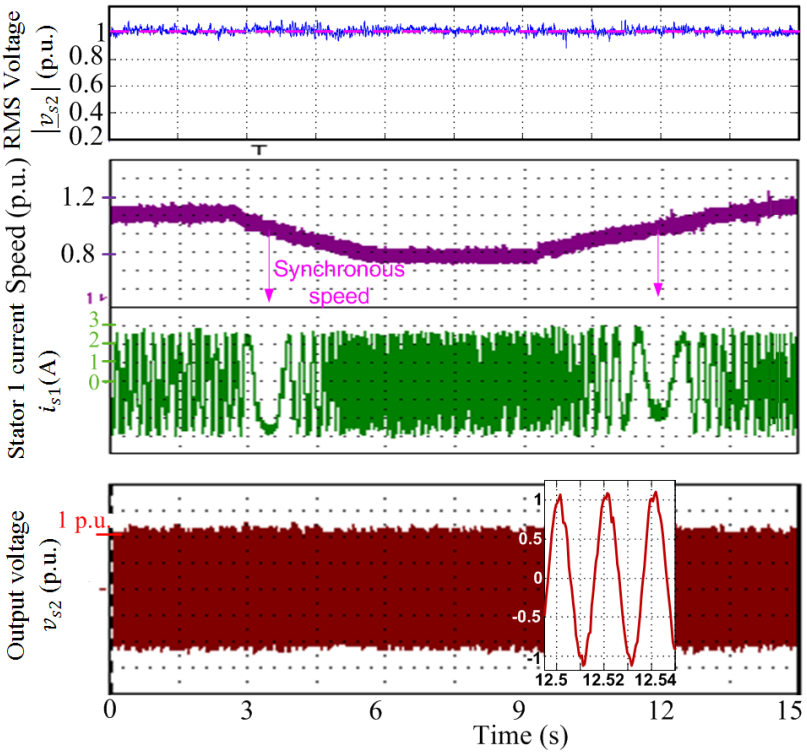

Figure 6.13: Experimental results under speed variation

The results show the precise tracking of the voltage amplitude to its reference. The speed disturbance is properly rejected by the controller. The grid frequency is maintained constant in spite of speed variation. The Control machine stator current reacts correctly, its frequency is adapted to compensate any speed change.

6.5 Impact of load imbalance

The previous results consider normal grid conditions. The generator supplies three-phase balanced load. However in standalone isolated applications, unsymmetrical conditions such as unbalanced loads happen much more frequently [103]. As a consequence, the performance of the controller under imbalance operation is to be considered. Two types of unbalance may occur at the stator terminals[103]:

– type I: one-phase imbalance where one phase load impedance unequals the two others,

– type II: three-phase imbalance with three unequal load impedances.

Hereinafter, the generator is tested under three-phase unbalanced load condition (type II with 70% load imbalance i.e. $Z_a = Z_n, Z_b = Z_a/0.3$ and $Z_c = Z_b/0.3$). The generator is first operating at normal grid conditions (balanced load). Then at $t = 2$s, unbalanced load is introduced. The generator is driven at $\Omega = 1.1$p.u. The simulation results are collected in Figure 6.14.

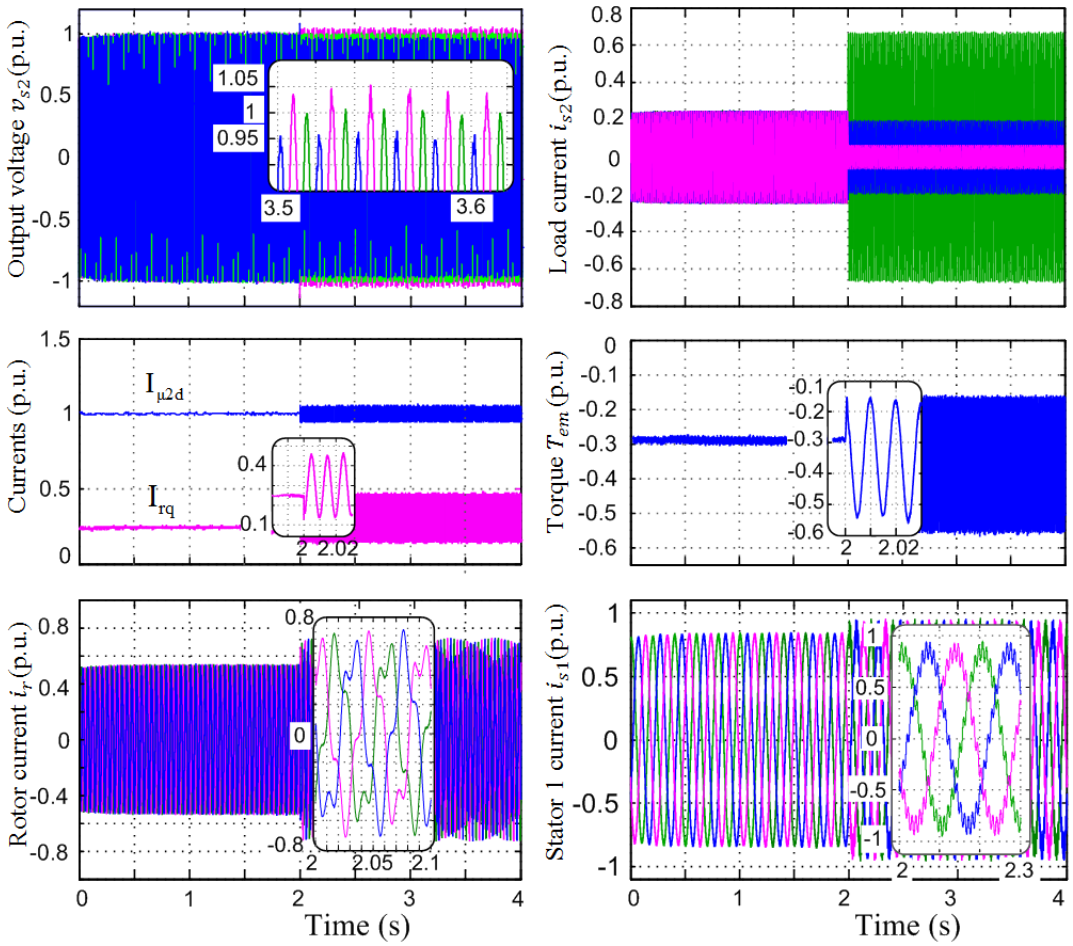

Figure 6.14: Response of the CDFIG under load imbalance

As can be seen, the quantities in the (dq_2) frame are no longer constant. They include a DC component and an AC component at double the output frequency $2\omega_{s2}$. The rotor and the control stator currents are distorted. Besides, the presence of unbalanced loads causes torque pulsations on the generator at twice the supply frequency, unbalanced load current, and output voltage imbalance (voltage unbalance factor of 8%) that degrades the dynamic performance of the control system. This behavior arises from the existence of a negative sequence component, and will be detailed and explained in the next chapter. The results confirm that the traditional vector control approach is unable to compensate the output voltage unbalance induced by the connected unbalanced load. Therefore, improved control methods of the CDFIG are to be

implemented.

Conclusion

The modeling and control of a standalone variable speed CDFIG feeding an isolated load at constant voltage and frequency is investigated in this chapter. The application for embedded aircraft power generation system is considered. Despite the complex structure of the generator, an efficient controller design is elaborated with just two cascaded loops. Decoupled vector control using stator field orientation is implemented for the regulation of the output stator voltage. In this approach, the Power machine stator flux is controlled instead of the voltage amplitude by action on the rotor current d-component; whereas the q-component is adjusted to force the orientation of the reference frame. The indirect orientation reduces the voltage harmonics and protects the frame angle from measurement noise. Simulations performed under a wide range of load and speed variations validate the effectiveness of the proposed strategy. Experiments are performed on the laboratory scale CDFIM as well. The experimental results attest the control performance.

The study is extended to reveal the behavior of the controlled system under unbalanced load. It is shown that under such conditions, the traditional vector strategy with PI controllers involves torque pulsations, current distortion and output voltage unbalance due to the effect of the negative sequence component. Therefore more accurate compensation methods and advanced control techniques are required to balance the stator output voltage.

Chapter 7

CDFIG Feeding Unbalanced Load

Introduction

This chapter addresses the imbalance issue of a standalone CDFIG caused by unbalanced loads at the stator terminals. Under this operating condition, the Power machine stator voltage will be unbalanced due to the load effect. Two compensation methods are proposed to balance the output voltage. The first approach is an improved form of the traditional vector control strategy with conventional PI controllers. It is based on a dual rotating reference frames, called positive and negative frame, to control simultaneously the positive and the negative sequence components of the machine quantities. The second proposed compensation strategy deals with only one rotating frame. It is developed based on a repetitive control method implemented in the rotor current controller.

The chapter is organized as follows. Section 7.1 analyzes the unbalance problems of the CDFIG during unbalanced operation conditions. The behavior of the generator under unbalanced connected load is validated by experimental measurements. Then, the two proposed methods for controlling the unbalanced system are discussed sequentially in sections 7.2 and 7.3 and tested by simulation with Matlab/Simulink.

7.1 Analysis of the CDFIG under unbalanced grid conditions

Standalone generators are generally characterized by their weak networks and unsymmetrical conditions such as network disturbances, unbalanced grid voltages or unbalanced loads. As reported in [42], [83], induction machines are sensitive to unbalanced operation. It is the source of heating problems and reduced efficiency. In fact, large stator current imbalance is induced due to the negative sequence component.

The unbalanced current gives rise to unbalanced heating in the machine windings, leading to faster thermal aging. Unbalanced conditions also generate pulsations in the reactive power and electrical torque at twice the supply frequency, which increase the mechanical stress and the acoustic noise [23].

7.1.1 Unbalanced output stator voltage

The connection of unbalanced loads to the stator terminals of a standalone generator induces unbalanced three-phase voltage at the PCC due to the unbalanced load current [104]. The connection interface between the CDFIG and different load types at the PCC is illustrated in Figure 7.1. The unbalanced load current i_{UL} causes an unbalanced voltage drop v_U across the internal stator impedance of the CDFIG, which results in unbalanced stator voltage at the PCC.

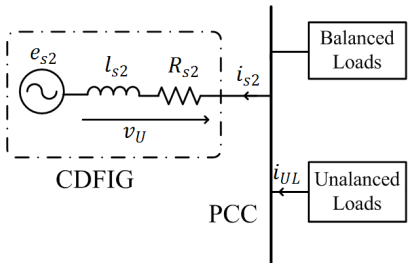

Figure 7.1: Connection interface at the PCC

If such voltage imbalance is not taken into consideration in standalone operation, it seriously reduces the quality of stator voltage of the CDFIG. Thus the overall performance of the system will be considerably degraded, which disturbs the behavior and response of the generator and other connected loads. Accordingly, an appropriate control of the terminal stator voltage of the CDFIG is required to compensate the voltage imbalance and improve the voltage quality of the standalone generator.

7.1.2 Behavior of the CDFIG under unbalanced conditions

Assuming no zero-sequence components (the neutral point is not grounded), a three-phase quantity is decomposed into positive and negative sequence components when unbalanced operation occurs. In the stationary ($\alpha\beta_{s2}$) reference frame, the positive sequence component operates at ω_{s2} and the negative sequence component evolves at $-\omega_{s2}$ [98], [147]. Thus, any unbalanced vector can be written in terms of its positive and negative sequence components as follows in ($\alpha\beta_{s2}$) frame. $\underline{x}$ represents the voltage, current or flux. The superscripts + and − represent the positive and

negative components.

$$\underline{x} = \underline{x}^{+} + \underline{x}^{-} \tag{7.1}$$
$$= \sqrt{2}X^{+}e^{j(\omega_{s2}t+\varphi^{+})} + \sqrt{2}X^{-}e^{-j(\omega_{s2}t+\varphi^{-})} \tag{7.2}$$

X^{+} and X^{-} are respectively the RMS values of the positive and negative sequence components of quantity x, and φ^{+} and φ^{-} the phase shifts.

In order to describe the behavior of the CDFIG under unbalanced conditions, two rotating frames are introduced: The positive reference frame $\left(dq_2^{+}\right)$ rotating at an angular speed ω_{s2}, and the negative reference frame $\left(dq_2^{-}\right)$ that turns at $-\omega_{s2}$ [103], [147]. The different reference frames are depicted in Figure 7.2. The stationary stator frame ($\alpha\beta_{s2}$), the positive rotating frame $\left(dq_2^{+}\right)$ and the negative rotating frame $\left(dq_2^{-}\right)$ are identified.

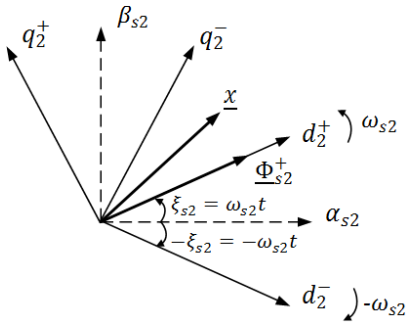

Figure 7.2: Vector diagram describing the dual rotating frames

The transformation from one reference frame to the other is given in (7.3) and (7.4).

$$(\underline{x})_{dq_2^{+}} = e^{-j\omega_{s2}t}(\underline{x})_{\alpha\beta_{s2}} = e^{-j2\omega_{s2}t}(\underline{x})_{dq_2^{-}} \tag{7.3}$$
$$(\underline{x})_{dq_2^{-}} = e^{j\omega_{s2}t}(\underline{x})_{\alpha\beta_{s2}} = e^{j2\omega_{s2}t}(\underline{x})_{dq_2^{+}} \tag{7.4}$$

Taking into account the positive and the negative sequence components, the vector $\underline{x}$ can be expressed by (7.5) and (7.6) in each rotating frame.

$$(\underline{x})_{dq_2^{+}} = (\underline{x}^{+})_{dq_2^{+}} + (\underline{x}^{-})_{dq_2^{+}} = (\underline{x}^{+})_{dq_2^{+}} + e^{-j2\omega_{s2}t}(\underline{x}^{-})_{dq_2^{-}} \tag{7.5}$$
$$(\underline{x})_{dq_2^{-}} = (\underline{x}^{+})_{dq_2^{-}} + (\underline{x}^{-})_{dq_2^{-}} = e^{j2\omega_{s2}t}(\underline{x}^{+})_{dq_2^{+}} + (\underline{x}^{-})_{dq_2^{-}} \tag{7.6}$$

Applying (7.3)-(7.6) to (7.2), the voltage, current, and flux quantities are then expressed by (7.7) and (7.8) in the positive and the negative synchronous rotating

frames.

$$(\underline{x})_{dq_2^+} = \sqrt{2}X^+ e^{j\varphi^+} + \sqrt{2}X^- e^{-j(2\omega_{s2}t+\varphi^-)} \tag{7.7}$$

$$(\underline{x})_{dq_2^-} = \sqrt{2}X^+ e^{j(2\omega_{s2}t+\varphi^+)} + \sqrt{2}X^- e^{-j\varphi^-} \tag{7.8}$$

As shown in (7.7) and (7.8), the vector $\underline{x}$ in the $\left(dq_2^+\right)$ or $\left(dq_2^-\right)$ frame is the sum of a DC component and an AC component at twice the synchronous frequency. In the positive rotating frame, the positive sequence component is a DC component and the negative sequence component produces an AC component with a resulting frequency of $-2\omega_{s2}$. When referred to the negative rotating frame, the resulting frequencies of the positive and negative sequence components are $2\omega_{s2}$ and 0 (DC) respectively. In the rotor and the Control machine coordinates the frequency of the negative sequence component will be $\omega_r^- = -\omega_{s2} - p_2\Omega$ and $\omega_{s1}^- = \Sigma p\Omega + \omega_{s2}$ respectively. Thus the resultant current and voltage quantities are distorted. The operation of the positive and negative components in each frame is resumed in Table 7.1. A low pass filter or a notch filter tuned at twice of the synchronous frequency, can be used to extract the DC component in the $\left(dq_2^+\right)$ or $\left(dq_2^-\right)$ reference frame [103].

Reference frame	$\alpha\beta_{s2}$	dq_2^+	dq_2^-	$\alpha\beta_r$	$\alpha\beta_{s1}$
Positive sequence	ω_{s2}	0	$2\omega_{s2}$	$\omega_{s2} - p_2\Omega$	$\Sigma p\Omega - \omega_{s2}$
Negative sequence	$-\omega_{s2}$	$-2\omega_{s2}$	0	$-\omega_{s2} - p_2\Omega$	$\Sigma p\Omega + \omega_{s2}$

Table 7.1: Analysis of the positive and negative sequence components

Moreover, to explain the torque pulsation during unbalanced operation, the electromagnetic torque of the CDFIG is recalled in (7.9)

$$T_{em} = T_{em1} + T_{em2} \tag{7.9}$$

with

$$T_{em1} = -\frac{3}{2}p_1 M_{sr1} \Im\left\{(\hat{\underline{i}}_{s1})_{dq_2^+} (\underline{i}_r)_{dq_2^+}\right\} \tag{7.10}$$

$$T_{em2} = \frac{3}{2}p_2 M_{sr2} \Im\left\{(\underline{i}_{s2})_{dq_2^+} (\hat{\underline{i}}_r)_{dq_2^+}\right\} \tag{7.11}$$

Applying (7.7) to the stator and rotor currents results in the following electromagnetic torque expressions:

$$T_{em1}=-\frac{3}{2}p_1 M_{sr1}\Im\left\{2I_{s1}^{+}I_r^{+}e^{j(\varphi_r^{+}-\varphi_1^{+})}+2I_{s1}^{-}I_r^{-}e^{j(\varphi_1^{-}-\varphi_r^{-})}\right.$$
$$\left.+\ 2I_{s1}^{-}I_r^{+}e^{j(2\omega_{s2}t+\varphi_1^{-}+\varphi_r^{+})}+2I_{s1}^{+}I_r^{-}e^{-j(2\omega_{s2}t+\varphi_r^{-}+\varphi_1^{+})}\right\} \quad (7.12)$$

$$T_{em2}=\frac{3}{2}p_2 M_{sr2}\Im\left\{2I_{s2}^{+}I_r^{+}e^{j(\varphi_2^{+}-\varphi_r^{+})}+2I_{s2}^{-}I_r^{-}e^{j(\varphi_r^{-}-\varphi_2^{-})}\right.$$
$$\left.+\ 2I_{s2}^{+}I_r^{-}e^{j(2\omega_{s2}t+\varphi_r^{-}+\varphi_2^{+})}+2I_{s2}^{-}I_r^{+}e^{-j(2\omega_{s2}t+\varphi_2^{-}+\varphi_r^{+})}\right\} \quad (7.13)$$

As noted in (7.12) and (7.13), T_{em} comprises DC terms arising from the interaction between the stator and rotor currents of the same sequence (i.e. (i_s^+, i_r^+) and (i_s^-, i_r^-)), together with oscillating terms at double supply frequency due to the interaction between the quantities of opposite sequence (i_s^+, i_r^-) and (i_s^-, i_r^+). The same procedure can be followed to reveal the oscillations in the active and reactive powers. It can be concluded that when the grid is unbalanced, the power and torque will oscillate around a non-zero average value, the Power machine current and voltage are unbalanced, while the rotor and the Control machine current and voltage are distorted.

The control of the MSC does not provide enough degrees of freedom to achieve several control targets simultaneously. For instance, reduce or eliminate the torque and power pulsation, eliminate the negative sequence component of the rotor voltage and current and eliminate the stator current and voltage imbalance.
The operation of a grid-connected doubly fed induction machines (DFIG and CDFIG) under unbalanced supply voltage have been treated in the literature. Under such conditions, induction generators are normally switched out of the network for their own protection. This can further weaken the grid. Therefore, control methods are investigated in order to reduce the torque pulsation [28], [55], active and reactive power pulsations [22],[123], and/or power stator current imbalance that normally occur when the network is unbalanced [23], [39], [147], [143]. This will allow the generator to remain connected to the grid and meet the demanding requirements of grid codes. However, in an unbalanced standalone application, the main concern is to control and balance the output voltage in order to preserve the overall dynamic system performance and protect the behavior of other connected loads [104]. Accordingly, the development of an appropriate control strategy is required to reject the impact of unbalanced load on the stator voltages at the PCC.

In order to balance the output voltage, the negative sequence component of the generated stator voltage must be detected and eliminated by injecting the appropriate negative component of the rotor current. The traditional vector control scheme in the positive synchronous frame using conventional PI controllers does not provide the desired performance and induces tracking errors. In fact, the reference control variables

are composed of the negative sequence component at twice the supply frequency that PI controller cannot regulate precisely due to its limited bandwidth. Therefore, to increase the control accuracy and enhance the compensation capability, new strategies are to be implemented due to the effect of the negative sequence component. In the following sections two new control algorithms for an autonomous CDFIG supplying unbalanced loads are elaborated. The proposed control methods are performed in the MSC to compensate the output stator voltage imbalance. The first compensation method uses both the positive and negative synchronous reference frames of the CDFIG to control respectively the positive and the negative sequence components of the rotor current. The second strategy is based on a repetitive controller implemented in the rotor current loop. It is developed to increase the current control bandwidth and enhance the control accuracy and system stability. The whole scheme is implemented in the positive rotating frame where no sequential decomposition of the rotor current is needed.

7.1.3 Experiments

The behavior of the CDFIG under unbalanced condition is evaluated experimentally. Unbalanced load is connected to the generator (60% load imbalance). The results are collected in Figure 7.3. As observed, the output stator current and voltage are unbalanced. The rotor and Control machine current are distorted due to the influence of the negative sequence component. It shall be noted that the voltage and current waveform comply perfectly with those obtained by simulations (refer to Figure 6.14).

7.2 Unbalanced voltage compensation strategy based on dual rotating frames

The proposed strategy uses the two rotating reference frames $\left(dq_2^+\right)$ and $\left(dq_2^-\right)$ to control both the positive and negative sequences of the rotor current. The strategy adopted has a main controller implemented in $\left(dq_2^+\right)$ frame and an auxiliary controller implemented in $\left(dq_2^-\right)$ frame. In the positive synchronous frame, the positive sequence current controller aims to regulate the output stator voltage magnitude and frequency of the CDFIG. In the negative synchronous frame, the rotor current negative sequence is regulated to eliminate the voltage imbalance (i.e. compensate the stator voltage negative sequence).

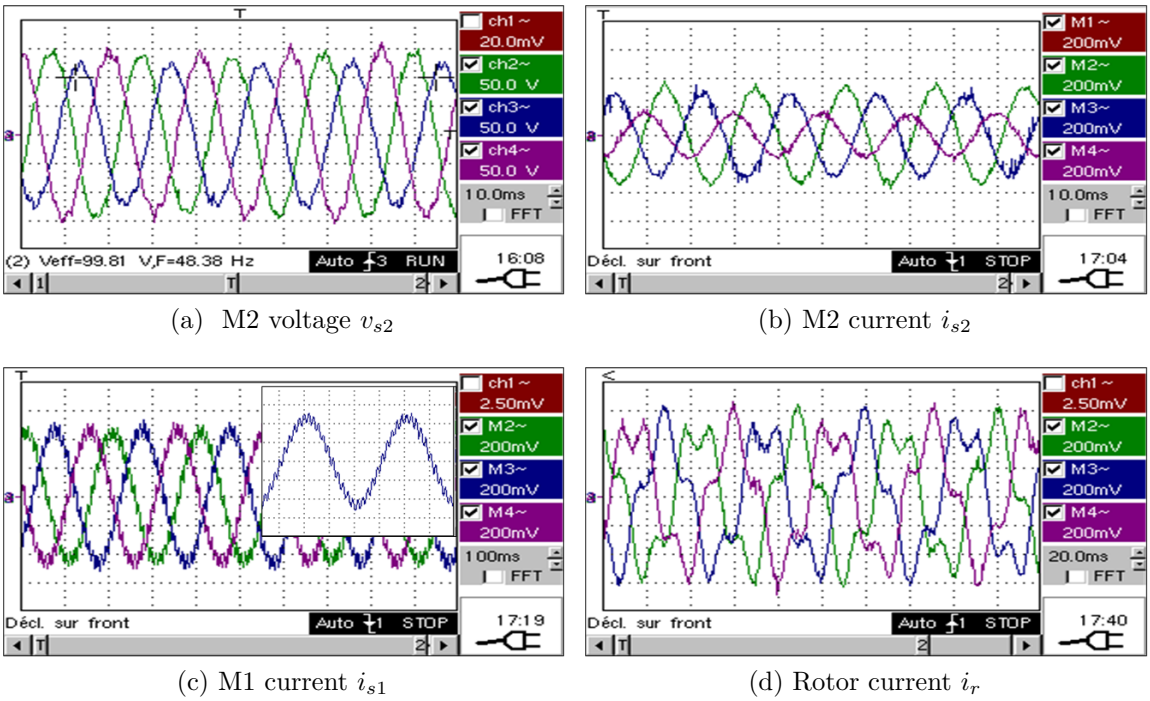

(a) M2 voltage v_{s2} (b) M2 current i_{s2}

(c) M1 current i_{s1} (d) Rotor current i_r

Figure 7.3: Experimental results during unbalanced load conditions

7.2.1 Control in the positive reference frame

The dynamic behavior of the CDFIG in the positive rotating frame $\left(dq_2^+\right)$ is given by (6.1)-(6.6). The control system for positive sequence components is designed in the same way as the conventional method presented in section 6.2, when no imbalance is considered. The cascaded control loops using PI controllers are illustrated by the block diagram in Figure 7.4.

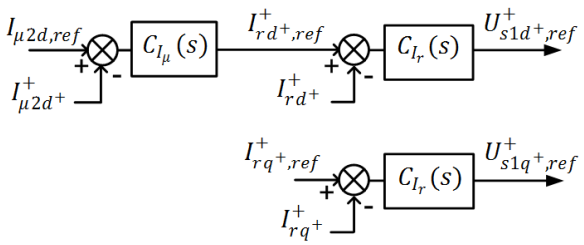

Figure 7.4: Control of the positive components in the positive rotating frame

The subscripts + and − are related to the positive and negative synchronous reference frames, respectively. Thus, the quantities $X^+_{d^+}$ and $X^+_{q^+}$ are the d-q axis components of positive sequence in the positive reference frame. As shown in Figure 7.4, the direct rotor current $I^+_{rd^+}$ in the positive reference frame regulates the stator magnetizing current which induces the stator voltage magnitude. The magnetizing current demand

is derived by (7.14)

$$I_{\mu 2d,ref} = \frac{\left|\underline{v}_{s2}^{+}\right|_{ref}}{L_{s2}\omega_{s2,ref}} \tag{7.14}$$

The output of the stator magnetizing current PI controller forms the d-axis positive sequence component of the rotor reference current $I_{rd^+,ref}^{+}$. The q-axis rotor current $I_{rq^+}^{+}$ forces the orientation of the reference frame along the positive sequence of the stator flux $\underline{\Phi}_{s2}^{+}$. The q-axis rotor reference current is computed as:

$$I_{rq^+,ref}^{+} = -\frac{L_{s2}}{M_{sr2}} I_{s2q^+}^{+} \tag{7.15}$$

The inner rotor current control loop generates the *d-q* positive sequence components of the Control machine reference stator voltage, $U_{s1d^+,ref}^{+}$ and $U_{s1q^+,ref}^{+}$, in the $\left(dq_2^{+}\right)$ synchronous frame.

7.2.2 Control in the negative reference frame

The negative sequence current is controlled in order to eliminate the negative sequence component of the output stator voltage. In the negative synchronous frame $\left(dq_2^{-}\right)$, the dynamic behavior of the CDFIG is described by the following equations:

$$\underline{v}_{s2} = R_{s2}\underline{i}_{s2} + \frac{d}{dt}\underline{\Phi}_{s2} - j\omega_{s2}\underline{\Phi}_{s2} \tag{7.16}$$

$$\underline{v}_{s1} = R_{s1}\underline{i}_{s1} + \frac{d}{dt}\underline{\Phi}_{s1} + j\left(-\omega_{s2} - \Sigma p\Omega\right)\underline{\Phi}_{s1} \tag{7.17}$$

$$0 = R_r\underline{i}_r + \frac{d}{dt}\underline{\Phi}_r + j\left(-\omega_{s2} - p_2\Omega\right)\underline{\Phi}_r \tag{7.18}$$

$$\underline{\Phi}_{s2} = L_{s2}\underline{i}_{s2} + M_{sr2}\underline{i}_r = L_{s2}\underline{i}_{\mu 2} \tag{7.19}$$

$$\underline{\Phi}_{s1} = L_{s1}\underline{i}_{s1} - M_{sr1}\underline{i}_r \tag{7.20}$$

$$\underline{\Phi}_r = L_r\underline{i}_r + M_{sr2}\underline{i}_{s2} - M_{sr1}\underline{i}_{s1} \tag{7.21}$$

As can be noticed, the machine has similar behavior as in the positive rotating frame. Thus, following a similar approach to the positive frame, relationships between the negative components can be computed in the negative synchronous frame. The open-loop transfer function to be regulated is derived in Figure 7.5.

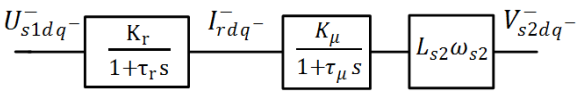

Figure 7.5: Open loop transfer function in the negative synchronous frame

As can be deduced, the negative sequence components of the stator voltage $V_{s2d^-}^{-}$ and

$V^-_{s2q^-}$ can be regulated to zero by action on the negative sequence *d-q* components of the rotor current $I^-_{rd^-}$ and $I^-_{rq^-}$ respectively. The latter are adjusted through the regulation of the Control machine stator voltage negative components $U^-_{s1d^-}$ and $U^-_{s1q^-}$. Accordingly, a decoupled vector control with two nested loops is implemented in the negative rotating frame using PI controllers. An outer loop adjusts the negative sequence *d-q* components of the stator voltage. The reference values are set to zero. The outputs of the voltage loop controllers are the negative sequence component references of the rotor current $I^-_{rd^-,ref}$ and $I^-_{rq^-,ref}$. The inner loop controls the rotor current and forms the negative sequence component references of the Control machine stator voltages $U^-_{s1d^-,ref}$ and $U^-_{s1q^-,ref}$. The cascaded control scheme of the negative components in the negative rotating frame is illustrated in Figure 7.6.

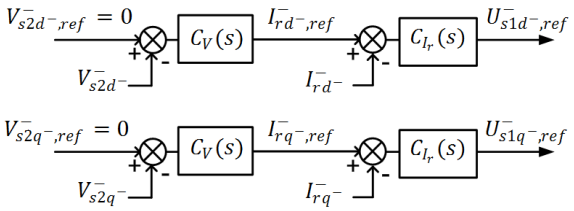

Figure 7.6: Control of the negative components in the negative rotating frame

7.2.3 Overall control scheme

In the proposed compensation method, both positive and negative sequence components have to be extracted from the voltages, currents, and flux. As the decomposition process involves significant time delays and adds amplitude and phase errors to the signals, the performance and stability of the system can be reduced especially under transient conditions [142]. In this regard, an improved form of the control algorithm is presented. The main controller can be implemented in the positive synchronous frame $\left(dq_2^+\right)$ without involving positive and negative sequence separation i.e. $I_{rdq^+}, I_{\mu 2d^+}$ are controlled instead of $I^+_{rdq^+}, I^+_{\mu 2d^+}$. While for the auxiliary controller, it is designed specifically to regulate the stator voltage negative component and is implemented in the negative rotating frame $\left(dq_2^-\right)$ with negative sequence components extracted. The overall control scheme of the standalone CDFIG with stator voltage compensation based on the dual rotating frame technique is shown in Figure 7.7. The two hierarchical vector controls, for the main and the auxiliary controllers, implemented on each rotating frame are identified. Based on the measured values of the Power machine stator voltage and current, the stator flux and the rotor current are estimated using (6.30) and (6.31). From the Park frame angles $\xi_{s2} = \int \omega_{s2,ref} dt$ and $-\xi_{s2}$, the quantities can be referred to the two synchronous

rotating frames $\left(dq_2^+\right)$ and $\left(dq_2^-\right)$ respectively according to the vector transformation relations established in (7.3) and (7.4).

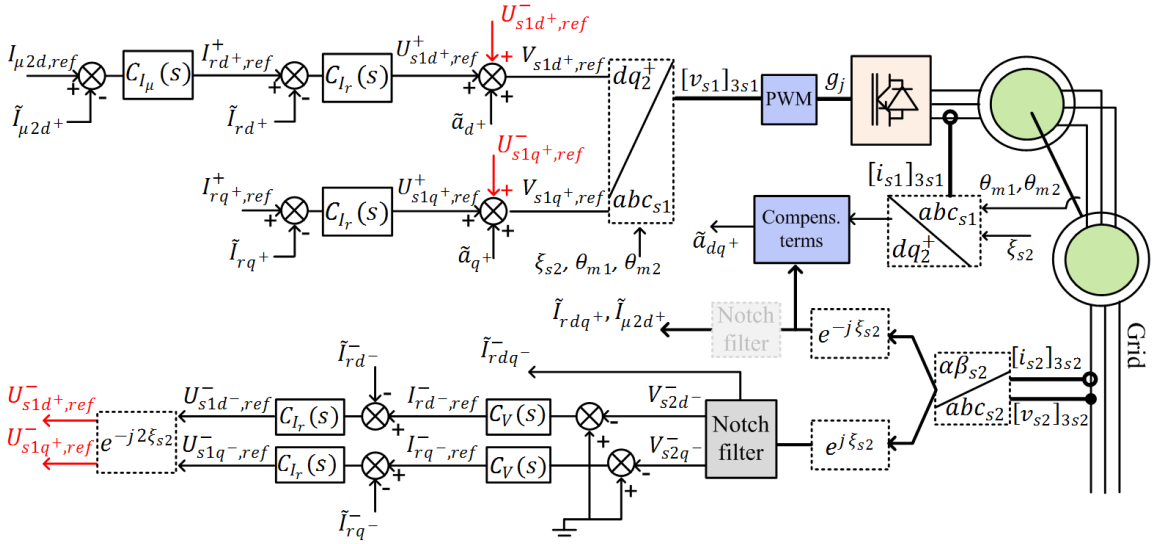

Figure 7.7: Improved control scheme of the CDFIG in a dual rotating frame

The double frequency AC components are eliminated by using notch filters tuned at $2\omega_{s2}$. A typical second order notch filter is given by the transfer function (7.22).

$$F(s) = \frac{s^2 + \omega_z^2}{s^2 + \frac{\omega_c}{Q_f}s + \omega_c^2} \tag{7.22}$$

Numerically, $\omega_z = \omega_c = 2\omega_{s2}$; $Q_f = 0.1$.
The negative sequence reference voltages at the output of the auxiliary controller $U^-_{s1d^-,ref}$ and $U^-_{s1q^-,ref}$ are in the $\left(dq_2^-\right)$ rotating reference frame. Referring to (7.3), these voltages are transformed into positive coordinates $\left(dq_2^+\right)$ using the angle $2\xi_{s2}$ as follows:

$$U^-_{s1d^+,ref} + jU^-_{s1q^+,ref} = e^{-j2\xi_{s2}}\left(U^-_{s1d^-,ref} + jU^-_{s1q^-,ref}\right) \tag{7.23}$$

The resultant control stator reference voltage is the combination of the outputs from the main and the auxiliary controllers. Thus, in $\left(dq_2^+\right)$ it will be the sum of the positive and negative sequence references, i.e. the AC and DC components, obtained as:

$$U_{s1d^+,ref} = U^+_{s1d^+,ref} + U^-_{s1d^+,ref} \tag{7.24}$$

$$U_{s1q^+,ref} = U^+_{s1q^+,ref} + U^-_{s1q^+,ref} \tag{7.25}$$

Compensation terms $\tilde{a}_{d^+}$, $\tilde{a}_{q^+}$ are added by feed-forward action. Finally the Con-

trol machine stator voltage references are transformed back into (abc_{s1}) coordinate using (6.34).

7.2.4 Simulation results

Simulation test is performed on Matlab/Simulink in order to verify the behavior of the proposed compensation method. The same load conditions of section 6.5 are considered. The results are collected in Figure 7.8.

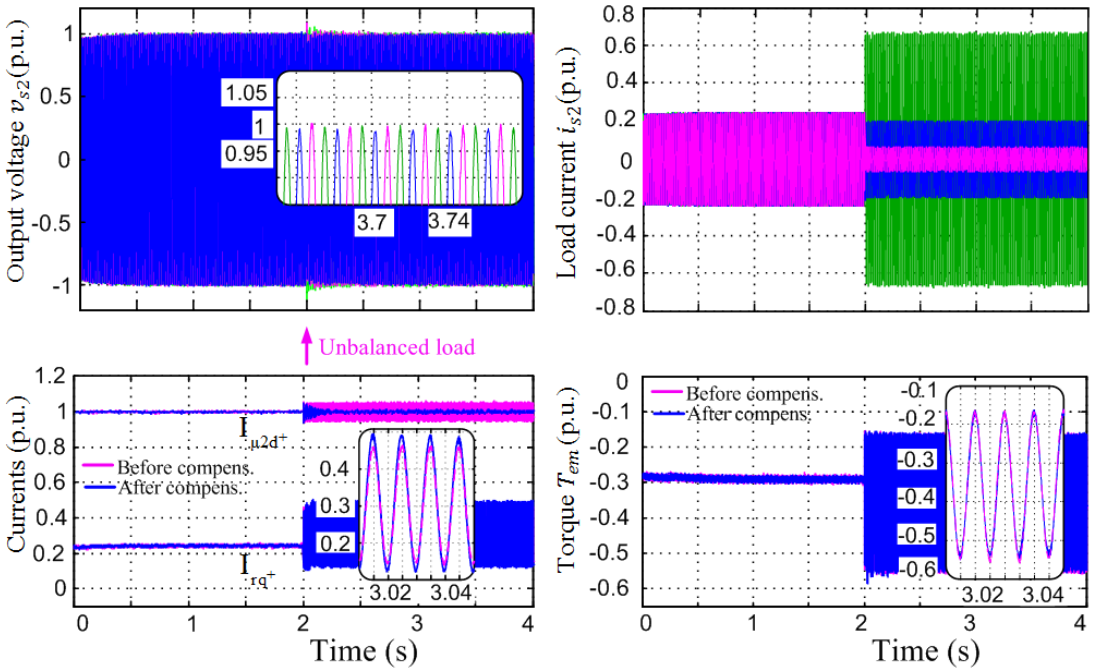

Figure 7.8: Simulation results of the proposed dual rotating frames compensation strategy

The negative sequence component of the output stator voltage is compensated in steady state. The double frequency oscillations in the magnetizing current (i.e. the voltage magnitude) is extremely reduced. Thus the generated stator voltages become balanced after applying the proposed compensation method to the MSC of the standalone CDFIG. Besides, the voltage amplitude remains equal to its set reference despite the presence of unbalanced load. The rotor current *d-q* components in the positive rotating frame consist of a DC component and an AC component at double the synchronous frequency. This is due to the fact that the proposed compensation method is based on injecting negative components into the rotor currents, in order to eliminate the stator voltage unbalance. Consequently, the three-phase rotor currents are distorted as a result of the injected negative sequence component. As mentioned before, the control of the MSC does not provide enough degrees of freedom to achieve several control targets simultaneously. Therefore the voltage compensation technique

does not eliminate the torque pulsation and the negative sequence components of the stator/rotor currents.

7.3 Compensation method using repetitive controller

The previous compensation method controls the rotor current in two separate, positive and negative, reference frames. It is based on conventional and easy to implement PI controllers, but involves frame transformations and sequential decomposition of the rotor current, which increase significantly the time delay and degrade the system stability [103]. To overcome this problem, a new control approach for the unbalanced standalone CDFIG, implemented solely in the positive rotating frame is proposed hereinafter. The rotor current control loop, based on a repetitive controller, can directly regulate both positive and negative sequence components in $\left(dq_2^+\right)$ frame without sequence separation. The suggested repetitive control is developed to increase the control bandwidth and achieve good tracking of the rotor periodic reference currents. These references are generated by an outer voltage control loop and a negative sequence component, injected to compensate the stator voltage imbalance.

The proposed voltage compensation strategy of the standalone CDFIG is presented in Figure 7.9.

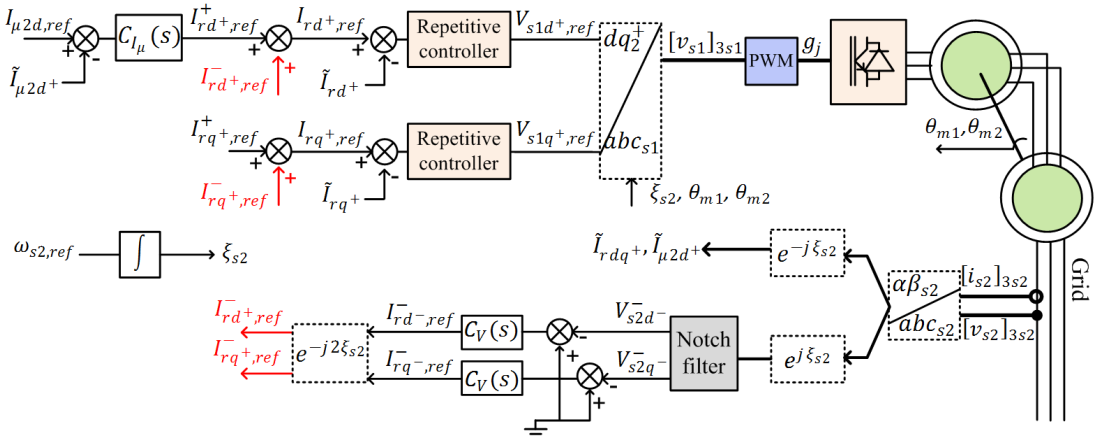

Figure 7.9: Repetitive control scheme of the CDFIG in a single rotating frame

The stator voltage negative sequence components $V^-_{s2d^-}$ and $V^-_{s2q^-}$ are regulated to zero in $\left(dq_2^-\right)$ by means of PI controllers. The outputs of these controllers form the negative component references of the rotor current $I^-_{rd^-,ref}$ and $I^-_{rq^-,ref}$ established in $\left(dq_2^-\right)$ coordinate. Theses reference currents are expressed in the positive frame using

(7.26).

$$I^{-}_{rd^{+},ref} + jI^{-}_{rq^{+},ref} = e^{-j2\xi_{s2}} \left(I^{-}_{rd^{-},ref} + jI^{-}_{rq^{-},ref} \right) \tag{7.26}$$

The principal of the proposed compensation method is to add the rotor negative reference current in the current controller. Therefore, the total rotor reference currents for the inner loop repetitive controller, implemented in the positive frame, is the sum of the positive and the negative sequence components (i.e. both AC and DC components) calculated by (7.27) and (7.28).

$$I_{rd^{+},ref} = I^{+}_{rd^{+},ref} + I^{-}_{rd^{+},ref} \tag{7.27}$$

$$I_{rq^{+},ref} = I^{+}_{rq^{+},ref} + I^{-}_{rq^{+},ref} \tag{7.28}$$

$I^{+}_{rd^{+},ref}$ is the output of the outer loop PI controller. It is implemented to control the stator magnetizing current and adjust the output voltage magnitude. $I^{+}_{rq^{+},ref}$ is given by (7.15) for the orientation of $\left(dq^{+}_{2}\right)$ d-axis along the stator flux. The outputs of the rotor current repetitive controller form the Control machine stator reference voltages $V_{s1d^{+},ref}$ and $V_{s1q^{+},ref}$ which are transformed into (abc_{s1}) coordinate using (6.34).

7.3.1 Repetitive control

The AC component of the rotor reference current $(2\omega_{s2})$ cannot be tracked precisely using classical PI controllers due to their limited bandwidth. Therefore, repetitive controllers, that offer high control bandwidth, are implemented in order to achieve good tracking of the rotor periodic reference current. The repetitive control is a useful tool to track a periodic reference input or reject a periodic disturbance, where only the signal period is required [65]. It was first introduced by Inoue, Nakano and their colleagues in 1981 [52] in order to achieve a high accuracy control of a magnetic power supply for a proton synchrotron. Then studies dealing with the stability of a repetitive control system were addressed particularly in [45], [46].

The repetitive control design is based on the internal model principle [41]. It states that the output of a stable system can track a class of reference signals with zero steady state error if the generator of these references is included in the closed-loop system. For instance, a particular common case is a step reference command. No steady state error occurs for a step input if the stable system control loop contains an integrator, which is the generator of step functions. The generator of a sinusoidal signal $\sin(2\pi t/L)$ is a resonant filter with the transfer function $\dfrac{1}{s^2 + (2\pi/L)^2}$. Thus, to ensure proper tracking of a periodic signal $r(t)$ of period L that has an infinite number of harmonic components, an infinite number of resonant filters given by (7.29)

shall be included in the control loop [149].

$$K(s) = \frac{1}{s}\prod_{n=1}^{+\infty}\frac{(2\pi n/L)^2}{s^2+(2\pi n/L)^2} \tag{7.29}$$

However, in the repetitive control approach, a simple delay in a proper feedback can be used to produce an infinite number of poles and hence simulate a bank of an infinite resonant filters. In fact, a periodic signal with period L can be generated by a linear system that includes a time delay L corresponding to the period of the signals as illustrated in Figure 7.10 [46], [149].

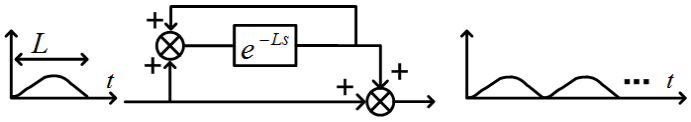

Figure 7.10: Periodic signal generator

The time delay system reported in Figure 7.10 constitutes the repetitive controller with the following transfer function.

$$K(s) = \frac{1}{1-e^{-Ls}} \tag{7.30}$$

The regulator defined in (7.30) has an infinite number of poles on the imaginary axis, at the points $\pm j2\pi n/L$ with $n = 0, 1, 2, ...$ The Bode plot of this function is depicted in Figure 7.11. It consists of a set of peaks centered at the fundamental and harmonic frequencies.

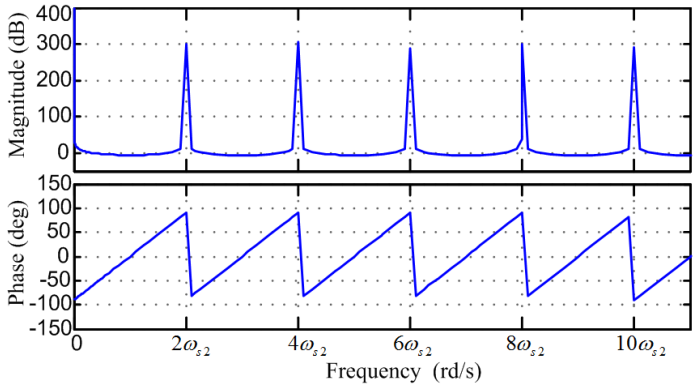

Figure 7.11: Bode diagram of the repetitive controller $K(s) = \dfrac{1}{1-e^{-\frac{2\pi}{2\omega_{s2}}s}}$

The gain at these resonant frequencies is theoretically infinite, which amplifies the high frequencies harmonics. It is proven in [45] that systems with repetitive controller, containing the regulator defined in (7.30), that can be stable are limited and do not

include strictly proper systems. In fact, in strictly proper systems, the open-loop transfer function to be regulated $G(s)$ converges to zero when the frequency tends to infinity, whilst the repetitive controller continues to create unstable poles at infinite gain in the loop [46]. Since the CDFIG is a strictly proper system, the rotor current control loop cannot be stabilized using the simple repetitive controller in (7.30). To tackle this problem, the gain of the repetitive controller has to be reduced at high frequencies. Thus, a modified repetitive controller is proposed by replacing the pure delay by $Q(s)e^{-Ls}$ [46]. The modified repetitive controller is then expressed as:

$$K(s) = \frac{1}{1 - Q(s)e^{-Ls}} \tag{7.31}$$

$Q(s)$ is a stable rational function verifying $|Q(j\omega)| \leq 1 \ \forall\omega$ [46]. A typical repetitive control system is shown in Figure 7.12. $G(s)$ is the transfer function to be regulated, $K(s)$ is the repetitive controller, $r(t)$ is the reference input, $y(t)$ is the system output and $w(t)$ the disturbance.

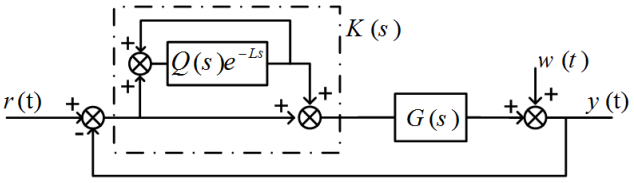

Figure 7.12: Repetitive control system

By applying the small gain theorem, the closed-loop system in Figure 7.12 is stable if the following conditions are satisfied [46]:

$$\frac{G(s)}{1 + G(s)} \text{ is proper and stable} \tag{7.32}$$

$$\left\| \frac{Q(s)}{(1 + G(s))} \right\|_\infty < 1 \tag{7.33}$$

$||.||_\infty$ denotes the H_∞-norm of a stable transfer function [40]. The above conditions imply that the design of $Q(s)$ will affect the stability and response of the controlled system. In order to ensure a stable system, it is necessary to have $|Q(j\omega)| < 1$ at high frequencies. The stability margins extend as $|Q(j\omega)|$ goes smaller. On the other hand, the tracking error is completely eliminated only if $Q(s) = 1$ at the harmonics of the reference periodic signal. Therefore, the controller design must achieve a trade-off between the system stability and tracking performance. An adequate choice of $Q(s)$ is a low pass filter which cutoff frequency ω_q delimits the rotor current harmonics. Increasing the operating bandwidth reduces the tracking error, however, the cutoff frequency should be limited by the stability condition (7.33). It should be noted

that the repetitive controller is sensitive to frequency variation since the peak gain decreases sharply at the resonant frequencies, which may degrade the performance of the control system for small variations of the input frequency [75]. To overcome this problem, a gain $K < 1$ may be added to the filter $Q(s)$ [65]. As the gain K decreases, the peak amplitude is reduced while the bandwidth of each peak increases, which increases the robustness of the controller with respect to frequency variations. However, small values of K deteriorate the tracking performance, because the desired poles for precise tracking are altered by $Q(s)$.

7.3.2 Design of the controller

Although the repetitive controller is able to track a periodic input perfectly at steady state, it does not provide the desired dynamic performance and transient response [133]. Therefore, a classic controller can be added to the closed-loop control system to stabilize the system to be controlled and adjust the transient response. This type of control is named plug-in repetitive control.
For the CDFIG, the open loop transfer function of the rotor current dynamic $G_{I_r}(s)$ in the positive rotating frame is given by (6.27). The system without regulation is stable. Here, a proportional gain k_I is cascaded to the repetitive controller for the regulation of the rotor current response. The block diagram of the proposed repetitive control system is described in Figure 7.13.

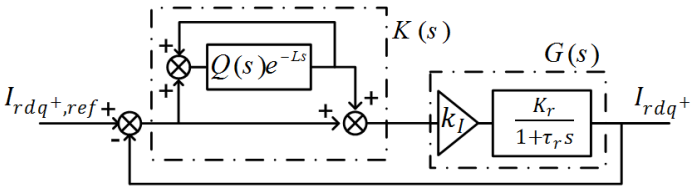

Figure 7.13: Block diagram of the rotor current loop using repetitive control

The repetitive controller is tuned at $L = 2\pi/(2\omega_{s2})$. The following low pass filter is adapted to achieve a compromise between stability and precision. Numerically $K = 0.995$ and $\omega_q = 32\omega_{s2}$.

$$Q(s) = \frac{K}{1 + \frac{s}{\omega_q}} \tag{7.34}$$

The Bode plot of the compensated open-loop transfer function $G_1(s) = k_I G_{I_r}(s) K(s)$ is shown in Figure 7.14. The rotor current waveform with respect to a periodic reference input is illustrated in Figure 7.15. As observed a small tracking error is induced due to the presence of the low pass filter in the repetitive controller.

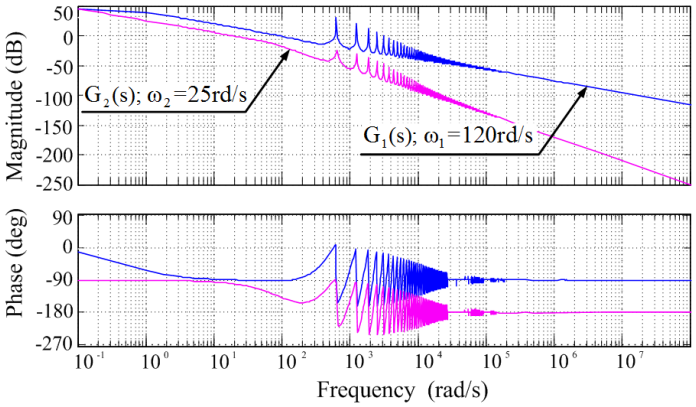

Figure 7.14: Bode plots of the compensated loops

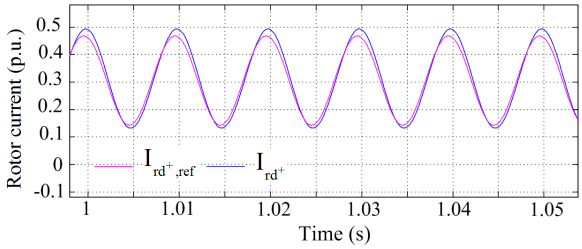

Figure 7.15: Rotor current tracking performance with the repetitive controller

For the regulation of the outer magnetizing current loop, the closed-loop dynamic of the rotor current F_{I_r} is taken into account. The block diagram is similar to Figure 6.5. A PI controller C_{I_μ} is synthesized to achieve the following specifications:

- Zero steady state error
- The cutoff frequency ω_2 of the compensated open-loop transfer function is five times smaller than the inner loop cutoff frequency ω_1.

The Bode plot of the compensated open-loop transfer function of the magnetizing current $G_2(s) = C_{I_\mu}(s)F_{I_r}(s)G_{I_\mu}(s)$ is shown in Figure 7.14.

7.3.3 Simulation results

Simulation results of the proposed compensation method are presented in Figure 7.16. As noted, the output voltage is properly controlled. The imbalance is well compensated to satisfy the control target. The rotor current tracking error is compensated by the action of the outer voltage loop. The *d-q* rotor currents are composed of both DC and AC components, in which the negative components are injected to eliminate the negative sequence components of the stator voltage. As a result, the generated voltages become balanced. The repetitive approach regulates both the positive and negative sequence rotor current components without sequential decomposing.

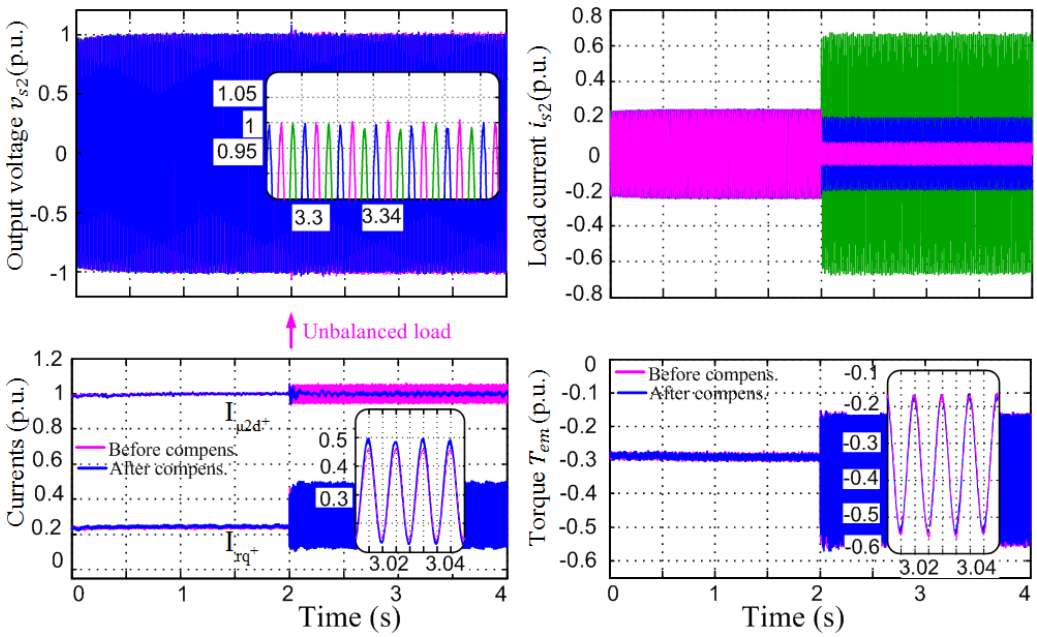

Figure 7.16: Simulation results of the proposed repetitive control compensation strategy

Conclusion

This chapter deals with the analysis and control of a standalone CDFIG connected to unbalanced loads. The unbalanced condition yields to unbalanced output voltage and generates a negative sequence component. Two compensation strategies are elaborated to eliminate the negative component and balance the output stator voltages by injecting a proper rotor current. Both elaborated methods achieve good tracking of the output voltage demand and compensation of stator voltage unbalance. The first approach uses two rotating reference frames to control separately the positive and the negative sequence components of the current. The control scheme is based on classic conventional PI controllers implemented on each axis, but it involves frame transformations and sequential decomposition of the rotor current, which can significantly increase the control time delay and degrade the system stability. To tackle this problem a second control approach for the unbalanced stand-alone CDFIG system is introduced. The method is implemented in a single positive reference frame with a repetitive controller that regulates both the positive and negative sequences of the rotor current. The two compensation strategies are tested and validated by simulation using Matlab/Simulink.

Chapter 8

CDFIG Supplying Isolated DC Loads

Introduction

The next generation aircraft systems tend to use HVDC electric distribution network. This standard is currently adopted in military aircraft platforms e.g. Boeing–Sikorsky military project Comanche RAH-66 and Lockheed F22 Raptor [53]. In this regard, the operation of the CDFIG as a standalone DC generator is investigated in this chapter. The brushless machine is connected to a diode bridge rectifier supplying an isolated load. A decoupled vector control is established to regulate the DC bus voltage. The controller aims to retain a constant output DC voltage regardless of load and speed variations.

Section 8.1 is devoted to the modeling of the autonomous DC generator. The diode bridge rectifier is modeled and the system bloc diagram is built. The regulation of the DC voltage is detailed in section 8.2. A vector control consisting of just two loops is implemented. The transient envelops of the output voltage are specified by MIL-STD-704F1 [1]. This standard specifies the electric power characteristics and requirements in military aircrafts. The control approach is validated by performing simulations on Matlab/Simulink in section 8.3.

8.1 DC generator model

The configuration of an autonomous CDFIG supplying an isolated DC grid is presented in Figure 8.1. The stator of the Power machine is cascaded with a diode bridge rectifier connected to a DC bus capacitor, whereas the stator of the Control

1. Military Standard, Department of Defense, USA: Aircraft electric Power Characteristics

machine is supplied by a bidirectional inverter allowing the generator to operate in subsynchronous and supersynchronous modes.

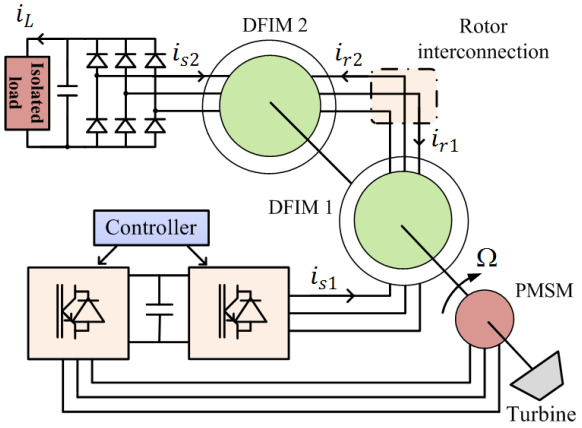

Figure 8.1: Configuration of an isolated DC grid based on a CDFIG

The set operates as a standalone DC generator connected to an isolated load in embedded aircraft systems. Note that the diode bridge could be replaced by a PWM rectifier, but the solution based on diode rectifier is more suitable for embedded applications due to its simple structure, high efficiency and high reliability. In addition, it provides a low cost solution in rectifying the AC voltage [94].

The model of the standalone DC generator is elaborated using a modular representation of the system based on the conventional model of two distinct DFIGs expressed in their own reference frames and combined in inverse coupling sequence. The system model bloc diagram is shown in Figure 8.2.

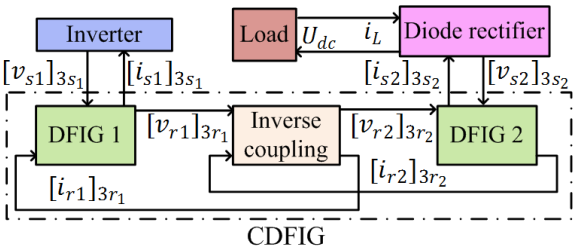

Figure 8.2: Global model of the standalone DC generator

DFIM1 operates as an autonomous voltage source and DFIM2 as a current source. The model and block diagram of the current source CDFIG are detailed in Section 1.3.2. The generator, including the CDFIG and the diode bridge connected to the DC capacitor, is a regulated autonomous voltage source. The loads connected to the grid can be modeled using an equivalent current source. The mechanical speed is considered to be a varying parameter imposed by external source, independently of load variation.

8.1.1 Diode bridge rectifier

The DC supply is derived by rectifying the AC output voltages of the three-phase CDFIG using a diode rectifier. Despite its apparent simplicity, this low cost solution is highly nonlinear and difficult to represent because the switching states are not controllable but depend on the three-phase stator currents of the Power machine M2. However a simplified model of the diode bridge can be elaborated under the assumption of "continuous conduction mode", ideal switches and no losses [74]. A generic model of the three-phase rectifier is presented in Figure 8.3.

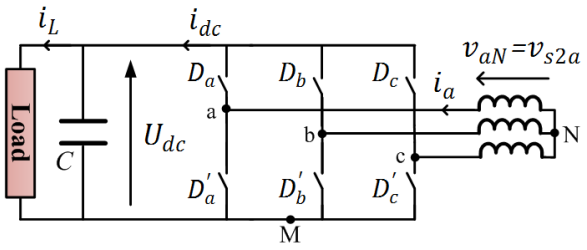

Figure 8.3: Generic model of a three-phase rectifier

This model is the dual form of the static converter modeled in paragraph 3.4.1 (Figure 3.9). Therefore, the voltage and current relationships remain valid. The only difference is that the switching functions associated with every bridge leg j ($j = a, b, c$) are Heaviside functions [74], [77]. k_j is the switching function associated with the leg j.

$$k_j = \begin{cases} 1 & \text{if } D_j \text{ is conducting and } D'_j \text{ is blocked} \\ & (i_j(t) > 0) \\ 0 & \text{if } D_j \text{ is blocked and } D'_j \text{ is conducting} \\ & (i_j(t) < 0) \end{cases} \tag{8.1}$$

Equation (8.2) computes the three-phase alternating voltages in terms of the DC voltage. Equation (8.3) describes the DC current in terms of the three-phase currents.

$$\begin{bmatrix} v_{s2a} \\ v_{s2b} \\ v_{s2c} \end{bmatrix} = \begin{bmatrix} v_{aN} \\ v_{bN} \\ v_{cN} \end{bmatrix} = \frac{U_{dc}}{3} \begin{bmatrix} 2 & -1 & -1 \\ -1 & 2 & -1 \\ -1 & -1 & 2 \end{bmatrix} \begin{bmatrix} k_a \\ k_b \\ k_c \end{bmatrix} \tag{8.2}$$

$$i_{dc} = k_a i_a + k_b i_b + k_c i_c \tag{8.3}$$

Note that in Figure 8.3, the line currents are in opposition with those of the CDFIG model $[i_{s2}]_{3s_2}$ established previously (supersynchronous motor convention).

$$[i_{s2}]_{3s_2} = -[i]_3 \tag{8.4}$$

The diode bridge rectifier is modeled using (8.2), (8.3).
In order to reduce the voltage ripples, the rectifier is cascaded with a capacitor filter at the DC side. The DC bus model is described by the following relation, where i_L is the DC load current.

$$\frac{d}{dt}U_{dc} = \frac{1}{C}\left(i_{dc} - i_L\right) \tag{8.5}$$

The block diagram of the DC generator is illustrated in Figure 8.4.

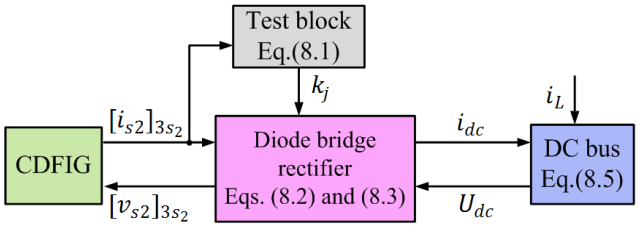

Figure 8.4: Block diagram of the standalone DC generator

Note that in case of a PWM rectifier, the "test block" does not exist. The switching functions k_j are directly applied to the rectifier by the controller.

8.2 Control strategy

In the proposed generating system, the output voltage of the DC generator is to be regulated at a constant level irrespective of load and speed variations. Based on the unified frame vector representation, a decoupled vector control of the system is elaborated. The control of the DC bus voltage is performed through hierarchical loops: an inner loop to adjust the stator currents of the CDFIG and then an outer loop dedicated to the DC voltage regulation. Since the rectifier considered is a diode bridge, only one degree of freedom is required to compensate the DC voltage. The other degree is manipulated to force the reference frame orientation [5].

Considering the unified Power machine synchronously rotating frame with the d-axis aligned along the stator current $\underline{i}_{s2}$, relation (8.6) is deduced. On the basis of a fundamental component model, the rectifier is equivalent to a resistance [88]. Thus, if the Park frame is chosen to cancel I_{s2q}, V_{s2q} is also canceled leading to (8.7).

$$I_{s2q} = 0 \quad \text{thus} \quad I_{s2d} = \underline{i}_{s2} \tag{8.6}$$

$$V_{s2q} = 0 \quad \text{thus} \quad V_{s2d} = \underline{v}_{s2} \tag{8.7}$$

Consequently, the CDFIG output active power is given by (8.8) in the mentioned rotating frame.

$$P_{s2} = \frac{3}{2}V_{s2d}I_{s2d} \tag{8.8}$$

Neglecting the converter losses (ideal model of the rectifier), the instantaneous AC power is equal to the DC power side. Then the power flow in the converter can be expressed as follows:

$$-\frac{3}{2}V_{s2d}I_{s2d} \simeq U_{dc}i_{dc} \tag{8.9}$$

Equation (8.9) describes a relation between the three-phase AC currents and DC current. The minus sign arises from the conventions adopted for the modeling of the system. Referring to (8.9) and the average model of the DC bus described by (8.5), it can be deduced that the output voltage U_{dc} can be controlled by action on the stator current d-component I_{s2d}. The stator current q-component constitutes a degree of freedom, and can be adjusted through (8.10) to force the vector orientation along the mentioned reference frame.

$$I_{s2q,ref} = 0 \tag{8.10}$$

Consequently the stator frame angle ξ_{s2} can be derived from a simple integral of the output frequency $\omega_{s2,ref}$. It does not have to be computed from stator current measurement, since the orientation of the reference frame is forced by the condition (8.10):

$$\xi_{s2} = \int \omega_{s2,ref} dt \tag{8.11}$$

As a result, the orientation is more stable and devoid of measurement noise and stator current harmonic distortion.

On the other side, a relation between the Control machine stator voltage $\underline{v}_{s1}$ and the Power machine stator current $\underline{i}_{s2}$ is established in Section 4.1. It is recalled hereinafter:

$$\begin{aligned}\underline{v}_{s1} = &-\frac{R_r L_{s1} L_{s2}}{M_{sr1} M_{sr2}}\underline{\dot{i}}_{s2} - \frac{L_{s2}}{M_{sr2}}\left(\frac{\sigma_p L_r L_{s1}}{M_{sr1}} - M_{sr1}\right)\frac{d}{dt}\underline{i}_{s2} + R_{s1}\underline{i}_{s1} + \frac{L_{s1}R_r}{M_{sr1}M_{sr2}}\underline{\Phi}_{s2} \\ &+ \left(\frac{L_r L_{s1}}{M_{sr1}M_{sr2}} - \frac{M_{sr1}}{M_{sr2}}\right)\frac{d}{dt}\underline{\Phi}_{s2} + j\left(g_c\omega_{s2}\frac{M_{sr1}L_{s2}}{M_{sr2}} - \omega_{r2}\frac{\sigma_p L_r L_{s1} L_{s2}}{M_{sr1}M_{sr2}}\right)\underline{i}_{s2} \\ &+ j\left(g_c\omega_{s2} - \omega_{r2}\right)L_{s1}\underline{i}_{s1} + j\left(\omega_{r2}\frac{L_r L_{s1}}{M_{sr1}M_{sr2}} - g_c\omega_{s2}\frac{M_{sr1}}{M_{sr2}}\right)\underline{\Phi}_{s2}\end{aligned} \tag{8.12}$$

Decomposing into *d-q* components in the adopted rotating frame yields to:

$$\frac{R_r L_{s1} L_{s2}}{M_{sr1} M_{sr2}}\dot{i}_{s2} + \frac{L_{s2}}{M_{sr2}}\left(\frac{\sigma_p L_r L_{s1}}{M_{sr1}} - M_{sr1}\right)\frac{d}{dt}I_{s2d} = -V_{s1d} + a_d = U_{s1d} \tag{8.13}$$

$$\frac{R_r L_{s1} L_{s2}}{M_{sr1} M_{sr2}}\dot{i}_{s2} + \frac{L_{s2}}{M_{sr2}}\left(\frac{\sigma_p L_r L_{s1}}{M_{sr1}} - M_{sr1}\right)\frac{d}{dt}I_{s2q} = -V_{s1q} + a_q = U_{s1q} \tag{8.14}$$

As noted, the two quantities $\underline{v}_{s1}$ and $\underline{i}_{s2}$ *d-q* components are linked by a first order

linear transfer function:

$$I_{s2d,q}(s) = \frac{K_p}{1+\tau_p s} U_{s1d,q}(s); \qquad K_p = \frac{M_{sr1}M_{sr2}}{R_r L_{s1} L_{s2}}; \qquad \tau_p = \left(\frac{\sigma_p L_r}{R_r} - \frac{M_{sr1}^2}{L_{s1} R_r} \right) \tag{8.15}$$

The d-q disturbances a_d and a_q, are given by:

$$\begin{aligned} a_d = {} & R_{s1} I_{s1d} + \frac{L_{s1} R_r}{M_{sr1} M_{sr2}} \Phi_{s2d} + \left(\frac{L_r L_{s1}}{M_{sr1} M_{sr2}} - \frac{M_{sr1}}{M_{sr2}} \right) \frac{d}{dt} \Phi_{s2d} - (g_c \omega_{s2} - \omega_{r2}) L_{s1} I_{s1q} \\ & - \left(\omega_{r2} \frac{L_r L_{s1}}{M_{sr1} M_{sr2}} - g_c \omega_{s2} \frac{M_{sr1}}{M_{sr2}} \right) \Phi_{s2q} \end{aligned} \tag{8.16}$$

$$\begin{aligned} a_q = {} & R_{s1} I_{s1q} + \frac{L_{s1} R_r}{M_{sr1} M_{sr2}} \Phi_{s2q} + \left(\frac{L_r L_{s1}}{M_{sr1} M_{sr2}} - \frac{M_{sr1}}{M_{sr2}} \right) \frac{d}{dt} \Phi_{s2q} + (g_c \omega_{s2} - \omega_{r2}) L_{s1} I_{s1d} \\ & + \left(g_c \omega_{s2} \frac{M_{sr1} L_{s2}}{M_{sr2}} - \omega_{r2} \frac{\sigma_p L_r L_{s1} L_{s2}}{M_{sr1} M_{sr2}} \right) I_{s2d} + \left(\omega_{r2} \frac{L_r L_{s1}}{M_{sr1} M_{sr2}} - g_c \omega_{s2} \frac{M_{sr1}}{M_{sr2}} \right) \Phi_{s2d} \end{aligned} \tag{8.17}$$

Therefore, the DFIM2 stator currents I_{s2d} and I_{s2q} are compensated through the action on the DFIM1 stator voltages V_{s1d} and V_{s1q} respectively. Based on the previous relations, the open loop transfer function of the DC generator in the predefined synchronous frame is derived in Figure 8.5.

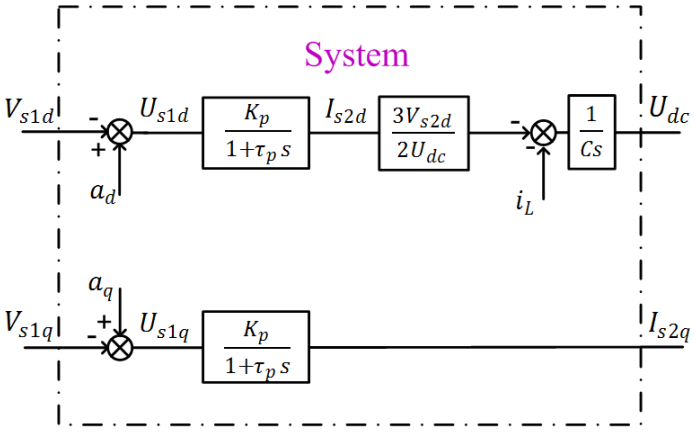

Figure 8.5: Open loop transfer function of the standalone DC generator

As can be seen, a vector control of the output DC voltage can be achieved through hierarchical loops using PI controllers (refer to Figure 8.8). The DC voltage is compensated in an outer control loop. The inner loop controls the stator current and forces the indirect orientation of the rotating frame. The stator current d-axis demand is provided by DC voltage controller. The outputs of the current controllers form the voltage references $V_{s1d,ref}, V_{s1q,ref}$ which are generated in the synchronously rotating frame. Compensation terms $\tilde{a}_d$, $\tilde{a}_q$ are added by a feed-forward action to the output of the PI controllers, to overcome the coupling perturbation and ensure good dynamic response and tracking of the current demands. Note that the terms

related to the stator flux do not need to be included since PI controllers are able to suppress their effect in steady state. The same applies to derivative terms that are nil at steady state.

8.2.1 Stator current control loop

The stator current control loop is recalled in Figure 8.6. The current compensator is designed in order to achieve the following specifications:

- Zero steady state error
- The settling time of the closed-loop is equal to the open-loop settling time.

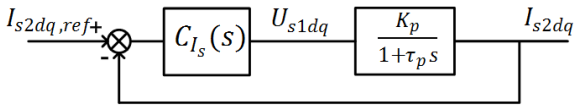

Figure 8.6: Stator current loop block diagram

Numerically, the closed-loop bandwidth is equal to $\omega_{I_s} = 164$ rad/s. $F_{I_s}(s)$ represents the inner loop dynamic.

$$F_{I_s}(s) = \frac{1}{1 + 0.0061s} \tag{8.18}$$

8.2.2 DC voltage control loop

The outer loop block diagram is illustrated in Figure 8.7. The stator current dynamic is taken into consideration. The open-loop transfer function is given by (8.19).

$$G_U(s) = \frac{U_{dc}}{I_{s2d,ref}} = F_{I_s}(s)\frac{3V_{s2q}}{2U_{dc}}\frac{1}{Cs} \tag{8.19}$$

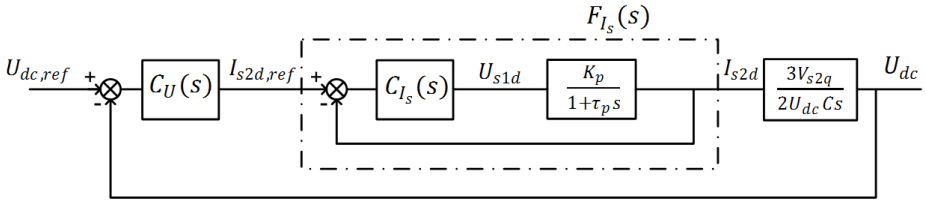

Figure 8.7: DC voltage loop block diagram

For a three-phase diode rectifier, the average output voltage is expressed as (8.20) [96].

$$U_{dc} = \frac{3\sqrt{6}}{\pi}V_{s2} \tag{8.20}$$

Therefore under the assumption of sinusoidal voltages the open-loop transfer function is approximated by (8.21).

$$G_U(s) = \frac{U_{dc}}{I_{s2d,ref}} = F_{I_s}(s)\frac{\pi}{2\sqrt{3}}\frac{1}{Cs} \tag{8.21}$$

The PI controller $C_U(s)$ is synthesized to meet the following specifications:

- Zero steady state error
- The cutoff frequency of the compensated open-loop transfer function $G_U(s)C_U$ is five times smaller than the inner loop cutoff frequency.

8.2.3 Control scheme

The control scheme of the standalone DC generator in the synchronous stator current oriented frame (dq_2) is shown in Figure 8.8.

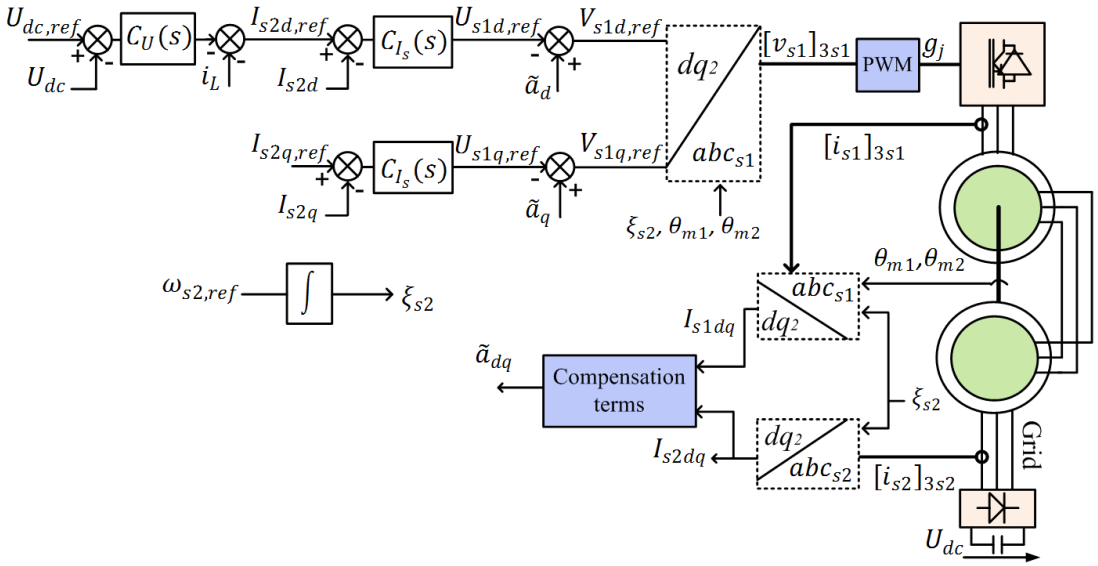

Figure 8.8: Control scheme of standalone DC generator

The measured DFIM2 stator currents are transformed from the original (abc_{s2}) to the rotating (dq_2) frame by performing a Clarke transformation followed by a Park transformation using (6.32). Besides, in order to compute the compensation terms, the DFIM1 stator currents are also changed from their natural (abc_{s1}) axes to the unified synchronous frame (dq_2) through a Clarke transformation followed by the vector transformation (6.33). Finally, to be able to pass the voltages at the output of the controller as reference values into the inverter, the signal have to be transformed into DFIM1 three-phase stator frame, using relation (6.34).

8.3 Simulation results

Simulation is done using Matlab/Simulink software. The control performances are tested for different loads at constant speed in a first place, then at constant load under speed variation. The output voltage must be adapted to the machine used for simulation (Appendix B.1, Section B.1). The HVDC is currently used in military aircraft platforms. Hence, the results are evaluated according to the MIL-STD-704F guidelines. The transient envelopes of the DC bus voltage as specified by this standard are shown in Figure 8.9

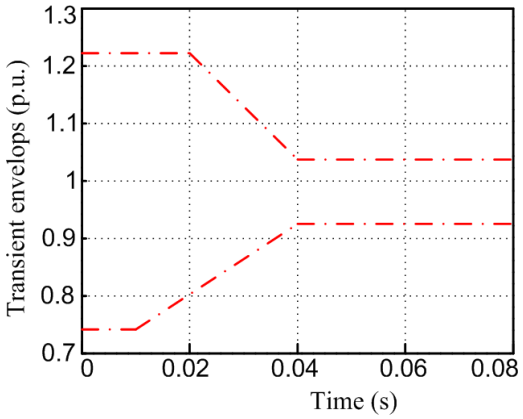

Figure 8.9: Transient envelopes of the DC voltage as specified by MIL-STD-704F

8.3.1 Simulation with load variation

In the first simulation test, the generator is driven at a constant speed (e.g. $\Omega = 1.1$p.u.) with a load varying from 10% up to 100% of the rated power. The results are collected in Figure 8.10. It can be seen that, in spite of load variations, the output DC voltage is properly regulated and its dynamic response (i.e. the transient and steady state response) remains within the limit envelops imposed by the MIL-STD-704F guidelines at steady state.

8.3.2 Simulation with speed variation

The simulation is performed at 60% of the nominal load with a rotor speed varying between -30% and $+30\%$ of the CDFIG synchronous speed ($\Omega_s = 1$p.u.). The response of the CDFIG to speed variations is illustrated in Figure 8.11. As observed the DC bus voltage is keeping a good track of its reference value irrespective of the speed disturbances. The limit bounds specified by the MIL-STD-704F are completely satisfied.

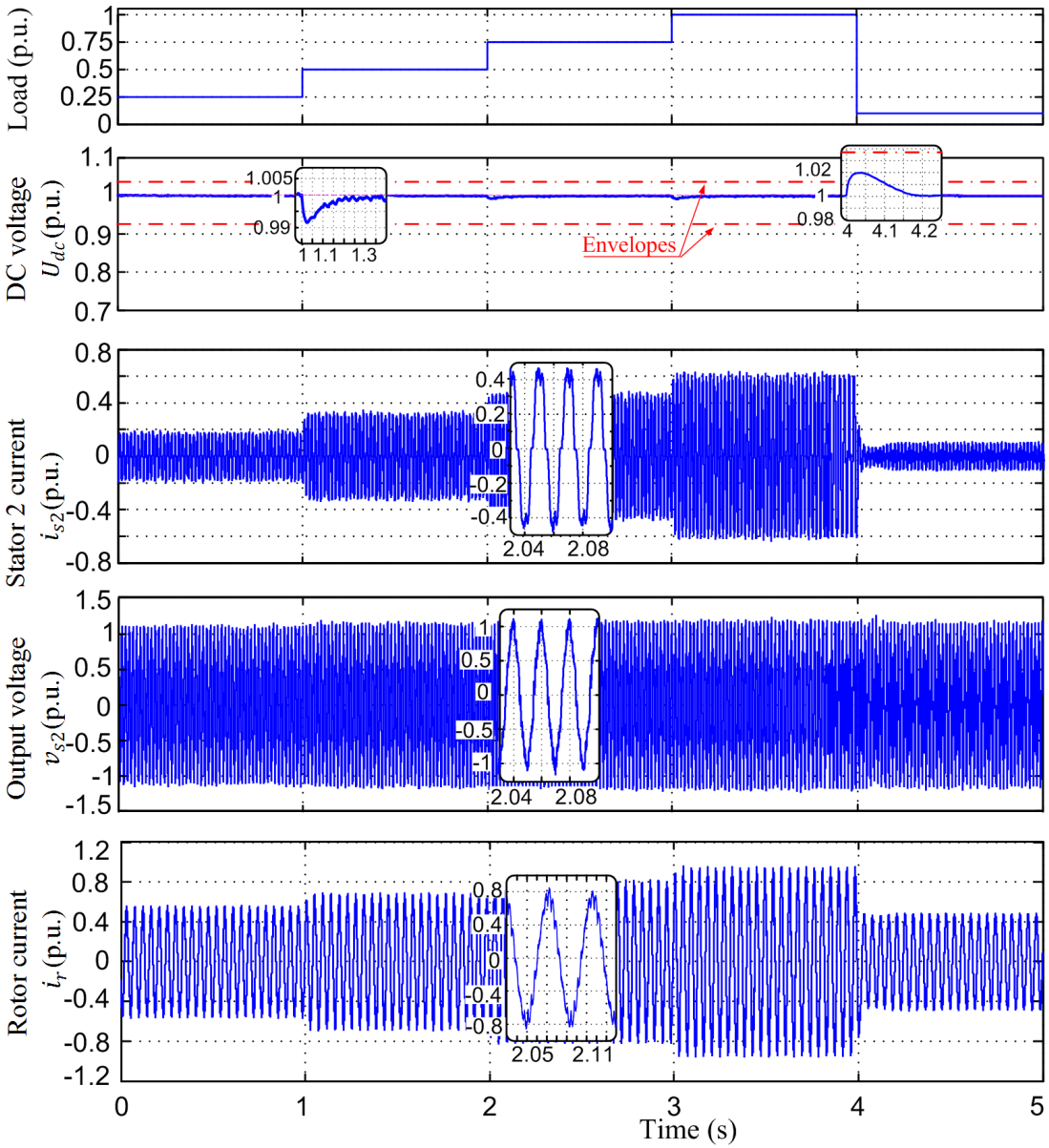

Figure 8.10: Response of the CDFIG under load variations

At this point, it is convenient to mention the advantage of this vector control approach, regarding the electric power quality generated at the machine side. In fact, despite the variable speed operation and the important amount of non linear loads, the controller induces quasi sinusoidal AC voltage and current at constant frequency (1p.u.) at the output of the CDFIG. This enhances the quality of the electric power generated by the machine. The output frequency ω_{s2} can be further adjusted to ensure the machine being operated below its rated voltage.

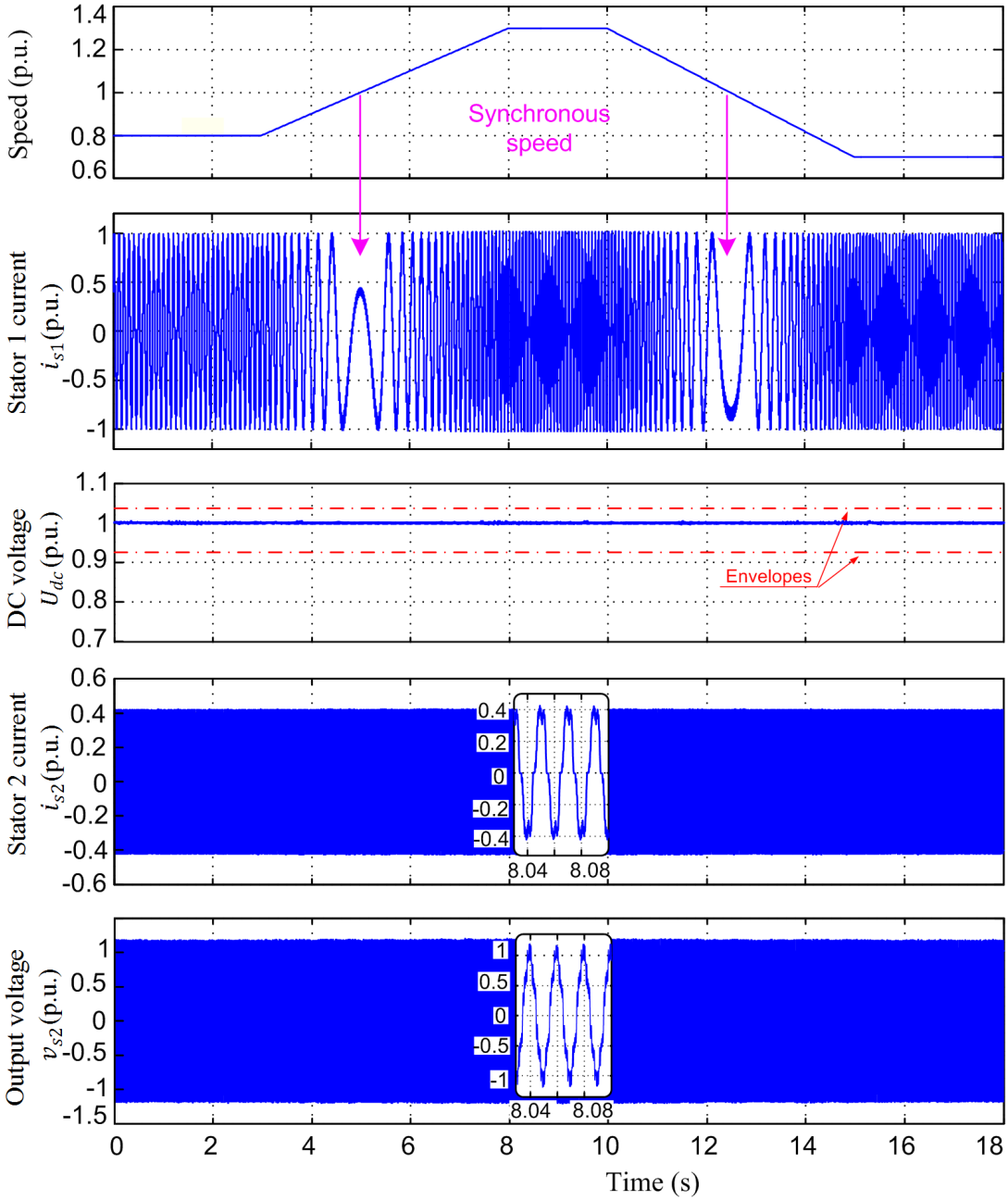

Figure 8.11: Response of the CDFIG under speed variation

Conclusion

This chapter presents the brushless CDFIG associated to a diode bridge rectifier to be used as a standalone DC generator. A modular representation of the system is presented first. Then the vector control of the DC bus voltage is studied. It is elaborated based on the representation of the CDFIG in the unified synchronous frame, and the steady state model of the diode rectifier. The controller consists of only two loops. The regulation of the output DC voltage is achieved by action on the Power machine stator current d-component. The q-component forms a degree of

freedom and is adjusted to force the indirect orientation of the rotating frame. The control approach is validated by simulation. The results prove the capability of the generator to operate properly over a wide range of load and speed variations.

Conclusion and Perspectives

Summary

This thesis is a contribution to the power sizing and the control of the CDFIG. With its brushless structure and reduced size converters, this variable speed constant frequency generator is an interesting solution for many industrial applications where high level of reliability is required. It shows commercial promises for either grid-connected or standalone operation.

The CDFIM model for simulation is based on a modular representation of the system. It is derived from the conventional Park model of two distinct wound rotor induction machines expressed in their own reference frame. The two DFIMs are interconnected through inverse rotor coupling sequence, this configuration being the most promising architecture for generating systems. The mathematical model of the machine is then expressed in a unified reference frame. This representation is convenient for the power sizing of the machine and it helps the control design of the generator in grid-connected and standalone applications.

The steady state operating limits of the CDFIM in terms of active and reactive powers are investigated in Part I. A rigorous generic analytic method is suggested to derive the CDFIM power margins. Limitations with regard to nominal quantities are considered. It is shown that the CDFIG is able to provide reactive power over a wide active power domain. For a given speed range the power capability of the machine is determined by the stator current maximum values. In under-excited mode the limiting variable is the Power machine stator current while in over-excited mode, the capacitive reactive power generation is limited by the Control machine stator current. The power limit area can be subject to additional limitations resulting from terminal voltage drops. The impact of magnetic circuit saturation is also investigated in the study, and a new limit bound is derived. As it is expected, saturation significantly limits the capability of the machine to generate reactive power because of significant effect on the the control current. The power capability limits of the CDFIG are tested experimentally using a laboratory scale machine. The experimental results validate

the proposed analytical approach with and without saturation. It shall be pointed that the reactive power capability of the CDFIM is reduced in comparison with the single DFIM.
The active-reactive power diagram developed in this manuscript is essential for the design and control of a generating unit in order to plan the reactive power resources and clarify the contribution of the machine to reactive power production required by grid codes. Particularly in wind energy systems where grid utilities require extended reactive power supply in support of grid voltage not only during voltage dips but also during steady-state operation.

The CDFIM is presented, in Part II, as a contender machine to replace the DFIM presently in use in most high power WECS. A new mean MPPT technique is applied to a grid-connected WT based on a CDFIG. The controlled unit generates the maximum constant power associated to the average value of the wind speed, predicted over a predefined interval. Thus, the impact of turbulence component is eliminated and the grid is fed by quasi-constant power irrespective of wind oscillations. Compared to the well-known instantaneous MPPT method, the proposed new strategy improves the quality of the injected power and decreases the stress on the grid side for network stability purposes. Nevertheless, the system efficiency is somewhat reduced as the controlled unit optimizes the power that refers to the slow varying component of the wind speed instead of its instantaneous value.
The complete model and control scheme of the integrated wind power plant are presented in this study. The active and reactive power flow are regulated by means of a new decoupled sensorless vector control based on a virtual flux orientation, applied to both converters. In addition to real power optimization, the generating unit is dynamically controlled to provide additional reactive power and ensure power factor regulation according to the new grid code requirements. In this regard, the steady state operating domain of the global generating unit is established. It is shown that the reactive power capability of the system can be enlarged by including the contribution of the GSC. The MPPT approaches are validated on Matlab/Simulink environment using a non stationary wind speed model based on spectral analysis.

Part III studies the CDFIG operating as an autonomous brushless generator supplying an isolated load. A particular application considered for simulation is the embedded aircraft power generation system. Two distribution networks are studied: the constant frequency AC network and the DC network. In the latter, the CDFIG is cascaded to a diode bridge rectifier. In both cases a decoupled vector control is implemented in the MSC and aims to adjust the output voltage irrespective of load and speed variations. Simulation with Matlab/Simulink software validates the performance

and efficiency of the controller. The control of the standalone generator feeding three-phase load is also validated by experiments with a laboratory scale CDFIM. The obtained results are satisfactory. The operation of the standalone CDFIG supplying unbalanced three-phase load is investigated too. Under this working condition, the output voltages become unbalanced and give rise to a negative sequence component. The classic vector control strategy does not provide the desired performance. Thus, advanced control schemes are proposed to balance the stator output voltage and reject the effect of the unbalanced load. Two compensation methods are elaborated. The first considers two rotating reference frames to control separately the positive and the negative sequence components of the rotor current. This control strategy uses conventional and easy to implement PI controllers. Nevertheless, it requires frame transformations and sequential decomposition of the rotor current, which can significantly increase the time delay and degrade the system stability. On that basis, a second compensation approach that deals with only one rotating frame is elaborated. It is based on a repetitive rotor current controller that regulates both the positive and negative components in the positive reference frame without involving sequence separation. Simulation with Matlab/Simulink attests of the feasibility and effectiveness of the two control methods to compensate voltage imbalance. It is pointed that all the control schemes developed, in this part, for the standalone generator are not restricted to the embedded aircraft industry. With minor modifications in the generating system model, they can be adopted to other autonomous applications such as wind energy and hydro power systems.

Prospects

The experimental and simulation results presented in this work give way to new prospects.

In this thesis, the CDFIM modeling is based on a Park first harmonic model of the induction machine with simplified assumptions. The mathematical model shall be improved by including the iron losses and taking into account the magnetic circuit saturation effect. It shall also include higher order harmonics for more accurate simulation.

Concerning the power sizing of the machine, the results have revealed the reduced capability of the generator to provide reactive power. This aspect is an important issue in generating system, particularly in grid-connected WECS. Hence, the following prospects are raised.

– The simplified limit curve expressions suggest that a possible revision of the design of the machine might yield to better performances in terms of power

capability. The reactive power generation can be substantially expanded by increasing the mutual reactance and decreasing the rotor reactance. Accordingly, research attentions and design procedures are needed to optimize the CDFIM design and improve its reactive power capability in order to meet the market demand and achieve a more compact structure with high power density.

– Another interesting point is to derive the appropriate combination of Power and Control machines that achieves the optimal reactive power generation domain of the cascade.

In grid-connected wind generating application, a new MPPT method is proposed to enhance the power quality by feeding quasi-constant power. In future work, advanced points can be considered.

– Testing the proposed algorithm under more severe conditions including fast or sudden variations in the wind speed.
– Finding new methods to improve the mean wind speed prediction method along with the choice of the interval length.
– Analyzing the impact of the mean MPPT strategy on the WT mechanical structure.
– Experimental validation of the mean MPPT approach and testing the control robustness to parametric uncertainties of the system.
– Studying the behavior of the CDFIG and control performance during grid faults. New control schemes shall be implemented for ride-through capability and participation to voltage regulation.

With regard to the CDFIG in standalone operation, several prospects come next.

– Validate experimentally the proposed control approaches and test the robustness to parametric variations and the performance of the controller with different type of loads for both AC and DC networks.
– Elaborate a coordinate control of the GSC and MSC to achieve simultaneously several control targets during unbalanced load (eliminate torque oscillation, current imbalance, etc...).
– During unbalanced operation, take into consideration the zero-sequence component for a grounded neutral point and its influence on the control performance.
– Finally, it is interesting to study the performance of the standalone generator during short circuit conditions.

Appendix A

Mathematical transformations

A.1 Clarke transformation

It is a transformation from a three-phase (abc) reference frame to a bi-phase ($\alpha\beta$) frame.

$$\begin{bmatrix} X_\alpha \\ X_\beta \\ X_o \end{bmatrix} = T_{23} \begin{bmatrix} x_a \\ x_b \\ x_c \end{bmatrix}, \qquad \begin{bmatrix} x_a \\ x_b \\ x_c \end{bmatrix} = T_{32} \begin{bmatrix} X_\alpha \\ X_\beta \\ X_o \end{bmatrix} \tag{A.1}$$

(A.2)

where

$$T_{23} = \frac{2}{3} \begin{bmatrix} 1 & -\frac{1}{2} & -\frac{1}{2} \\ 0 & \frac{\sqrt{3}}{2} & -\frac{\sqrt{3}}{2} \\ \frac{1}{2} & \frac{1}{2} & \frac{1}{2} \end{bmatrix}, \qquad T_{32} = \begin{bmatrix} 1 & 0 & 1 \\ -\frac{1}{2} & \frac{\sqrt{3}}{2} & 1 \\ -\frac{1}{2} & -\frac{\sqrt{3}}{2} & 1 \end{bmatrix}, \tag{A.3}$$

A.2 Park transformation

It describes a rotation of the coordinate

$$\begin{bmatrix} X_d \\ X_q \\ X_o \end{bmatrix} = P(\xi) \begin{bmatrix} X_\alpha \\ X_\beta \\ X_o \end{bmatrix}, \qquad \begin{bmatrix} X_\alpha \\ X_\beta \\ X_o \end{bmatrix} = P^{-1}(\xi) \begin{bmatrix} X_d \\ X_q \\ X_o \end{bmatrix} \tag{A.4}$$

where

$$P(\xi) = \begin{bmatrix} cos(\xi) & sin(\xi) & 0 \\ -sin(\xi) & cos(\xi) & 0 \\ 0 & 0 & 1 \end{bmatrix}, \qquad P^{-1}(\xi) = P(-\xi) \begin{bmatrix} cos(\xi) & -sin(\xi) & 0 \\ sin(\xi) & cos(\xi) & 0 \\ 0 & 0 & 1 \end{bmatrix}, \tag{A.5}$$

ξ denotes the angle between the (dq) rotating frame and the $(\alpha\beta)$ reference frame. In complex (phasor) form:

$$\underline{x} = X_q + jX_q = X_\alpha + jX_\beta \tag{A.6}$$

Thus, the Park transformation can be written as:

$$(\underline{x})_{dq} = e^{-j\xi}(\underline{x})_{\alpha\beta} \tag{A.7}$$

$$(\underline{x})_{\alpha\beta} = e^{j\xi}(\underline{x})_{dq} \tag{A.8}$$

Appendix B

Generating system parameters

B.1 Laboratory scale prototype

Machine parameters

The electric parameters of the laboratory prototype are identified according to the method described in [88].

Parameters	DFIM1	DFIM2	Units
Rated power active P_{s1n}, P_{s2n}	2.5	2.4	kW
Rated stator voltage V_{s1n}, V_{s2n}	230	220	V
Rated stator current I_{s1n}, I_{s2n}	5.5	5.5	A
Rated rotor current I_{r1n}, I_{r2n}	13	8	A
Rated rotor voltage V_{r1n}, V_{r2n}	100	150	V
Number of pole pairs p_1, p_2	2	2	-
Supply frequency	50	50	Hz
Stator resistance R_{s1}, R_{s2}	4.6576	1.2862	Ω
Rotor resistance R_{r1}, R_{r2}	0.9164	1.97	Ω
Stator self inductance l_{s1}, l_{s2}	0.3364	0.1908	Ω
Stator cyclic inductance L_{s1}, L_{s2}	473.277	268.54	mH
Rotor cyclic inductance L_{r1}, L_{r2}	81.072	138.21	mH
Rotor/stator mutual inductance M_{sr1}, M_{sr2}	191.43	182.76	mH
Stator to rotor turns ratio m_1, m_2	0.404	0.68	-
Point of regulation resistor R_{f1}, R_{f2}	10	20	kΩ
Point of regulation capacitor C_{f1}, C_{f2}	0.1	0.1	µF

Unbalanced load

Unbalanced resistive load: $R_a = 60.5, R_b = 201.66, R_c = 672.22\ \Omega$

DC side

DC bus $U_{dc} = 500$ V

Capacitor filter: $C = 2.2$ mF

B.2 Parameters of a 300 kW WECS

WT parameters

WT parameter	Value	Units
Rated power P_n	300	kW
Radius R_p	14	m
Gear box G	11	-
Combined moment of inertia J	2500	Kg.m^2
Cut-in wind speed v_{min}	4	m/s
Rated wind speed v_n	12	m/s
Maximum wind speed v_{max}	16	m/s
Air density ρ	1.22	Kg/m^3
Viscous friction f_v	2.2×10^{-3}	N $\cdot$ m $\cdot$ s/rad

CDFIM parameters

The cascaded machine is based on two identical DFIMs with the following parameters

Parameters	Value	Units
Rated power active P_{sn}	300	kW
Rated stator voltage V_{sn}	220	V
Rated stator current I_{sn}	530	A
Rated rotor current I_{rn},	365	A
Rated rotor voltage V_{rn}	317	V
Number of pole pairs p	2	-
Supply frequency	50	Hz
Stator resistance R_s	12.4	mΩ
Rotor resistance R_r	12.4	mΩ
Stator cyclic inductance L_s	4.1	mH
Rotor cyclic inductance L_r	8.496	mH
Rotor/stator mutual inductance M_{sr}	5.77	mH
Point of regulation resistor R_{f1}	1	kΩ
Point of regulation capacitor C_{f1}	2	µF

Back-to-back converter

DC-link voltage: $U_{dc} = 700$ V

Filter: $R_f = 0.01\ \Omega$, $L_f = 1$ mH

Capacitor: $C = 25$ mF

Appendix C

Simulation results for a 300 kW standalone CDFIG

C.1 CDFIG feeding a constant frequency grid

The simulation results under load variations with a lagging PF=0.9 are presented in Figure C.1.

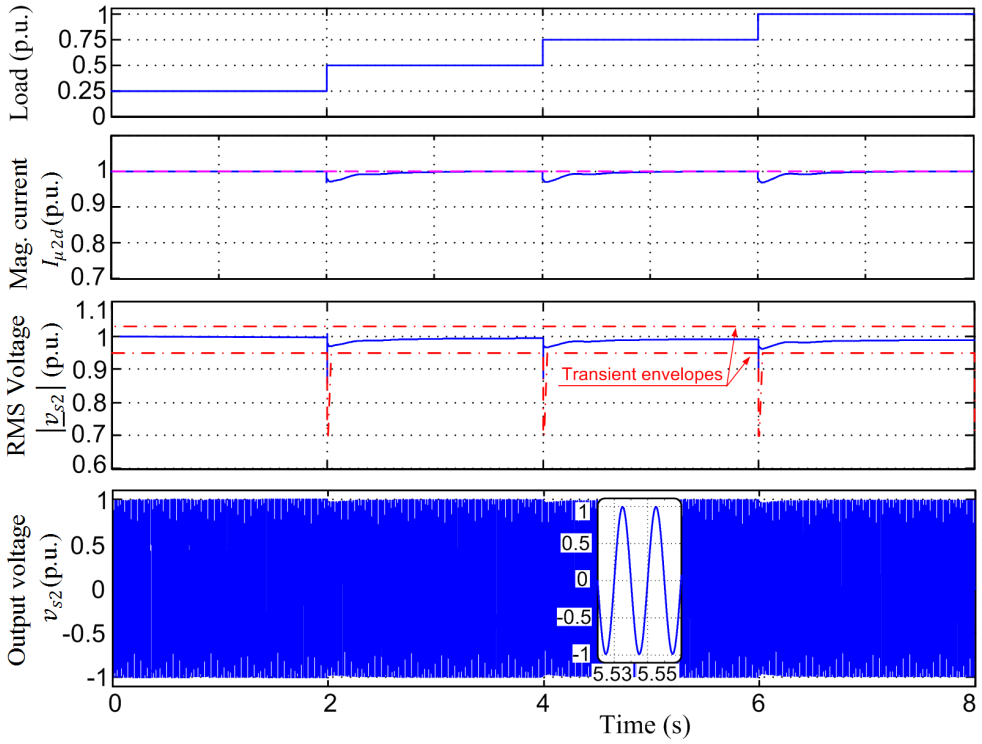

Figure C.1: Response of the CDFIG under load variation

The simulation results under speed variations at P_{max} are illustrated in Figure C.2.

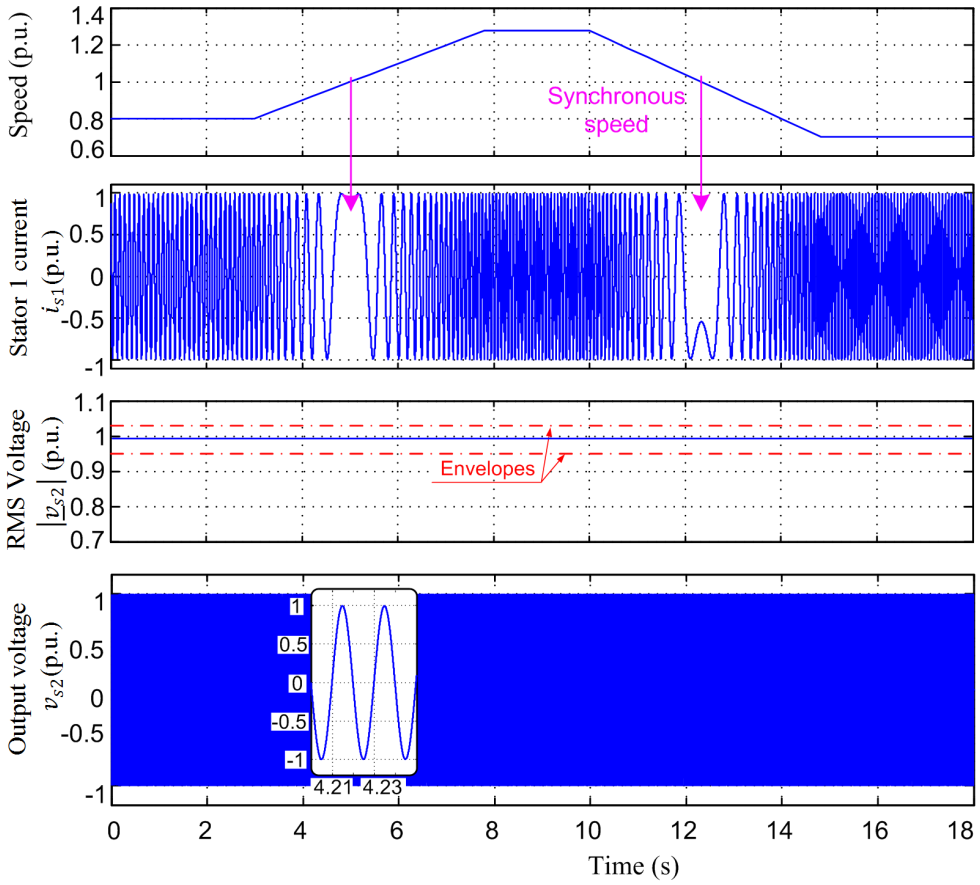

Figure C.2: Response of the CDFIG under speed variation

The simulation results during three-phase unbalanced load condition (70% load imbalance) are collected in Figure C.3.

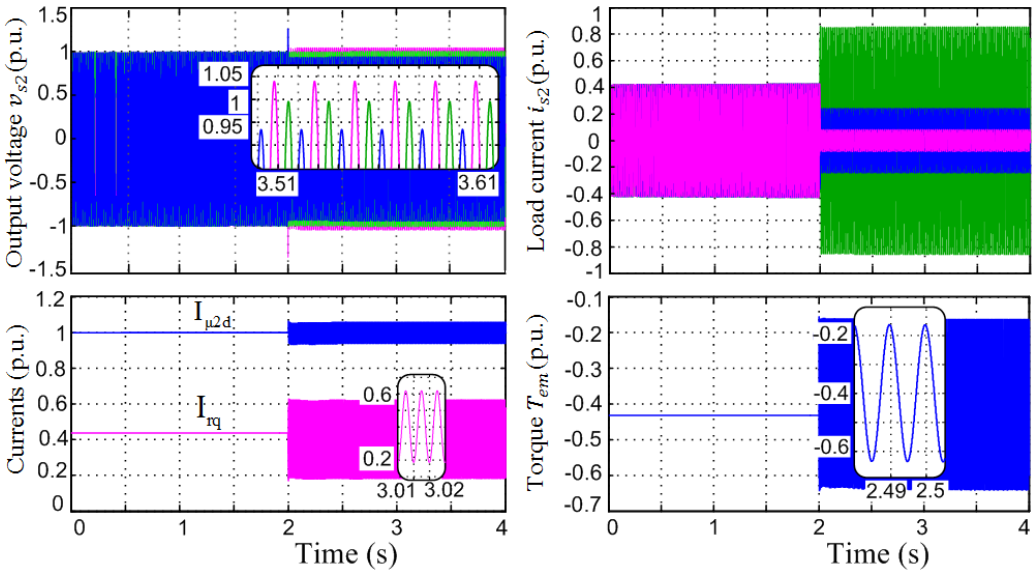

Figure C.3: Response of the CDFIG under load imbalance

C.2 CDFIG feeding unbalanced standalone load

The results of the compensation method based on dual rotating frames are given in Figure C.4.

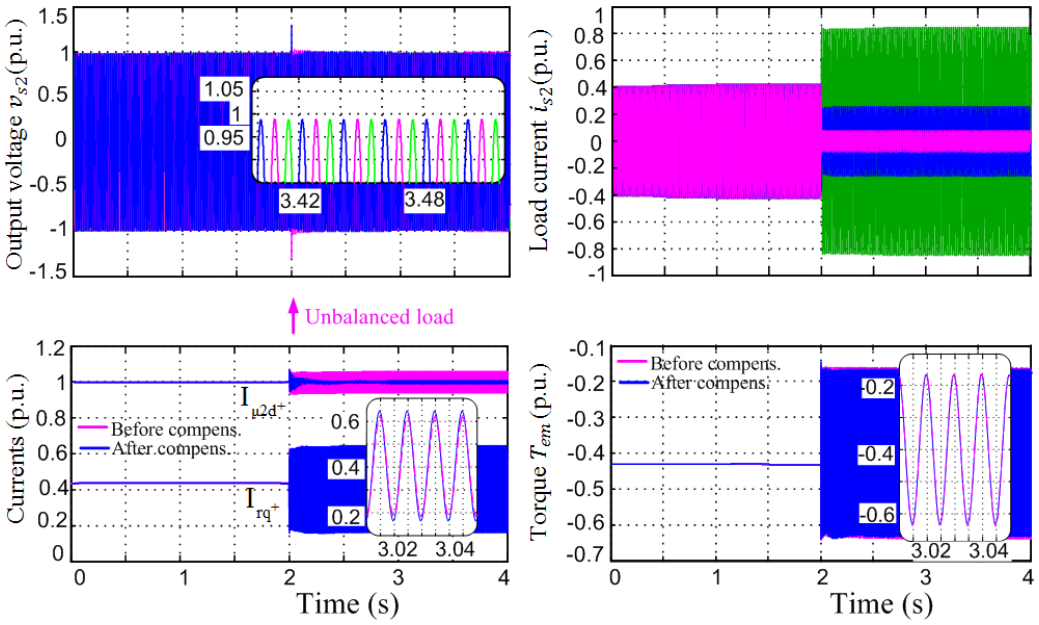

Figure C.4: Simulation results of the proposed dual rotating frames compensation strategy

The results corresponding tho the repetitive control strategy are depicted in Figure C.5.

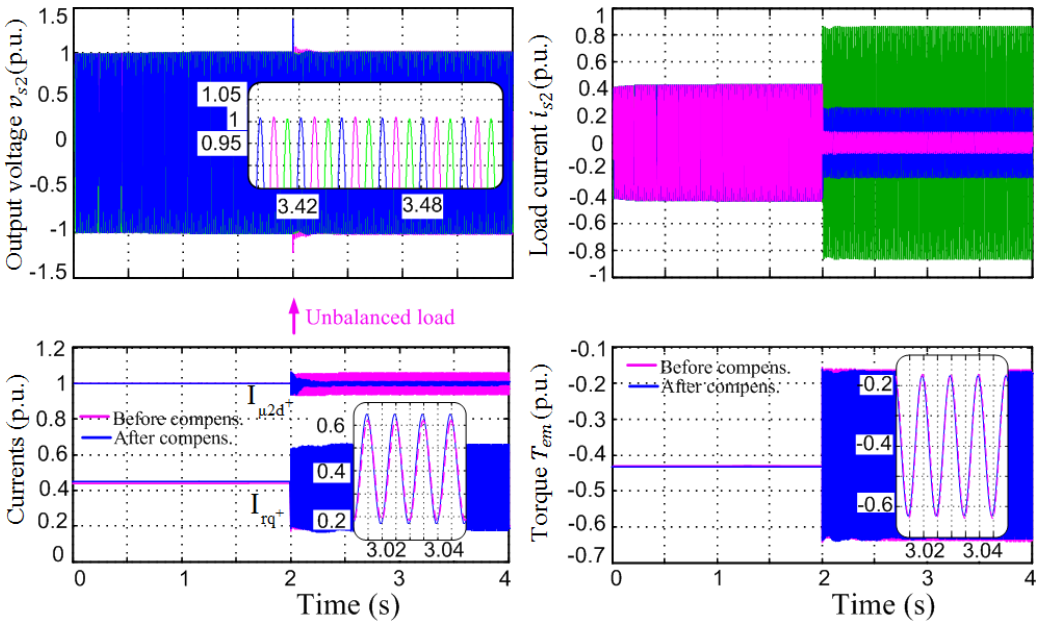

Figure C.5: Simulation results of the proposed repetitive control compensation strategy

C.3 CDFIG supplying an isolated DC grid

The simulation results during load variations are presented in Figure C.6.

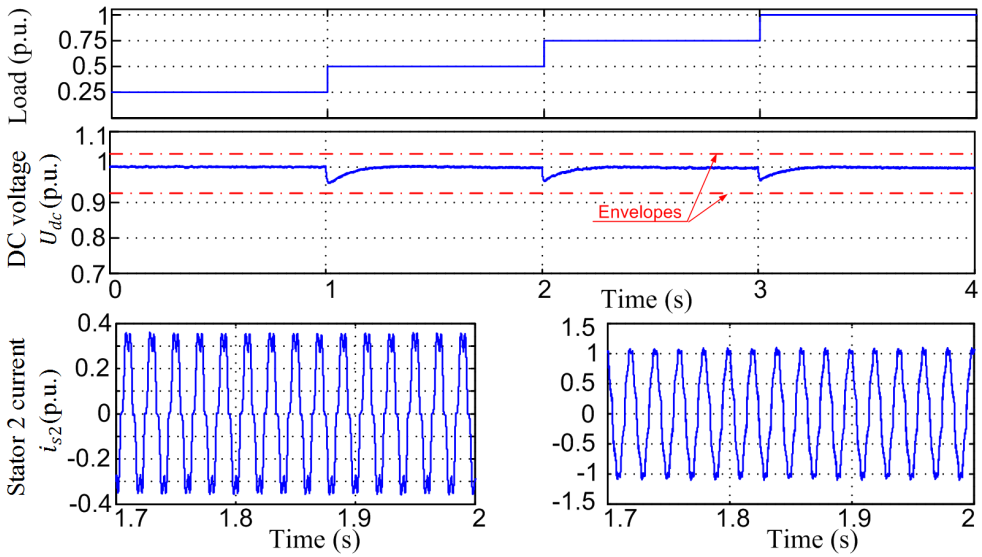

Figure C.6: Response of the CDFIG under load variations

The simulation results at 50% of the nominal load during speed variations are illustrated in Figure C.7.

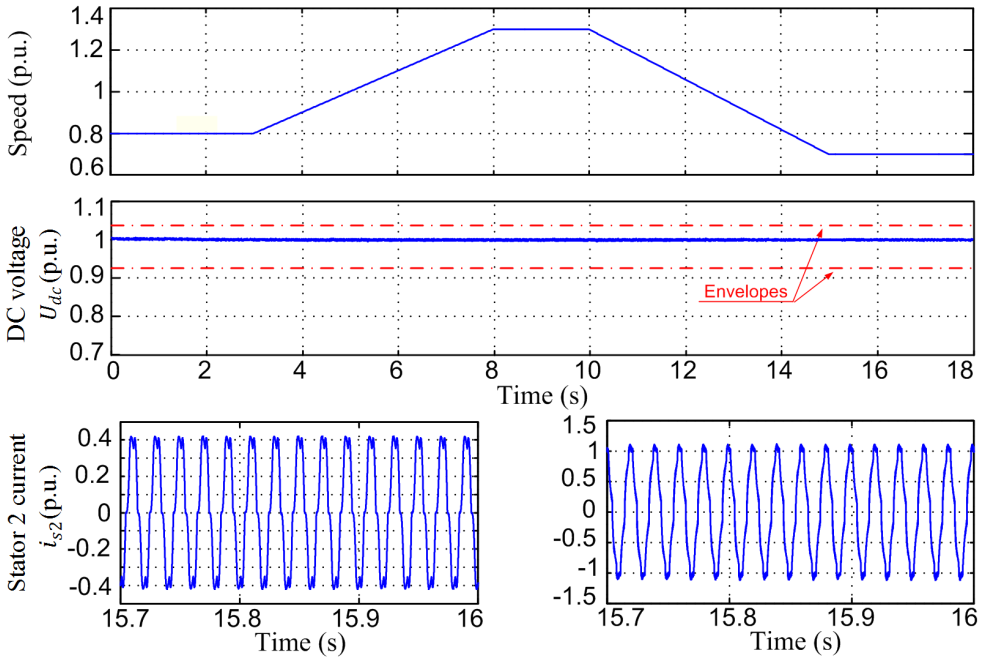

Figure C.7: Response of the CDFIG under speed variation

As in the case of the laboratory scale machine, the above results show a good dynamic behavior of the controller. The system is properly regulated and the output quantities are tracking their reference value in accordance with the grid code requisites.

Bibliography

[1] *Red Electrica de Espana: PO 12.2, PO 12.3.*

[2] E.S. Abdin and W. Xu. Control design and dynamic performance analysis of a wind turbine-induction generator unit. *IEEE Transactions on Energy Conversion*, 15(1):91–96, Mar 2000.

[3] A.G. Abo-Khalil and L. Dong-Choon. MPPT Control of Wind Generation Systems Based on Estimated Wind Speed Using SVR. *Industrial Electronics, IEEE Transactions on*, 55(3):1489 –1490, march 2008.

[4] N. Abu-Tabak. *Stabilité dynamique des systèmes électriques multimachines: modélisation, commande, observation et simulation (Dynamic stability of multi-machine electric systems: modeling, control, observation and simulation).* PhD thesis, L'école doctorale Électronique, Èlectrotechnique, Automatique de Lyon, 19 Novembre 2008.

[5] M. E. Achkar, R. Mbayed, G. Salloum, S. Le Ballois, N. Patin, and E. Monmasson. Control of a cascaded doubly fed induction generator supplying an isolated DC grid. In *Industrial Electronics Society, IECON 2015 - 41st Annual Conference of the IEEE*, pages 000737–000742, Nov 2015.

[6] M. E. Achkar, R. Mbayed, G. Salloum, N. Patin, S. Le Ballois, and E. Monmasson. Modeling and control of a stand alone cascaded doubly fed induction generator supplying an isolated load. In *Power Electronics and Applications (EPE'15 ECCE-Europe), 2015 17th European Conference on*, pages 1–10, Sept 2015.

[7] M. El Achkar, R. Mbayed, G. Salloum, S. Le Ballois, and E. Monmasson. Generic study of the power capability of a cascaded doubly fed induction machine. *International Journal of Electrical Power and Energy Systems*, 86:61 – 70, 2017.

[8] M. El Achkar, R. Mbayed, G. Salloum, S. Leballois, N. Patin, and E. Monmasson. new approach for maximum power tracking of a variable speed wt at constant power generation, under normal grid conditions. In *Mediterranean Electrotechnical Conference (MELECON), 2014 17th IEEE.*

[9] M. El Achkar, R. Mbayed, G. Salloum, S. Leballois, N. Patin, and E. Monmasson. New voltage sensorless approach for maximum constant power tracking of WECS based on a cascaded DFIG. In *Industrial Electronics Society, IECON 2014 - 40th Annual Conference of the IEEE*, pages 2185–2191, Oct 2014.

[10] M. El Achkar, R. Mbayed, G. Salloum, N. Patin, S. Le Ballois, and E. Monmasson. Power operating domain of a cascaded doubly fed induction machine. *Mathematics and Computers in Simulation*, 130:142 – 154, 2016.

[11] M. Adamowicz, R. Strzelecki, and D. Wojciechowski. Steady State Analysis of Twin Stator Cascaded Doubly Fed Induction Generator. In *Compatibility in Power Electronics, 2007. CPE '07*, pages 1–5, May 2007.

[12] S. EL Aimani. *Modélisation de différentes technologies d'éoliennes intégrées dans un réseau de moyenne tension (Modeling of different wind energy technologies integrated into a medium voltage network).* PhD thesis, Ecole centrale de Lille et Université des sciences et technologies de Lille, 6 December 2004.

[13] H. Amaris and M. Alonso. Coordinated reactive power management in power networks with wind turbines and FACTS devices. *Energy Conversion and Management*, 52(7):2575 – 2586, 2011.

[14] C.R. Avery, S.G. Burrow, and P.H. Mellor. Electrical generation and distribution for the more electric aircraft. In *Universities Power Engineering Conference, 2007. UPEC 2007. 42nd International*, pages 1007–1012, Sept 2007.

[15] S.M. Barakati, M. Kazerani, and J.D. Aplevich. A mechanical speed-sensorless maximum power tracking control for a wind turbine system including a matrix converter. In *Power and Energy Society General Meeting - Conversion and Delivery of Electrical Energy in the 21st Century, 2008 IEEE*, pages 1–8, July 2008.

[16] D. Basic, J. G. Zhu, and G. Boardman. Modeling and steady-state performance analysis of a brushless doubly fed twin stator induction generator. In *Proc. Australasian Power Engineering Conferencde AUPEC02, Melbourne Australia*, Sept-Oct 2002.

[17] B. Beltran, T. Ahmed-Ali, and M.E.H. Benbouzid. Sliding mode power control of variable-speed wind energy conversion systems. *IEEE Transactions on Energy Conversion*, 23(2):551–558, June 2008.

[18] R.E. Betz and M.G. Jovanovic. Theoretical analysis of control properties for the brushless doubly fed reluctance machine. *IEEE Transactions on Energy Conversion*, 17(3):332–339, Sep 2002.

[19] F.D. Bianchi, H. De Battista, and R.J. Mantz. *Wind turbine control systems: principles, modelling and gain scheduling design*. Advances in industrial control. Springer, 2007.

[20] M.S. Boger, A.K. Wallace, and R. Spee. Investigation of appropriate pole number combinations for brushless doubly fed machines applied to pump drives. *IEEE Transactions on Industry Applications*, 32(1):189–194, Jan 1996.

[21] A. Boglietti, A. Cavagnino, A. Tenconi, and S. Vaschetto. The safety critical electric machines and drives in the more electric aircraft: A survey. In *Industrial Electronics, 2009. IECON '09. 35th Annual Conference of IEEE*, pages 2587–2594, Nov 2009.

[22] T. Brekken and N. Mohan. A novel doubly-fed induction wind generator control scheme for reactive power control and torque pulsation compensation under unbalanced grid voltage conditions. In *Power Electronics Specialist Conference, 2003. PESC '03. 2003 IEEE 34th Annual*, volume 2, pages 760–764 vol.2, June 2003.

[23] T.K.A. Brekken and N. Mohan. Control of a doubly fed induction wind generator under unbalanced grid voltage conditions. *Energy Conversion, IEEE Transactions on*, 22(1):129–135, March 2007.

[24] A.R.W Broadway. Cageless induction machine. *Electrical Engineers, Proceedings of the Institution of*, 118(11):1593–1600, November 1971.

[25] A.R.W Broadway and L. Burbridge. Self-cascaded machine: a low-speed motor or high-frequency brushless alternator. *Electrical Engineers, Proceedings of the Institution of*, 117(7):1277–1290, July 1970.

[26] H. Camblong, I. Martinez de Alegria, M. Rodriguez, and G. Abad. Experimental evaluation of wind turbines maximum power point tracking controllers. *Energy Conversion and Management*, 47(18–19):2846 – 2858, 2006.

[27] A. Carlsson. *The Back to Back Converter: Control and Design*. Department of Industrial Electrical Engineering and Automation, Lund Institute of Technology, 1998.

[28] J. Chen, W. Zhang, B. Chen, and Y. Ma. Improved vector control of brushless doubly fed induction generator under unbalanced grid conditions for offshore wind power generation. *Energy Conversion, IEEE Transactions on*, PP(99):1–10, 2015.

[29] M. Cheng and Y. Zhu. The state of the art of wind energy conversion systems and technologies: A review. *Energy Conversion and Management*, 88:332 – 347, 2014.

[30] J.S. Cloyd. Status of the United States Air Force's More Electric Aircraft initiative. *IEEE Aerospace and Electronic Systems Magazine*, 13(4):17–22, Apr 1998.

[31] C.D. Cook and B.H. Smith. Stability and stabilisation of doubly-fed single-frame cascade induction machines. *Electrical Engineers, Proceedings of the Institution of*, 126(11):1168 –1174, november 1979.

[32] A.P. Deshpande, B.N. Chaudhari, and V.N. Pande. Design and simulation of back-to-back converter for modern wind energy generation system using dspace. In *Power, Signals, Controls and Computation (EPSCICON), 2012 International Conference on*, pages 1 –6, jan. 2012.

[33] M. El Achkar, R. Mbayed, G. Salloum, S. Leballois, N. Patin, and E. Monmasson. Power Capability study of a Casded Doubly Fed Indeuction Machine. In *11th International Conference on Modeling and Simulation of Electric Machines, Converters and Systems (Electrimacs14)*, Valencia, Spain, 19-22 May 2014.

[34] H.M. El-helw and S.B. Tennakoon. Vector control of a doubly fed induction generator for standalone wind energy application. In *Wind Power to the Grid - EPE Wind Energy Chapter 1st Seminar, 2008. EPE-WECS 2008*, pages 1–6, March 2008.

[35] A. Emadi and M. Ehsani. Aircraft power systems: technology, state of the art, and future trends. *Aerospace and Electronic Systems Magazine, IEEE*, 15(1):28–32, Jan 2000.

[36] S. Engelhardt, I. Erlich, C. Feltes, J. Kretschmann, and F. Shewarega. Reactive Power Capability of Wind Turbines Based on Doubly Fed Induction Generators. *Energy Conversion, IEEE Transactions on*, 26(1):364–372, 2011.

[37] I. Erlich, W. Winter, and A. Dittrich. Advanced grid requirements for the integration of wind turbines into the german transmission system. In *Power Engineering Society General Meeting, 2006. IEEE*, page 7 pp., 2006.

[38] G. Esfandiari, M. Ebrahimi, A. Tabesh, and M. Esmaeilzadeh. Dynamic Modeling and Analysis of Cascaded DFIMs in an Arbitrary Reference Frame. *IEEE Transactions on Energy Conversion*, 30(3):999–1007, Sept 2015.

[39] H. Fathabadi. Control of a DFIG-based wind energy conversion system operating under harmonically distorted unbalanced grid voltage along with nonsinusoidal rotor injection conditions. *Energy Conversion and Management*, 84:60 – 72, 2014.

[40] B.A. Francis. *A course in H_∞ control theory*, volume 88 of *Lecture notes in control and information sciences*. Springer-Verlag, 1987.

[41] B.A. Francis and W. M. Wonham. The internal model principle for linear multivariable regulators. *Applied Mathematics and Optimization*, 2(2):170–194, 1975.

[42] A.H. Ghorashi, S.S. Murthy, B. Singh, and Bhim Singh. Analysis of wind driven grid connected induction generators under unbalanced grid conditions. *Energy Conversion, IEEE Transactions on*, 9(2):217–223, Jun 1994.

[43] E. Gomez, J. Alvaro Fuentes, A. Molina, F. Ruz, F. Jimenez, and G. Eolica S.A. Results using different reactive power definitions for wind turbines submitted to voltage dips: Application to the spanish grid code. In *Power Systems Conference and Exposition, 2006. PSCE '06. 2006 IEEE PES*, pages 768–775, 2006.

[44] I.A. Gowaid, A.S. Abdel-Khalik, A.M. Massoud, and S. Ahmed. Ride-Through Capability of Grid-Connected Brushless Cascade DFIG Wind Turbines in Faulty Grid Conditions; A Comparative Study. *Sustainable Energy, IEEE Transactions on*, 4(4):1002–1015, Oct 2013.

[45] S. Hara, T. Omata, and M. Nakano. Synthesis of repetitive control systems and its application. In *Decision and Control, 1985 24th IEEE Conference on*, pages 1387–1392, Dec 1985.

[46] S. Hara, Y. Yamamoto, T. Omata, and Michio Nakano. Repetitive control system: a new type servo system for periodic exogenous signals. *Automatic Control, IEEE Transactions on*, 33(7):659–668, Jul 1988.

[47] B. Hopfensperger, D.J. Atkinson, and R. A Lakin. Stator flux oriented control of a cascaded doubly-fed induction machine. *Electric Power Applications, IEE Proceedings*, 146(6):597–605, Nov 1999.

[48] B. Hopfensperger, D.J. Atkinson, and R. A Lakin. Combined magnetising flux oriented control of the cascaded doubly-fed induction machine. *Electric Power Applications, IEE Proceedings*, 148(4):354–362, Jul 2001.

[49] B. Hopfensperger and G.J. Atkinson. Doubly-fed a.c. machines: classification and comparison. In *EPE Conf. Proceedings, Gratz, Austria, 2001.*

[50] A.M. Howlader, N. Urasaki, A. Yona, T. Senjyu, and A.Y. Saber. A review of output power smoothing methods for wind energy conversion systems. *Renewable and Sustainable Energy Reviews*, 26:135 – 146, 2013.

[51] Hunt. A new type of induction motor. *Electrical Engineers, Journal of the Institution of*, 39(186):648–667, September 1907.

[52] T. Inoue, M. Nakano, T. Kubo, S. Mutsumoto, and H. Baba. High accuracy control of a proton synchrotron magnet power supply. In *Proceedings of the 8th World Congress of IFAC*, 1981.

[53] D. Izquierdo, R. Azcona, F. del Cerro, C. Fernández, and B. Delicado. Electrical power distribution system (HV270DC), for application in more electric aircraft. In *Applied Power Electronics Conference and Exposition (APEC), 2010 Twenty-Fifth Annual IEEE*, pages 1300–1305, Feb 2010.

[54] E. Jeitani, G. Salloum, R. Mbayed, and E. Monmasson. Repetitive control of an unbalanced standalone doubly-fed induction generator. In *Renewable Energies for Developing Countries (REDEC), 2012 International Conference on*, pages 1–5, Nov 2012.

[55] J.Hu, J. Zhu, and D.G. Dorrell. A new control method of cascaded brushless doubly fed induction generators using direct power control. *Energy Conversion, IEEE Transactions on*, 29(3):771–779, Sept 2014.

[56] G.L. Johnson. *Wind energy systems*. Prentice Hall PTR, 1985.

[57] M. G. Jovanovic and R. E. Betz. Power factor control using brushless doubly fed reluctance machines. In *Industry Applications Conference, 2000. Conference Record of the 2000 IEEE*, volume 1, pages 523–530 vol.1, 2000.

[58] M.G. Jovanovic, R.E. Betz, and J. Yu. The use of doubly fed reluctance machines for large pumps and wind turbines. *IEEE Transactions on Industry Applications*, 38(6):1508–1516, Nov 2002.

[59] S. Kato, N. Hoshi, and K. Oguchi. Small-scale hydropower. *Industry Applications Magazine, IEEE*, 9(4):32–38, July 2003.

[60] M. Kayikci and J.V. Milanovic. Reactive Power Control Strategies for DFIG-Based Plants. *Energy Conversion, IEEE Transactions on*, 22(2):389–396, June 2007.

[61] R.J. Kennett. Integrated drive generators for aircraft. *Electronics and Power*, 17(2):73–76, February 1971.

[62] F. Khatounian, E. Monmasson, F. Berthereau, E. Delaleau, and J.-P. Louis. Control of a doubly fed induction generator for aircraft application. In *Industrial Electronics Society, 2003. IECON '03. The 29th Annual Conference of the IEEE*, volume 3, pages 2711–2716 Vol.3, Nov 2003.

[63] A.M. Knight, R.E. Betz, W.K. Song, and D G. Dorrell. Brushless doubly-fed reluctance machine rotor design. In *Energy Conversion Congress and Exposition (ECCE), 2012 IEEE*, pages 2308–2315, Sept 2012.

[64] A. Kusko and C. Somuah. Speed Control of a Single-Frame Cascade Induction Motor with Slip-Power Pump Back. *Industry Applications, IEEE Transactions on*, IA-14(2):97–105, March 1978.

[65] J. Leyva-Ramos, G. Escobar, P.R. Martinez, and P. Mattavelli. Analog circuits to implement repetitive controllers for tracking and disturbance rejection of periodic signals. *Circuits and Systems II: Express Briefs, IEEE Transactions on*, 52(8):466–470, Aug 2005.

[66] T. Long, S. Shao, E. Abdi, R.A. McMahon, and S. Liu. Asymmetrical low-voltage ride through of brushless doubly fed induction generators for the wind power generation. *Energy Conversion, IEEE Transactions on*, 28(3):502–511, Sept 2013.

[67] T. Long, S.i Shao, P. Malliband, E. Abdi, and R.A. McMahon. Crowbarless fault ride-through of the brushless doubly fed induction generator in a wind turbine under symmetrical voltage dips. *Industrial Electronics, IEEE Transactions on*, 60(7):2833–2841, July 2013.

[68] J. Makhoul. Linear prediction: A tutorial review. *Proceedings of the IEEE*, 63(4):561–580, 1975.

[69] M. Malinowski. *Sensorless Control Strategies for Three-Phase PWM Rectifiers*. PhD thesis, Warsaw University of Technology, 2001.

[70] M. Malinowski, M. Jasinski, and M.P. Kazmierkowski. Simple direct power control of three-phase PWM rectifier using space-vector modulation (DPC-SVM). *Industrial Electronics, IEEE Transactions on*, 51(2):447 – 454, April 2004.

[71] M. Malinowski, M. P. Kazmierkowski, S. Hansen, F. Blaabjerg, and G.D. Marques. Virtual-flux-based direct power control of three-phase PWM rectifiers. *IEEE Transactions on Industry Applications*, 37(4):1019–1027, Jul 2001.

[72] M. Malinowski and M.P. Kazmierkowski. Simulation study of virtual flux based direct power control for three-phase PWM rectifiers. In *Industrial Electronics Society, 2000. IECON 2000. 26th Annual Conference of the IEEE*, volume 4, pages 2620–2625 vol.4, 2000.

[73] M. Malinowski, G. Marques, M. Cichowlas, and M.P. Kazmierkowski. New direct power control of three-phase PWM boost rectifiers under distorted and imbalanced line voltage conditions. In *Industrial Electronics, 2003. ISIE '03. 2003 IEEE International Symposium on*, volume 1, pages 438–443 vol. 1, June 2003.

[74] G.D. Marques. A simple and accurate system simulation of three-phase diode rectifiers. In *Industrial Electronics Society, 1998. IECON '98. Proceedings of the 24th Annual Conference of the IEEE*, volume 1, pages 416–421 vol.1, Aug 1998.

[75] P. Mattavelli and F.P. Marafao. Repetitive-based control for selective harmonic compensation in active power filters. *Industrial Electronics, IEEE Transactions on*, 51(5):1018–1024, Oct 2004.

[76] R. Mbayed. *Contribution to the Control of the Hybrid Excitation Synchronous Machine for Embedded Applications*. PhD thesis, University of Cergy Pontoise, 2012.

[77] R. Mbayed, G. Salloum, L. Vido, E. Monmasson, and M. Gabsi. Control of a hybrid excitation synchronous generator connected to a diode bridge rectifier supplying a dc bus in embedded applications. *Electric Power Applications, IET*, 7(1):68–76, Jan 2013.

[78] R. Mbayed, G. Salloum, L. Vido, E. Monmasson, and M. Gabsi. Hybrid excitation synchronous generator in embedded applications: Modeling and control. *Mathematics and Computers in Simulation*, 90:60–73, 2013.

[79] R.A. McMahon, P.C. Roberts, X. Wang, and P.J. Tavner. Performance of BDFM as generator and motor. *Electric Power Applications, IEE Proceedings*, 153(2):289–299, March 2006.

[80] J. Mohammadi, S. Afsharnia, and S. Vaez-Zadeh. Efficient fault-ride-through control strategy of DFIG-based wind turbines during the grid faults. *Energy Conversion and Management*, 78:88 – 95, 2014.

[81] I. Moir. More-electric aircraft-system considerations. In *Electrical Machines and Systems for the More Electric Aircraft (Ref. No. 1999/180), IEE Colloquium on*, pages 10/1–10/9, 1999.

[82] S. Morimoto, H. Nakayama, M. Sanada, and Y. Takeda. Sensorless output maximization control for variable-speed wind generation system using IPMSG. In *Industry Applications Conference, 2003. 38th IAS Annual Meeting. Conference Record of the*, volume 3, pages 1464–1471 vol.3, Oct 2003.

[83] E. Muljadi, D. Yildirim, T. Batan, and C.P. Butterfield. Understanding the unbalanced-voltage problem in wind turbine generation. In *Industry Applications Conference, 1999. Thirty-Fourth IAS Annual Meeting. Conference Record of the 1999 IEEE*, volume 2, pages 1359–1365 vol.2, 1999.

[84] S. Muller, M. Deicke, and R. W. De Doncker. Adjustable speed generators for wind turbines based on doubly-fed induction machines and 4-quadrant IGBT converters linked to the rotor. In *Industry Applications Conference, 2000. Conference Record of the 2000 IEEE*, volume 4, pages 2249–2254 vol.4, Oct 2000.

[85] C. Nichita, D. Luca, B. Dakyo, and E. Ceanga. Large band simulation of the wind speed for real time wind turbine simulators. *Energy Conversion, IEEE Transactions on*, 17(4):523–529, 2002.

[86] T.H. Ortmeyer and W.U. Borger. Control of Cascaded Doubly Fed Machines for Generator Applications. *Power Apparatus and Systems, IEEE Transactions on*, PAS-103(9):2564–2571, Sept 1984.

[87] T.H. Ortmeyer and W.U. Borger. Control of control of cascaded doubly fed machines for generator applications. *Power Apparatus and Systems, IEEE Transactions on*, PAS-103(9):2564–2571, Sept 1984.

[88] N. Patin. *Analyse d'architectures, modélisation et commande de geńérateurs pour réseaux autonomes. Application aux générateurs de bord d'avions (Analyse of architecture, modeling and control of generator for autonomy power network).* PhD thesis, Ecole Normale Supérieure de Cachan, 2006.

[89] N. Patin, J.-P. Louis, and E. Monmasson. Control of a stand-alone variable speed constant frequency generator based on a doubly-fed induction generator. *EPE Journal*, 16(4):37–43, 2006.

[90] N. Patin, E. Monmasson, and J.-P. Louis. Active filtering applied to a doubly-fed induction generator supplying nonlinear loads on isolated grid. In *Power Electronics and Applications, 2005 European Conference on*, pages 10 pp.–p.10, Sept 2005.

[91] N. Patin, E. Monmasson, and J.-P. Louis. Modeling and Control of a Cascaded Doubly Fed Induction Generator Dedicated to Isolated Grids. *Industrial Electronics, IEEE Transactions on*, 56(10):4207 –4219, oct. 2009.

[92] N. Patin, E. Monmasson, and J.-P. Louis. Modeling and control of a cascaded doubly-fed induction generator based on dynamical equivalent circuits. *Mathematics and Computers in Simulation*, 81(2):225 – 238, 2010.

[93] N. Patin, E. Monmasson, and J.P. Louis. Analysis and control of a cascaded doubly-fed induction generator. In *Industrial Electronics Society, IECON 2005. 31st Annual Conference of IEEE*, nov. 2005.

[94] N. Patin, L. Vido, E. Monmasson, J.-P. Louis, M. Gabsi, and M. Lecrivain. Control of a hybrid excitation synchronous generator for aircraft applications. *Industrial Electronics, IEEE Transactions on*, 55(10):3772–3783, Oct 2008.

[95] W. Pearson. The more electric/all electric aircraft-a military fast jet perspective. In *All Electric Aircraft (Digest No. 1998/260), IEE Colloquium on*, pages 5/1–5/7, Jun 1998.

[96] P. Pejovic. *Three-Phase Diode Rectifiers with Low Harmonics*, chapter 2. Springer US, 2007.

[97] R. Pena, R. Cardenas, E. Escobar, J. Clare, and P. Wheeler. Control system for unbalanced operation of stand-alone doubly fed induction generators. *Energy Conversion, IEEE Transactions on*, 22(2):544–545, June 2007.

[98] R. Pena, R. Cardenas, E. Escobar, J. Clare, and P. Wheeler. Control strategy for a Doubly-Fed Induction Generator feeding an unbalanced grid or stand-alone load. *Electric Power Systems Research*, 79(2):355 – 364, 2009.

[99] R. Pena, J.C. Clare, and G.M. Asher. A doubly fed induction generator using back-to-back PWM converters supplying an isolated load from a variable speed wind turbine. *Electric Power Applications, IEE Proceedings* -, 143(5):380–387, Sep 1996.

[100] R. Pena, J.C. Clare, and G.M. Asher. Doubly fed induction generator using back-to-back PWM converters and its application to variable-speed wind-energy generation. *Electric Power Applications, IEE Proceedings*, 143(3):231 –241, May 1996.

[101] V.-T. Phan, S.-H. Kwak, and H.-H. Lee. An improved control method for dfig-based wind system supplying unbalanced stand-alone loads. In *Industrial Electronics, 2009. ISIE 2009. IEEE International Symposium on*, pages 1081–1086, July 2009.

[102] V.-T. Phan and H.-H. Lee. Control Strategy for Harmonic Elimination in Stand-Alone DFIG Applications With Nonlinear Loads. *Power Electronics, IEEE Transactions on*, 26(9):2662–2675, Sept 2011.

[103] V.-T. Phan and H.-H. Lee. Improved predictive current control for unbalanced stand-alone doubly-fed induction generator-based wind power systems. *Electric Power Applications, IET*, 5(3):275–287, March 2011.

[104] V.-T. Phan, T. Logenthiran, W.L. Woo, D. Atkinson, and V. Pickert. Analysis and compensation of voltage unbalance of a DFIG using predictive rotor current control. *International Journal of Electrical Power and Energy Systems*, 75:8 – 18, 2016.

[105] F. Poitiers, T. Bouaouiche, and M. Machmoum. Advanced control of a doubly-fed induction generator for wind energy conversion. *Electric Power Systems Research*, 79(7):1085 – 1096, 2009.

[106] J. Poza, E. Oyarbide, and D. Roye. New vector control algorithm for brushless doubly-fed machines. In *Industrial Electronics Society, IEEE 2002 28th Annual Conference of the, IECON 02*, volume 2, pages 1138–1143 vol.2, Nov 2002.

[107] J. Poza, E. Oyarbide, D. Roye, and M. Rodriguez. Unified reference frame dq model of the brushless doubly fed machine. *Electric Power Applications, IEE Proceedings*, 153(5):726–734, September 2006.

[108] J. Poza, E. Oyarbide, I. Sarasola, and M. Rodriguez. Vector control design and experimental evaluation for the brushless doubly fed machine. *Electric Power Applications, IET*, 3(4):247 –256, july 2009.

[109] K. Protsenko and X. Dewei. Modeling and control of brushless doubly-fed induction generators in wind energy applications. *Power Electronics, IEEE Transactions on*, 23(3):1191–1197, May 2008.

[110] W. Qiao, W. Zhou, J.M. Aller, and R.G. Harley. Wind Speed Estimation Based Sensorless Output Maximization Control for a Wind Turbine Driving a DFIG. *IEEE Transactions on Power Electronics*, 23(3):1156–1169, May 2008.

[111] R.E.J. Quigley. More electric aircraft. In *Applied Power Electronics Conference and Exposition, 1993. APEC '93. Conference Proceedings 1993., Eighth Annual*, pages 906–911, Mar 1993.

[112] M. Rahimi and M. Parniani. Grid-fault ride-through analysis and control of wind turbines with doubly fed induction generators. *Electric Power Systems Research*, 80(2):184 – 195, 2010.

[113] G.M. Raimondi, T. Sawata, M. Holme, A. Barton, G. White, J. Coles, P.H. Mellor, and N. Sidell. Aircraft embedded generation systems. In *Power Electronics, Machines and Drives, 2002. International Conference on (Conf. Publ. No. 487)*, pages 217–222, June 2002.

[114] D. Ramuz, M. Camara, M. Sebeloue, O. Tamarin, F. Roubaud, H. Clergeot, and J.-M. Kauffmann. Modelling and simulation of a doubly fed induction generator in stand alone variable speed hydro turbine. In *Power Electronics and Applications, 2005 European Conference on*, pages 10 pp.–P.10, 2005.

[115] G.H. Riahy and M. Abedi. Short term wind speed forecasting for wind turbine applications using linear prediction method. *Renewable Energy*, 33(1):35 – 41, 2008.

[116] P.C. Roberts, R.A. McMahon, P.J. Tavner, J.M. Maciejowski, and T.J. Flack. Equivalent circuit for the brushless doubly fed machine (BDFM) including parameter estimation and experimental verification. *IEE Proceedings - Electric Power Applications*, 152(4):933–942, July 2005.

[117] X. Roboam. New trends and challenges of electrical networks embedded in more electrical aircraft. In *Industrial Electronics (ISIE), 2011 IEEE International Symposium on*, pages 26–31, June 2011.

[118] I. Sarasola, J. Poza, E. Oyarbide, and M.A. Rodriguez. Stability Analysis of a Brushless Doubly-Fed Machine under Closed Loop Scalar Current Control. In *IEEE Industrial Electronics, IECON 2006 - 32nd Annual Conference on*, pages 1527–1532, Nov 2006.

[119] I. Scian, D. G. Dorrell, and P. J. Holik. Assessment of losses in a brushless doubly-fed reluctance machine. *IEEE Transactions on Magnetics*, 42(10):3425–3427, Oct 2006.

[120] T. Senjyu, R. Sakamoto, N. Urasaki, T. Funabashi, H. Fujita, and H. Sekine. Output power leveling of wind turbine generator for all operating regions by pitch angle control. *IEEE Transactions on Energy Conversion*, 21(2):467–475, June 2006.

[121] S. Shao, E. Abdi, F. Barati, and R. McMahon. Stator-flux-oriented vector control for brushless doubly fed induction generator. *Industrial Electronics, IEEE Transactions on*, 56(10):4220–4228, Oct 2009.

[122] S. Shao, E. Abdi, F. Barati, and R. McMahon. Stator-flux-oriented vector control for brushless doubly fed induction generator. *Industrial Electronics, IEEE Transactions on*, 56(10):4220–4228, Oct 2009.

[123] S. Shao, T. Long, E. Abdi, and R.A. McMahon. Dynamic control of the brushless doubly fed induction generator under unbalanced operation. *Industrial Electronics, IEEE Transactions on*, 60(6):2465–2476, June 2013.

[124] J.G. Slootweg, H. Polinder, and W.L. Kling. Representing wind turbine electrical generating systems in fundamental frequency simulations. *IEEE Transactions on Energy Conversion*, 18(4):516–524, Dec 2003.

[125] C.R. Spitzer. The All-Electric Aircraft: A Systems View and Proposed NASA Research Programs. *IEEE Transactions on Aerospace and Electronic Systems*, AES-20(3):261–266, May 1984.

[126] C.P. Steinmetz. Operating alternating motors, August 3 1897. US Patent 587,340.

[127] M. Suwan, T. Neumann, C. Feltes, and I. Erlich. Educational experimental rig for Doubly-Fed Induction Generator based wind turbine. In *Power and Energy Society General Meeting, 2012 IEEE*, pages 1–8, 2012.

[128] A. Tapia, G. Tapia, J.X. Ostolaza, and J.R. Saenz. Modeling and control of a wind turbine driven doubly fed induction generator. *Energy Conversion, IEEE Transactions on*, 18(2):194–204, June 2003.

[129] A. P. Tennakoon, J.B. Ekanayake, A. Atputharajah, and S.G. Abeyratne. Capability Chart of a Doubly Fed Induction Generation based on its ratings and stability margin. In *Universities Power Engineering Conference (UPEC), 2010 45th International*, pages 1–5, 2010.

[130] R. Teodorescu, M. Liserre, and P. Rodríguez. *Grid Converters for Photovoltaic and Wind Power Systems*. Wiley - IEEE. Wiley, 2011.

[131] S. Tohidi, H. Oraee, M.R. Zolghadri, S. Shao, and P. Tavner. Analysis and enhancement of low-voltage ride-through capability of brushless doubly fed induction generator. *Industrial Electronics, IEEE Transactions on*, 60(3):1146–1155, March 2013.

[132] S. Tohidi, P. Tavner, R. McMahon, H. Oraee, M.R. Zolghadri, S. Shao, and E. Abdi. Low voltage ride-through of DFIG and brushless DFIG: Similarities and differences. *Electric Power Systems Research*, 110:64 – 72, 2014.

[133] M.-C. Tsai and W.-S. Yao. Design of a plug-in type repetitive controller for periodic inputs. *Control Systems Technology, IEEE Transactions on*, 10(4):547–555, Jul 2002.

[134] J. Usaola, P. Ledesma, J.M. Rodriguez, J.L. Fernandez, D. Beato, R. Iturbe, and J.R. Wilhelmi. Transient stability studies in grids with great wind power penetration. Modelling issues and operation requirements. In *Power Engineering Society General Meeting, 2003, IEEE*, volume 3, page 4 vol. 2666, july 2003.

[135] I. Van der Hoven. Power spectrum of horizontal wind speed in the frequency range from 0.0007 to 900 cycle per hour. *Journal of Meteorology*, 14:160–164, 1957.

[136] P. Verdelho and G.D. Marques. DC voltage control and stability analysis of PWM-voltage-type reversible rectifiers. *Industrial Electronics, IEEE Transactions on*, 45(2):263 –273, apr 1998.

[137] A. K. Wallace, R. Spee, and G. C. Alexander. The brushless doubly-fed machine: its advantages, applications and design methods. In *Electrical Machines and Drives, 1993. Sixth International Conference on (Conf. Publ. No. 376)*, pages 511–517, Sep 1993.

[138] J.A. Weimer. The role of electric machines and drives in the more electric aircraft. In *Electric Machines and Drives Conference, 2003. IEMDC'03. IEEE International*, volume 1, pages 11–15 vol.1, June 2003.

[139] M. Wilch, V.S. Pappala, S.N. Singh, and I. Erlich. Reactive Power Generation by DFIG Based Wind Farms with AC Grid Connection. In *Power Tech, 2007 IEEE Lausanne*, pages 626–632, 2007.

[140] S. Williamson, A.C. Ferreira, and A.K. Wallace. Generalised theory of the brushless doubly-fed machine. I. Analysis. *IEE Proceedings - Electric Power Applications*, 144(2):111–122, Mar 1997.

[141] F. Xiong and X. Wang. Design and performance analysis of a brushless doubly-fed machine for stand-alone ship shaft generator systems. In *Electrical and Control Engineering (ICECE), 2011 International Conference on*, pages 2114–2117, Sept 2011.

[142] L. Xu. Coordinated Control of DFIG's Rotor and Grid Side Converters During Network Unbalance. *Power Electronics, IEEE Transactions on*, 23(3):1041–1049, May 2008.

[143] L. Xu. Enhanced Control and Operation of DFIG-Based Wind Farms During Network Unbalance. *Energy Conversion, IEEE Transactions on*, 23(4):1073–1081, Dec 2008.

[144] L. Xu, F. Liang, and T. A. Lipo. Transient model of a doubly excited reluctance motor. *IEEE Transactions on Energy Conversion*, 6(1):126–133, Mar 1991.

[145] L. Xu, Y. Tang, and L. Ye. Comparison study of rotor structures of doubly excited brushless reluctance machine by finite element analysis. *IEEE Transactions on Energy Conversion*, 9(1):165–172, Mar 1994.

[146] L. Xu and F. Wang. Comparative study of magnetic coupling for a doubly fed brushless machine with reluctance and cage rotors. In *Industry Applications Conference, 1997. Thirty-Second IAS Annual Meeting, IAS '97., Conference Record of the 1997 IEEE*, volume 1, pages 326–332 vol.1, Oct 1997.

[147] L. Xu and Y. Wang. Dynamic Modeling and Control of DFIG-Based Wind Turbines Under Unbalanced Network Conditions. *Power Systems, IEEE Transactions on*, 22(1):314–323, Feb 2007.

[148] M. Yamamoto and O. Motoyoshi. Active and reactive power control for doubly-fed wound rotor induction generator. *IEEE Transactions on Power Electronics*, 6(4):624–629, Oct 1991.

[149] Y. Yamamoto. *Essays on Control: Perspectives in the Theory and its Applications*, chapter Learning Control and Related Problems in Infinite-Dimensional Systems, pages 191–222. Birkhäuser Boston, Boston, MA, 1993.

[150] H. Zhang, C. Saudemont, B. Robyns, N. Huttin, and R. Meuret. Stability analysis on the dc power distribution system of more electric aircraft. In *Power Electronics and Motion Control Conference, 2008. EPE-PEMC 2008. 13th*, pages 1523–1528, Sept 2008.

Publications

Communications at international conferences with a lecturer committee

M. EL Achkar, R. Mbayed, G. Salloum, S. Leballois, N. Patin, and E. Monmasson. New approach for Maximum Power Tracking of a variable speed WT at constant power generation, under normal grid conditions. *17th IEEE Mediterranean Electrotechnical Conference (MELECON 2014)*, pp. 553-559, Beirut, Lebanon.

M. EL Achkar, R. Mbayed, G. Salloum, S. Le Ballois, N. Patin, and E. Monmasson. Power Capability Study of a Cascaded Doubly Fed Induction Machine. *11th International Conference on Modeling and Simulation of Electric Machines, Converters and Systems (ELECTRIMACS 2014)*, Valencia, Spain.

M. EL Achkar, R. Mbayed, G. Salloum, S. Le Ballois, N. Patin, and E. Monmasson. New voltage sensorless approach for Maximum Constant Power Tracking of WECS based on a Cascaded DFIG. *40th Annual Conference of the IEEE Industrial Electronics Society, (IECON 2014)*, pp. 2185-2191, Dallas, Texas.

M. EL Achkar, R. Mbayed, G. Salloum, S. Le Ballois, N. Patin, and E. Monmasson. Modeling and control of a stand alone Cascaded Doubly Fed Induction Generator supplying an isolated load. *17th European Conference on Power Electronics and Applications (EPE'15 ECCE-Europe)*, pp. 1-10, Geneva, Switzerland.

M. EL Achkar, R. Mbayed, G. Salloum, S. Le Ballois, N. Patin, and E. Monmasson. Control of a Cascaded Doubly Fed Induction Generator supplying an isolated DC grid. *41st Annual Conference of the IEEE Industrial Electronics Society (IECON 2015)*, pp. 737-742, Yokohama, Japan.

Articles at international journals with a lecturer committee

M. EL Achkar, R. Mbayed, G. Salloum, N. Patin, S. Le Ballois, and E. Monmasson. Power operating domain of a cascaded doubly fed induction machine. *Mathematics and Computers in Simulation, Elsevier*, 142:154-130. DOI: 10.1016/j.matcom.2015.02.002.

M. EL Achkar, R. Mbayed, G. Salloum, S. Le Ballois, and E. Monmasson. Generic study of the power capability of a cascaded doubly fed induction machine. *International Journal of Electrical Power and Energy Systems, Elsevier*, 61:70-86. DOI: 10.1016/j.ijepes.2016.09.011.